ISSN 1816-8957

No. 30, February 2022

Scientific Drilling

Reports on Deep Earth Sampling and Monitoring

The open-access ICDP and IODP journal • www.scientific-drilling.net

Editorial preface

Dear Reader,

This issue of your journal *Scientific Drilling* focusses on key aspects of geological rock cycling processes that have been addressed by drilling projects or that are on the agenda for the near future. It includes one study on orogenic exhumation, deformation, and emplacement of deep crustal metamorphic rocks in the Scandinavian Caledonicdes on the one hand (**p. 43**) and highlights on the other how mountains are affected by the most powerful abrasional mechanism – glacial erosion – and the related sediment deposition. Under favorable geological conditions and continuous long recording such sediment archives preserve important environmental information. In this respect, one science report highlights paleontological evidence from the tropics collected over decades of deep drilling in Colombia (**p. 1**), and another one is on the overdeepened Aare Valley in Switzerland that preserves sediment records throughout repeated glacial cycles (**p. 17**). In addition, a workshop report (**p. 101**) lays out the ambitious plan to recover Antarctic glacio-marine strata through sea-ice to shed light on the stability of ice sheets as a whole Two methodological studies, one on semiquantitative sediment characterization by smear slides (**p. 59**) and the other on laser ablation-inductively coupled plasma mass spectrometry on board D/V *Chikyu* (**p. 75**), complete this issue of *Scientific Drilling*. We wish you inspiring entertainment with this issue and look forward to new articles being published for the scientific drilling community in the forthcoming fall issue.

Your Editors

Ulrich Harms, Thomas Wiersberg, Jan Behrmann, Tomoaki Morishita, and Will Sager

Aims & scope

Scientific Drilling (SD) is a multidisciplinary journal focused on bringing the latest science and news from the scientific drilling and related programmes to the geosciences community. Scientific Drilling delivers peer-reviewed science reports from recently completed and ongoing international scientific drilling projects. The journal also includes reports on engineering developments, technical developments, workshops, progress reports, and news and updates from the community.

Editorial board

Additional information

ISSN 1816-8957 | eISSN 1816-3459

Copernicus Publications
The Innovative Open Access Publisher

Copernicus Publications
Bahnhofsallee 1e
37081 Göttingen
Germany
Phone: +49 551 90 03 39 0
Fax: +49 551 90 03 39 70

editorial@copernicus.org
production@copernicus.org

https://publications.copernicus.org

View the online library or learn more about Scientific Drilling on:
www.scientific-drilling.net

Cover figure: View northeastwards in the Barberton Greenstone Belt of South Africa, where the ICDP project BASE (Barberton Archean Surface Environments) is currently coring eight boreholes totaling ca. 4000 m length. Photographer: Christoph Heubeck.
Insert 1: Ms. Phumelele Mashele, geologist and outreach officer of BASE, explaining core to local pupils. Photograph by Christoph Heubeck.
Insert 2: The Funza 1 drill site in Columbia is producing lacustrine sediments from the northern Andes (Hooghiemstra et al., this volume).

Contents

Science Reports

Technical Developments

Workshop Reports

Sci. Dril., 30, 1–15, 2022
https://doi.org/10.5194/sd-30-1-2022

Scientific Drilling
Open Access

60 years of scientific deep drilling in Colombia: the north Andean guide to the Quaternary

Henry Hooghiemstra[1], Gustavo Sarmiento Pérez[2,a], Vladimir Torres Torres[1,3], Juan-Carlos Berrío[1,4], Lucas Lourens[5], and Suzette G. A. Flantua[1,6,7]

[1]Institute for Biodiversity and Ecosystem Dynamics, Department of Ecosystem and Landscape Dynamics, University of Amsterdam, Science Park 904, 1098 XH Amsterdam, the Netherlands
[2]Servicio Geológico de Colombia (Ingeominas), Bogotá, Colombia
[3]Exploration and New Ventures, ExxonMobil, 22777 Springwoods Village Parkway, Spring, Texas 77389, USA
[4]Department of Geography, University of Leicester, Leicester, UK
[5]Department of Geosciences, Utrecht University, Utrecht, the Netherlands
[6]Department of Biological Sciences, University of Bergen, 5020 Bergen, Norway
[7]Bjerknes Centre for Climate Research, University of Bergen, 5020 Bergen, Norway
[a]currently at: Departamento de Geociencias, Universidad Nacional de Colombia, Bogotá, Colombia

Correspondence: Henry Hooghiemstra (h.hooghiemstra@uva.nl) and Suzette G. A. Flantua (s.g.a.flantua@gmail.com)

Received: 30 October 2021 – Revised: 17 January 2022 – Accepted: 23 January 2022 – Published: 25 February 2022

Abstract. We sketch the initial history of collecting deep cores in terrestrial and marine sedimentary basins and ice cores to study environmental and climate change. Subsequently, we focus on the development of long records from the Northern Andes. The 586 m long pollen record from ancient Lake Bogotá reflects the last 2.25×10^6 years with ∼ 1.2 kyr resolution, whereas the sediment core reflects almost the complete Quaternary. The 58 m long composite core from Lake Fúquene covers the last 284 ka with ∼ 60 years resolution. We address the various challenges and limitations of working with deep continental cores. For the tropics, the presence of these deep cores has made the Northern Andes a key area in developing and testing hypotheses in the fields of ecology, paleobiogeography, and climate change. We summarize the results in the figures, and for details on the paleoenvironmental reconstructions, we refer to the corresponding literature. We provide an overview of the literature on long continental records from all continents (see the Supplement). Based on our 50 years of experience in continental core drilling, developing a research capacity to analyze the large amounts of samples, and keeping a team together to publish the results, we listed suggestions in support of deep continental records aimed at studying environmental and climate change over long intervals of time.

1 Introduction

Our understanding of past climate change at Quaternary timescales has mainly been fueled by records from deep seafloor sediments (e.g., Tiedeman et al., 1994) and the Greenland and Antarctic ice sheets (Andersen et al., 2004; Dansgaard et al., 1982). The coring of the Greenland ice sheet was initiated by the International Geophysical Year 1957–1958. The first deep ice core at Camp Century during 1963–1966 reached the bedrock at 1388 m (Dansgaard et al., 1969). Marine sediments were explored in the frame of the Deep Sea Drilling Project (DSDP), which started back in 1966 and was later continued under the names Ocean Drilling Program (ODP), Integrated Ocean Drilling Program (IODP), and International Ocean Discovery Program (IODP). Drilling and multi-proxy studies were organized by a consortia of research institutes, allowing a broad spectrum of proxy expertise and research capacity. High drilling costs

demanded critical preparation and well-organized logistics of the projects. The seaboard scientists had little time to study the results before the data had to be deposited and made available in open-access repositories, stimulating the development of new and fast methodologies to study a large number of proxy samples. Drilling in international waters and on desolate ice sheets pushed the need for efficient site selection and sample handling and contrasts with the permit-rich procedures in continental drilling.

Large ancient lakes have been widely recognized as continental archives of long-term climatic and environmental changes. Deep drilling of terrestrial continental sediments started in the 1950s, but compared to drilling deep marine records, the number of long continental records lagged behind.

Traditionally, ecologists assumed high levels of climatic and environmental stability in tropical and Mediterranean ecosystems to explain their stunning biodiversity. The 1960s were characterized by research aimed at studying the past dynamics of these systems and became a decade of discovery. In Greece, the famous 195 m deep Tenaghi Philippon core was collected (Van der Hammen et al., 1965; Wijmstra, 1969). Pollen analysis needed 2 decades, and the main results were published between 1979 and 1987. In the 1990s, the age–depth model of this core was improved and a land–sea correlation consequently developed (Tzedakis et al., 1997, 2001, 2006). Together with the long continental records from the Padul Basin, Spain (Florschütz et al., 1971; Pons and Reille, 1988; Torres et al., 2020), and the Grande Pile (Woillard, 1978), and Les Échets in France (de Beaulieu and Reille, 1984), to Clear Lake (Adam et al., 1981) and Tule Lake (Adam et al., 1989) in the USA, the continental drilling scene was set. However, continental records spanning the last $\sim$ 50 000 years before present (50 ka), with a reasonable to high temporal resolution, were still rare. Long continental records received attention at the 12th International Union for Quaternary Research (INQUA) Congress in Ottawa, Canada (Kukla, 1989). Although the symposium organizers (George Kukla and David Adam) did not clearly define what was meant with a long continental record, the presented records included oscillations of a glacial–interglacial rank, with dominant frequencies of 40 and 100 kyr, and oscillations of the interstadial–stadial rank. A reviewed and updated compilation of long pollen records of this kind is presented in Table S1 and File S2 in the Supplement, of which the longest ($>$ 125 ka) are shown in Fig. 1.

The development of a continental counterpart of the IODP was driven by a lack of climate stratigraphical information to frame marine records into a terrestrial perspective, among other reasons. Of the few continental records existing at that time, datasets were not freely accessible to the international research community. The 1995 Workshop Continental Drilling for Paleoclimate Records in Potsdam collected expertise and formulated first recommendations (PAGES, 1996), and the International Continental Scientific Drilling Program (ICDP) was inaugurated in 1996. The ICDP stipulations relied much on the drilling knowledge and experience of the IODP, e.g., a thorough scientific preparation of the drilling expeditions. Nevertheless, the preparation time for a successful drilling operation still varies between 3 and 8 years (https://www.icdp-online.org/home/, last access: 9 September 2021), and results from continental records suffer from slow data processing, such as the manual and time-consuming analyses of biotic proxies such as pollen, diatoms, and phytoliths (Flenley, 1984, 1985). Extensive processing requirements of long records may take 10 to 15 years, which rarely is convenient for young scientists. Ideally, analyses of slow proxies should be combined with rapid grain size and geochemical analyses based on X-ray fluorescence (XRF) to obtain a series of results over the course of a long continental drilling project.

2 Long continental records from the Northern Andes

Sediment cores are preferably collected in areas where tectonic activity caused the subsidence of the basin floor, giving rise to uninterrupted lacustrine sedimentation. A Dutch professor, Thomas Van der Hammen, envisioned a high potential of the basin sediments of Bogotá (2550 m above sea level – a.s.l.; Fig. 2) when the first deep sediment core was recovered in 1956 on the premises of the Colombian Geological Survey. As a geologist and palynologist, he anticipated that this basin might include an unprecedented record of vegetation and climate change in a tropical mountain setting. The surrounding mountains of Bogotá, representing several sections of the Miocene to early Pleistocene age, depicted pollen assemblages that reflected warmer conditions when these sediments were located at lower elevations. The increasingly lower temperatures shown by pollen assemblages of successively younger sediments suggested that mountain uplift had been taking place since the late Miocene times (Van der Hammen et al., 1973; Wijninga, 1996; Hooghiemstra et al., 2006). Later, exhumation histories were improved by paleoaltimetric estimates, using a range of modern techniques from different disciplines (Hoorn et al., 2010; Restrepo-Moreno et al., 2019; Boschman, 2021).

Drilling boreholes for water supply occurred regularly around the basin, but raising a core of undisturbed sediments was a challenging endeavor. A first 30 m core (named CUX – Ciudad Universitaria-X) was drilled near the border of the ancient Lake Bogotá, followed in 1957 by a 195 m deep core (named CUY – Ciudad Universitaria-Y) reaching the bedrock (Van der Hammen, 1968). Although the record of CUY suffered from numerous hiatuses caused by water level fluctuations, the record convincingly revealed a sequence of glacial and interglacial cycles, the altitudinal migration of upper montane forest and páramo along the mountain slopes, and pollen taxa which made their first appearances during

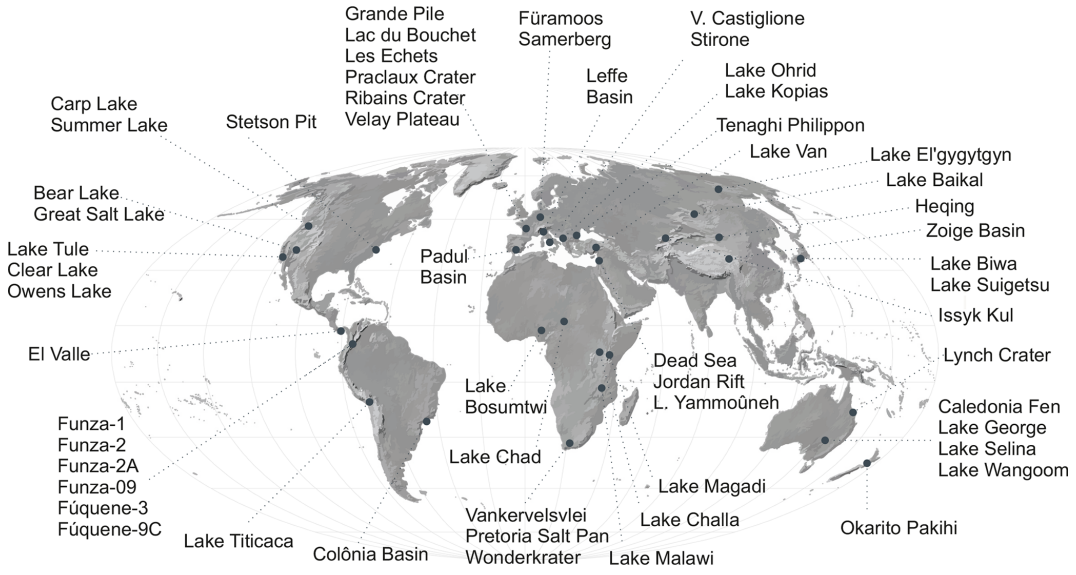

Figure 1. Global compilation of long continental fossil pollen records (> 125 ka). See also Table S1.

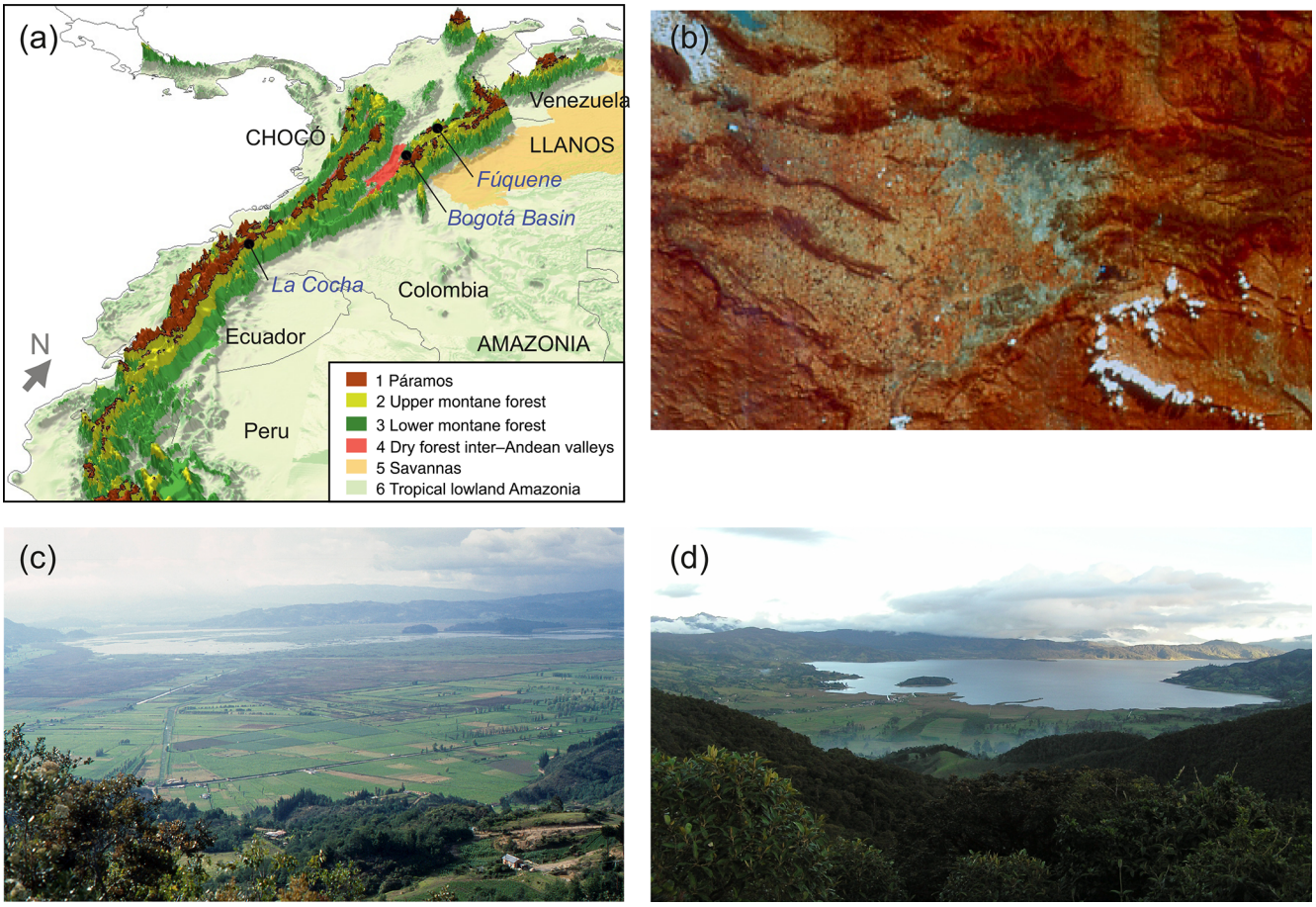

Figure 2. **(a)** Map of the Northern Andes showing the sedimentary basins discussed in the text. Photographs of the basins of Bogotá **(b)**, Lake Fúquene **(c)**, and Lake La Cocha **(d)**. Figure supplied by Suzette G. A. Flantua).

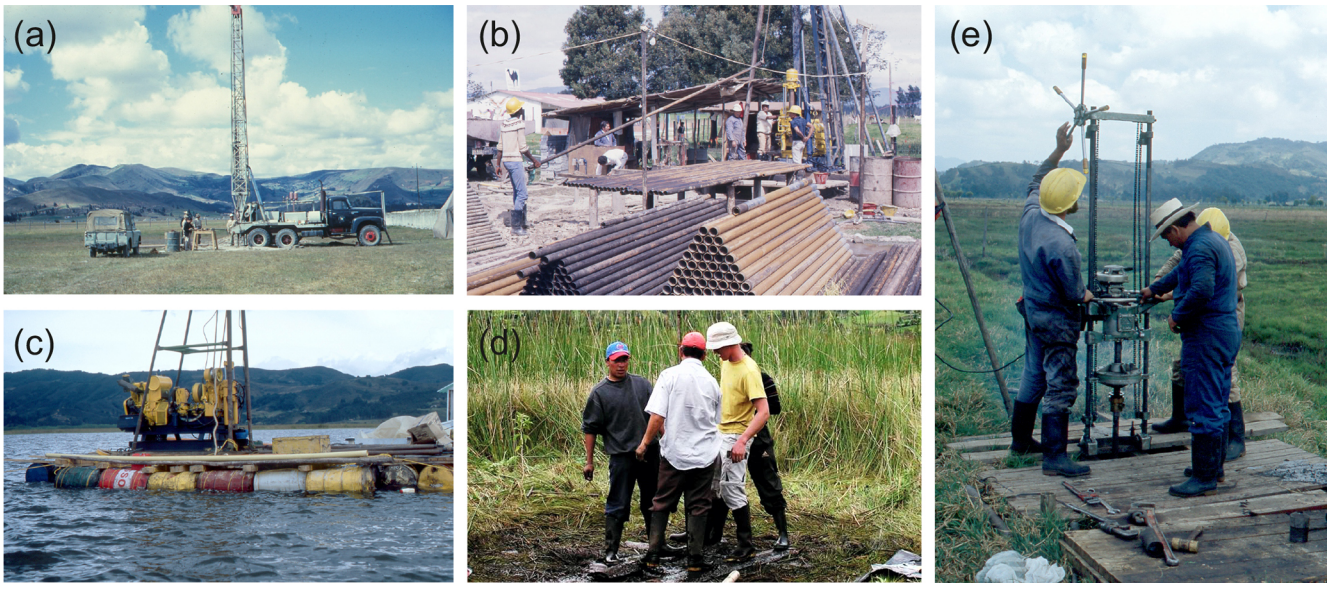

Figure 3. Photographs of the drilling sites at Funza 1 **(a)**, Funza 2 **(b)**, Fúquene 4 **(c)**, La Cocha **(d)**, and Fúquene 9 and 10 **(e)**.

the Pleistocene (Van der Hammen, 1981). The CUY record formed the basis of a much-needed biostratigraphical framework for the Northern Andes. The enormous potential of the Bogotá sediments to uncover an unparalleled history of flora, vegetation, and climate in the tropics was convincing. These results stimulated the collection, in 1969, of the first 12 m core in Lake Fúquene (Van Geel and Van der Hammen, 1973), and in 1973, a subsequent core from the Bogotá basin near the village of Funza. The latter, the Funza 1 borehole, reached 357 m and was more centrally located in the basin, where geologists anticipated the deepest point until reaching the bedrock (Hooghiemstra, 1984; Fig. 3).

3 Bogotá basin: Funza 1 record

Fracking and faulting of continental plates in the Eastern Colombian Cordillera (Restrepo-Moreno et al., 2019) caused gradual subsidence during most part of the Quaternary period (Fig. 4). The initial fluvio-lacustrine conditions changed at 1.6×10^6 years before present (1.6 Ma) into a permanent lake with water levels maximally up to 50 m (Hooghiemstra, 1984). The sediment infill of the basin is kept in equilibrium with subsidence, which explains the unique continuous sediment archive covering the last 2×10^6 years. The Bogotá River and its tributaries served as the main drainage system, with varying energy influx as documented by the silts, sands, and gravels along its courses, while, elsewhere in the basin, lacustrine conditions prevailed (Van der Hammen, 1998). The Funza 1 borehole consisted of intervals of coarse-grained sediments that often carry subterraneous water flows, which cause severe technical problems when collecting sediments and regularly leave hiatuses in the sediment core or, even worse, prevent deeper coring.

The initial age–depth model of the Funza 1 pollen record was problematic and based on the fission track and uranium–thorium (U-Th) dates of intercalated volcanic ashes with large uncertainties of the order of 300 to 500 kyr. To set a chronological time frame to the record, the European climate stratigraphy was used for reference, as other dating approaches were unavailable at that time (Zagwijn, 1960; Van der Hammen et al., 1971). Originally, the Funza 1 record was thought to be 3.5 Ma (Hooghiemstra 1984), but an updated revision of the age model dated the basis at ∼ 1.5 Ma (Torres et al., 2013). The detailed record of glacial–interglacial cycles and the altitudinal dynamics of Andean ecosystems was unprecedented. The record witnessed the first appearance of *Alnus* and *Quercus* that became important biostratigraphical markers as evidence of immigration of Northern Hemisphere arboreal taxa into the Northern Andes and the South American continent. It was estimated that, in response to the Quaternary climate fluctuations, the upper forest line migrated between ∼ 2000 and ∼ 3500 m a.s.l., reflecting a temperature amplitude of ∼ 9 °C at 2550 m a.s.l. characteristic of the lowest glacial temperatures of the last 1 Ma. An average 1200-year resolution showed the asymmetry of glacial cycles, the continuous altitudinal shifts of vegetation distributions and inherent temperature oscillations reflecting stadial–interstadial cycles, and temperature related cycles in the lake-level record.

4 Bogotá basin: Funza 2 and Funza 2A records

Coring at Funza 1, unfortunately, failed to reach the basin floor, the age model was insufficiently constrained, and grain size analysis was missing to understand how sediment infill had taken place. After a postdoctoral period in Göttingen,

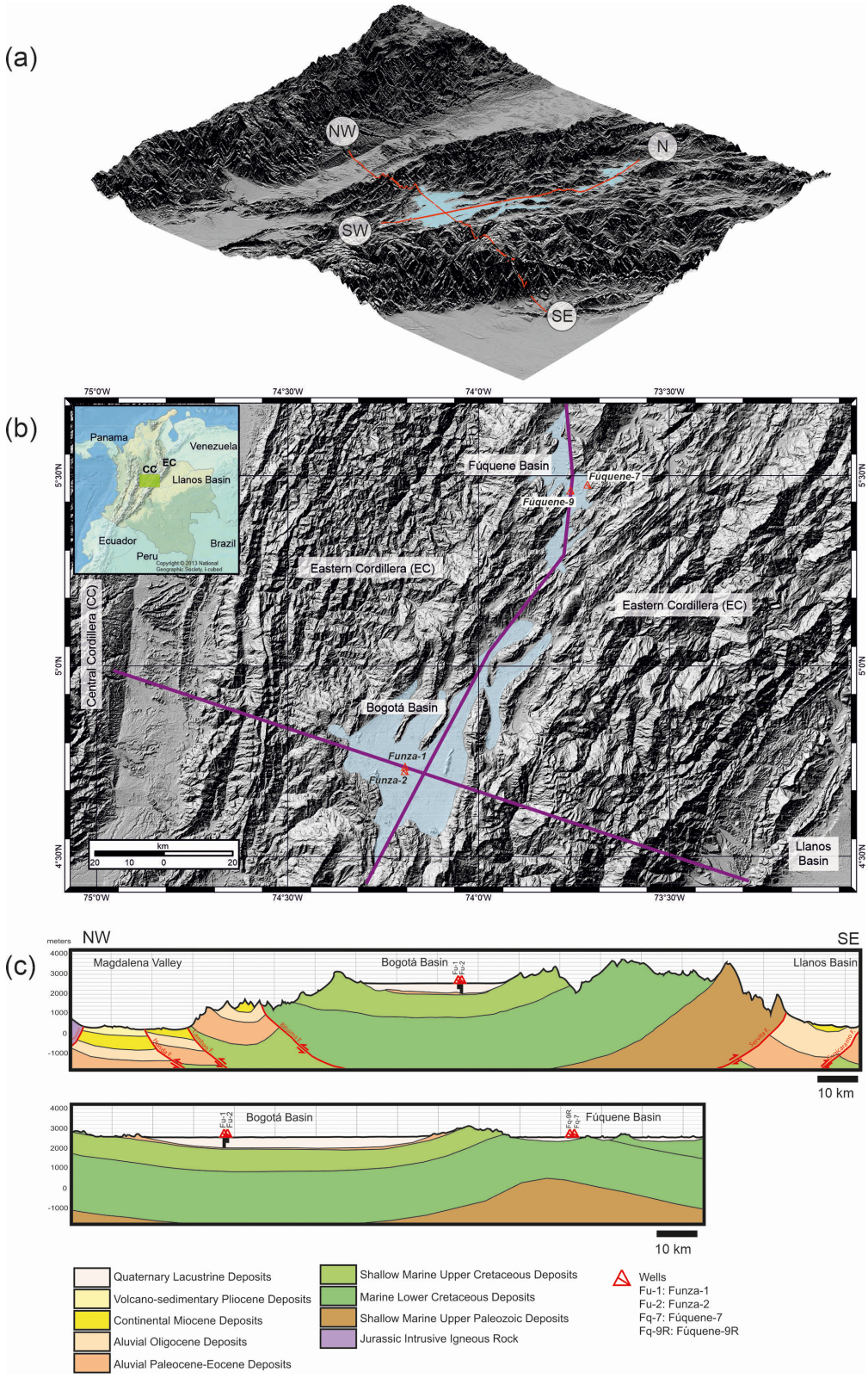

Figure 4. Cross section **(a)** and top view **(b)** of the Bogotá basin at 2550 m a.s.l. (above sea level) in the Eastern Cordillera, Colombia. During the early Quaternary, an accelerated subsidence of the basin floor gave rise to the development of the ancient Lake Bogotá. The lower sediment infill contains gravels, sands, silty clays, and lignite horizons. The middle and upper part of the sediments are lacustrine silts and clays. **(c)** Tentative cross section of the basin of Lake Fúquene; the thickness of the sediment accumulation is unknown (figure by Gustavo Sarmiento Pérez).

Germany, studying marine cores off the coast of northwestern Africa, Dutch paleoecologist Henry Hooghiemstra (lead author) returned to Amsterdam in 1987, where Thomas van der Hammen was based, and started a new coring project to reach the floor of the Bogotá basin. As the required permissions for deep-core drilling made the choice of sites limited, Funza 2 was drilled in the backyard of a school located at ca. 1 km distance from Funza 1 and ca. 50 m from a tributary of the Bogotá River. Subterraneous water under high pressure again imposed challenges and prevented the recovery of the 160–205 m interval, and consequently, a complete sediment sequence could not be collected. Funza 1 sediments were used to fill the hiatus of the Funza 2 record at this depth interval. Drilling rods of 3 in. (76.2 mm; 0–320 m), 2 in. (50.8 mm; 320–370 m), and 1.5 in. (38.1 mm; below 370 m) diameter were used, while the casing of the borehole reached up to 380 m core depth. The lowermost 200 m of the borehole was stabilized with bentonite only, and collecting these deepest sediments consumed most of the 5-week drilling operation. At 586 m core depth, the sampler touched the bedrock and, thus, the floor of the Bogotá basin. The sudden change to drilling in hard rock caused a break in the drilling rods at ∼ 250 m above the basin floor. The sampler, including the last sediments collected, and some 250 m of drilling rods were lost and now form an eternal testimony in the deepest sediments of the basin.

Dating the intercalated volcanic ash horizons for the age–depth model was again challenging, as these were heavily contaminated with lacustrine clays. The fine-grained ashes originated from the volcanic Central Cordillera were wind-blown into the Eastern Cordillera, where no volcanoes are present. The chronological uncertainty of the 1984 age–depth model of Funza 1 was replicated in the 1993 age–depth model of Funza 1 and 2 (Andriessen et al., 1993). To circumvent the poor quality of the absolute chronological control, a frequency analysis of the records of selected pollen taxa showed to which degree orbital forcing was potentially a driver of climate and vegetation change (Hooghiemstra et al., 1993).

In the period 1993 to 2002, little progress was made in the Funza project, as funding had ended. With new funding obtained in 2002, pollen analysis of the lower part of core Funza 2 was completed by Vladimir Torres Torres during the 4 following years. A grain size analysis provided insights into the sedimentary environment on the basin floor (Torres et al., 2005). Still, the existing age–depth model was deficient at that moment (Torres Torres, 2006) due to insufficient absolute age control and unfinished analysis of signals of orbital forcing. The age–depth model of the Bogotá sediments received new attention in the frame of the Fúquene Project (running from 2002 to 2012). The most reliable parts of the two Funza records, namely the 2–256 m interval from Funza 1 and the 254–586 m interval from Funza 2, were merged into the composite pollen record Funza 09 (Fig. 5). The final age–depth model was obtained using the ^{14}C ages from the top of the record, a curve matching procedure with marine δ^{18}O records of sites ODP 846 and 849 for the upper 1 Ma, and orbital tuning for the lowermost part of the record based on arboreal pollen fluctuations (Torres et al., 2013).

The sediment record appeared extremely helpful in understanding the history of the sedimentary basin. The change from forested wetlands, lakes, and rivers on the floor of the Bogotá basin to the permanent lake conditions (Torres et al., 2013) evidenced the accelerated subsidence of the basin floor at 1.4 Ma, leading to the birth of the ancient Lake Bogotá. The composite record extended the vegetation and climate history back to 2.25 Ma, whereas the sediment record possibly covers almost the complete Quaternary period (Vladimir Torres Torres and Henry Hooghiemstra, unpublished data). The immigration events of *Alnus* and *Quercus* were definitively set at 1.01 Ma and 430 ka, respectively (Torres et al., 2013), clearly illustrating the difference in latitudinal migration and regional (altitudinal) expansion capacities between the pioneer *Alnus* and the late successional tree *Quercus*. To date, the Funza 2A record (Mommersteeg, 1998) still needs a revision of its age–depth model.

5 Records from Lake Fúquene

The drainage basin of Lake Fúquene is separated from the basin of Bogotá by a water divide at 3200 m. The basin of Lake Fúquene most probably received its sediment infill after a landslide in the narrow drainage outlet of the valley north of the current lake. Behind the colluvial dam, the proximal part of the valley developed into a wetland that served as a plug to keep a water body in the distal (southern) part of the valley, where Lake Fúquene is now located. A ridge of Cretaceous sandstone forms a constriction between the proximal and distal parts of the basin, stabilizing its sediment infill (Figs. 2, 3; Sarmiento et al., 2008). The maximum thickness of the sediments in Lake Fúquene is still unknown. A 12 m core obtained from the swamps along the eastern border produced a ∼ 35 ka long record (Van Geel and Van der Hammen, 1973). A follow-up core up to 14 m depth (Fúquene 7) was obtained in 1994, where soft sediments prevailed. Deeper sediments (13–18 m interval) were collected at 7.5 m distance, with drilling equipment stabilized on top of a small dike (Fúquene 4). In total, eight radiocarbon-dated samples varying between 38 400 and 6040 ^{14}C years BP suggested that the 17.7–2.8 m interval of composite record Fúquene 7C reflects the period between ca. 88 and 6 ka (Mommersteeg, 1998).

In 1999, the lead author participated in the European Research Conference on Polar Regions and Quaternary Climate in Giens (France). This conference inspired him to increase the temporal resolution of pollen records in the Northern Andes by an order of magnitude to reveal the vegetational and climatic changes up to better-than-century-scale detail within a glacial–interglacial cycle. The 43 m long pollen record,

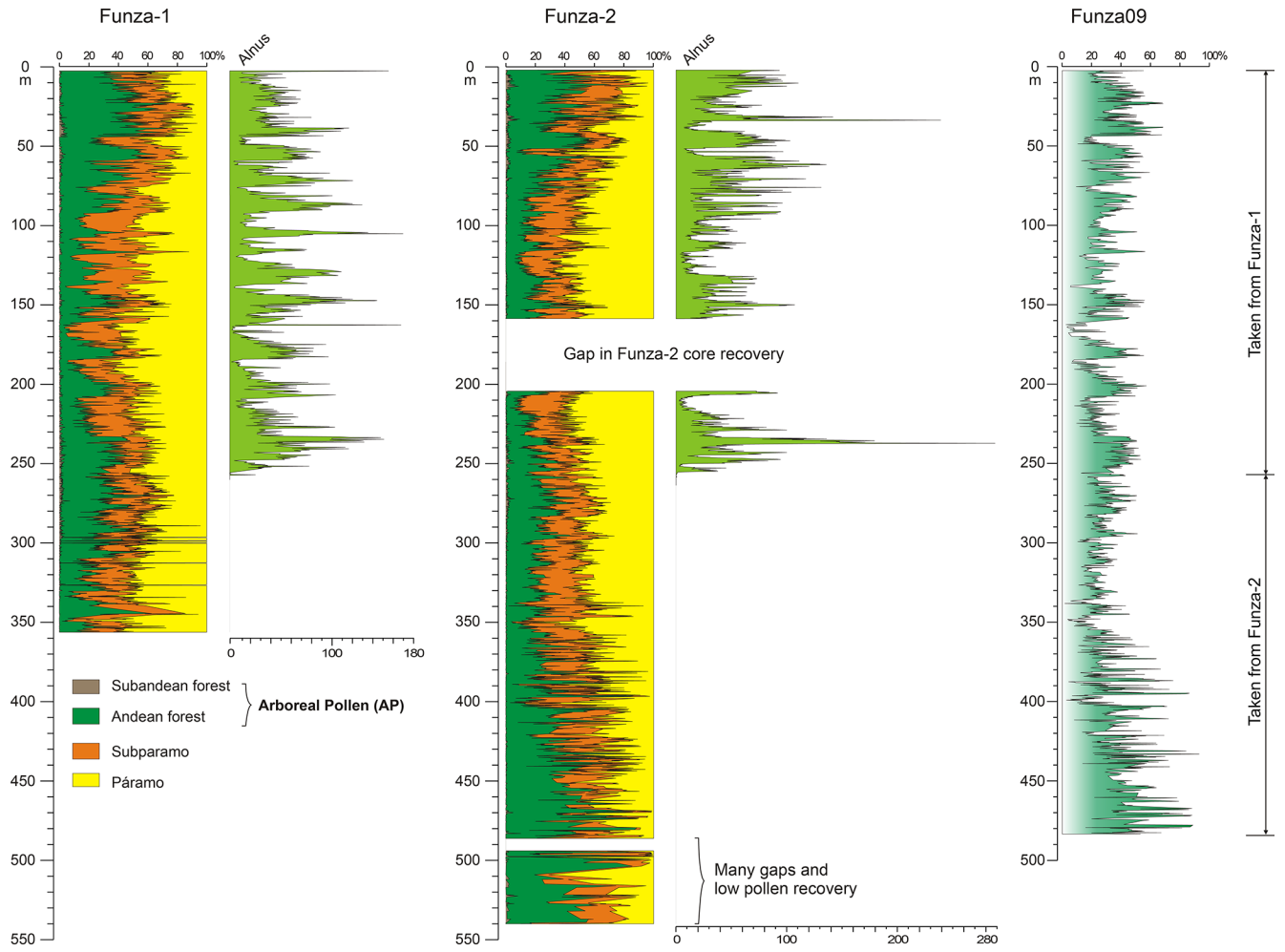

Figure 5. Stacked pollen records of Funza 1 and 2 and the composite record of Funza 09 showing changing percentages of four altitudinal vegetation belts. *Alnus* is excluded from the pollen sum (records are separately shown) and mainly reflects changes in surface area of *Alnus*-dominated swamp forest driven by lake-level changes. The Bogotá basin lies halfway between the lowermost and uppermost position of the upper forest line and makes the record of *Alnus* a sensitive recorder of glacial–interglacial cycles.

Fúquene 3, was estimated to reach ∼ 125 ka, thus ending close to the last interglacial (Eemian), corresponding to the Marine Isotope Stage 5e (MIS 5e; Van der Hammen and Hooghiemstra, 2003). It was decided to core up to ∼ 60 m to be sure to sample the complete MIS 5. A total of two parallel cores (Fúquene 9 and Fúquene 10) were drilled from a floating platform by a commercially hired drilling company (Fig. 3), recovering sediments from 1.5–58 m below the lake floor. During the drilling operation, heavy rains increased the water depth significantly, and the drilling halted when methane gas suddenly escaped from the drilling hole and continued to do so for about 15 h. Later on, it became clear that peat layers of Eemian age at 22 m core depth had degassed to such an extent that it had caused a 60 cm lowering of the lake floor around the drilling location.

The successfully obtained 115 core intervals of 100 cm length and 8 cm diameter were subsequently transported by airfreight. Diplomatic protection allowed the cores to arrive undamaged and unopened in the Netherlands. The cores were cut into a sampling half and a museum half and photographed (Fig. 6). Subsequently, the sediment cores were analyzed with an X-ray fluorescence (XRF) scanner at 1 cm distance, and 46 samples were radiocarbon dated. Based on lithology and XRF stratigraphy from both parallel cores, one single composite core, Fúquene 9C, was constructed (Groot et al., 2011). Subsequently, along the composite core at 1 cm sample distance, grain size distributions and fossil pollen were analyzed (Bogotá-A et al., 2015; Groot et al., 2013). The preparation capacity of the pollen laboratory in Amsterdam was consequently upscaled. There were two Amsterdam-based doctoral students assisted by five well-trained pollen analysts working at the Universidad Nacional in Bogotá, Colombia. Unfortunately, the 46 ^{14}C ages were inconclusive for various reasons (Groot et al., 2014). The final age–

depth model was based on nine ^{14}C radiocarbon ages at the top, while an orbital tuning approach provided 13 calibration points based on the detected 41 kyr obliquity forcing signal (Groot et al., 2011). The final 4138 sample pollen record was dated to cover 284 to 27 kyr and reflects an average resolution of 62 years (Fig. 7). The rapid proxies (XRF and GSDs – grain size distributions) provided a stratigraphical framework within a year (Vriend et al., 2012). This project showed, for the first time and with unprecedented precision, the high degree of climate-change-driven dynamics in vegetation distribution, floral composition, and ecological characteristics as experienced by tropical ecosystems, i.e., the anatomy of an ice age cycle in a tropical mountain setting (Bogotá-A et al., 2011, 2015; Groot et al., 2011, 2014).

There is much speculation with respect to why the sedimentary record in the central part of Lake Fúquene stopped at 27 ka. Remarkably enough, the sediment accumulation also ceased around the same time in the nearby Bogotá basin. An optional explanation is that sediment accumulation in both basins was disturbed by a regional tectonic event. Another plausible hypothesis is that the Bogotá basin overfilled with sediment, and at Lake Fúquene, a change in the water current from an eastern trajectory to a more centrally located trajectory in the lake basin locally prevented further sediment accumulation. These issues are unresolvable with the current understanding of the sedimentary stratigraphies lacking geophysical surveys such as gamma ray logs, resistivity logs, sonic logs, or seismic logs. The massive research investment in the Bogotá basin and Lake Fúquene in the Colombian Andes had still left the Holocene unstudied in sufficient detail. This observation motivated us to core Lake La Cocha to develop a high-resolution Holocene record.

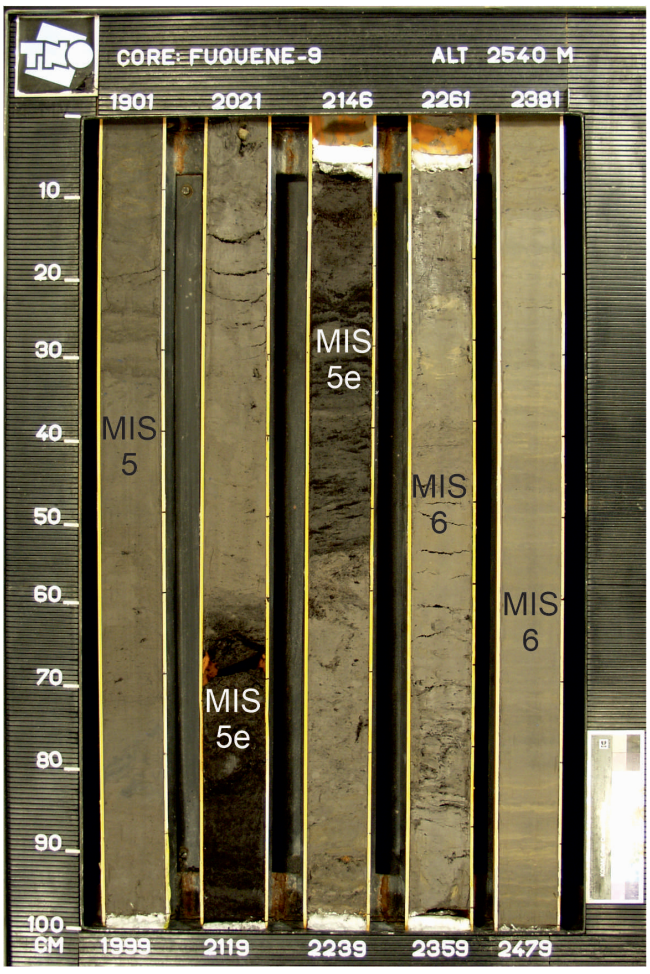

Figure 6. Lithological sequence of the 1901–2479 cm interval of core Fúquene 9, reflecting approximately the period from 118 to 135 ka. Almost laminated glacial silty clays (2479–2200 cm; MIS 6) change into dark organic rich sediments (2190–2090 cm), reflecting the compressed peat of the last interglacial (MIS 5e) age and indicating that low water tables prevailed. The younger part of MIS 5 was cooler (less evaporation), with higher lake levels explaining the accumulation of silty clays (2080–1900 cm). Cores 9 and 10 were lined up using XRF-based geochemical records, as shown in Groot et al. (2011). Composite pollen record of Fúquene 9C mainly consists of Fúquene 9 sediments. At intervals where core Fúquene 10 provided a more reliable stratigraphy, small intervals of core 9 were replaced by core 10. Photograph courtesy of TNO Core Laboratory, Utrecht, The Netherlands.

6 Lake La Cocha basin

In 2004, a swamp area at the border of Lake La Cocha (2780 m a.s.l.) was cored up to 12 m depth with a hand-operated Russian corer. Sediments were sampled for pollen, charcoal, diatoms, and ^{14}C dating. The age–depth model was based on 18 ^{14}C samples, and the record reflects the last 14 kyr (González-Carranza et al., 2012). With 550 pollen samples analyzed, the record shows vegetation dynamics at an average resolution of 27 years. The record shows a 7 kyr long trend, from 9 to 2 ka, of an increasing share of arboreal pollen, reflecting the increasing temperature at the start of the Holocene and an increase in precipitation due to the southward migration of the ITCZ (Intertropical Convergence Zone) during that time interval. From ca. 8 ka onwards, the record of arboreal vs. herbaceous vegetation shows centennial-scale oscillations hinting to the start of the El Niño–Southern Oscillation (ENSO). Climate-driven and internal forest dynamics are evidenced by a suite of non-analogue forest associations that are different from today. The last 1.4 kyr of the record show significant evidence of human impact through deforestation.

The relevance and added value of high-resolution pollen analyses in long continental records has been widely debated. Opinions may be driven by the required large investment in research time. So far, efforts of automated pollen counting have not resulted in a feasible methodology (France et al., 2000). Here, we compare the La Cocha pollen record plotted at a commonly used ∼210-year resolution (16 cm sam-

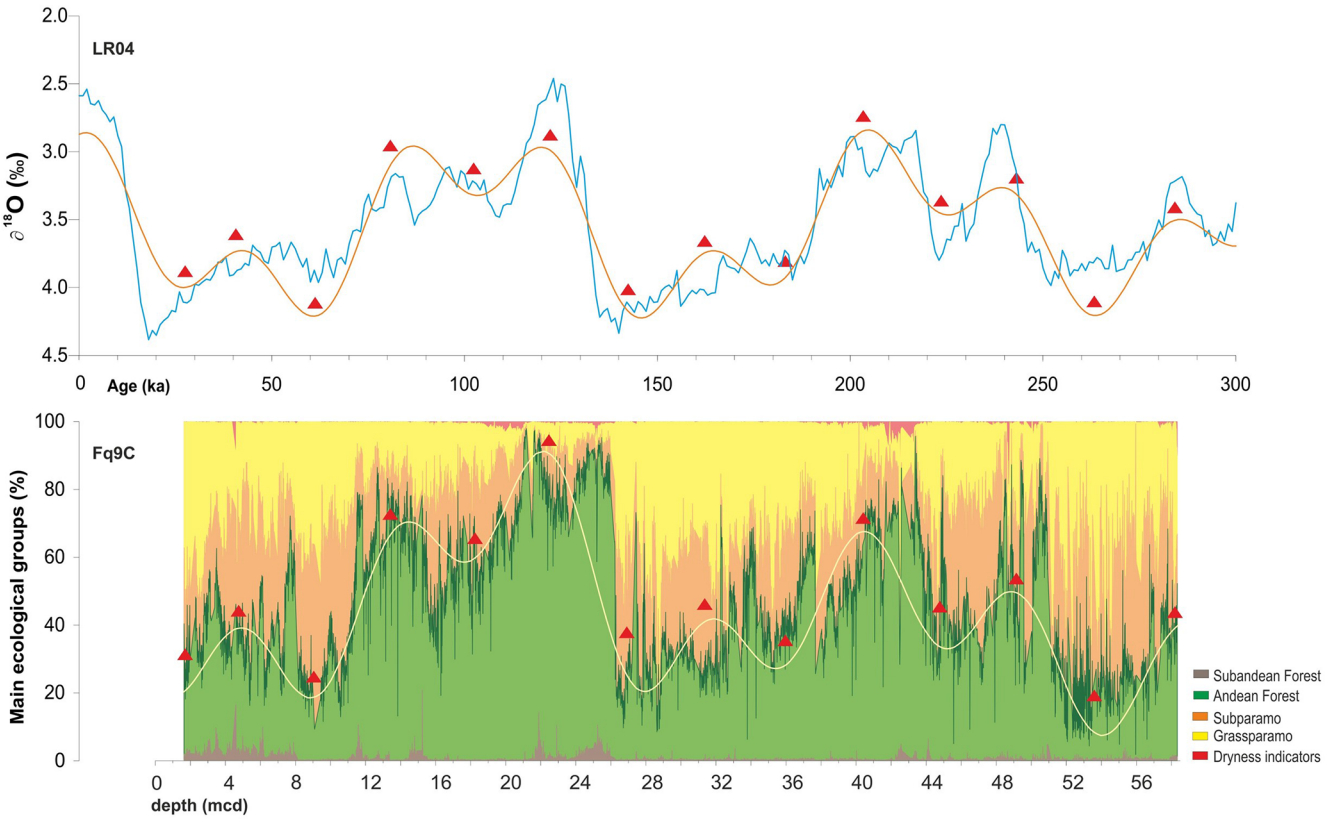

Figure 7. Pollen record of Lake Fúquene 9C (2540 m a.s.l.) plotted on a linear depth scale (3–58 m core interval). The records show the vegetation change through time in 4138 samples. Changing proportions between montane forest (green) and treeless páramo (orange – shrubs; yellow – herbs) reflect the altitudinal shifts in the mainly temperature-driven upper forest line. The oxygen isotope record LR04 (Lisiecki and Raymo, 2005) is plotted on a linear timescale. In both records, the 41 kyr obliquity forcing is evident (orange line). Control points (red triangles) show the correlation between the records (for details and age model development, see Groot et al., 2011).

ple distance) with a high-resolution sample distance of 2 cm (ca. 27-year resolution; Fig. 8; González et al., unpublished data). In the high-resolution record, the emergence of centennial climate variability becomes obvious and can provide crucial insights for comparison with high-resolution proxies, e.g., stalagmites from cave records. Importantly, information in high-resolution pollen records can support observations in ecological studies that include time series covering the last 50 years (Chacón-Moreno et al., 2021).

Developing a link between current and past ecosystem dynamics has high relevance for exploring operating mechanisms and developing a societally relevant understanding. For instance, several rapid warming events in this record show that montane forest near the upper forest line can shift upslope very fast. The cool subpáramo above the upper forest line was at times unable to respond at the same speed, resulting in a temporal disappearance as a consequence (González-Carranza et al., 2012). Due to habitat connectivity with other locations where subpáramo occurred (Flantua et al., 2014), this vegetation type returned within a few centuries, showing that the loss of an elevational belt with subpáramo shrub was a temporary effect.

7 Long continental records globally and in the Andes: conclusions and perspectives

The late 1950s, a decade before the official start of IODP in 1966, saw an exciting start of deep scientific drilling in the marine, continental, and ice sheet archives. It was the start of unveiling the long series of ice ages that characterized the Quaternary period and a much better understanding of time by the discovery of radiocarbon dating (Libby et al., 1949) and the development of the oxygen isotope stratigraphy (Emiliani 1957, 1966, 1970, Shackleton, 1987). In marine sediment cores, the start of the Quaternary was based on the change in paleomagnetism, reflecting the Brunhes–Matuyama paleomagnetic reversal dated at 1.66 Ma. However, continental evidence showed ∼ 2.5 Ma as a logical start of the Quaternary, with a first ice age of significant cooling (Zagwijn, 1960, 1992), which caused controversial opinions and debates on the beginning of the Quaternary in the paleoecological community. The debate between proxies continued for half a century (see also Hooghiemstra and Hoek, 2019), but terrestrial arguments eventually provided conclusive evi-

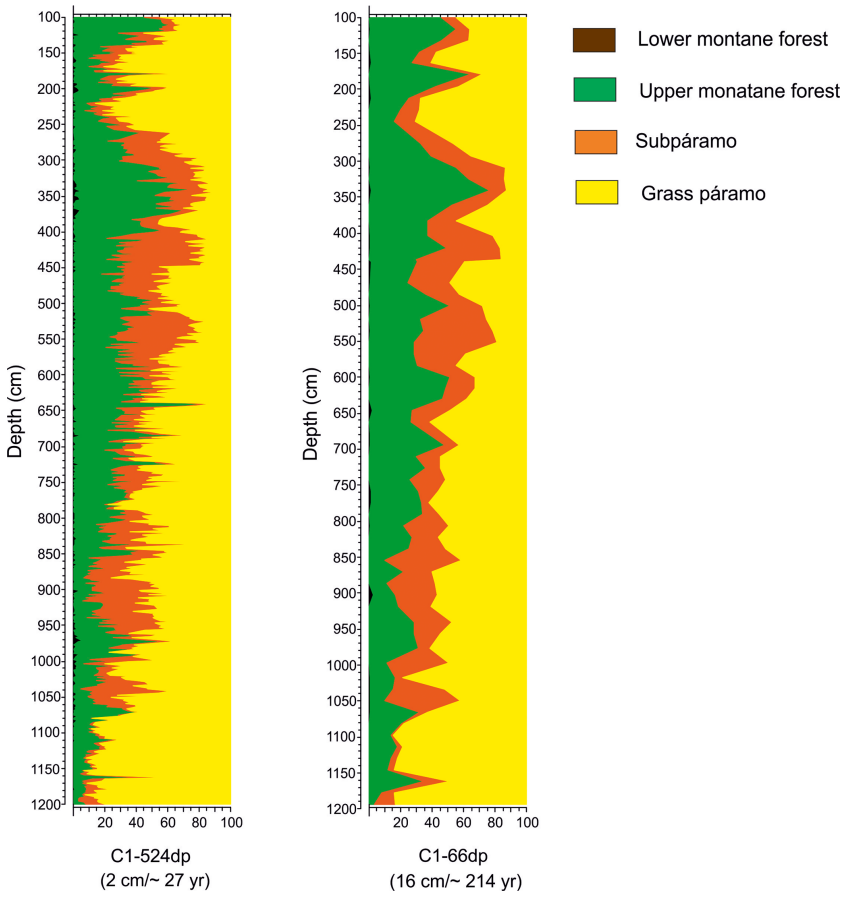

Figure 8. Pollen record from Lake La Cocha 1 (2780 m a.s.l.; 12 m long core) shows climate-driven altitudinal shifts of the main vegetation belts during the last 14 kyr. Vegetation change is shown at 16 cm sample distance (reflecting a ~210-year resolution) and at 2 cm sample distance (reflecting a ~27-year resolution). Centennial-scale climate oscillations are evident at high resolution (figure courtesy of Zaire González Carranza).

dence for the start of the Quaternary at 2.59 Ma (Gibbard et al., 2010).

Marine and ice core drilling projects developed rapidly into research consortia of global relevance. Paleoclimate research based on continental drilling continued mainly as a curiosity-satisfying enterprise driven by single persons. However, with an increasing number of high-quality marine and ice core records, it became tantalizing to see how continental ecosystems had survived Quaternary climate dynamics and the tropical ecosystems in particular (Hooghiemstra and Flantua, 2019; Hooghiemstra and Van der Hammen, 2004). The foundation of an ICDP in 1996 was a logical step. ICDP requirements were rooted in the long and professional experience of its marine counterpart IODP. As a result, deep continental drilling became rapidly professionalized and replaced low-budget projects.

In this paper, experiences of half a century of deep continental drilling in the Northern Andes are brought together, serving new initiatives within and beyond ICDP-framed studies (see File S3). The main message is that deep continental drilling is optimally served by high-tech ICDP coring facilities. However, national geological surveys may potentially offer alternative possibilities to raise deep undisturbed sediment cores for past climate research. Obtaining a good quality long sediment core is a prerequisite, but practice shows that analyzing the huge amounts of samples, developing sound age–depth models, and writing research papers before team members at the end of a project are radiating into different directions and is even more challenging. While marine and ice core studies reflect the Earth's dynamics in uninhabited parts of the world, long continental records may be retrieved from densely populated areas, providing a record of how the environment of humans has changed over longer timescales. Revisiting earlier studied sedimentary basins might be attractive when new methods have become available. The quality of a recovered sediment core, the variety of proxies analyzed, and the temporal resolution of sampling may substantially improve. However, when revisiting basins, the balance between available understanding and additions to be expected must be carefully considered.

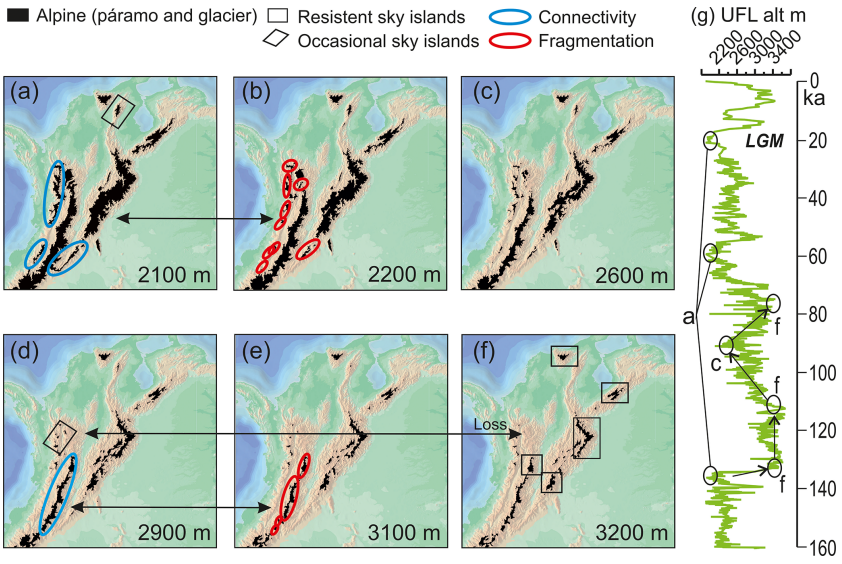

Figure 9. The 160 ka interval of composite pollen record of Fúquene 9C **(g)**, showing that the upper forest line (UFL) positions varied between 2000 and 3200 m **(a–f)**. Using UFL positions as input for a digital elevation model, simplified maps of the spatial distribution of páramo vegetation were reconstructed (Flantua and Hooghiemstra, 2018). In the Northern Andes, páramo distribution varied between a glacial maximum extension (UFL at 2000 m) and an interglacial minimum extension (UFL at 3200 m). During periods of increased temperatures (at the frequent stadial–interstadial transitions and during the few glacial–interglacial transitions), the distribution of páramo vegetation shows marked events of fragmentation in the Western Cordillera (UFL at 2200 m), Venezuelan Cordillera (UFL at 2600 m), Eastern Cordillera (UFL at 2900 m), and Central Cordillera (UFL at 3100 m), depending on the mountain-specific profile or mountain fingerprint (Flantua and Hooghiemstra, 2018; Flantua et al., 2019). Long continental pollen records serve a new field of research and hypothesis testing for different disciplines.

Archiving terrestrial sediment cores depends on the institutional facilities and is another hurdle in revisiting existing cores in good condition.

We are at the start of developing an understanding of the spatial dynamics of mountain ecosystems in which long continental records play a crucial role. For instance, superimposing the shifting altitudinal position of the upper forest line of the last 1×10^6 years on a digital elevation model of the Northern Andes allowed new insights into the consequences of temporal change on spatial changes of forest and páramo dynamics (Flantua et al., 2014; Flantua and Hooghiemstra, 2018; Flantua et al., 2019) (Fig. 9). Such new approaches open and stimulate a new field of ecological and paleobiogeographical research questions to be assessed, and long continental records from tropical mountain areas play a new role in understanding Quaternary environmental dynamics.

Marine sediments and ice caps have proven to be unparalleled archives to boost our understanding of environmental and climatic change. High-resolution long continental records meticulously show the changes in environments where significant parts of the world's population live. Although continental drilling requires loads of national and international permits, ICDP serves a societal and scientific relevance to help humankind be guided to its future. To support the dissemination of current understanding on how Quaternary environmental and climate dynamics have driven biodiversity in mountain areas to high levels, we provide a visualization (https://www.youtube.com/watch?v=-Wcp18vBDK4, last access: 2 February 2022). The clues to the future are in the past.

Data availability. Visit https://www.latinamericapollendb.com/ (last access: 2 February 2022, Flantua, 2022) for an overview of modern and fossil pollen sequences in Latin America, as reviewed by Flantua et al. (2015). Raw pollen counts of the Latin American Pollen Database (LAPD) can be obtained from the Neotoma Paleoecology Database (https://www.neotomadb.org/, last access: 2 February 2022; Williams et al., 2018). Visit https://www2.le.ac.uk/departments/geography/people/jcb34 (last access: 2 February 2022, Berrío and Hooghiemstra, 2022) for data from Fúquene 09.

Video supplement. Visit https://figshare.com/articles/Appendix_6_Visualization_of_the_flickering_connectivity_system_in_the_Northern_Andes/7408643 (Giraldo et al., 2022) for a visualization of a current understanding of the Pleistocene environmental and climate dynamics in the Northern Andes.

Supplement. Table S1 shows a list of the Quaternary long continental pollen records, with a special focus on sediment cores drilled before the initiation of the International Continental Scien-

tific Drilling Program (ICDP) in 1996. The term "long record" is not precisely defined here. The current list is the result of a review of the literature. Specific information of the cores is provided. References are found in File S2. Supplement 2 shows the list of references for Table S1. Supplement 3 has recommendations for developing long continental pollen records based on experience from the Northern Andes. The supplement related to this article is available online at: https://doi.org/10.5194/sd-30-1-2022-supplement.

Author contributions. HH designed and wrote the paper. All authors contributed equally to the text. The sequence of the first four authors (HH, GSP, VTT, and JCB) reflects their chronological contribution to developing long continental pollen records in Colombia, while SGAF transformed our understanding of the past from a temporal into a spatial scale. GSP and SGAF developed the illustrations. LL developed the age–depth models.

Competing interests. The contact author has declared that neither they nor their co-authors have any competing interests.

Disclaimer. Publisher's note: Copernicus Publications remains neutral with regard to jurisdictional claims in published maps and institutional affiliations.

Acknowledgements. Thomas van der Hammen (deceased) initiated and explored scientific drilling in the Colombian basins. We thank the Colombian Geological Survey (currently Servicio Geológico Colombiano) of Bogotá, Colombia, for supporting drilling activities. We thank the Instituto de Ciencias Naturales, Bogotá (Orlando Rangel), Colombia, for the laboratory support. The Centre for Isotope Research (Groningen; Hans Van der Plicht), Netherlands Institute for Sea Research (Texel; Fred Jansen), Vrije Universiteit Amsterdam (Jef Vandenberghe), TNO (Utrecht, Wim Westerhof; deceased), and Mirella Groot and Giovanni Bogotá-A are greatly acknowledged, for their contributions to various research projects. We thank Catalina Giraldo-Pastrana for the visualization, which has been supported financially by the Hugo de Vries Fonds (Amsterdam).

Financial support. This research has been supported by the Netherlands Foundation for the Advancement of Tropical Research (WOTRO, grant nos. W75-168, WB84-552 and WB84-636), the Netherlands Organization for Scientific Research (NWO, grant nos. H75-284/CCH, 854.00.007/ALW, 2012/13248/ALW), the University of Amsterdam grants, Hugo de Vries Foundation (Amsterdam), AlBAN/EU (grant no. E04D033907CO), and the European Research Council (ERC) under the European Union's Horizon 2020 research and innovation program (grant no. 741413).

Review statement. This paper was edited by Ulrich Harms and reviewed by C. Jaramillo and one anonymous referee.

References

Adam, D. P., Sims, J. D., and Throckmorton, C. K.: 130 000-yr continuous pollen record from Clear Lake, Lake County, California, Geology, 9, 373–377, https://doi.org/10.1130/0091-7613(1981)9<373:YCPRFC>2.0.CO;2, 1981.

Adam, D. P., Sarna-Wojcicki, A. M., Rieck, H. J., Bradbury, J. P., Dean, W. E., and Forester, R. M.: Tulelake, California: the last 3 million years, Paleogeogr. Paleoclimatol. Paleoecol., 72, 89–103, https://doi.org/10.1016/0031-0182(89)90134-X, 1989.

Andersen, K. K., Azuma, N., Barnola, J. M., Bigler, M., Biscaye, P., Caillon, N., Chappellaz, J., Clausen, H. B., Dahl-Jensen, D., Fischer, H., Flückiger, J., Fritzsche, D., Fujii, Y., Goto-Azuma, K., Grønvold, K., Gundestrup, N. S., Hansson, M., Huber, C., Hvidberg, C. S., Johnsen, S. J., Jonsell, U., Jouzel, J., Kipfstuhl, S., Landais, A., Leuenberger, M., Lorrain, R., Masson-Delmotte, V., Miller, H., Motoyama, H., Narita, H., Popp, T., Rasmussen, S. O., Raynaud, D., Rothlisberger, R., Ruth, U., Samyn, D., Schwander, J., Shoji, H., Siggard-Andersen, M. L., Steffensen, J. P., Stocker, T., Sveinbjörnsdóttir, A. E., Svensson, A., Takata, M., Tison, J. L., Thorsteinsson, T., Watanabe, O., Wilhelms, F., White, J. W., and North Greenland Ice Core Project Members: High-resolution record of Northern hemisphere climate extending in to the last interglacial period, Nature, 431, 147–151, https://doi.org/10.1038/nature02805, 2004.

Andriessen, P. A. M., Helmens, K. F., Hooghiemstra, H., Riezebos, P. A., and Van der Hammen, T.: Absolute chronology of the Pliocene-Quaternary sediment sequence of the Bogotá area, Colombia, Quaternary Sci. Rev., 12, 483–501, https://doi.org/10.1016/0277-3791(93)90066-U, 1993.

Berrío, J. C. and Hooghiemstra, H.: Information on Fúquene Pollen Data, University of Leicester, https://www2.le.ac.uk/departments/geography/people/jcb34, last access: 2 February 2022.

Bogotá-A., R. G., Groot, M. H. M., Hooghiemstra, H., Lourens, L. J., Van der Linden, M., and Berrío, J. C.: Rapid climate change from north Andean Lake Fúquene pollen records driven by obliquity: implications for a basin-wide biostratigraphic zonation, Quaternary Sci. Rev., 30, 3321–3337, https://doi.org/10.1016/j.quascirev.2011.08.003, 2011.

Bogotá-A, R. G., Hooghiemstra, H., and Berrio, J.-C.: North Andean environmental and climatic change at orbital to submillennial time-scales: vegetation, water-levels and sedimentary regimes from lake Fúquene from 284 to 130 ka, Rev. Palaeobot. Palynol., 226, 91–107, https://doi.org/10.1016/j.revpalbo.2015.09.007, 2015.

Boschman, L. M.: Andean mountain building since the Late Cretaceous: a paleoelevation reconstruction, Earth-Sci. Rev., 220, 103640, https://doi.org/10.1016/j.earscirev.2021.103640, 2021.

Chacón-Moreno, E., Rodriguez-Morales, M., Paredes, D., Suárez del Moral, P., and Albarrán, A.: Impacts of global change on the spatial dynamics of treeline in Venezuelan Andes, Front. Ecol. Evol., 9, 615223, https://doi.org/10.3389/fevo.2021.615223, 2021.

Dansgaard, W., Johnson, S. J., Møller, J., and Langway Jr., C. C.: One thousand centuries of climate record from Camp Century on the Greenland ice sheet, Science, 166, 377–380, https://doi.org/10.1126/science.166.3903.377, 1969.

Dansgaard, W., Clausen, H. B., Gundestrup, N., Hammer, C. U., Johnsen, S. F., Kristinsdottir, P. M., and Reeh, N.: A new Greenland deep ice core, Science, 218, 1273–1277, https://doi.org/10.1126/science.218.4579.1273, 1982.

De Beaulieu, J. L. and Reille, M.: A long Upper Pleistocene pollen record from Les Echets, near Lyon, France, Boreas, 13, 111–132, https://doi.org/10.1111/j.1502-3885.1984.tb00066.x, 1984.

Emiliani, C.: Temperature and age analysis of deep-sea cores, Science, 1235, 383–385, https://doi.org/10.1126/science.125.3244.383, 1957.

Emiliani, C.: Isotopic paleotemperatures, Science, 154, 851–857, https://doi.org/10.1126/science.154.3751.851, 1966.

Emiliani, C.: Pleistocene paleotemperatures, Science, 168, 822–825, https://doi.org/10.1126/science.168.3933.822, 1970.

Flantua, S. G. A.: Inventory of modern and paleo-records of pollen in Latin America, Latin America Pollen Database, https://www.latinamericapollendb.com/, last access: 2 February 2022.

Flantua, S. G. A. and Hooghiemstra, H.: Historical connectivity and mountain biodiversity, in: Mountains, climate and biodiversity, edited by: Hoorn, C., Perrigo, A., and Antonelli, A., Wiley, UK, 171–185, ISBN 9781119159896, 2018.

Flantua, S. G. A., Hooghiemstra, H., Van Boxel, J. H., Cabrera, M., González-Carranza, Z., and González-Arango, C.: Connectivity dynamics since the Last Glacial Maximum in the northern Andes; a pollen-driven framework to assess potential migration, in: Paleobotany and Biogeography: A Festschrift for Alan Graham in His 80th Year, edited by: Stevens, W. D., Montiel, O. M., and Raven, P. H., Missouri Botanical Garden, St. Louis, 98–123, ISBN 978-0-915279-97-5, 2014.

Flantua, S. G. A., Hooghiemstra, H., Grimm, E. C., Behling, H., Bush, M. B., González-Arango, C., Gosling, W., Ledru, M.-P., Lozano-García, S., Maldonado, A., Prieto, A., Rull, V., and Van Boxel, J. H.: Updated site compilation of the Latin American Pollen Database; challenging new research, Rev. Palaeobot. Palynol., 223, 104–115, https://doi.org/10.1016/j.revpalbo.2015.09.008, 2015.

Flantua, S. G. A., O'Dea, A., Onstein, R., Giraldo, C., and Hooghiemstra, H.: The flickering connectivity system of the north Andean páramos, J. Biogeogr., 46, 1808–1825, https://doi.org/10.1111/jbi.13607, 2019.

Flenley, J. F.: Andean guide to Pliocene-Quaternary climate, Nature, 311, 702–703, https://doi.org/10.1038/311702b0, 1984.

Flenley, J. R.: A long land-based core, J. Biogeogr., 12, 192–194, https://doi.org/10.2307/2844844, 1985.

Florschütz, F., Menéndez Amor, J., and Wijmstra, T.A.: Palynology of a thick Quaternary succession in southern Spain, Palaeogeogr. Palaeoclimatol. Palaeoecol., 10, 233–264, https://doi.org/10.1016/0031-0182(71)90049-6, 1971.

France, I., Duller, A. W. G., Duller, G. A. T., and Lamb, H. F.: A new approach to automated pollen analysis, Quaternary Sci. Rev., 19, 537–546, https://doi.org/10.1016/S0277-3791(99)00021-9, 2000.

Gibbard, P. L., Head, M. J., and Walker, M. J. C.: Formal ratification of the Quaternary System/Period and the Pleistocene Series/Epoch with a base at 2.58 Ma, J. Quat. Sci., 25, 96–102, https://doi.org/10.1002/jqs.1338, 2010.

Giraldo, C., Flantua, S. G. A., and Hooghiemstra, H.: Sky Islands: A time travel of the Andes Mountains, figshare [video], https://figshare.com/articles/Appendix_6_Visualization_of_the_flickering_connectivity_system_in_the_Northern_Andes/7408643, last access: 2 February 2022.

González-Carranza, Z., Hooghiemstra, H., and Vélez, M. I.: Major altitudinal shifts in Andean vegetation on the Amazonian flank show temporary loss of biota in the Holocene, Holocene, 22, 1227–1241, https://doi.org/10.1177/0959683612451183, 2012.

Groot, M. H. M., Bogotá, R. G., Lourens, L. J., Hooghiemstra, H., Vriend, M., Berrio, J. C., Tuenter, E., Van der Plicht, J., Van Geel, B., Ziegler, M., Weber, S. L., Betancourt, A., Contreras, L., Gaviria, S., Giraldo, C., González, N., Jansen, J. H. F., Konert, M., Ortega, D., Rangel, O., Sarmiento, G., Vandenberghe, J., Van der Hammen, T., Van der Linden, M., and Westerhoff, W.: Ultra-high resolution pollen record from the northern Andes reveals rapid shifts in montane climates within the last two glacial cycles, Clim. Past, 7, 299–316, https://doi.org/10.5194/cp-7-299-2011, 2011.

Groot, M. H. M., Hooghiemstra, H., Berrio, J.-C., and Giraldo, C.: North Andean environmental and climatic change at orbital to submillennial time-scales: vegetation, water-levels, and sedimentary regimes from Lake Fúquene during 130–27 ka, Rev. Palaeobot. Palynol., 197, 186–204, https://doi.org/10.1016/j.revpalbo.2013.04.005, 2013.

Groot, M. H. M., Van der Plicht, J., Hooghiemstra, H., Lourens, L. J., and Rowe, H. D.: Age modelling for Pleistocene lake sediments: a comparison of methods from the Andean Fúquene Basin (Colombia) case study, Quat. Geochron., 22, 144–154, https://doi.org/10.1016/j.quageo.2014.01.002, 2014.

Hooghiemstra, H.: Vegetational and climatic history of the high plain of Bogotá, Colombia, Doctoral dissertation, University of Amsterdam, Dissertationes Botanicae, 79, 1–368, Cramer, Vaduz, ISBN 3-7682-1404-4, 1984.

Hooghiemstra, H. and Flantua, S. G. A.: Colombia in Quaternary: an overview of environmental and climatic change, in: The Geology of Colombia Book, edited by: Gómez-Tapias, J., Servicio Geológico Colombiano, vol. 4, 43–104, https://doi.org/10.32685/pub.esp.38.2019, 2019.

Hooghiemstra, H. and Hoek, W. Z.: Waldo Heliodoor Zagwijn (1928–2018): the instigator and architect of European chronostratigraphy, Neth. J. Geosci., 98, e7, https://doi.org/10.1017/njg.2019.9, 2019.

Hooghiemstra, H. and Van der Hammen, T.: Quaternary ice-age dynamics in the Colombian Andes: developing an understanding of our legacy, Phil. Trans. Roy. Soc. London B, 359, 173–181, https://doi.org/10.1098/rstb.2003.1420, 2004.

Hooghiemstra, H., Mélice, J. L., Berger, A., and Shackleton, N. J.: Frequency spectra and paleoclimatic variability of the high-resolution 30–1450 ka Funza I pollen record (Eastern Cordillera, Colombia), Quaternary Sci. Rev., 12, 141–156, https://doi.org/10.1016/0277-3791(93)90013-C, 1993.

Hooghiemstra, H., Wijninga, V. M., and Cleef, A. M.: The paleobotanical record of Colombia: implications for biogeography and biodiversity, Ann. Missouri Bot. Gard., 93, 297–324, https://doi.org/10.3417/0026-6493(2006)93[297:TPROCI]2.0.CO;2, 2006.

Hoorn, C., Wesselingh, F. P., Ter Steege, H., Bermudez, M. A., Mora, A., Sevink, J., Sanmartín, I., Sanchez-Meseguer, A., Anderson, C. L., Figueiredo, J. P., Jaramillo, C., Riff, D., Negri, F. R., Hooghiemstra, H., Lundberg, J., Stadler, T., Särkinen, T., and Antonelli, A.: Amazonia through time: Andean uplift, cli-

mate change, landscape evolution, and biodiversity, Science, 330, 927–931, https://doi.org/10.1126/science.1194585, 2010.

Kukla, G.: Long continental records of climate; an introduction, Paleogeogr. Palaeoclimatol. Palaeoecol., 72, 1–9, https://doi.org/10.1016/0031-0182(89)90128-4, 1989.

Libby, W. F., Andersen, E. C., and Arnold, J. R.: Age determination by radiocarbon content: world wide assay of natural radiocarbon, Science, 109, 227–228, https://doi.org/10.1126/science.109.2827.227, 1949.

Lisiecki, L. E. and Raymo, M. E.: A Pliocene-Pleistocene stack of 57 globally distributed benthic ∂^{18}O records, Paleoceanogr., 20, PA1003, https://doi.org/10.1029/2004PA001071, 2005.

Mommersteeg, H.: Vegetation development and cyclic and abrupt climatic change during the late Quaternary, Doctoral dissertation, University of Amsterdam, 191 pp., ISBN 90-9011649-4, 1998.

PAGES: Continental drilling for paleoclimatic records. Recommendations from an international workshop, edited by: Colman, S. M., Workshop Continenal Drilling for Paleoclimatic Recods, 30 June–2 July 1995, GeoForschungsZentrum, Postdam, Germany, Series 1996-4, 104 pp., 1996.

Pons, A. and Reille, M.: The Holocene and upper Pleistocene pollen record from Padul (Granada, Spain): a new study, Palaeogeogr. Palaeoclimatol. Palaeoecol., 66, 243–249, https://doi.org/10.1016/0031-0182(88)90202-7, 1988.

Restrepo-Moreno, S. A., Foster, D. A., Bernet, M., Min, K., and Noriega, S.: Morphotectonic and orogenic development of the Northern Andes of Colombia: a low-temperature thermochronology perspective, in: Geology and tectonics of northwestern South America, edited by: Cediel, R. and Shaw, R. P., Springer, Frontiers in Earth Sciences, 749–832, https://doi.org/10.1007/978-3-319-76132-9_11, 2019.

Sarmiento, G., Gaviria, S., Hooghiemstra, H., Berrio, J.-C., and Van der Hammen, T.: Landscape evolution and origin of Lake Fúquene (Colombia): tectonics, erosion and sedimentation processes during the Pleistocene, Geomorph., 100, 563–575, https://doi.org/10.1016/j.geomorph.2008.02.006, 2008.

Shackleton, N. J.: Oxygen isotopes, ice volume and sea level, Quat. Sci.Rev., 6, 183–190, https://doi.org/10.1016/0033-5894(84)90085-1, 1987.

Tiedeman, R., Sarnthein, M., and Shackleton, N. J.: Astronomic timescale for the Pliocene Atlantic ∂^{18}O and dust flux records of Ocean Drilling Program site 659, Paleoceanogr., 9, 619–638, https://doi.org/10.1029/94PA00208, 1994.

Torres, T., Valle, M., Ortiz, J. E., Soler, V., Araujo, R., Rivas, M. R., Delgado, A., Julià, R., and Sánchez-Palencia, Y.: 800 ka of Palaeoenvironmental changes in the southwestern Mediterranean realm, J. Iberian Geol., 46, 117–144, 2020.

Torres, V., Vandenberghe, J., and Hooghiemstra, H.: An environmental reconstruction of the sediment infill of the Bogotá basin (Colombia) during the last 3 million years from abiotic and biotic proxies, Palaeogeogr. Palaeoclimatol. Palaeoecol., 226, 127–148, https://doi.org/10.1016/j.palaeo.2005.05.005, 2005.

Torres, V., Hooghiemstra, H., Lourens, L. J., and Tzedakis, P. C.: Astronomical tuning of long pollen records reveals the dynamic history of montane biomes and lake levels in the tropical high Andes during the Quaternary, Quaternary Sci. Rev., 63, 59–72, https://doi.org/10.1016/j.quascirev.2012.11.004, 2013.

Torres Torres, V.: Pliocene-Pleistocene evolution of flora, vegetation and climate: a palynological and sedimentological study of a 586-m core from the Bogotá basin, Colombia, Doctoral dissertation, University of Amsterdam, 181 pp., ISBN 90-76894-64-7, 2006.

Tzedakis, P. C., De Beaulieu, J.-L., Crowhurst, S., Follieri, M., Hooghiemstra, H., Magri, D., Reille, M., Shackleton, N. J., and Wijmstra, T. A.: Comparison of terrestrial and marine records of changing climate of the last 500 000 years, Earth Planet. Sc. Lett., 150, 171–176, https://doi.org/10.1016/S0012-821X(97)00078-2, 1997.

Tzedakis, P. C., Andrieu, V., De Beaulieu, J.-L., Birks, H. J. B., Crowhurst, S., Follieri, M., Hooghiemstra, H., Magri, D., Reille, M., Sadori, L., Shackleton, N. J., and Wijmstra, T. A.: Establishing a terrestrial chronological framework as a basis for biostratigraphical comparisons. Quaternary Sci. Rev., 20, 1583–1592, https://doi.org/10.1016/S0277-3791(01)00025-7, 2001.

Tzedakis, P. C., Hooghiemstra, H., and Palike, H.: The last 1.35 milion years at Tenaghi Philippon: revised chronostratigraphy and long-term vegetation trends, Quaternary Sci. Rev., 25, 3416–3430, https://doi.org/10.1016/j.quascirev.2006.09.002, 2006.

Van der Hammen, T.: Climate and vegetational succession in the equatorial Andes of Colombia, in: Geo-ecology of the mountainous regions of the tropical Americas, edited by: Troll, C., Coll. Geogr., 9, 187–194, 1968.

Van der Hammen, T.: The Pleistocene changes of vegetation and climate in the Northern Andes, in: The glaciation of the Ecuadorian Andes, edtied by: Hastenrath, S., Balkema, Rotterdam, 125–145, ISBN 90-6191-038-2, 1981.

Van der Hammen, T.: Plan ambiental de la cuenca alta del Río Bogotá, Corpocación Autónoma Regional (CAR) de Cundinamarca, Bogotá, 142 pp., http://sie.car.gov.co/bitstream/handle/20.500.11786/33796/28263.pdf?sequence=1&isAllowed=y (last access: 4 February 2022), 1998.

Van der Hammen, T. and Hooghiemstra, H.: Interglacial-glacial Fúquene-3 pollen record from Colombia: an Eemian to Holocene climate record, Glob. Planet. Change, 36, 181–199, https://doi.org/10.1016/S0921-8181(02)00184-4, 2003.

Van der Hammen, T., Wijmstra, T. A., and Van der Molen, W. H.: Palynological study of a very thick peat section in Greece and the Würm-glacial vegetation in the Mediterranean region, Geol. Mijnb., 44, 37–39, 1965.

Van der Hammen, T., Wijmstra, T. A., and Zagwijn, W. H.: The floral record of the late Cenozoic of Europe, in: Late Cenozoic glacial ages, edited by: Turekian, K. K., Yale Univ. Press, 391–424, ISBN 0-300-01420-1, 1971.

Van der Hammen, T., Werner, J. H., and Van Dommelen, H.: Palynological record of the upheaval of the Northern Andes; a study of the Pliocene and Lower Quaternary of the Colombian Eastern Cordillera and the early evolution of its high-Andean biota, Palaeogeogr. Palaeoclimatol. Palaeoecol., 16, 1–122, https://doi.org/10.1016/0034-6667(73)90031-6, 1973.

Van Geel, B. and Van der Hammen, T.: Upper Quaternary vegetational and climatic sequence of the Fúquene area (Eastern Cordillera, Colombia), Palaeogeogr. Palaeoclimatol. Palaeoecol., 14, 9–92, https://doi.org/10.1016/0031-0182(73)90064-3, 1973.

Vriend, M., Groot, M. H. M., Hooghiemstra, H., Bogotá-Angel, R. G., and Berrio, J. C.: Changing depositional environments in the Colombian Fúquene Basin at submillennial time-scales during 284–27 ka from unmixed grain-size distri-

butions and aquatic pollen, Neth. J. Geosci., 91, 199–214, https://doi.org/10.1017/S0016774600001591, 2012.

Wijmstra, T. A.: Palynology of the first 30 metres of a 120 m deep section in Northern Greece, Acta Bot. Neerl., 18, 511–527, https://doi.org/10.1111/j.1438-8677.1969.tb00591.x, 1969.

Wijninga, V. M.: Neogene ecology of the Salto de Tequendama site (2475 m alt. Cordillera Oriental, Colombia): the paleobotanical record of montane and lowland forests, Rev. Palaeobot. Palynol., 92, 97–156, 1996.

Williams, J. W., Grimm, E. C., Blois, J. L., Charles, D. F., Davis, E. B., Goring, S. J., Graham, R. W., Smith, A. J., Anderson, M., Arroyo-Cabrales, J., Ashworth, A. C., Betancourt, J. L., Bills, B. W., Booth, R. K., Buckland, P. I., Curry, B. B., Giesecke, T., Jackson, S. T., Latorre, C., Nichols, J., Purdum, T., Roth, R. E., Stryker, M., and Takahara, H.: The Neotoma Paleoecology Database, a multiproxy, international, community-curated data resource, Quaternary Res., 89, 156–177, https://doi.org/10.1017/qua.2017.105, 2018.

Woillard, G. M.: Grande Pile peat bog: a continuous pollen record for the last 140 000 years, Quaternary Res., 12, 152–155, https://doi.org/10.1016/0033-5894(78)90079-0, 1978.

Zagwijn, W. H.: Aspects of the Pliocene and early Pleistocene vegetation of the Netherlands, Meded. Geol. Stichting, Serie C-III-1(5), 1–78, 1960.

Zagwijn, W. H.: The beginning of the ice age in Europe and its major subdivisions, Quaternary Sci. Rev., 11, 583–591, https://doi.org/10.1016/0277-3791(92)90015-Z, 1992.

Sci. Dril., 30, 17–42, 2022
https://doi.org/10.5194/sd-30-17-2022

Scientific Drilling
Open Access

From glacial erosion to basin overfill: a 240 m-thick overdeepening–fill sequence in Bern, Switzerland

Michael A. Schwenk[1], Patrick Schläfli[1,2,3], Dimitri Bandou[1], Natacha Gribenski[1], Guilhem A. Douillet[1], and Fritz Schlunegger[1]

[1]Institute of Geological Sciences, University of Bern, Bern, Switzerland
[2]Institute of Plant Sciences, University of Bern, Bern, Switzerland
[3]Oeschger Centre for Climate Change Research, University of Bern, Bern, Switzerland

Correspondence: Michael A. Schwenk (michael.schwenk@geo.unibe.ch)

Received: 1 October 2020 – Revised: 30 May 2021 – Accepted: 31 May 2021 – Published: 25 February 2022

Abstract. We drilled a 210 m-thick succession of Quaternary sediments and extended it 30 m upsection with information that we collected from an adjacent outcrop. In the 240 m-thick succession we identified 12 different lithofacies, grouped them into five facies assemblages, and distinguished two major sedimentary sequences. A sharp contact at 103 m depth cuts off cross-beds in sequence A and separates them from the overlying horizontal beds in sequence B. Although the lowermost facies assemblage of each sequence includes a till deposited during a period of ice cover, the two tills differ from each other. In particular, the till at the base of sequence A is dominated by large clasts derived from the underlying Molasse bedrock, whereas the till at the base of sequence B has no such Molasse components. Furthermore, the till in sequence A bears evidence of glaciotectonic deformation. Both tills are overlain by thick assemblages of subaqueous, most likely glaciolacustrine and lacustrine facies elements. The cross-bedded and steeply inclined sand, gravel, and diamictic beds of sequence A are interpreted as deposits of density currents in a subaqueous ice-contact fan system within a proglacial lake. In contrast, the lacustrine sediments in sequence B are considered to record a less energetic environment where the material was most likely deposited in a prodelta setting that gradually developed into a delta plain. Towards the top, sequence B evolves into a fluvial system recorded in sequence C, when large sediment fluxes of a possibly advancing glacier resulted in a widespread cover of the region by a thick gravel unit. Feldspar luminescence dating on two samples from a sand layer at the top of sequence B provided uncorrected ages of 250.3 ± 80.2 and 251.3 ± 59.8 ka. The combination of these ages with lithostratigraphic correlations of sedimentary sequences encountered in neighboring scientific drillings suggests that sequence B was deposited between Marine Isotope Stage 8 (MIS 8; 300–243 ka) and MIS 7 (243–191 ka). This depositional age marks the end of one stage of overdeepening–fill in the perialpine Aare Valley near Bern.

1 Introduction

Periods of global cooling have caused fluctuations in ice volume throughout the Quaternary, which is, for example, recorded in marine sediments (Lisiecki and Raymo, 2005). During these cool periods, ice sheets and glaciers have advanced from the polar areas to lower latitudes and from mountainous regions to the lowlands. The European Alps and their forelands were affected by these glaciations multiple times, as pointed out more than 100 years ago (Heim, 1885; Penck and Brückner, 1909). The most famous initial reconstruction of the number and chronology of glacial advances in the Alps by Penck and Brückner (1909) has evolved towards a detailed knowledge about the complexity of this chronology, yet these details have still been a matter of scientific debate in the past years (e.g., Fiebig and Preusser, 2008; Ehlers et al., 2018). This debate is further complicated by the fact that glacial advances from the Alps to their forelands were regionally variable through the course of the Quaternary. On the global scale, it was recognized that the peri-

odicity of glacial cycles increased from 41 to 100 ka, probably due to an increased eccentricity forcing (e.g., Ruddiman et al., 1986; Lisiecki, 2010) during the Middle Pleistocene climatic Transition (MPT, 1250–700 ka; Clark et al., 2006). Studies of the topographic evolution in the Central Swiss Alps suggest that glacial valley erosion started to increase during the MPT (Haeuselmann et al., 2007b; Valla et al., 2011). It was also proposed that glacial overdeepening of valleys in the northern Alps and in their foreland was initiated during the MPT (Schlüchter, 2004). Overdeepenings are local bedrock troughs where the rock surface is below the present-day base level. These bedrock depressions thus provide accommodation space where fragmented and potentially intact glacial–interglacial sedimentary sequences could accumulate after glacial retreat. Hence, overdeepenings have the potential to preserve the sedimentary record throughout repeated glacial cycles (Preusser et al., 2010; Cook and Swift, 2012). Numerous extensive overdeepenings were formed in the Swiss Alps and on the Swiss Plateau (Fig. 1a, b), where a minimum of eight Quaternary glaciations has been recognized so far in the sedimentary record, including archives recovered from these overdeepenings (Keller and Krayss, 2010; Preusser et al., 2011). One of these large glacial troughs, which is referred to as the Aare Valley overdeepening, is situated in the greater Bern area between the Jura Mountains and the Aar Massif in the Central Alps (Fig. 1a, b; Reber and Schlunegger, 2016).

Among the various glacial archives, surficial deposits of the Last Glacial Maximum (LGM, i.e., the state of local maximum ice extent; Ehlers et al., 2018), such as moraines, have been thoroughly investigated because of their easy accessibility. Hence, the LGM is probably the most investigated and best reconstructed glacial advance among the Quaternary glaciations in the Alps. Dating of Alpine LGM moraines suggests a correlation with the timing of the maximum global ice volume during Marine Isotope Stage 2 (MIS 2, 29–14 ka; e.g., Ivy-Ochs et al., 2008). On the Swiss Plateau and in the Jura Mountains, moraines and boulders, situated beyond the LGM ice extent, were tentatively assigned to the MIS 6 (191–130 ka), yet the scatter in the assigned ages is large (e.g., Bickel et al., 2015; Graf et al., 2015). An MIS 6 age has also been proposed for the basal sediments encountered in a drilling about 150 km northeast of Bern (site Niederweningen; Dehnert et al., 2010). The sedimentary record of the oldest glaciations in the Northern Alpine Foreland, which occurred during the Early Pleistocene (2.58–0.77 Ma), is preserved on top of local heights in the "Deckenschotter" deposits (Bolliger et al., 1996; Haeuselmann et al., 2007a; Akçar et al., 2017; Claude et al., 2019). However, results from a recent study that employed a probabilistic framework to interpret cosmogenic nuclide-based ages (Knudsen et al., 2020) contradict the biostratigraphic correlation with the Early Pleistocene (Bolliger et al., 1996). Apart from the Deckenschotter deposits, the majority of Mid-Pleistocene sediments is rather unlikely to be preserved at the surface and is therefore hardly accessible. Nevertheless, Mid-Pleistocene sedimentary sequences were encountered by drillings in overdeepenings at different locations across the Swiss Plateau, including the area investigated in the present study (e.g., Schlüchter, 1989; Preusser et al., 2005; Dehnert et al., 2010; Buechi et al., 2017). Although these drillings showed that the overdeepening fill mainly comprises fluvio-lacustrine sediments postdating the MPT, they currently present point information within a limited regional context. Accordingly, a tight network of drillings is required to fill the gaps in information and particularly to improve our understanding of the Quaternary history of the Alps (e.g., the "Drilling Overdeepened Alpine Valleys project", Anselmetti et al., 2014).

Here, we conducted such a drilling in the confluence area of the Rhône and Aare glaciers (Fig. 1c) with an effort to reconstruct the sedimentary and landscape dynamics that can be expected in a glacial-to-glaciolacustrine setting (Buechi et al., 2017; Fabbri et al., 2018; Sutherland et al., 2019). We selected the Bern area for this drilling because the recently modeled bedrock topography implied a sediment thickness of 150 m (Fig. 1d; Reber and Schlunegger, 2016). Furthermore, previous drillings in the region (Sect. 3), mapping (Geologiebüro Kellerhals et al., 2000; Isler, 2005), and outcrops provide a stratigraphic frame, which allows us to place the point information of the drilling in a regional context.

2 Geological setting

The study area is located in the Middle Aare Valley (MAV) between the border of the Alps and the city of Bern (Fig. 1b, d). Glaciers originating in the Central Alps advanced into the MAV repeatedly during the Quaternary (e.g., Schlüchter, 1989; Preusser et al., 2005; Wüthrich et al., 2018). During the LGM the confluence of the more voluminous Valais/Rhône lobe and the Aare glacier was located at the downstream terminus of the MAV (Fig. 1c; Bini et al., 2009; Ehlers et al., 2011). Abundant traces of the LGM are present in the Bern area as terminal moraines, drumlins, till cover, and outwash plains (Fig. 1c). The Aare glacier retreated from the Bern area ca. 20 ka ago (Wüthrich et al., 2018). The region was ice free by 17 ka at the latest (Meichtry, 2016). In the 1980s, two scientific drillings were conducted to unravel the glaciation history of the region beyond the LGM cover (Meikirch and Thalgut, Fig. 1c, d). The cored material was analyzed for pollen biostratigraphy and luminescence dating (Welten, 1982, 1988; Schlüchter, 1989; Preusser and Schlüchter, 2004; Preusser et al., 2005). The results of the investigated drillings showed that the sediment infill of the overdeepened MAV is locally as old as MIS 11 (424–374 ka; Koutsodendris et al., 2012) or possibly even older (Sect. 3).

In the MAV, the bedrock consists of early Miocene fluvial sandstones and overbank fines, which are referred to as the Lower Freshwater Molasse (LFM; Platt and Keller,

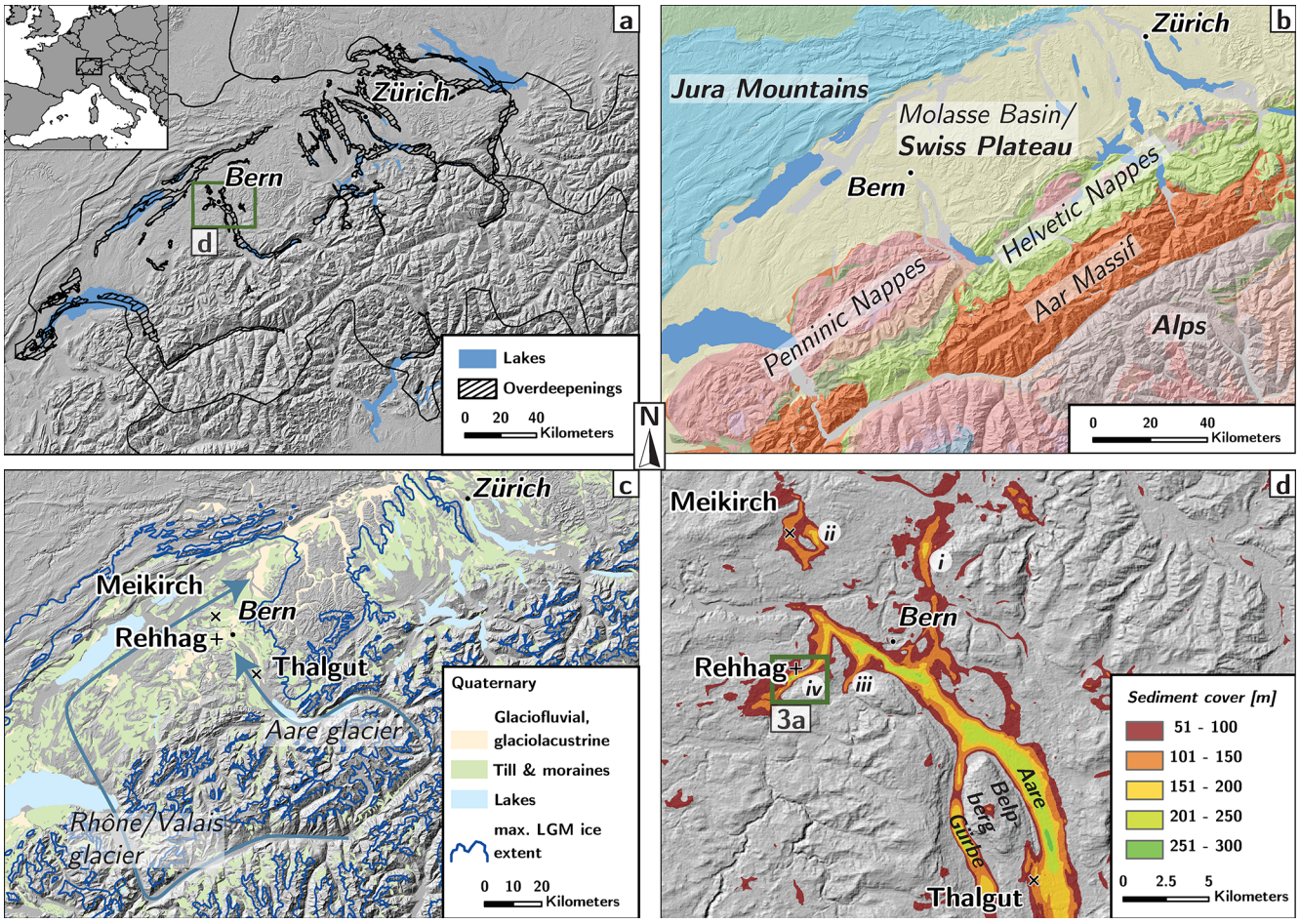

Figure 1. **(a)** Distribution of overdeepenings in the Swiss Alps and Plateau. For data availability, see below. The green box outlines the extent of the study area as shown in **(d)**. **(b)** Location map of the geographic (bold font) and geologic (normal font) settings in the vicinity of the study area. **(c)** Surface distribution of deposits from the last glaciation. The maximum extent of glaciers during the LGM is indicated along with the flow directions (green arrows) of the Rhône and Aare ice streams (modified from Ehlers et al., 2011). The locations of the Meikirch, Rehhag, and Thalgut drill sites are marked. **(d)** This map shows the varying thickness of the sediment fill in the MAV overdeepening as derived from the bedrock model (see below). The locations of the Meikirch, Rehhag, and Thalgut drill sites are marked. Numbers (i) to (iv) indicate branches of the MAV overdeepening as mentioned in the text (Sect. 2). These branches are (i) the N-directed continuation of the main overdeepening, which is ca. 8.5 km long, (ii) an isolated bedrock depression (Meikirch trough) located 2 km north of the distal termination of the main trough, (iii) a ca. 2 km-long SW-oriented branch situated about 1 km SW of Bern, and (iv) a ca. 6.5 km-long SW-directed branch, referred to as the Bümpliz trough. The green box shows the location of the map in Fig. 3, in which the local geology and morphology at the Rehhag site atop the Bümpliz trough (iv) are presented in more detail. All elevation data are based on ASTER (NASA/METI/AIST/Japan Spacesystems and U.S./Japan ASTER Science Team, 2019). The Reber and Schlunegger (2016) bedrock topography in **(d)** is part of the bedrock surface model for Switzerland in **(a)**. The Swiss-wide model is a composite of various data sets (Jordan, 2010; Dürst Stucki et al., 2010; Dürst Stucki and Schlunegger, 2013; Reber and Schlunegger, 2016), and the model is available via the Federal Office of Topography (Swisstopo). A free-of-charge high-resolution reconstruction of the bedrock topography in the Canton of Bern (Reber and Schlunegger, 2016) with a 10 m resolution in elevation is available through the canton's geodatabase (http://www.geo.apps.be.ch/de, last access: 24 June 2021). The thickness of the Quaternary fill has been determined through the elevation difference between the modern topography and the bedrock surface (e.g., Dürst Stucki and Schlunegger, 2013).

1992). The bedrock surface model of the MAV (Reber and Schlunegger, 2016) shows the occurrence of an overdeepening beneath the current valley surface (Fig. 1d). According to estimations by Dürst Stucki and Schlunegger (2013), the Quaternary sediment infill in the MAV varies in thickness between 150 and 300 m, yet the thickness reaches local maxima with more than 500 m. The MAV main trough is divided into two branches (Aare and Gürbe) separated by a bedrock ridge (Belpberg, Fig. 1d). At its terminus, four lateral troughs depart from the main overdeepening (i–iv, Fig. 1d).

3 Previous scientific drilling in the MAV

A first 160 m-deep drilling on the western flank of the Aare branch (Fig. 1d) did not reach the base of the Quaternary glacial fill (Fig. 2 left; Welten, 1982, 1988; Schlüchter, 1989; Preusser and Schlüchter, 2004). At the deepest level between 462 and 536 m a.s.l., this Thalgut drilling encountered pollen (*Pterocarya* and *Fagus*) embedded in lacustrine deposits. The pollen assemblage was correlated with the Holsteinian interglacial, the equivalent to MIS 11 (cf. de Beaulieu et al., 2001; Koutsodendris et al., 2012). Attempts to use luminescence dating on this part of the Thalgut section encountered saturated samples, which supports the assignment of a relatively old age through palynology (Lowick et al., 2012). The overlying unit up to 593 m a.s.l. consists of a 50 m-thick sequence of deltaic gravel foresets, 4 m of till, and 4 m of lacustrine deposits, which were interpreted as deposits of an advancing and retreating glacier (possibly during MIS 8, 300–243 ka). A hiatus is located at 593 m a.s.l. The section overlying this hiatus includes 15 m-thick glaciofluvial gravel foresets, which are overlain by 3 m-thick interglacial lacustrine deposits and 3 m-thick glaciofluvial gravel beds. Results of luminescence dating (Preusser and Schlüchter, 2004) and pollen analyses (Welten, 1982, 1988) allowed these authors to link the lacustrine sediments to the Eemian, which corresponds to MIS 5e (129–111 ka; e.g., Brauer et al., 2007). Paleosol formation at 614 m a.s.l. and below indicates a time span without sedimentation and thus points towards the occurrence of another hiatus. Preusser and Schlüchter (2004) linked this hiatus to an interstadial prior to the LGM. The uppermost 6 m-thick succession consists of glaciofluvial gravel beds and of an LGM till (MIS 2).

A second drilling conducted north of Bümpliz into the Meikirch trough (Fig. 1c) retrieved a continuous sedimentary succession that spans from 518 to 608 m a.s.l. (Fig. 2 right; Welten, 1982, 1988). The suite is characterized by lacustrine mud beds, containing three segments with different interglacial pollen assemblages. The sequence is topped by a 6 m-thick suite of glaciofluvial gravel. The 110 m-thick sequence is framed by two glacial tills at the base and at the top. Luminescence dating allowed Preusser et al. (2005) to link these sediments to two successive glaciations, which were interrupted by an interglacial period. The aforementioned authors considered the sediments to chronicle the time interval from MIS 8 through MIS 7 (243–191 ka) to MIS 6 (191–123 ka). A hiatus separates the succession described above from an LGM till (MIS 2) at the top.

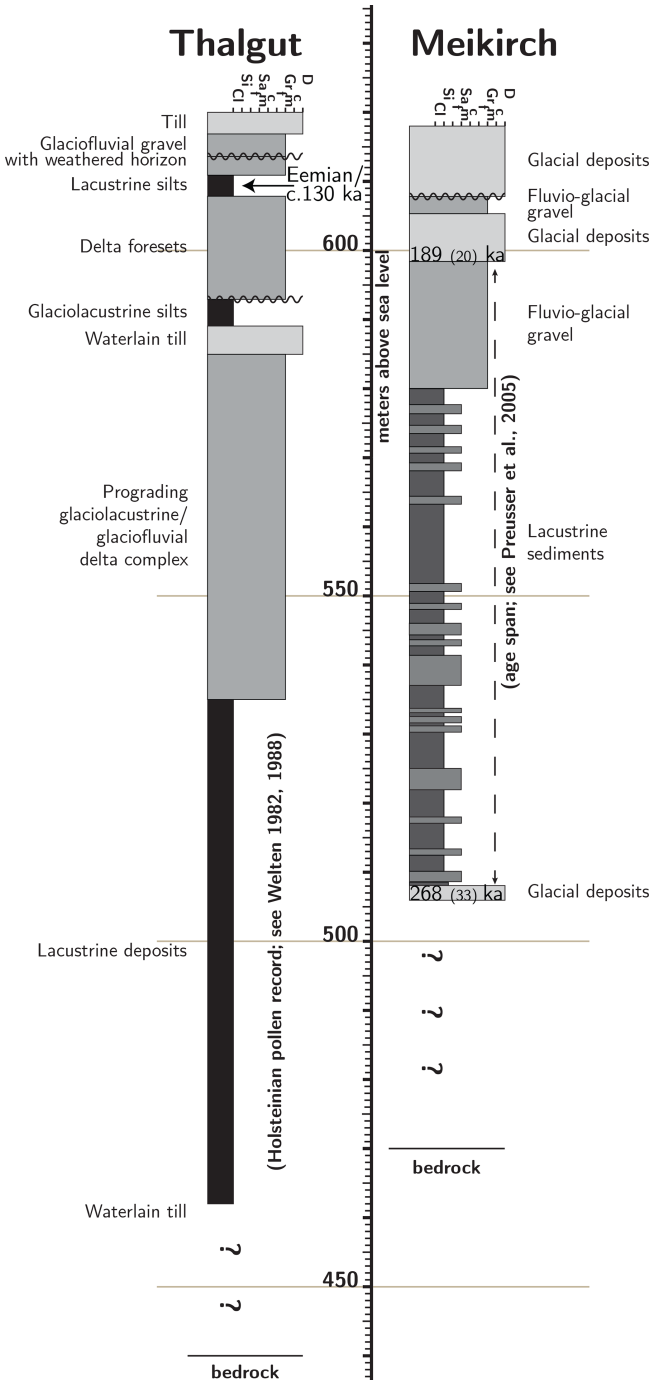

Figure 2. Left: modified log of the Thalgut drill core (Welten, 1982, 1988; Schlüchter, 1989; Preusser and Schlüchter, 2004). Right: modified log of the Meikirch drill core (Welten, 1982, 1988; Preusser et al., 2005). The luminescence ages and respective errors (in brackets) of the uppermost and lowermost samples as determined by Preusser et al. (2005) are displayed in the log (508 and 600 m a.s.l.).

4 Site survey and drilling

The main goal of this study was to recover the record of at least one glacial–interglacial cycle, which should, preferably, include the Eemian (i.e., MIS 5e) or any older interglacial. We considered locations with inferred sediment thicknesses over 100 m to increase the probability of recov-

ering one full glacial–interglacial cycle. Furthermore, the newly drilled section should potentially allow a correlation with the previously drilled MAV suites. Thus, we collected information from drilling reports and geological maps to assess the stratigraphic architecture of the MAV sedimentary fill. We targeted outcrops of Pleistocene lacustrine deposits during this reconnaissance, because they had the greatest potential to contain fine-grained sediments that could be enriched in pollen and were most likely formed within the desired age range. Using these constraints, we located the drilling above the Bümpliz trough (Fig. 1d, location iv; position CH1903+/LV95: 2595232, 1197952; WGS 84: 46.9326, 7.3760) near an abandoned clay pit, referred to as the Rehhag outcrop, which we trenched, sampled, and mapped in the field and acquired aerial images of (Fig. 3). This outcrop is located on the western flank of the Wangen Valley (Fig. 3a) and unveils a 35 m-thick (567–602 m a.s.l.) sedimentary succession of lacustrine deposits that underlie a thick glaciofluvial gravel unit (locally ca. 30 m; Fig. 3b; Isler, 2005). The outcrop exposes a shift from a lacustrine environment to a fluvial setting and was used to extend the sedimentary sequence recovered in the drilling. Additionally, two samples from a well-sorted sand unit within the succession were collected for optically stimulated luminescence dating (OSL; see below).

Drilling was conducted by Fretus AG between February and May 2019, using a Nordmeyer DSB 1/6 mobile rig to a total depth of 211.5 m. A total of 207 core sections, each 1 m long, and 9 sections, 0.5 m in length, were retrieved in plastic liners. A down-the-hole percussion coring tube was used up to a depth of 37 m, and it was replaced by a CSK-146 wireline diamond coring system for the remaining 171.5 m of unconsolidated sediment and 3 m of bedrock. The first 30 m were cased with 324 mm casing, followed by 6 m with a 280 mm casing, while the lower diamond coring section remained uncased. When the rod was removed to exchange the drill bit, the hole was stabilized by a drilling mud consisting of water with additions of biodegradable polymer and bentonite. Water inflow was recorded at depths of 3–4 and 8–9 m. Major drilling fluid losses occurred at a depth of 168–169 m. A core recovery rate of 92.3 % was achieved, 6.6 % of the core had lost all structures due to disturbance during drilling, and only 1.1 % of the core was physically lost.

After retrieval, the liners were capped, provisionally marked, and kept in wooden boxes with direction markers, name tags, and the respective driller depth to allow proper storage. The cores were weighed in as a first estimate of core recovery. Parallel to the drilling operations, cores were regularly transported to the Institute of Geological Sciences, University of Bern, for their investigation in the off-site core laboratory. The drill hole was cemented after the completion of the drilling operations, following official cantonal regulations. The core is stored in the Swisstopo core repository and is available for further investigation.

5 Methods

5.1 Core logging and sampling

We measured γ density, loop magnetic susceptibility, and P-wave velocity values at a 0.5 cm resolution (Schultheiss and Weaver, 1992) with a Multi Sensor Core Logger (MSCL; Geotek Ltd.) at the off-site core laboratory. Because the coupling between the P-wave instrument, the liner, and the core material could not be maintained, we did not consider these values for further investigations. The data set of the density and loop magnetic susceptibility, which consists of more than 42 000 readings per parameter, includes outliers that were measured at both ends of a liner. These were disregarded from the subsequent analysis. After logging with the MSCL, the liners were opened under light-sensitive conditions (i.e., in a dimmed room and under red light). One half of the core was packed and stored in two layers of lightproof tubular film to preserve the material for future extraction of luminescence samples.

After splitting, individual cores were logged (Sect. 5.2), and the material was scanned with a digital line scanner on the MSCL under stable lighting conditions to ensure consistent colors on the photos. We then measured the shear strength values particularly of fine-grained and silt-rich material with a vane meter (max. 250 kPa; Eijkelkamp, 2012) to complement the information yielded by the γ density analysis. However, the degree of consolidation was locally too high to allow penetration with the vane meter. As the last step, we collected samples for the determination of the pollen and carbon content (total carbon TC, total inorganic carbon TIC, and total organic carbon TOC).

5.2 Sediment description

The sediment was logged at the scale of individual beds in the direction of the drilling, i.e., downsection. The description followed a modified template of Krüger and Kjær (1999) for deposits in glacial environments. We then followed state-of-the-art approaches to characterize and interpret the sedimentological observations (e.g., Rose and Menzies, 2002; Buechi et al., 2017; Rosenblume and Powell, 2019; Sutherland et al., 2019). Accordingly, each sediment bed was first assigned to a lithofacies based on upper and lower bed contacts, the bed thickness, the grain size, the clast shape, and the sedimentary structures. This information built the basis for inferring a transport and deposition mechanism for individual lithofacies (Sect. 6.1 and Appendix A). As a final step, the encountered strata were grouped into different facies assemblages (FAs) based on their position within the cored sedimentary succession, their lithofacies, and distinct changes in the succession of lithofacies (Sect. 7). The lithofacies assemblages then built the basis for developing a scenario of how the sedimentary environment has evolved through time (Sect. 8.2).

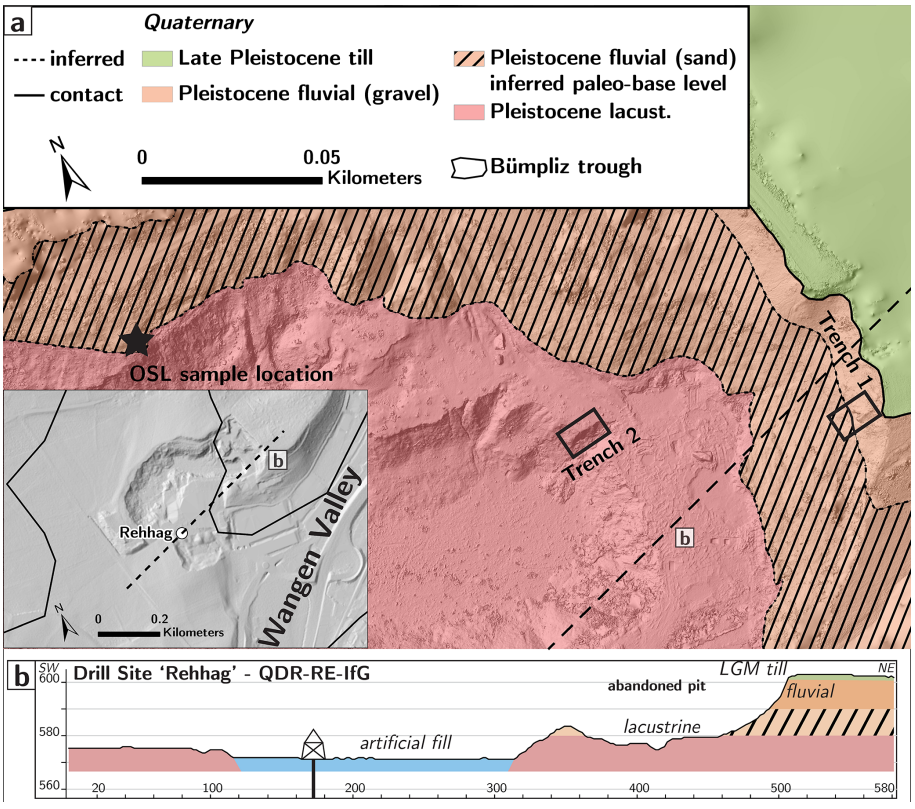

Figure 3. **(a)** Detailed overview of the abandoned Rehhag clay pit with the OSL sample location and two trenches. At these three positions, the composition, texture, and fabric of the sediment were analyzed in more detail, as these are the sites that record the transition from a lacustrine to a fluvial environment. The displayed geological map resulted from our mapping in the clay pit. More detailed information is available in Sect. 4. The outcrop sequence overlaps with the sedimentary sequence recovered in the drilling at an elevation of 567 m. a.s.l. or 4 m core depth. The map inlet shows the entire Rehhag clay pit and the location of the drill site. Furthermore, the position of the cross section in **(b)** is indicated, along with the outline of the overdeepening and part of the adjacent Wangen Valley. **(b)** SW–NE-oriented cross section through the study site, showing the geological details at the Rehhag (2× exaggerated). The lacustrine sediments correspond to the top of sequence B, whereas the fluvial gravel beds correspond to sequence C in this paper (Forstschotter; Sect. 8.2). In the section, the LGM till is only a few meters thick. Note the 23° shift relative to the north. The elevation data in the main map were produced from a drone survey. Elevation data in the inlet map with 2 m resolution from © Swisstopo.

5.3 Optically stimulated luminescence dating

Two samples (RE-01 and RE-03) from a well-sorted, 10 m-thick sand unit within the succession at the Rehhag outcrop were collected for feldspar luminescence dating (Fig. 3). We used 18 cm-long, 4.6 cm-wide, capped, and lightproof PVC tubes to collect the unconsolidated sand. Dose rate samples were scraped around the tubes into plastic bags prior to the extraction of the tubes. Feldspar infrared stimulated luminescence (IRSL) signals from multi-grain aliquots (1 mm) were measured at 50 and 225 °C with a Risø luminescence reader and a single-aliquot regenerative-dose (SAR; Murray and Wintle, 2000) post-IR IRSL protocol based on Buylaert et al. (2009). Further methodological details are described in Appendix B.

Luminescence measurements were analyzed with the R.Luminescence package (Kreutzer et al., 2012). In a first step, in addition to the standard quality criterion, the saturation of the apparent equivalent dose (D_e) per individual aliquot was tested (by the $2D_0$ rule: $D_e > 2D_0 \hat{=}$ saturation; Wintle and Murray, 2006). The sample equivalent dose (ED) was then calculated from the apparently unsaturated aliquot D_e data using the Central Age Model (CAM; Galbraith and Roberts, 2012). In a second step, a fading correction based on Kars et al. (2008) was individually applied to each unsaturated aliquot D_e, the results of which were then tested again for saturation and eventually used for the calculation of a fading-corrected age. The K, Th, and U contents were measured by high-resolution gamma spectrometry to determine the natural dose rate for each sample in order to calculate the sample ages. Further methodological details are available in Appendix B. The R script that was written for this analysis can be accessed at the drilling data repository (Schwenk et al., 2021).

5.4 Palynology

A total of 10 samples (2 cm^3 each) were collected for a preliminary palynological analysis. The samples were taken from different fine-grained beds within the upper 72 m of the core to identify segments where pollen concentrations are suitable for a more extensive analysis. Before the chemical treatment, all samples were soaked in distilled water, and *Lycopodium* tablets were added (Stockmarr, 1971). The standard lab protocol was applied following Moore et al. (1991) using HCl, KOH, HF, and acetolysis. The hydrofluoric acid treatment was repeated due to the high content of lithogenic components in all samples. For pollen identification, a transmitted light microscope with different magnifications, palynological keys (Moore et al., 1991; Beug, 2004), the palynological atlas of Reille (1992), and the reference collection of the Institute of Plant Sciences, University of Bern, were used.

5.5 Organic and inorganic carbon

Throughout the core, 16 clayey silt layers and an additional 49 silt and sand layers were sampled for the determination of their carbon content. The TC, TIC, and TOC concentrations were measured with a Thermo Scientific Flash 2000 Smart (Thermo Fischer, Waltham, MA, USA). The $CaCO_3$ content of the sediment can be determined under the assumption that the measured inorganic carbon was solely bound in carbonate minerals. The multiplication of the TIC by a stoichiometric factor of 8.33 results in the respective carbonate concentration.

6 Results

6.1 Sediment inventory

6.1.1 Bedrock

The Rehhag drilling recovered a total of 211.5 m of core material (Fig. 4). In the lowermost 3 m the drilled section consists of red, yellow, and predominantly green-gray fine-grained sandstone beds that are interbedded with thin and light-colored siltstone, which displays abundant mottling. Given the high grade of consolidation, reddish color, mottling, and fabric of the sediments, these sandstones are attributed to the Lower Freshwater Molasse Group (LFM; Platt and Keller, 1992) and are considered to represent the bedrock at the base of the overdeepening. The overlying Quaternary sediments follow upon a sharp contact with the Molasse bedrock. Accordingly, we place the top of the bedrock at an elevation of 362.5 m a.s.l.

6.1.2 Lithofacies of the Quaternary suite

The overlying 208.5 m-thick Quaternary suite (Fig. 4) and the sediments exposed in the Rehhag clay pit (Fig. 3a, b) were categorized into 12 lithofacies (lfs; Fig. 4). Please refer to Table 1 and to Appendix A for a full description of the lithofacies and to Fig. 5 for illustrations of specific sedimentary features. In general, the Quaternary succession is dominated by well-sorted sand beds or characterized by units with a sandy component. Fine-grained sediments such as clayey silt beds also contribute to the succession but are less frequently observed than the sandy layers. Coarse-grained material such as pebble and gravel beds (and larger grain sizes), however, is less frequent but dominates the lithofacies on top of the cored suite (i.e., Forstschotter, Sect. 4). Generally, a good to moderate degree of sorting is present in lfs 1 to 10. The stratified diamicts of lithofacies 11 (Dms) and the massive diamicts of lithofacies 12 (Dmm) deviate from this picture as the material is poorly sorted (Dms and Dmm) and lacks a sedimentary organization of the material (Dmm). Interestingly, Dmm deposits are encountered in two depth intervals between 83 and 103 m and at the base of the drilled Quaternary suite between 194 and 208.5 m depth (Fig. 4). Accordingly, we used these diamicts to subdivide the Quaternary succession into a lower sequence A (between 208.5 and 103 m depth) and an upper sequence B (uppermost 103 m) where each sequence starts with a > 10 m-thick succession including massive diamicts. In this context, the massive diamicts are referred to as Dmm.1 or Dmm.2 if they occur at the base of sequence A or sequence B, respectively.

6.1.3 Oversteepened beds, strike-slip faults, and subhorizontal shear planes

Contacts with a dip angle $> 40°$ are present in the core sections at 108–109 m and 119–120 m depths and occur within successions of beds with variable grain sizes in the range of sand and variable admixture of a silty component (e.g., Fig. 5i). The encountered dipping angles are steeper than can be expected from silt and sand deposits (e.g., Beakawi Al-Hashemi and Baghabra Al-Amoudi, 2018). Hence, we consider these beds to be evidence for localized oversteepening, which occurred after the deposition of the material.

A staircase structure cuts across the contact between a medium-grained sand and a silty fine-grained sand in the center (46 cm section depth) of the core section 124–125 m. This staircase consists of three steps that have relative vertical displacements of 4 and 1.5 cm from the lower left-hand to upper right-hand sides of the core, respectively. Upsection of the staircase, beds appear to be displaced along two subvertical, undulating lines that separate the three steps. Downsection of the staircase, the displacement becomes less visible, and it dissipates into small-scale ruptures and irregularities from 55 cm and below. We consider these steps to result from a displacement of the material along a set of two subvertical shear planes (i.e., faults). Because the fault traces dissipate downsection of the staircase, we interpret this structure as resulting from strike-slip rather than normal faulting.

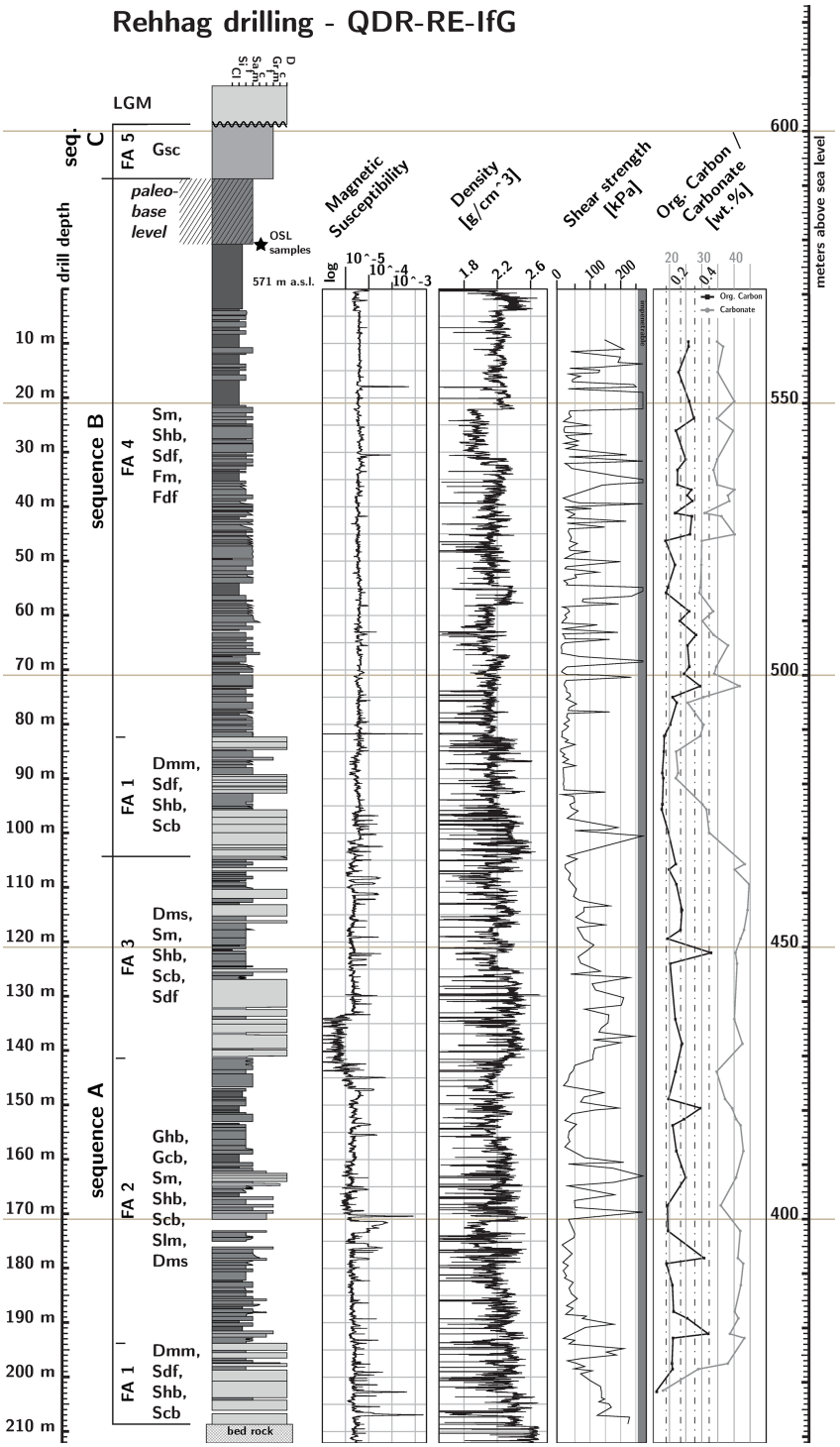

Figure 4. Drill log of the presented Rehhag drilling and the sequentially overlying outcrop in the Rehhag clay pit. Blank spaces in the log show considerable core loss. The depth from the top of the drilling is shown on the left-hand side and absolute elevation on the right-hand side of the figure. The figure also displays the logging results of the magnetic susceptibility, γ density, shear strength, TOC and $CaCO_3$ concentration measurements. The left-hand side of the log illustrates the distribution of lithofacies assemblage, and the respective lithofacies are noted. The sedimentary succession can be divided into two major sequences that were each initiated by a glacial advance. The basal till in each sequence is overlain by a thick assemblage of lacustrine deposits. The lower sequence A was formed in an ice-contact fan environment of a proglacial lake. The upper sequence B was formed from turbid underflows in a proglacial lake or deposited by turbid underflows in a lacustrine prodelta environment. The entire sequence is overlain by fluvial braidplain deposits, which can be considered a third sequence C, as this unit potentially transitions to another glacial period. An LGM till (Holocene) unconformably overlies the considerably older, Pleistocene sequence.

Table 1. This is a summary of the 12 lithofacies elements identified in the drill core, their main properties, and interpretation. Detailed descriptions can be found in Appendix A. Illustrative core photos are displayed in Fig. 5.

No.	Lithofacies	Description	Interpretation
1, Gsc	Gravel with basal scours (Fig. 5a), outcrop only	Moderately sorted, clast-supported, subrounded to rounded, fine-grained to cobble-sized gravel, sandy matrix; 10–100 cm-thick beds; concave-upward features, imbrication, normal, inverse, and normal to inverse grading; Alpine lithologies Appendix A	(Glacio)fluvial gravel
2, Ghb	Horizontal-bedded gravel, below 185 m	Moderately sorted, clast- and matrix-supported, subangular to rounded, fine- to medium-grained gravel, sandy matrix; 3–70 cm-thick beds; horizontally bedded; normal, inverse, and inverse-to-normal grading; Alpine lithologies	Hyperconcentrated (or concentrated) density flows (proximal)
3, Gcb	Cross-bedded gravel, below 185 m	Moderately sorted, clast- and matrix-supported, subangular to rounded, fine- to medium-grained, sandy matrix; 5–70 cm-thick beds; inclined at 15–30°; normal, inverse, and inverse-to-normal grading; Alpine lithologies	Concentrated (or hyperconcentrated) density flows (proximal)
4, Sm	Massive sand, core only	Well-sorted silty fine- to medium-grained sand; 30–100 cm-thick beds; massive, clusters of outsized clasts	Hyperconcentrated density flows
5, Shb	Horizontal-bedded sand (Fig. 5b), entire core & outcrop	Well-sorted silty fine- to medium-grained sand; 5–40 cm-thick beds; horizontally bedded; massive, normal, inverse, inverse-to-normal grading	Quasi-steady hyperpycnal turbidity currents or braidplain
6, Scb	Cross-bedded sand, below 107 m	Well-sorted silty fine- to medium-grained sand; 5–40 cm-thick beds; inclined at 10–35°; massive, normal, inverse, inverse-to-normal grading, cross-beds	Concentrated density flows
7, Slm	Laminated sand (Fig. 5c), below 185 m	Well-sorted silty fine- to medium-grained sand; 20–50 cm-thick beds; horizontal, inclined at 10–35°; silt-rich or silt laminae, subparallel; cross-beds	Turbidity flows
8, Sdf	Deformed sand, core only	Well-sorted silty fine- to medium-grained sand; 5–50 cm-thick beds; horizontal and inclined; disorganized, wavy, and folded structures	synsedimentary convolution or water escape
9, Fdf	Deformed mud and sand (Fig. 5d), above 21 m & outcrop	Clayey silt, silty to fine-sandy medium-grained sand; distorted and folded interbeds; thickness undiscernible	Synsedimentary convolution
10, Fm	Massive mud (Fig. 5e), core only	Very well-sorted clayey silt; 1 to > 100 cm-thick beds; massive	Settling in stagnant water or Bouma T_e
11, Dms	Stratified diamict (Fig. 5f), below 103 m	Poorly sorted, silty fine-grained sand, outsized clasts of coarse-grained sand to cobble-sized material; 10 to > 100 cm-thick beds; horizontal, inclined at 20–30°; massive matrix; subangular to rounded clasts, Alpine lithologies; bands of clasts indicating bedding orientation	Hyperconcentrated density flow (proximal)
12, Dmm	Massive diamict (Fig. 5g and h), core only	Poorly sorted, matrix-supported, silty to medium-sandy matrix, coarse sand to cobble-sized clasts; 20 to > 100 cm; massive, unstratified; subangular to rounded clasts, Alpine lithologies; at the bedrock contact angular to subangular clasts, coarse sand to boulder, Molasse sandstone	Subglacial deposition

A third feature was found in the lowermost 3.5 m (205–208.5 m) above the bedrock contact within diamictic beds of Dmm.1 (Fig. 4). The corresponding beds contain subhorizontal clay bands up to 5 cm thick, which are, on a smaller scale, composed of thinner wavy sub-bands with a large variety of colors, including green, yellow, brown, and red. Each of the larger bands includes a singular, dark straight line, which upon core opening shows a plane that reflects the light similar to slickensides (Fig. 5j). One such band (Fig. 5h) hosts a dark red and trapezoid clast, where the band mate-

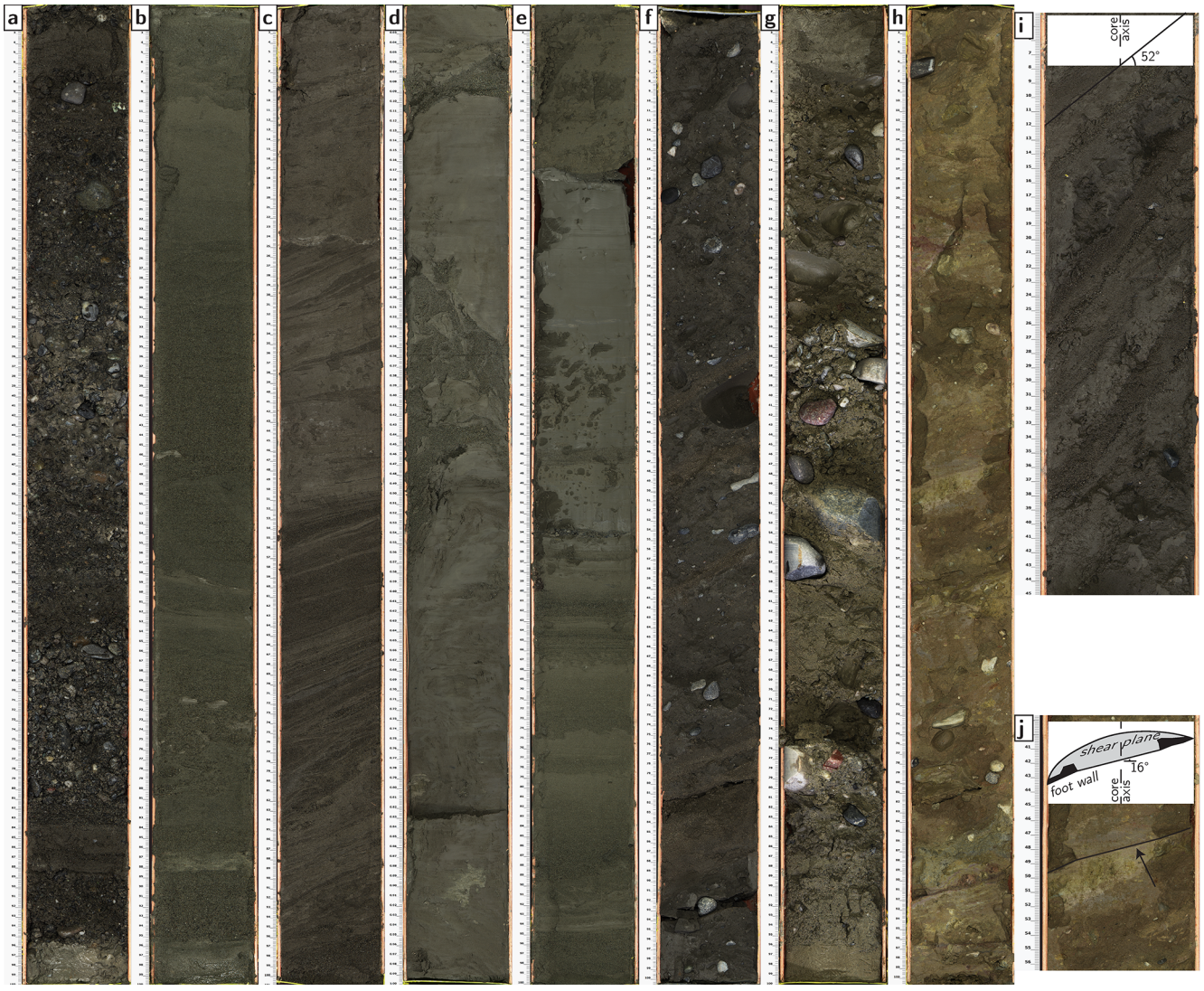

Figure 5. Photos of eight illustrative core sections. For lithofacies descriptions, see Appendix A and Table 1. **(a)** Ghb, QDR-RE-IfG 175, 170–171 m: clast-supported, fine- to medium-grained gravel beds with a sandy and silty matrix and sand interbeds. **(b)** Shb, QDR-RE-IfG 063, 59–60 m: sandy deposits with a distinct normal grading between 10 and 57 cm. **(c)** Slm, QDR-RE-IfG 187, 182–183 m: cross-bedded, laminated sand beds. **(d)** Fdf, QDR-RE-IfG 011, 10–11 m: fine-grained sediments showing deformation, most probably due to slumping. **(e)** Fm, QDR-RE-IfG 043, 39–40 m: thick clayey silt layer with a gradual contact atop a normally graded sand. The upper contact is sharp. **(f)** Dms, QDR-RE-IfG 144, 139–140 m: mud beds with outsized clasts showing an inclined bedding and arrays of clasts where the *a*–*b* planes are aligned parallel to the bedding. **(g)** Dmm.2, QDR-RE-IfG 106, 101–102 m: upper till void of sedimentary structures. **(h)** Dmm.1, QDR-RE-IfG 212, 207–208 m: lower till showing colored clay bands hosting glaciotectonic shear planes at 49, 60, 81, 90, and 97 cm. Note the probably rotated clast at 90 cm depth. **(i)** QDR-RE-IfG 115, 108–109 m: example of oversteepened beds. The apparent dip is ca. 52°. **(j)** QDR-RE-IfG 212, 207–208 m: example of a shear plane (arrow) in Dmm.1. The inset shows the apparent dip of the plane and a projection of the plane into the cored material based on the prepared foot wall surface (black polygons).

rial is wrapped around the particle and forms a blanket that tapers off on both sides of the clast. These structures share similarities to shear planes that can be formed by the glaciotectonic brittle deformation of a till (e.g., van der Wateren, 2002; Phillips, 2018). Probably, the clay bands atop or on both sides of these shear planes represent a fault gouge. In this context, the trapezoid clast described above could resemble an augen-like rotational clast right above such a shear plane.

6.2 Shear strength and γ density

The mean density within the bedrock section of the core is as high as 2.55 g cm^{-3} and then decreases distinctly at the transition from the Lower Freshwater Molasse bedrock into

the unconsolidated Quaternary sediment at 208.5 m depth (Table 2 and Fig. 4). Within the entire sediment infill, the mean density is slightly increased in the assemblages which contain the Dmm (2.28 ± 0.24 and $2.17 \pm 0.24\,g\,cm^{-3}$) and Dms ($2.24 \pm 0.18\,g\,cm^{-3}$) lithofacies. The assemblages that mainly consist of sand show reduced density values (2.17 ± 0.19 and $2.13 \pm 0.14\,g\,cm^{-3}$). Overall, the density of the lower sequence A is notably higher than that of the overlying sequence B. The highest density values in the sedimentary suite are well aligned with peaks in the shear strength data. The highest shear strength values are measured for cohesive sediments, i.e., silt or silty beds, whereas sand beds show the lowest shear strengths throughout the entire core.

6.3 Magnetic susceptibility

After the rejection of outliers, the magnetic susceptibility (MS) data show two distinct patterns along the core (Fig. 4). A higher MS amplitude is measured in the lower half of the core up to a depth of 85 m, where the signal is attenuated. The signal then remains at lower levels upsection. The mean MS values in sequences A ($59.90 \pm 330.83 \times 10^{-6}$) and B ($59.56 \pm 105.97 \times 10^{-6}$) are closely aligned despite the different scatter of the data.

Generally, MS peaks are caused by fine-grained sediment particles or gravel clasts with an iron component. Highest MS peaks can be caused by metallic particles chipped off the drill head and rod. Furthermore, data peaks are encountered in core sections that were disturbed by the drilling (e.g., meters 171–173).

6.4 Optically stimulated luminescence measurements

Following the first step of the R routine, which was applied to the IRSL measurements of samples RE-01 and RE-03, the D_e of all aliquots but one were kept for the IR50 signal, while half and one-third of the D_e of the aliquots were dismissed for the pIRIR225 signal due to clear saturation ($D_e > 2D_0$; Table 3). Apparent sample EDs of 520.4 ± 121.2 and 474.8 ± 115.4 Gy for the IR50 signal and of 555.2 ± 173.8 and 586.4 ± 132.4 Gy for the pIRIR225 signal were calculated for RE-01 and RE-03, respectively, which are equivalent to ages of 234.6 ± 57.0 ka/203.4 ± 51.7 ka (IR50) and 250.3 ± 80.2 ka/251.3 ± 59.8 ka (pIRIR225). After fading correction and further evaluation of possibly saturated aliquots, an ED of 788.9 ± 379.3 Gy was derived (from CAM) for sample RE-03 for the IR50 signal, which yielded a fading-corrected age of 338.0 ± 164.5 ka. No fading-corrected ages could be calculated for the pIRIR225 and for the sample RE-01 (either signal) as all aliquots clearly indicated saturation after fading correction. All results from luminescence and related measurements are presented in Table 3.

6.5 Palynology and carbon content

Despite the additional hydrofluoric acid treatment, the concentrations of fine-grained lithogenic components in the pollen samples were still remarkably high. Pollen concentrations were extremely low in all samples. In fact, pollen was found in only 4 of the 10 samples, and never more than three grains were encountered. Four grains could be identified as either *Poaceae* (39.24; 36.38; 20.89 m) or *Rumex acetosa* (35.11 m) type. All other grains ($n = 3$) were either corroded or fragmented beyond determinability. Abundant *Lycopodium* spores were identified in all samples, ensuring that low pollen concentrations do not reflect a loss of pollen during chemical treatment.

The mean TOC throughout the core is 0.19 ± 0.08 wt %, and the mean TIC is 4.32 ± 0.73 wt %, or correspondingly, the mean calcium carbonate concentration is 36.02 ± 6.12 wt %. The mean TOC concentrations in sequences A and B are very similar and are at 0.19 ± 0.09 wt % and 0.19 ± 0.08 wt %, respectively. The lowest TOC concentrations were measured for the Dmm and the neighboring sediments (Dmm.1 0.11 ± 0.06 wt %, Dmm.2 0.08 ± 0.02 wt %; Fig. 4 and Table 2). The $CaCO_3$ concentrations in sequence A are higher (39.72 ± 5.28 wt %) than in sequence B (33.04 ± 5.07 wt %). Most significant is the drop in the carbonate concentration around the two sections of the sequence that contain Dmm beds, where the mean concentrations are as low as 28.32 ± 10.05 (Dmm.1) and 27.16 ± 4.71 wt % (Dmm.2; Table 2). However, it has to be noted that the mean $CaCO_3$ concentration around the Dmm.1 beds is based on the results of three readings only (17.98 wt % and 28.92 wt % for Dmm.1 beds and 38.06 wt % for a Scb bed). In total, seven TIC measurements were obtained around the beds of Dmm.2, where the corresponding carbonate concentrations range between 21.94 wt % and 32.27 wt %. Here, two measurements (87–88 m, 22.04 wt %; 103–104 m, 32.27 wt %) were obtained from Dmm.2 beds. The remaining five readings were obtained from sand beds, including the lowest value in the range (21.94 wt %).

7 Interpretation

The sorting, stratification, and fabric encountered in lithofacies 1 to 10 point towards a deposition mechanism with support by water (Sect. 6.1, Table 1 and Appendix A). Furthermore, the gray colors observed in lfs 2 to 10 are an indicator of the deposition in a non-oxidizing aquatic environment. After the carving or excavation of the investigated glacial overdeepening, the bedrock trough was most likely filled with water simultaneously to the glacial retreat and to the onset of the waterlain deposition, thereby forming a > 100 m-deep lake. Accordingly, lithofacies elements 2 through 10 were most likely formed in a lacustrine environment. The beds of lithofacies 1 were most probably deposited in a fluvial setting. However, the interpretation of the diamic-

Table 2. This is a summary of the identified lithofacies assemblages, their extent from the top of the drilling, their extent in absolute elevation (surface 571 m a.s.l.), and the different lithofacies they comprise. The table also shows how the facies assemblages are grouped into the major sequences. Along with the assemblages, the mean values of the measured γ density, TOC content, and $CaCO_3$ concentration are presented. The $CaCO_3$ concentration of the bedrock is based on Blaser et al. (1994).

Facies assemblage	Driller's depth (m)	Elevation (m a.s.l.)	Lithofacies	Sequence	Magnetic susceptibility ($\times 10^{-6}$)	γ density ($g\,cm^{-3}$)	TOC (wt %)	$CaCO_3$ (wt %)
Bedrock	211.5–208.5	359.5–362.5			45.91 ± 6.95	2.55 ± 0.31		0–20
FA 1	208.5–194.0	362.5–377.0	Dmm.1, Sdf, Shb, Scb		154.94 ± 845.58	2.28 ± 0.24	0.11 ± 0.06	28.32 ± 10.05
FA 2	194.0–141.0	377.0–430.0	Ghb, Gcb, Sm, Shb, Scb, Slm, Dms	A	50.89 ± 132.58	2.17 ± 0.19	0.20 ± 0.09	40.32 ± 2.55
FA 3	141.0–103.0	430.0–468.0	Dms, Sm, Shb, Scb, Sdf		36.21 ± 39.34	2.24 ± 0.18	0.19 ± 0.09	42.18 ± 1.68
FA 1	103.0–84.0	468.0–487.0	Dmm.2, Sdf, Shb, Scb	B	54.43 ± 31.28	2.17 ± 0.24	0.08 ± 0.02	27.16 ± 4.71
FA 4	84.0–(+20)	487.0–591.0	Sm, Shb, Sdf, Fm, Fdf		61.12 ± 119.77	2.13 ± 0.14	0.22 ± 0.07	34.46 ± 4.07
FA 5	(+20)–(+30)	591.0–601.0	Gsc	(C)	Outcrop only			

Table 3. Details of the IR50 and pIRIR225 luminescence analyses of samples RE-01 and RE-03, including the details of the first step analysis of the apparent (i.e., uncorrected) D_e, the details of the second step analysis for fading correction (Kars et al., 2008), and inputs for the calculation of the natural dose with DRAC (Durcan et al., 2015). The table has "NaN" (not a numeric) entries where age calculations were attempted but failed due to the elimination of saturated aliquots.

ID/signal			OD (%)	Step 1 $n_{used}/n_{measured}$	ED_{app} (Gy)	Apparent age (ka)
RE-01/IR 50 °C			20	11/12	520.4 ± 121.2	234.6 ± 57.0
RE-01/pIRIR 225 °C			17	6/12	555.2 ± 173.8	250.3 ± 80.2
RE-03/IR 50 °C			22	12/12	474.8 ± 115.4	203.4 ± 51.7
RE-03/pIRIR 225 °C			8	9/12	586.4 ± 132.4	251.3 ± 59.8
	g_{2d} (% per decade)	ρ'		Step 2 $n_{used}/n_{measured}$	ED_{corr} (Gy)	Corrected age (ka)
RE-01/IR 50 °C	3.5 ± 0.1	$2.4 \times 10^{-6} \pm 7.7 \times 10^{-8}$		0/12	NaN	NaN
RE-01/pIRIR 225 °C	1.7 ± 0.1	$1.2 \times 10^{-6} \pm 6.6 \times 10^{-8}$		0/12	NaN	NaN
RE-03/IR 50 °C	3.3 ± 0.2	$2.2 \times 10^{-6} \pm 1.4 \times 10^{-7}$		2/12	788.9 ± 379.3	338.0 ± 164.5
RE-03/pIRIR 225 °C	1.5 ± 0.2	$1.0 \times 10^{-6} \pm 1.2 \times 10^{-7}$		0/12	NaN	NaN
	U (ppm)	Th (ppm)	K (%)	Dose rate ($Gy\,ka^{-1}$)		
RE-01/IR 50 °C RE-01/pIRIR 225 °C	0.73 ± 0.11	3.24 ± 0.12	1.49 ± 0.01	2.22 ± 0.14		
RE-03/IR 50 °C RE-03/pIRIR 225 °C	1.12 ± 0.13	4.50 ± 0.14	1.42 ± 0.02	2.33 ± 0.14		

tic beds (Dmm, Dms) is equivocal as several transport mechanisms (such as cohesive debris flows, glacial processes, and flow of glacigenic material at the ice front) can be invoked to explain the related structures (see Appendix A).

7.1 Assignment of the Dmm lithofacies to a glacial till

We interpret Dmm as a subglacial till because the lowest $CaCO_3$ concentrations encountered in Dmm.1 and Dmm.2 beds (Sect. 6.5 and Table 2) point to the admixture of Molasse bedrock material (carbonate content between 0 % and 20 %; Blaser et al., 1994) to material derived from more carbonate-rich sources (e.g., Helvetic and Penninic nappes). This admixture of Molasse material most likely occurred through in situ glacial carving, because the Dmm.1 directly overlies the bedrock and comprises angular and subangular Molasse blocks. In addition, the partial green, red, and yellow colors of the Dmm.1 matrix resemble the colors of the bedrock very well. Since the LFM units are poorly consolidated (Platt and Keller, 1992) and have one of the lowest erodibilites reported for the rocks in Switzerland (Kühni and Pfiffner, 2001), the presence of angular to subangular Molasse clasts points to a very short transport distance. Active erosion by subaqueous cohesive debris flows is unlikely (see Appendix A; Iverson, 1997; Mulder and Alexander, 2001). Therefore, we suggest that Dmm.1 was formed by subglacial

processes and that the Molasse rafts could have been derived from in situ plucking and dragging of bedrock pieces by the glacier. At 103 m depth, Dmm.2 follows upon a sharp contact, where the underlying >35 m-thick suite of cross-bedded lithofacies is abruptly cut off by this contact. We interpret the contact between the upper Dmm.2 beds and their substratum as an erosional contact and thus as a major unconformity. As subaqueous cohesive debris flows are unlikely to form such unconformities (see references above), we suggest that erosion probably occurred during a glacial advance. Accordingly, Dmm.2 above the unconformity rather corresponds to a till than to a debris flow deposit. The inferred occurrence of erosion is also supported by the low $CaCO_3$ concentration (27.16 ± 4.71 wt %; see above), and a glacial mechanism is consistent with published interpretations on the origin of distinct glacigenic sedimentary layers within the MAV overdeepening during MIS 8 and probably even during MIS 10 (374–337 ka; Preusser and Schlüchter, 2004; Preusser et al., 2005, 2011).

7.2 Interpretation of oversteepeened beds, faults and shear planes as glaciotectonic features

If the interpretation of the Dmm as subglacial till is correct, then the oversteepened beds, strike-slip faulting, and subhorizontal shear planes described in Sect. 6.1.3 could be explained by glaciotectonic deformation.

The oversteepening described as the first structure in Sect. 6.1.3 is possibly representative of such a glaciotectonic deformation. In this context, oversteepening can occur when the bedded preglacial substratum is tilted by the overriding glacier (e.g., Phillips et al., 2002). According to Boulton et al. (2001) the tilting of the unlithified sediments occurs if the water pressure beneath the glacier and in the substratum is high enough to promote such motion and deformation. Accordingly, we interpret these oversteepeened beds as a glaciotectonite (Evans et al., 2006).

Subvertical faults and displaced bedding in the preglacial substratum could be the result of loading and the anisotropic compaction of the subglacial stratum. Alternatively, differences in the longitudinal motion of the glacier and differences in the motion transfer to an anisotropic substratum could result in the occurrence of strike-slip faulting. However, we are not aware that similar structures have previously been described and explained by glaciotectonics. Thus, the ambiguity in determining the formation process of the second feature in Sect. 6.1.3 remains.

Subhorizontal shear planes with slickensides as encountered at the base of the Quaternary suite were also observed beneath Breiðamerkurjökull (Benn, 1995) and were considered to indicate the occurrence of shear fractures (Boulton et al., 2001). These shear planes are formed due to an increase in the consolidation of the subglacial till and to a decrease in both the subglacial water pressure and water content, thereby promoting a downward increase in strain within the till (Boulton et al., 2001). The interpretation of such a consolidation in the Dmm.1 lithofacies is additionally supported by the highest sediment density values (2.26 ± 0.29 g cm^{-3}, Table 2) and the associated high shear strengths (Fig. 4). Hence, we interpret the observed shear planes (third feature in Sect. 6.1.3) as a result of brittle deformation in the simple shear regime and in a water-poor subglacial setting at the base of a till section (3.5 m above the bedrock). Additionally, we identified a rotational bedrock intraclast attached to one of the shear planes, which supports the interpretation of deformation through simple shear (Phillips, 2018).

In summary, the subglacial tills represented by the lithofacies Dmm.1 and Dmm.2 as well as their subjacent beds bear deformation features that most likely resulted from glaciotectonic processes (Broster, 1991; Hart and Boulton, 1991; Phillips, 2018). Therefore and following Evans et al. (2006), we interpret these tills as subglacial traction tills.

7.3 Facies assemblage and interpretation of the sedimentary environment

In this section, we group the 12 lithofacies elements into 5 FAs (Fig. 4 and Table 2), which we use as a basis for reconstructing the depositional environment and the related evolution of the landscape surrounding the Bümpliz trough (Sect. 8).

FA 1 comprises beds of Dmm with interbedded Sdf, Shb, and Scb. This assemblage is encountered at depths between 84 and 103 m as well as 194 and 208.5 m and is dominated by the presence of Dmm beds, which overlie their substratum with sharp contacts. The structures preserved by the Dmm beds have been interpreted as recording the occurrence of glaciotectonic processes, which we have linked with the shear mechanisms that occur below a moving glacier. In such an environment, the interbeds could be interpreted as subglacial deposits that were detached from the substratum and thrust between layers of till as floes of intact sediment or reworked sediment patches (Sdf; Aber and Ber, 2007). However, we have not observed any evidence for thrust faults between the Dmm and its interbeds, which would be required for such an interpretation. Alternatively, the interbeds could have been deposited in subglacial or englacial conduits and ponds (Shb and Scb; e.g., Buechi et al., 2017). Accordingly, we refer to the lithofacies ensemble in FA 1 as subglacial traction till with interbeds.

FA 2 comprises an ensemble of the seven lfs Ghb, Gcb, Sm, Shb, Scb, Slm, and Dms and occurs at depths between 141 and 194 m upon a gradual contact with FA 1 sediments. Planar cross-bedding (10–30°) and (sub)horizontal bedding are the dominant sediment structures in FA 2. Evidence for trough cross-bedding can be identified only in Scb and Slm. In a glaciolacustrine environment as inferred for the Bümpliz trough, such deposits could be formed by density flows at a delta/fan apron or in a prodelta/fan environment. These flows

could originate from surges on a delta plane or collapses of the delta front, including ice-marginal deltas (Postma, 1990; Lønne, 1995; Winsemann et al., 2018). Alternatively, the density flows could also be ejected by (sub)glacial conduits in an ice-contact lake, or they could originate from collapses at the front of an ice-contact fan (Powell, 1990; Lønne, 1995; Mulder and Alexander, 2001; Winsemann et al., 2018). Because FA 2 directly overlays a subglacial traction till, we tentatively prefer the second interpretation. In such a context, the steep foresets (20–30°) could form in front of subaqueous ice-contact fans or in front of deep-water deltas, including ice-contact deltas (Lønne, 1995). The subhorizontal beds could then accumulate in channels that are cut into the delta/fan foresets. Because the FA 2 sediments reveal a fining upward trend, the sourcing glacier was most likely retreating during deposition of FA 2.

FA 3 assembles beds of the five lfs Dms, Sm, Shb, Scb, and Sdf. This assemblage is found at depths between 103 and 141 m and overlies FA 2 upon a gradual contact. In contrast to the FA 2 sediments, FA 3 comprises up to 50 % of Dms beds recording the dominance of hyperconcentrated density flows. Because such currents could result from the efflux of subglacial conduits, we consider that the Dms beds record the occurrence of an ice-contact fan (Lønne, 1995). The thickness (ca. 6 m) and steep inclination (20–30°) of individual Dms layers are consistent with such an interpretation as these structures point to the existence of steeply dipping foresets in front of an ice-contact fan. Because of the relatively (in comparison with FA 2) immature texture of the FA 3 deposits, we suggest that the sediment source (i.e., the glacier grounding line) had advanced relatively close to the depositional site (see also Lønne, 1995). In particular, we envisage a mechanism where the glacier either shifted closer to the depositional site or where it moved over the previously formed ice-contact fan. As discussed in Sect. 7.2, the oversteepening and faulting encountered in the uppermost 20 m of FA 3 (Sect. 6.1.3) were possibly formed by glaciotectonic deformation.

FA 4 assembles beds of Sm, Shb, Sdf, Fm, and Fdf. This assemblage is found in the outcrop +20 m above the top of the drilling and down to a depth of 84 m. This fourth FA is dominated by sand deposits with a massive texture or a grading that suggest deposition from hyperconcentrated density flows that escaped the glacier (Fitzsimons and Howarth, 2018) and quasi-steady hyperpycnal turbidity currents with sources in a delta/prodelta environment (Nemec, 1990; Postma, 1990; Fitzsimons and Howarth, 2018). Because FA 4 shows an overall fining-upward trend and follows upon FA 1 (Fig. 4), we envisage a scenario where the flows originated first from a glacier and then from a deltaic environment. Accordingly, the basin was finally fed by a braided river system that developed small mouth bars at the delta front (e.g., mouth bar-type deltas; Postma, 1990). Such a delta is expected to prograde towards the point of observation, resulting in a continuous filling of the lake. We do see evidence for such a development by the occurrence of the ca. 30 m-thick Fdf succession. These sediments are then overlain by Shb sands, which show evidence (ocher to brown color) for oxidation and thus for incipient pedogenesis. This allows us to allocate the approximate elevation of a local paleo-base level at the top of FA 4 at about 580 m a.s.l.

FA 5 comprises beds of Gsc only. This assemblage is found only in the outcrop within the Rehhag clay pit at heights of +30 to +20 m above the top of the drilling (Figs. 3 and 4). We interpret this lf as a fluvial deposit (Table 1). However, it is noteworthy that this fifth FA resides above the paleo-base level determined by FA 4. In this context, Isler (2005) interpreted this gravel unit as a sign of an advancing glacier (i.e., Vorstossschotter). We follow this interpretation based on (i) the large spatial extent, (ii) the large thickness exceeding 30 m, (iii) the occurrence of clasts up to cobble size, and (iv) the superposition of these gravel beds on top of the lacustrine sequence encountered at the Rehhag. We find it plausible that such tick gravel deposits can be linked to increased erosion, sediment transport, and water supply in response to the onset of another glacier advance.

8 Discussion

8.1 Assignment of a depositional age

The pollen content of the encountered sedimentary suite was too low to allow a relative chronological positioning of the sedimentary succession and a paleoenvironmental reconstruction. We explain the low pollen concentration by the energetic depositional environment, which was dominated by the sediment supply through different density and turbidity flows. For pollen to accumulate, a persistently stagnant water column would be required, as was probably the case at the Meikirch and Thalgut sites. In fact, we have not encountered laminated and organic- and pollen-rich silt and clay layers in the drilled sedimentary suite.

The luminescence dating on a well-sorted sand of the mouth bar delta in FA 4 was more successful than the pollen analysis. Yet the luminescence signal of the tested sediment lies in the high dose range of the feldspar luminescence system (Fig. B1), possibly reflecting an old (ca. 10^5-year time range) depositional age of the sediment. Alternatively, the high dose range might also reflect an inherited signal due to the lack of light exposure of the feldspar grains prior to deposition (so-called "partial bleaching"), which is common in glacial environments as sediment is typically transported in suspension over short distances and in turbid water (Duller, 2006). We, however, interpret the high luminescence signals as mainly resulting from an old depositional age rather than a significant partial bleaching effect, because the sampled lithofacies shows evidence for incipient pedogenesis, which is indicative of an ice-free and light-exposed environment. The inferred sufficient exposure is additionally supported by the observed moderate overdispersion (OD $\leqq$ 20 %) of

the individual aliquot D_e distributions, which are within the common range of OD reported for well-bleached fluvial/glaciofluvial sediments (e.g., Galbraith et al., 2005; Jacobs et al., 2006; Gaar et al., 2014). Furthermore, the differences between the apparent IR50 and pIRIR225 ages (10 % to 25 %) lie within the typical range of age differences induced by differential fading (Buylaert et al., 2009; Li et al., 2014). Accordingly, a minimum age of about 250 ka is provided by two apparent (i.e., non-fading-corrected) pIRIR225 measurements, which are considerably more stable and underestimate ages to a smaller degree compared to the IR50 measurements. We note that a significantly higher single age (338.0 ± 164.5 ka, RE-03 IR50) was obtained after fading correction. However, this age needs to be taken with caution because (i) it is based on only two aliquots, it shows an unusual age increase (66 %), and it has a significant error, and (ii) a significant portion of aliquots D_e from both signals lie below the $2D_0$ saturation limit criterion (Table 2) and, thus, do not support a much older (i.e., several 100 ka) depositional age, despite a potential fading artifact (King et al., 2018). Considering the ensemble of these constraints, we tentatively suggest a depositional age > 250 ka for sequence B (minimum apparent pIRIR225 ages). This age is consistent with the regional stratigraphic context provided by the Thalgut and Meikirch drillings (Sect. 3), where sediments in an age range from MIS 11 to MIS 6 have been recovered so far. Most noteworthy, such an age is supported by sedimentological evidence, because the transition from a lacustrine to fluvial environment (paleo-base level) is recorded at an elevation of about 580 m. a.s.l. at both the Meikirch and Rehhag sites. This facies change was dated to lie within the MIS 7 in the Meikirch sedimentary succession (Preusser et al., 2005). Therefore, we tentatively assign an MIS 8 (300–243 ka) to MIS 7 (243–191 ka) depositional age to the well-sorted sand unit at the top of FA 4 because of the apparent similarities in the stratigraphic architectures of the Meikirch and Rehhag sedimentary successions.

8.2 Evolution of the Bümpliz trough

In the following, we use the succession of distinct FAs encountered in the Rehhag core and clay pit to reconstruct a scenario of how the landscape evolved throughout the deposition of the analyzed sedimentary succession (Fig. 6). The entire suite starts with a glacial till (FA 1), which contains evidence for active bedrock erosion and glaciotectonic processes. This basal till was thus most likely formed during a glacial advance into the Bümpliz trough (Fig. 6a). Although there is ample evidence for the occurrence of bedrock erosion during this glacial period, the formation of the Bümpliz overdeepening through this particular glacier is a possible hypothesis, which, however, cannot be tested with the available observations. The sediments of the overlying FA 2 record the retreat of possibly the same glacier that deposited the basal till. As a result, the overdeepening was filled with meltwater, and a > 150 m-deep proglacial lake was formed. A range of subaqueous density flow deposits accumulated in a distal ice-contact fan environment (Fig. 6b), recording a further retreat of the glacier.

Subsequently, flow tills (i.e., hyperconcentrated density flows) dominated the sedimentary processes in a proximal ice-contact fan environment (FA 3), thus documenting a second advance of a glacier close to the depositional site (Fig. 6c). At this stage, we are not capable of determining whether this was the same glacier as the one that formed the basal till above the bedrock. Abruptly, the flow till deposits were cut by the same or another glacial advance, as evidenced by the upper and thus stratigraphically younger till (Fig. 6d) that has a similar lithofacies assemblage and thickness to the basal till. This glacier dragged or thrust the underlying beds into an oversteepened position, thereby leaving distinct features of glaciotectonic deformation. After the retreat of this particular glacier, accommodation space was again available to be filled with water, which was ca. 80 m deep, and subsequently with sediment (Fig. 6e). During this time, sedimentation was dominated by concentrated density flows and turbidity currents. These flows were probably first generated from underflows that were sourced by conduits escaping the glacier. They subsequently originated from floods on a delta top or collapses on a delta flank. As sediment accumulation continued, the lake basin was eventually filled to a paleo-base level. Following the filling of the lake basin, the area was gradually covered by thick glaciofluvial gravel beds (Fig. 6f), which could point towards another glacial advance.

Overall, the sediment that was retrieved from the Bümpliz trough documents a shallowing-up sequence. Following an erosional glacial advance, the formation of the sequence started in an underfilled trough or a basin. After one break of the sequence, the lake basin was filled to a paleo-base level and evolved into overfill conditions. This overfill probably occurred in parallel with the third advance of a glacier close to the Bümpliz trough. Therefore, and as already suggested in Sect. 6.1, the sedimentary sequence within the Bümpliz trough can be subdivided into two main stratigraphic sequences, the lower sequence A and the upper sequence B. Both sequences started with the formation of a glacial till that was subsequently covered by thick glaciolacustrine and lacustrine deposits. Finally, the occurrence of the glaciofluvial gravel beds on top of sequence B could be regarded as a further sequence C, when overfill conditions prevailed and when the region evolved into a large fluvial braidplain.

The segmentation of sequences A and B is additionally supported by the results of the γ density, magnetic susceptibility, and carbon content measurements and could reflect distinct changes in environmental conditions. First, the higher γ density of the sequence A deposits could indicate that the material of this sequence was loaded and compacted by more glacial advances than the material in the upper sequence B, yet the loading by the sediment column itself can have a similar effect. Second, the relatively high MS signal

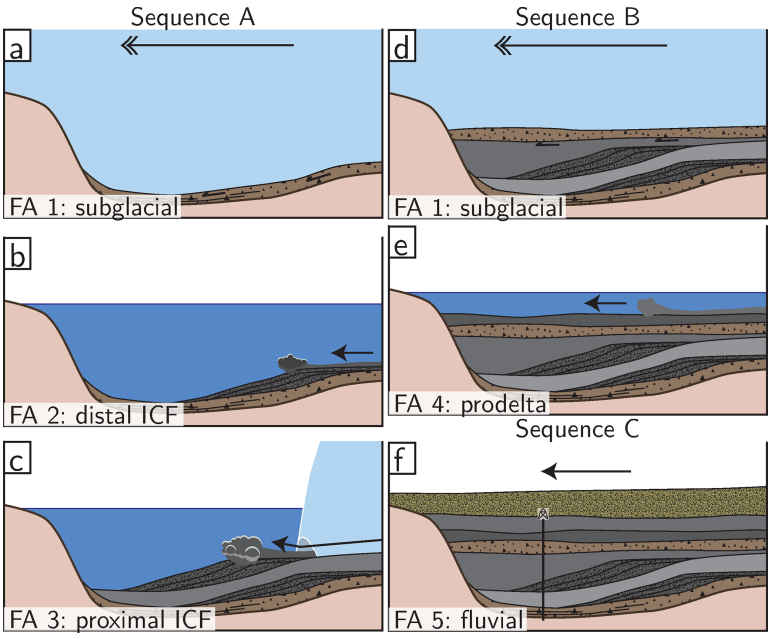

Figure 6. Schematic figures showing the evolution of the Bümpliz trough (Sect. 8.2 and Fig. 1d) as inferred from the retrieved sediment core. The relative core position is indicated by a vertical black line in **(f)**. The facies assemblages related to each phase in the model are specified in the figures. Glacier ice is colored light blue, ice motion is indicated by a double-headed arrow, lake water is dark blue, and single-headed arrows indicate sediment flow. **(a)** First glacial advance with bedrock erosion and brittle shearing of the subglacial till. **(b)** Retreat of the glacier and fining-up aggradation in a distal ice-contact fan (ICF) setting. **(c)** Deposition of "flow tills" after overcoming a threshold on the lake bed and/or a glacial advance (ICF). **(d)** Erosion and cutting off foresets due to a second glacial advance with formation of a glaciotectonite (oversteepening). **(e)** Deposition from underflows in a proglacial lake or from turbulent density flows on a lacustrine prodelta. **(f)** Overfilled lake basin covered by thick glaciofluvial gravel beds.

amplitude in sequence A and in the upper till could be related to the abundance of coarse-grained material in these deposits. Third, the drop in the carbonate concentration between sequences A and B could indicate a more pronounced input and admixture of Molasse bedrock during the deposition of sequence B. Potentially, there is a connection between the observed MS signal and the carbonate concentration in that the sediment composition varies between the two sequences and that the sediment routing and supply were modified during the lacustrine phase in sequence B.

9 Conclusions

We analyzed 208.5 m of unconsolidated Quaternary sediment and 3 m of Molasse bedrock in a drill core recovered from the Bümpliz trough, a branch of the overdeepening in the MAV. It is the first scientific drilling in the MAV that reached bedrock. The retrieved sediments revealed two major sequences, A (lower) and B (upper), with each of them starting with a till deposited when the area was glaciated. Each glacial period was accompanied by erosion of Molasse bedrock as documented by the relative depletion of the $CaCO_3$ concentration in either till. Molasse rafts and shear planes in the lower till provide evidence for the occurrence of erosion and glaciotectonic deformation during the first recorded glacial advance. Similarly, the formation of the upper till was accompanied by glaciotectonic deformation of the substratum during the second glacial advance. Each till is overlain by subaqueous (glacio)lacustrine sediments that record the filling of the overdeepened trough after the ice retreated from the area. The lower sequence A documents the supply and deposition of sediment by a range of density and turbidity currents. It was formed in a grounding line setting, where the ice was submerged in a proglacial lake and where sediment-laden (sub)glacial conduits formed ice-contact fans. The upper sequence B chronicles the supply and deposition of sediment mainly by turbidity currents. It was formed in a delta apron to prodelta environment, where the turbid flows were generated either from underflows in a proglacial lake, from flooding events on the delta plain, or from gravitational collapses at the delta front. Measurements of IRSL signals indicate that the deposition of the upper, stratigraphically younger sequence B probably occurred in a phase of global cooling during MIS 8 and the subsequent interglacial MIS 7. Hence, sequence B of the presented drilling is likely an equivalent to the sedimentary sequence recovered in the nearby scientific drilling in Meikirch. Finally, sequence B evolved into overfilled conditions, recorded by the fluvial braidplain deposits of sequence C.

Appendix A: Lithofacies description and interpretation

A1 Lithofacies 1: Gsc, gravel with basal scours (outcrop only)

This lf is composed of an amalgamation of moderately to well-sorted, clast-supported, fine-grained to cobble-sized gravel beds and is only encountered in the Rehhag outcrop (Fig. 3). The matrix can vary from fine- to coarse-grained sand with light-brown to gray-brown color. Individual gravel beds are between 10 and 100 cm thick and have mostly gradual basal contacts. They display a stacking of beds with inverse-to-normal grading. Additionally, beds with concave-upward, sharp basal contacts are present. These beds often contain a layer of sand along the contact. Well-sorted gravel beds show clast imbrication. The clasts are subrounded to rounded and comprise rather durable lithologies that are derived from the Alpine nappes. In particular, we encountered the following clast types: (i) limestones, siliceous limestones, and dolomites that were most likely derived from the Helvetic and Penninic Prealpine thrust nappes, (ii) arkose sandstone clasts, which might be derived from the Permian/Triassic suite overlying the Aar Massif, (iii) quartzite constituents, which could be derived from either the Triassic cover of the Penninic Bernhard nappe or which represent recycled material from Miocene Molasse conglomerates, and (iv) rare metamorphic or granitic/granodioritic clasts (Fig. 1b; Institut für Geologie, Universität Bern and Bundesamt für Wasser und Geologie, 2005). The latter crystalline lithologies are either derived from the Aar Massif or the crystalline Penninic nappes. Alternatively, crystalline clasts might also represent recycled material from the Miocene Molasse conglomerates (Matter, 1964). Granitic/granodioritic and quartzite constituents are more abundant in Gsc than in any other lf and dominate the cobble fraction.

Interpretation. Concave-up structures point towards the occurrence of basal scouring. Well-sorted gravel with basal scours is commonly encountered where water flow is funneled in channels. Sorting and particularly imbrication indicate fluctuating transport energies, including localized upper flow regime conditions (e.g., Garefalakis and Schlunegger, 2019). The well-sorted nature of this lithofacies together with the clast fabric indicates that the material had been transported over some distances before the gravel was deposited. Overall, this fabric is characteristic of a transport and deposition by water, possibly by a braided river (Rust, 1978; Miall, 1985).

A2 Lithofacies 2: Ghb, horizontal-bedded gravel (below 185 m depth)

This lf is composed of moderately sorted, clast- and matrix-supported, fine- to medium-grained gravel beds. The matrix can vary from fine- to coarse-grained sand, which has a brownish-gray to gray color (Fig. 5a). The bed thicknesses vary between 3 and 70 cm. Because individual beds do not show any evidence for inclination, we consider them to be horizontally bedded. Individual gravel beds that are > 5 cm thick commonly have a sharp basal contact, whereas thinner gravel beds can gradually evolve from underlying sand beds and thus display gradual basal contacts. Normal and inverse gradings are most common in beds that are > 10 cm thick. In addition, intra-bed transitions from inverse to normal grading occur where beds are > 50 cm thick. In normally graded beds, grain size can decrease to thin layers solely composed of sand. Gravel components are subangular to rounded and comprise lithologies that are indicative of an Alpine origin (see Gsc).

Interpretation. This lf was probably deposited from waxing and waning concentrated or hyperconcentrated density flows, which were generated by gravitational instabilities in a delta/fan environment (Mulder and Alexander, 2001) or by underflows in an ice-contact lake (Fitzsimons and Howarth, 2018). We base this interpretation on the presence of normal and inverse grading, the moderate sorting, and the clast- and matrix-supported fabric (Lowe, 1982; Mulder and Alexander, 2001). Occasionally, the density of these flows decreased to such a degree that only sand was transported and deposited, as indicated by thin sand intercalations. We consider the coarse-grained composition of this lf together with the inferred transport mechanism as evidence for a relative proximity to the sediment source (Mulder and Alexander, 2001).

A3 Lithofacies 3: Gcb, cross-bedded gravel (below 185 m depth)

This lf comprises moderately sorted, clast- and matrix-supported, fine- to medium-grained gravel beds. The matrix is composed of fine- to coarse-grained sand, which is brownish gray to gray. Individual beds are between 5 and 70 cm thick and show inclinations where the dip angles range from 15 to 30°. Normal and inverse grading is frequently observed. Similarly to Ghb, transitions from inverse-to-normal grading within individual beds are often present where beds are > 50 cm thick. The clasts are subangular to rounded and comprise lithologies that are indicative of an Alpine origin (see Gsc).

Interpretation. The angles (15–30°) observed in this lf correspond to dip angles of bed sets in cross-beds. We therefore consider this lf to be cross-bedded. Steeply dipping cross-beds can be indicative of large-scale foresets in deltas and fans (Lønne, 1995). Additionally, the observed dip angles can be indicative of foresets and backsets in scours formed around chutes-and-pools or for backsets into scours that formed behind an isolated hydraulic jump, both under supercritical flow conditions within fans and deltas, which formed in proglacial lakes (Hornung et al., 2007; Lang et al., 2017, 2021). The required supercritical flow can either result from motion on steep slopes or from the confinement of

channels (Parker et al., 1986; Mulder and Alexander, 2001). In such a context, the formation of channels and scours by currents eroding their substratum is more likely to occur through concentrated density flows, due to an increased flow velocity compared to hyperconcentrated density flows (Parker et al., 1986). The spatial extent and further characteristics of these cross-beds could not be observed in the cored sediment. Otherwise, this lf is similar to Ghb. Therefore, we suggest a similar mechanism where concentrated or hyperconcentrated density flows transported and deposited the material in a delta or fan environment.

A4 Lithofacies 4: Sm, massive sand

This lf is composed of well-sorted, massive, silty fine- to medium-grained sand beds. The color of the material varies between brownish gray and gray brown. Individual beds are between 30 and 100 cm thick and commonly have a sharp base. Individual beds and layers do not show any evidence for inclination, and thus we consider them to be horizontally bedded. Isolated clasts of coarse-grained sand to medium-sized gravel are embedded within the silty sand and are considered outsized clasts. Such clusters of outsized clasts are encountered throughout entire beds or in limited sections within individual beds.

Interpretation. The lack of stratification and the presence of gravel clusters in entire or in parts of individual beds are probably signs of confined particle motion (saltation and/or fluid turbulence are absent) in a hyperconcentrated density flow (Mulder and Alexander, 2001). Such flows need a considerably inclined bed to move, and they come to a fast halt through frictional freezing (Lowe, 1982; Mulder and Alexander, 2001). In submerged basins fed by subglacial conduits, these flows can also be quasi-steady and might not point to the occurrence of short-lived pulses (Plink-Björklund, 1999).

A5 Lithofacies 5: Shb, horizontal-bedded sand (entire core and outcrop)

This lf comprises well-sorted, silty fine- to coarse-grained sand. In the core, the color varies between brownish gray and gray brown (Fig. 5b). In the Rehhag outcrop, the color of this lf depends on the grain size. In particular, the coarsest grains cause a gray tone, whereas the finer-grained sand particles are responsible for an ocher and brown color. Individual beds are 5 to 40 cm thick, have a sharp base, and bear no sign of inclination. Gradual contacts can occur with both underlying or overlying gravel beds. The sand can be massive or shows either a normal or inverse grading. Inverse-to-normal grading occurs in thicker beds. Normally and inversely graded beds can include thin layers of fine- to medium-sized gravel.

Interpretation. The grading in this lf suggests that the proportion of fluid to solid material in the flow was larger during deposition of its beds than during transport and accumulation of the Sm layers (see above). With a higher proportion of fluid in the flow, turbulences become important for keeping particles aloft, with the consequence that the transport of particles larger than medium-grained gravel cannot be accomplished (Mulder and Alexander, 2001). In a lacustrine delta-front to prodelta setting, Mulder and Alexander (2001) consider the oscillation of grading in sand beds as resulting from the waning and waxing of quasi-steady hyperpycnal turbidity currents. Similar (sub)horizontal sand beds can, however, be formed in fluvial braidplains that can occur on an active delta plain (Miall, 1985; Postma, 1990).

A6 Lithofacies 6: Scb, cross-bedded sand (below 107 m depth)

This lf comprises well-sorted, silty fine- to medium-grained sand. Bed thicknesses range from 5 to 40 cm. The color varies between brownish gray and gray brown. Individual beds have a sharp base, and they are inclined with dip angles between 10 and 35°. Opposite dip directions were formed on a scale that is small enough for them to be present within a single core section. Gradual contacts can occur with underlying gravel layers. Beds are massive or show normal and inverse grading. Inverse-to-normal grading is present within individual beds and can include thin gravel layers.

Interpretation. Similarly to Gcb, we consider the dip angles between 10 and 35° as a sign of cross-bedding and that the opposite dip directions within single core sections are evidence for the occurrence of a trough cross-bedding. The presence of such cross-beds could be a sign of concentrated density flows within the lower flow regime (e.g., Bouma T_c; Bouma, 1962). Compared to the Sm lithofacies, however, these flows were possibly more diluted because the formation of cross-bedding requires that the grains were able to saltate.

A7 Lithofacies 7: Slm, laminated sand (below 185 m depth)

This lf is composed of well-sorted, silty fine- to medium-grained sand. The color varies between brownish gray and gray brown. Individual beds are between 20 and 50 cm thick and have a sharp basal contact. The layers are either horizontally bedded or inclined with dip angles between 10 and 35°. Beds of this lf bear intercalated silt laminae or sand laminae with increased silt content and with sharp contacts with the surrounding sand (Fig. 5c). These laminae show a subparallel alignment with an inhomogeneous spacing. Within individual core sections, multiple stacks of laminae can dip in opposite directions.

Interpretation. The presence of laminae, which are the main feature in this lf, suggests deposition in both the upper (T_b) or lower (T_d) flow regimes. In this context, the cross-stratified laminations with opposite dip orientations could form either in a T_b to T_d setting (Bouma, 1962).

A8 Lithofacies 8: Sdf, deformed sand

This lf comprises well-sorted, silty fine- to medium-grained sand. The color varies between brownish gray and gray brown. Individual beds are between 5 and 50 cm thick and have either sharp or gradual basal contacts. The beds can be horizontally bedded or are occasionally inclined. Internally, this lf shows a slightly chaotic arrangement of layers as well as wavy and folded structures. These waves and folds are visible due to slight changes in sediment composition.

Interpretation. The presence of folded structures within inclined beds could hint towards the occurrence of synsedimentary deformation of beds by sliding. More chaotic structures could also result from the escaping of water after the sudden loading of water-saturated sediment layers. The chaotic structures might thus be similar to ball-and-pillow structures.

A9 Lithofacies 9: Fdf, deformed mud and sand (above 21 m depth and outcrop)

This lf comprises layers that are composed of clayey silt and beds with silty to fine-sandy medium-grained sand. The color varies between olive gray and gray brown (Fig. 5d). The sediment is characterized by a chaotic pattern in which the alternation of sand and silt layers is disrupted, folded, and crumpled. These deformed beds form successions that are several decimeters to meters thick and display sharp contacts with other lf.

Interpretation. This lf shows flame-like structures together with a chaotic bedding and convolute structures. We consider these observations as evidence for deformation, for example, trough sliding. However, indicators for inclination were not encountered, which might have been lost during the synsedimentary deformation.

A10 Lithofacies 10: Fm, massive mud

This lf comprises massive, very well-sorted clayey silt layers (Fig. 5e). The thicknesses of individual beds vary between 1 and > 100 cm. The color ranges between olive gray and dark gray. Mud beds that are between 1 and 5 cm thick are encountered at depths below 100 m. The thickness of layers gradually increases upsection, and mud beds are thickest at ca. 20 m depth. The contacts with the overlying beds are sharp. However, the contacts with the underlying coarser-grained lf can be sharp or gradual.

Interpretation. The very fine-grained composition of this lf hints at a deposition by settling in very quiet or stagnant water, for example, in a lake. Stagnant water conditions can occur temporally, e.g., during different seasons, or spatially, e.g., at a considerable distance from the location of a water influx. However, lamination is absent in this lithofacies. Layers of massive silt can for example be formed on top of a Bouma sequence after the preceding turbulent flow has ceased (T_e; Bouma, 1962).

A11 Lithofacies 11: Dms, stratified diamict (below 103 m depth)

This lf is poorly sorted and comprises subangular to rounded outsized clasts that range in size from coarse sand to cobble and that are embedded in a silty fine-grained sand matrix (Fig. 5f). The matrix is massive and dominant in volume. Therefore, this lf can be categorized as a clast-poor diamict. The matrix color ranges from light-brownish gray to dark gray. The beds are between 10 and > 100 cm thick. Individual layers of Dms can have apparent thicknesses of ca. 6 m, yet this estimate could be biased by the core liner length. The basal contacts are sharp and are either horizontal or dip at angles between 20 and 30°. The outsized clasts can be disorganized, or they are arranged in strings of clasts. In these strings, the *a*–*b* plane of individual clasts is aligned in one direction. Furthermore, these strings are oriented parallel to the dip of the basal contacts or to the inclined interbeds of other lfs. The lithologies of these clasts are identical to those in lf 1.

Interpretation. This lf is markedly different from all lfs described above due to its diamictic composition. Similarly to Sm, such a composition can develop from hyperconcentrated density flows (Mulder and Alexander, 2001). Yet the Dms is different as the clasts' *a*–*b* planes can be aligned, which hints towards the occurrence of a flow-internal shear component (Nemec, 1990; Nemec et al., 1999). Furthermore, the diamictic composition indicates that the deposition occurred close to the sediment source (because of a lack of sediment sorting) or alternatively points towards a large grain size variety of the entrained and supplied material. Although such a diamict could be a glacigenic deposit, we interpret the continued and noticeable inclination of the beds as evidence for their deposition as foresets. Other authors might previously have referred to similar deposits as flow tills if they were encountered in a glacial environment (e.g., Dreimanis, 1989).

A12 Lithofacies 12: Dmm, massive diamict

This lf is very poorly sorted, matrix-supported, and comprises coarse-grained sand to cobble-sized clasts that are embedded in a silt to medium-grained sand matrix with a brown to ocher color (Fig. 5g and h). The abundance of clasts is variable. Locally, this diamict can vary in composition from clast-poor to clast-rich. The thicknesses of individual beds range from 20 to > 100 cm. The basal contacts are sharp and horizontal. The beds are massive without any evidence for a stratification. The clasts are subangular to rounded, and their lithologies are identical to those in lf 1. Generally, the encountered clasts do not show striation and grinding marks. Although all the layers within the Dmm share the above properties, the Dmm beds at the bottom (Dmm.1) and the center (Dmm.2) of the drilled core show markedly different sedimentary features.

The beds of Dmm.1 at the base of the cored sediment contain sandstone clasts of the LFM bedrock. These clasts range from coarse-grained sand to boulder size with the largest components close to the bedrock, and these are angular to subangular. Alpine clasts are absent within the lowermost meter of the cored sediment. Above this lowermost meter the proportion of Alpine to Molasse constituents increases upsection. Furthermore, patches and bands in the Dmm.1 matrix have a similar or even the same color as the red-, yellow-, and green-colored Molasse bedrock. The beds of Dmm.2 only contain Alpine clasts, and blocks derived from the LFM are missing.

Interpretation. This lf is similar to Dms in composition, yet it shows a difference in color and does not bear signs of a stratification. These are distinct differences to all previous lfs. Deposits with a disorganized distribution of coarse-grained material can result from cohesive debris flows in which a silt and clayey matrix provides cohesion to the moving material (Mulder and Alexander, 2001). These subaqueous cohesive debris flows have a low erosive power, possibly due to motion on a thin water layer (Iverson, 1997; Mulder and Alexander, 2001). Alternatively, such diamictic material with a disorganized distribution of clasts can be observed in glacigenic deposits. Therefore, the interpretation of the formation process of Dmm is ambiguous. This ambiguity can only be resolved in a larger context, which is provided when lithofacies elements are grouped into lithofacies assemblages. These assemblages are presented in Sect. 7.

Appendix B: Optically stimulated luminescence dating

Two samples (RE-01 and -03) were recovered from a ca. 10 m-thick set of Shb within FA 4 for the measurement of infrared stimulated luminescence at 50 °C (IR50) and 225 °C (pIRIR225) on feldspar grains. We used 18 cm-long, 4.6 cm-wide, capped, and lightproof PVC tubes to collect the unconsolidated sand. The tubes were run into the sediment using a hammer. Dose rate samples were scraped around the tubes into plastic bags prior to the extraction of the tubes. After treatment with H_2O_2 and HCl (both 15 %), the grain size interval between 180 and 212 µm was separated for the measurements. Feldspar minerals were then extracted using a sodium poly-tungstate heavy liquid. Per sample, 12 aliquots with 1 mm mask diameter were prepared for the equivalent dose analysis. A single-aliquot regenerative-dose (SAR; Murray and Wintle, 2000) post-IR IRSL protocol based on Buylaert et al. (2009) was used (Table B1). The luminescence measurements were conducted on an automated Risø TL/OSL reader. The aliquots were illuminated with IR LEDs (max. ca. 130 mW cm^{-2}; 100 s at 90 %). The emitted signals passed through a 410 nm interference filter (LOT-Oriel D410/30 nm) and one Schott BG-39 and were detected by an EMI 9235QB photo-multiplier tube. Fading measurements were conducted on six (RE-01) and seven (RE-03) aliquots per sample in order to derive the average fading parameter ρ' for both samples and each signal (Auclair et al., 2003; Huntley and Lamothe, 2001). The K, Th, and U content was determined by high-resolution gamma spectrometry on ca. 400 g of sample. Then, the natural dose rate was calculated with the DRAC online tool (Durcan et al., 2015).

Table B1. Modified post-IR IRSL 225 °C (Buylaert et al., 2009) protocol applied to measure the luminescence signals from feldspar.

Step	Procedure
1	Natural/regenerative dose
2	Heat to 250 °C for 60 s
3	IR stimulation for 100 s at 50 °C
4	IR stimulation for 100 s at 225 °C
5	Test dose (T_x)
6	Heat to 250 °C for 60 s
7	IR stimulation for 100 s at 50 °C
8	IR stimulation for 100 s at 225 °C
	Repeat

IRSL measurements were analyzed using the R.Luminescence package (Kreutzer et al., 2012) and an R script specifically written to allow for a routine multistep analysis. The apparent equivalent dose of individual aliquots (D_e) for both signals was determined with a single exponential saturation function (Fig. B1a). The measurement quality of individual aliquots was tested by applying a recycling ratio (10 % of unity) and a recuperation (5 % of the natural signal) criterion. To evaluate aliquot saturation, the $2D_0$ rule was applied ($D_e > 2D_0 \mathrel{\hat{=}}$ saturation; Wintle and Murray, 2006). The reliability of the measurement protocol was confirmed through dose recovery tests (DRTs) that were conducted on each sample. The DRT results lay within 15 % of the given dose for both signals. In a first step, the R routine performed a saturation test on the D_e of individual aliquots, which passed the recycling ratio and the recuperation criterion. After the rejection of saturated aliquots, the equivalent dose for each sample (ED) and per signal was calculated, using the Central Age Model (CAM; Galbraith and Roberts, 2012), which was then used to determine the respective apparent ages. In a second step, the remaining aliquots were individually corrected for fading, using the model of Kars et al. (2008). The fading-corrected aliquots were then tested for saturation again, and only aliquots that passed this second test were used to determine a fading-corrected age (Fig. B1b).

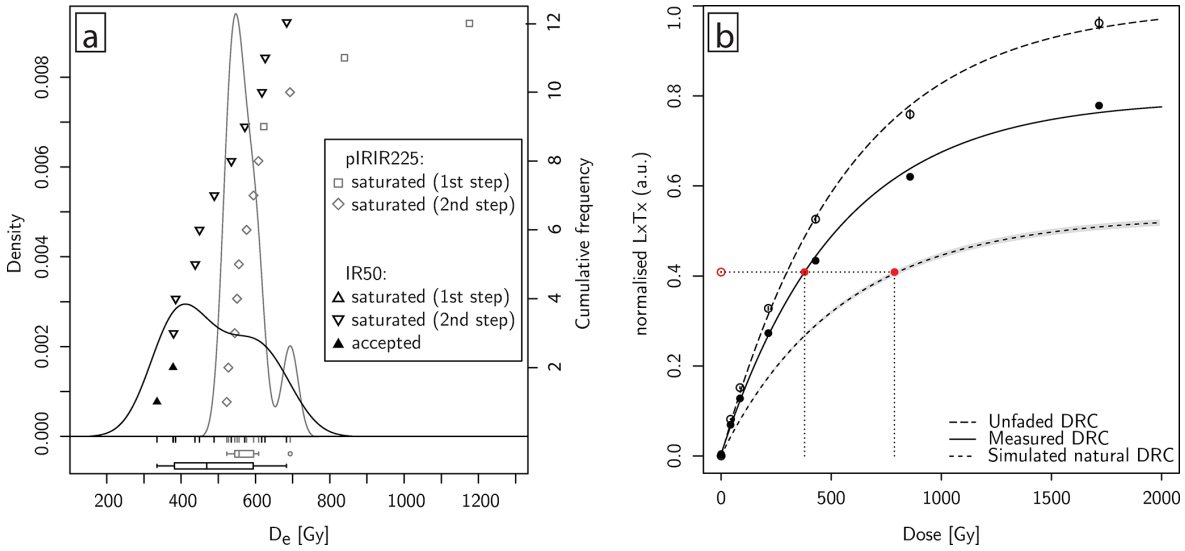

Figure B1. Analysis of luminescence measurements for sample RE-03, using R.Luminescence (Kreutzer et al., 2012). **(a)** Plot of the apparent D_e distribution for the IR50 (triangle symbols) and pIRIR225 (square symbols) signals. **(b)** Dose response curves (DRCs) of one of the two aliquots that passed both steps of saturation testing. This plot shows both the measured laboratory DRC and the modeled/simulated fading-corrected DRC based on Kars et al. (2008).

Code and data availability. All data obtained during the core processing and luminescence measurements as well as the respective analyses can be found in a separate data publication (https://doi.org/10.5880/fidgeo.2021.021, Schwenk et al., 2021).

Author contributions. MAS analyzed the data and wrote the paper, with support by FS. MAS designed the drilling campaign and FS organized the funding. PS conducted the pollen analysis, and DB was responsible for the gravity survey. NG supported the OSL dating, and GAD provided input during fieldwork and core analysis. All the authors approved the text and the figures.

Competing interests. The authors declare that they have no conflict of interest.

Disclaimer. Publisher's note: Copernicus Publications remains neutral with regard to jurisdictional claims in published maps and institutional affiliations.

Acknowledgements. We acknowledge the professional drilling by Fretus AG that provides a core with excellent quality. Special thanks also go to Toggenburger AG for dislocating their equipment and for giving access to the drill site and to Rehhag AG (Roland Schütz) for offering the ground for drilling. Peter Hayoz is kindly thanked for transporting the drilled material to the Swisstopo core repository, where the material is currently being stored. The carbon content analyses were run by Julia Krbanjevic, Institute of Geological Sciences, University of Bern. Gamma spectrometry was carried out by Sönke Szidat, Department of Chemistry and Biochemistry, University of Bern. We thank the research group for paleoecology of Willy Tinner at the Institute of Plant Sciences, University of Bern, for providing their facilities for the palynological investigation. We thank Urs Marti at Swisstopo for providing the gravimeter for the conduction of the gravimetry survey. We are grateful to the Direktion für Tiefbau, Verkehr und Stadtgrün of Bern for helping with the carving of trenches in the Rehhag clay pit.

Financial support. This research has been supported by the Schweizerischer Nationalfonds zur Förderung der Wissenschaftlichen Forschung (grant no. 175555), Swisstopo, the Stiftung Landschaft und Kies, the Gebäudeversicherung GVB, the Aaretal Kies AG (KAGA), and the city of Bern.

Review statement. This paper was edited by Ulrich Harms and reviewed by Cesare Ravazzi, Volker Wennrich, and one anonymous referee.

References

Aber, J. S. and Ber, A.: Glaciotectonism, Elsevier, London, UK, 2007.

Akçar, N., Ivy-Ochs, S., Alfimov, V., Schlunegger, F., Claude, A., Reber, R., Christl, M., Vockenhuber, C., Dehnert, A., Rahn, M., and Schlüchter, C.: Isochron-burial dating of glaciofluvial deposits: First results from the Swiss Alps, Earth Surf. Proc. Land., 42, 2414–2425, https://doi.org/10.1002/esp.4201, 2017.

Anselmetti, F. S., Preusser, F., Bavec, M., Crouzet, C., Fiebig, M., Gabriel, G., Ravazzi, C., and Spoetl, C.: Drilling overdeepened Alpine valleys (DOVE), EGU General Assembly Conference Abstracts, 12–17 April 2014, Vienna, Austria, p. 12437, 2014.

Auclair, M., Lamothe, M., and Huot, S.: Measurement of anomalous fading for feldspar IRSL using SAR, Radiat. Meas., 37, 487–492, https://doi.org/10.1016/S1350-4487(03)00018-0, 2003.

Beakawi Al-Hashemi, H. M. and Baghabra Al-Amoudi, O. S.: A review on the angle of repose of granular materials, Powder Technol., 330, 397–417, https://doi.org/10.1016/j.powtec.2018.02.003, 2018.

Benn, D. I.: Fabric signature of subglacial till deformation, Breidamerkurjökull, Iceland, Sedimentology, 42, 735–747, https://doi.org/10.1111/j.1365-3091.1995.tb00406.x, 1995.

Beug, H.: Leitfaden der Pollenbestimmung für Mitteleuropa und angrenzende Gebiete, Verlag Dr. Friedrich Pfeil, München, Germany, 542 pp., 2004.

Bickel, L., Lüthgens, C., Lomax, J., and Fiebig, M.: The timing of the penultimate glaciation in the northern Alpine Foreland: new insights from luminescence dating, P. Geologist. Assoc., 126, 536–550, https://doi.org/10.1016/j.pgeola.2015.08.002, 2015.

Bini, A., Buoncristiani, J., Couterrand, S., Ellwanger, D., Felber, M., Florineth, D., Graf, H., Keller, O., Kelly, M., and Schlüchter, C.: Die Schweiz während des letzteiszeitlichen Maximums (LGM), Bundesamt für Landestopografie swisstopo, Bern-Wabern, Switzerland, 2009.

Blaser, P., Gubler, T., Küpfer, T., Marschall, P., Matter, A., Matyas, J., Meier, B., Müller, W., Schlanke, S., Schlunegger, F., Siber, N., and Wyss, E.: Geothermiebohrung Bassersdorf. Charakterisierung der Oberen Meeresmolasse und Unteren Süsswassermolasse, Tech. Rep. NTB 94-01, Nagra, Wettingen, Switzerland, 1994.

Bolliger, T., Fejfar, O., Graf, H., and Kälin, D.: Vorläufige Mitteilung über Funde von pliozänen Kleinsäugern aus den höheren Deckenschottern des Irchels (Kt. Zürich), Eclogae Geol. Helv., 89, 1043–1048, 1996.

Boulton, G., Dobbie, K., and Zatsepin, S.: Sediment deformation beneath glaciers and its coupling to the subglacial hydraulic system, Quatern. Int., 86, 3–28, https://doi.org/10.1016/S1040-6182(01)00048-9, 2001.

Bouma, A. H.: Sedimentology of Some Flysch Deposits: a Graphic Approach to Facies Interpretation, Elsevier, Amsterdam, the Netherlands, 1962.

Brauer, A., Allen, J. R., Mingram, J., Dulski, P., Wulf, S., and Huntley, B.: Evidence for last interglacial chronology and environmental change from Southern Europe, P. Natl. Acad. Sci. USA, 104, 450–455, https://doi.org/10.1073/pnas.0603321104, 2007.

Broster, B.: Glacitectonic deformation in sediment and bedrock, Hat Creek, British Columbia, Geogr. Phys. Quatern., 45, 5–20, 1991.

Buechi, M. W., Frank, S. M., Graf, H. R., Menzies, J., and Anselmetti, F. S.: Subglacial emplacement of tills and meltwater deposits at the base of overdeepened bedrock troughs, Sedimentology, 64, 658–685, https://doi.org/10.1111/sed.12319, 2017.

Buylaert, J. P., Murray, A. S., Thomsen, K. J., and Jain, M.: Testing the potential of an elevated temperature IRSL signal from K-feldspar, Radiat. Meas., 44, 560–565, https://doi.org/10.1016/j.radmeas.2009.02.007, 2009.

Clark, P. U., Archer, D., Pollard, D., Blum, J. D., Rial, J. A., Brovkin, V., Mix, A. C., Pisias, N. G., and Roy, M.: The middle Pleistocene transition: characteristics, mechanisms, and implications for long-term changes in atmospheric pCO^2, Quaternary Sci. Rev., 25, 3150–3184, https://doi.org/10.1016/j.quascirev.2006.07.008, 2006.

Claude, A., Akçar, N., Ivy-Ochs, S., Schlunegger, F., Kubik, P. W., Christl, M., Vockenhuber, C., Kuhlemann, J., Rahn, M., and Schlüchter, C.: Changes in landscape evolution patterns in the northern Swiss Alpine Foreland during the mid-Pleistocene revolution, GSA Bulletin, 131, 2056–2078, https://doi.org/10.1130/B31880.1, 2019.

Cook, S. J. and Swift, D. A.: Subglacial basins: Their origin and importance in glacial systems and landscapes, Earth-Sci. Rev., 115, 332–372, https://doi.org/10.1016/j.earscirev.2012.09.009, 2012.

de Beaulieu, J.-L., Andrieu-Ponel, V., Reille, M., Grüger, E., Tzedakis, C., and Svobodova, H.: An attempt at correlation between the Velay pollen sequence and the Middle Pleistocene stratigraphy from central Europe, Quaternary Sci. Rev., 20, 1593–1602, https://doi.org/10.1016/S0277-3791(01)00027-0, 2001.

Dehnert, A., Preusser, F., Kramers, J. D., Akçar, N., Kubik, P. W., Reber, R., and Schlüchter, C.: A multi-dating approach applied to proglacial sediments attributed to the Most Extensive Glaciation of the Swiss Alps, Boreas, 39, 620–632, https://doi.org/10.1111/j.1502-3885.2010.00146.x, 2010.

Dreimanis, A.: Tills: their genetic terminology and classification, in: Genetic classification of glacigenic deposits, edited by: Goldthwait, R. P. and Matsch, C. L., Balkema, Rotterdam, the Netherlands, 17–84, 1989.

Duller, G. A.: Single grain optical dating of glacigenic deposits, Quat. Geochronol., 1, 296–304, https://doi.org/10.1016/j.quageo.2006.05.018, 2006.

Durcan, J. A., King, G. E., and Duller, G. A.: DRAC: Dose Rate and Age Calculator for trapped charge dating, Quat. Geochronol., 28, 54–61, https://doi.org/10.1016/j.quageo.2015.03.012, 2015.

Dürst Stucki, M. and Schlunegger, F.: Identification of erosional mechanisms during past glaciations based on a bedrock surface model of the central European Alps, Earth Planet. Sc. Lett., 384, 57–70, https://doi.org/10.1016/j.epsl.2013.10.009, 2013.

Dürst Stucki, M., Reber, R., and Schlunegger, F.: Subglacial tunnel valleys in the Alpine foreland: An example from Bern, Switzerland, Swiss J. Geosci., 103, 363–374, https://doi.org/10.1007/s00015-010-0042-0, 2010.

Ehlers, J., Gibbard, P. L., and Hughes, P. D.: Quaternary Glaciations – Extent and Chronology – A Closer Look, vol. 15 of Developments in Quaternary Sciences, Elsevier, 1st edn., https://doi.org/10.1016/C2009-0-20217-0, 2011.

Ehlers, J., Gibbard, P., and Hughes, P.: Quaternary Glaciations and Chronology, in: Past Glacial Environments, edited by: Menzies, J. and van der Meer, J. J., 2nd edn., Elsevier, 77–101, https://doi.org/10.1016/B978-0-08-100524-8.00003-8, 2018.

Eijkelkamp: 14.10 Pocket vane tester. Operating instructions, Eijkelkamp Agrisearch Equipment, Giesbeek, the Netherlands, 2012.

Evans, D. J. A., Phillips, E. R., Hiemstra, J. F., and Auton, C. A.: Subglacial till: formation, sedimentary characteristics and classification, Earth-Sci. Rev., 78, 115–176, https://doi.org/10.1016/j.earscirev.2006.04.001, 2006.

Fabbri, S. C., Buechi, M. W., Horstmeyer, H., Hilbe, M., Hübscher, C., Schmelzbach, C., Weiss, B., and Anselmetti, F. S.: A subaquatic moraine complex in overdeepened Lake Thun (Switzerland) unravelling the deglaciation history of the Aare Glacier, Quaternary Sci. Rev., 187, 62–79, https://doi.org/10.1016/j.quascirev.2018.03.010, 2018.

Fiebig, M. and Preusser, F.: Pleistocene glaciations of the northern Alpine Foreland, Geogr. Helv., 63, 145–150, https://doi.org/10.5194/gh-63-145-2008, 2008.

Fitzsimons, S. and Howarth, J.: Glaciolacustrine Processes, in: Past Glacial Environments, edited by Menzies, J. and van der Meer, J. J., 2nd edn., Elsevier, 309–334, https://doi.org/10.1016/B978-0-08-100524-8.00009-9, 2018.

Gaar, D., Lowick, S. E., and Preusser, F.: Performance of different luminescence approaches for the dating of known-age glaciofluvial deposits from Northern Switzerland, Geochronometria, 41, 65–80, https://doi.org/10.2478/s13386-013-0139-0, 2014.

Galbraith, R., Roberts, R., and Yoshida, H.: Error variation in OSL palaeodose estimates from single aliquots of quartz: a factorial experiment, Radiat. Meas., 39, 289–307, https://doi.org/10.1016/j.radmeas.2004.03.023, 2005.

Galbraith, R. F. and Roberts, R. G.: Statistical aspects of equivalent dose and error calculation and display in OSL dating: An overview and some recommendations, Quat. Geochronol., 11, 1–27, https://doi.org/10.1016/j.quageo.2012.04.020, 2012.

Garefalakis, P. and Schlunegger, F.: Tectonic processes, variations in sediment flux, and eustatic sea level recorded by the 20 Myr old Burdigalian transgression in the Swiss Molasse basin, Solid Earth, 10, 2045–2072, https://doi.org/10.5194/se-10-2045-2019, 2019.

Geologiebüro Kellerhals, Häfeli AG, and Staeger, D.: Blatt 1166 Bern. Geol. Atlas Schweiz 1 : 25 000, Karte 100, Bern-Wabern, Switzerland, 2000.

Graf, A., Akc, N., Strasky, I.-o. S., Kubik, P. W., Christl, M., Burkhard, M., Wieler, R., and Schlüchter, C.: Multiple advances of Alpine glaciers into the Jura Mountains in the Northwestern Switzerland, Swiss J. Geosci., 108, 225–238, https://doi.org/10.1007/s00015-015-0195-y, 2015.

Haeuselmann, P., Fiebig, M., Kubik, P. W., and Adrian, H.: A first attempt to date the original "Deckenschotter" of Penck and Brückner with cosmogenic nuclides, Quatern. Int., 164-165, 33–42, https://doi.org/10.1016/j.quaint.2006.12.013, 2007a.

Haeuselmann, P., Granger, D. E., Jeannin, P. Y., and Lauritzen, S. E.: Abrupt glacial valley incision at 0.8 Ma dated from cave deposits in Switzerland, Geology, 35, 143–146, https://doi.org/10.1130/G23094A, 2007b.

Hart, J. K. and Boulton, G. S.: The interrelation of glaciotectonic and glaciodepositional processes within the glacial environment, Quaternary Sci. Rev., 10, 335–350, https://doi.org/10.1016/0277-3791(91)90035-S, 1991.

Heim, A.: Handbuch der Gletscherkunde, J. Engelhorn, Stuttgart, Germany, 1885.

Hornung, J. J., Asprion, U., and Winsemann, J.: Jet-efflux deposits of a subaqueous ice-contact fan, glacial Lake Rinteln, northwestern Germany, Sediment. Geol., 193, 167–192, https://doi.org/10.1016/j.sedgeo.2005.11.024, 2007.

Huntley, D. J. and Lamothe, M.: Ubiquity of anomalous fading in K-feldspars and the measurement and correction for it in optical dating, Can. J. Earth Sci., 38, 1093–1106, https://doi.org/10.1139/cjes-38-7-1093, 2001.

Institut für Geologie, Universität Bern and Bundesamt für Wasser und Geologie: Geologische Karte der Schweiz 1 : 500 000 = Carte géologique de la Suisse 1 : 500 000, Bern-Ittigen, Switzerland, 2005.

Isler, A.: Erläuterungen zum geologischen Atlas der Schweiz 1 : 25 000, Blatt Bern 1166, Bern-Ittigen, Switzerland, 2005.

Iverson, R. M.: The physics of debris flows, Rev. Geophys., 35, 245–296, https://doi.org/10.1029/97RG00426, 1997.

Ivy-Ochs, S., Kerschner, H., Reuther, A., Preusser, F., Heine, K., Maisch, M., Kubik, P. W., and Schlüchter, C.: Chronology of the last glacial cycle in the European Alps, J. Quaternary Sci., 23, 559–573, https://doi.org/10.1002/jqs.1202, 2008.

Jacobs, Z., Duller, G. A., Wintle, A. G., and Henshilwood, C. S.: Extending the chronology of deposits at Blombos Cave, South Africa, back to 140 ka using optical dating of single and multiple grains of quartz, J. Hum. Evol., 51, 255–273, https://doi.org/10.1016/j.jhevol.2006.03.007, 2006.

Jordan, P.: Analysis of overdeepened valleys using the digital elevation model of the bedrock surface of Northern Switzerland, Swiss J. Geosci., 103, 375–384, https://doi.org/10.1007/s00015-010-0043-z, 2010.

Kars, R. H., Wallinga, J., and Cohen, K. M.: A new approach towards anomalous fading correction for feldspar IRSL dating - tests on samples in field saturation, Radiat. Meas., 43, 786–790, https://doi.org/10.1016/j.radmeas.2008.01.021, 2008.

Keller, O. and Krayss, E.: Mittel- und spätpleistozäne Stratigraphie und Morphogenese in Schlüsselregionen der Nordschweiz, Quaternary Sci. J., 59, 88–119, https://doi.org/10.3285/eg.59.1-2.08, 2010.

King, G. E., Burow, C., Roberts, H. M., and Pearce, N. J.: Age determination using feldspar: evaluating fading-correction model performance, Radiation Measurements, 119, 58–73, https://doi.org/10.1016/j.radmeas.2018.07.013, 2018.

Knudsen, M. F., Nørgaard, J., Grischott, R., Kober, F., Egholm, D. L., Hansen, T. M., and Jansen, J. D.: New cosmogenic nuclide burial-dating model indicates onset of major glaciations in the Alps during Middle Pleistocene Transition, Earth Planet. Sc. Lett., 549, 116491, https://doi.org/10.1016/j.epsl.2020.116491, 2020.

Koutsodendris, A., Pross, J., Müller, U. C., Brauer, A., Fletcher, W. J., Kühl, N., Kirilova, E., Verhagen, F. T., Lücke, A., and Lotter, A. F.: A short-term climate oscillation during the Holsteinian interglacial (MIS 11c): An analogy to the 8.2ka climatic event?, Global Planet. Chang., 92–93, 224–235, https://doi.org/10.1016/j.gloplacha.2012.05.011, 2012.

Kreutzer, S., Schmidt, C., Fuchs, M., Dietze, M., Fischer, M., and Fuchs, M.: Introducing an R package for luminescence dating analysis, Ancient TL, 30, 1–8, available at: http://ancienttl.org/ATL_30-1_2012/ATL_30-1_Kreutzer_p1-8.pdf (last access: 24 June 2021), 2012.

Krüger, J. and Kjær, K. H.: A data chart for field description and genetic interpretation of glacial diamicts and associated sediments - with examples from Greenland, Iceland, and Denmark, Boreas, 28, 386–402, https://doi.org/10.1111/j.1502-3885.1999.tb00228.x, 1999.

Kühni, A. and Pfiffner, O.: The relief of the Swiss Alps and adjacent areas and its relation to lithology and structure: topographic analysis from a 250-m DEM, Geomorphology, 41, 285–307, https://doi.org/10.1016/S0169-555X(01)00060-5, 2001.

Lang, J., Sievers, J., Loewer, M., Igel, J., and Winsemann, J.: 3D architecture of cyclic-step and antidune deposits in glacigenic subaqueous fan and delta settings: Integrating outcrop and ground-penetrating radar data, Sediment. Geol., 362, 83–100, https://doi.org/10.1016/j.sedgeo.2017.10.011, 2017.

Lang, J., Le Heron, D. P., Van den Berg, J. H., and Winsemann, J.: Bedforms and sedimentary structures related to supercritical flows in glacigenic settings, Sedimentology, 68, 1539–1579, https://doi.org/10.1111/sed.12776, 2021.

Li, B., Jacobs, Z., Roberts, R., and Li, S.-H.: Review and assessment of the potential of post-IR IRSL dating methods to circumvent the problem of anomalous fading in feldspar luminescence, Geochronometria, 41, 178–201, https://doi.org/10.2478/s13386-013-0160-3, 2014.

Lisiecki, L. E.: Links between eccentricity forcing and the 100,000-year glacial cycle, Nat. Geosci., 3, 349–352, https://doi.org/10.1038/ngeo828, 2010.

Lisiecki, L. E. and Raymo, M. E.: A Pliocene-Pleistocene stack of 57 globally distributed benthic δ^{18}O records, Paleoceanography, 20, PA1003, https://doi.org/10.1029/2004PA001071, 2005.

Lønne, I.: Sedimentary facies and depositional architecture of ice-contact glaciomarine systems, Sediment. Geol., 98, 13–43, https://doi.org/10.1016/0037-0738(95)00025-4, 1995.

Lowe, D. R.: Sediment gravity flows; II, Depositional models with special reference to the deposits of high-density turbidity currents, J. Sediment. Res., 52, 279–297, https://doi.org/10.1306/212F7F31-2B24-11D7-8648000102C1865D, 1982.

Lowick, S. E., Trauerstein, M., and Preusser, F.: Testing the application of post IR-IRSL dating to fine grain waterlain sediments, Quat. Geochronol., 8, 33–40, https://doi.org/10.1016/j.quageo.2011.12.003, 2012.

Matter, A.: Sedimentologische Untersuchungen im östlichen Napfgebiet, Eclogae Geol. Helv., 57, 315–428, https://doi.org/10.5169/seals-163142, 1964.

Meichtry, N.: Last Deglaciation of the Aare Valley, Master's thesis, Instiute of Geological Science, University of Bern, Bern, Switzerland, 2016.

Miall, A. D.: Architectural-element analysis: a new method of facies analysis applied to fluvial deposits, Earth-Sci. Rev., 22, 261–308, https://doi.org/10.1016/0012-8252(85)90001-7, 1985.

Moore, P. D., Webb, J. A., and Collison, M. E.: Pollen analysis, Blackwell scientific publications, Oxford, UK, 1991.

Mulder, T. and Alexander, J.: The physical character of subaqueous sedimentary density flows and their deposits, Sedimentology, 48, 269–299, https://doi.org/10.1046/j.1365-3091.2001.00360.x, 2001.

Murray, A. S. and Wintle, A. G.: Luminescence dating of quartz using an improved single-aliquot regenerative-dose protocol, Radiat. Meas., 32, 57–73, https://doi.org/10.1016/S1350-4487(99)00253-X, 2000.

NASA/METI/AIST/Japan Spacesystems and U.S./Japan ASTER Science Team: ASTER Global Digital Elevation Model V003, https://doi.org/10.5067/ASTER/ASTGTM.003, 2019.

Nemec, W.: Aspects of sediment movement on steep delta slopes, in: Coarse-grained deltas, edited by: Colella, A. and Prior, D., vol. 10 of International Association of Sedimentologists Special Publication, Blackwell Scientific Publications, Oxford, UK, 29–73, 1990.

Nemec, W., Lønne, I., and Blikra, L. H.: The Kregnes moraine in Gauldalen, west-central Norway: anatomy of a Younger Dryas proglacial delta in a palaeofjord basin, Boreas, 28, 454–476, https://doi.org/10.1111/j.1502-3885.1999.tb00234.x, 1999.

Parker, G., Fukushima, Y., and Pantin, H. M.: Self-accelerating turbidity currents, J. Fluid Mech., 171, 145–181, https://doi.org/10.1017/S0022112086001404, 1986.

Penck, A. and Brückner, E.: Die Alpen im Eiszeitalter, Tauchnitz, Leipzig, Germany, 1909.

Phillips, E.: Glacitectonics, in: Past Glacial Environments, edited by: Menzies, J. and van der Meer, J. J., 2nd edn., Elsevier, 467–502, https://doi.org/10.1016/B978-0-08-100524-8.00014-2, 2018.

Phillips, E., Evans, D., and Auton, C.: Polyphase deformation at an oscillating ice margin following the Loch Lomond Readvance, central Scotland, UK, Sediment. Geol., 149, 157–182, https://doi.org/10.1016/S0037-0738(01)00250-0, 2002.

Platt, N. H. and Keller, B.: Distal alluvial deposits in a foreland basin setting – the Lower Freshwater Miocene), Switzerland: sedimentology, architecture and palaeosols, Sedimentology, 39, 545–565, https://doi.org/10.1111/j.1365-3091.1992.tb02136.x, 1992.

Plink-Björklund, P.: Depositional processes and internal architecture of Late Weichselian ice-margin submarine fan and delta settings, Swedish west coast, Sedimentology, 46, 215–234, https://doi.org/10.1046/j.1365-3091.1999.00195.x, 1999.

Postma, G.: Depositional architecture and facies of river and fan deltas: a synthesis, in: Coarse-grained deltas, edited by: Colella, A. and Prior, D., vol. 10 of International Association of Sedimentologists Special Publication, Blackwell Scientific Publications, Oxford, UK, 13–27, 1990.

Powell, R. D.: Glacimarine processes at grounding-line fans and their growth to ice-contact deltas, Geological Society, London, Special Publications, 53, 53–73, https://doi.org/10.1144/GSL.SP.1990.053.01.03, 1990.

Preusser, F. and Schlüchter, C.: Dates from an important early Late Pleistocene ice advance in the Aare valley, Switzerland, Eclogae Geol. Helv., 97, 245–253, https://doi.org/10.1007/s00015-004-1119-4, 2004.

Preusser, F., Drescher-Schneider, R., Fiebig, M., and Schlüchter, C.: Re-interpretation of the Meikirch pollen record, Swiss Alpine Foreland, and implications for Middle Pleistocene chronostratigraphy, J. Quaternary Sci., 20, 607–620, https://doi.org/10.1002/jqs.930, 2005.

Preusser, F., Reitner, J. M., and Schlüchter, C.: Distribution, geometry, age and origin of overdeepened valleys and basins in the Alps and their foreland, Swiss J. Geosci., 103, 407–426, https://doi.org/10.1007/s00015-010-0044-y, 2010.

Preusser, F., Graf, H., Keller, O., Krayss, E., and Schlüchter, C.: Quaternary glaciation history of northern Switzerland, Quaternary Sci. J., 60, 282–305, https://doi.org/10.3285/eg.60.2-3.06, 2011.

Reber, R. and Schlunegger, F.: Unravelling the moisture sources of the Alpine glaciers using tunnel valleys as constraints, Terra Nova, 28, 202–211, https://doi.org/10.1111/ter.12211, 2016.

Reille, M.: Pollen et spores d'Europe et d'Afrique du Nord, Laboratoire de Botanique historique et Palynologie, Marseille, France, 1992.

Rose, J. and Menzies, J.: 15 – Glacial stratigraphy, in: Modern and Past Glacial Environments, edited by: Menzies, J., Butterworth-Heinemann, Oxford, UK, 445–473, https://doi.org/10.1016/B978-075064226-2/50018-0, 2002.

Rosenblume, J. A. and Powell, R. D.: Glacial sequence stratigraphy of ANDRILL-1B core reveals a dynamic subpolar Antarctic Ice Sheet in Ross Sea during the late Miocene, Sedimentology, 66, 2072–2097, https://doi.org/10.1111/sed.12592, 2019.

Ruddiman, W., Raymo, M. E., and McIntyre, A.: Matuyama 41,000-year cycles: North Atlantic Ocean and northern hemisphere ice sheets, Earth Planet. Sc. Lett., 80, 117–129, https://doi.org/10.1016/0012-821X(86)90024-5, 1986.

Rust, B. R.: Depositional models for braided alluvium, in: Fluvial Sedimentology, eidted by: Miall, A. D., Canadian Society of Petroleum Geologists, Memoirs, 5, 605–625, 1978.

Schlüchter, C.: The most complete quaternary record of the Swiss Alpine Foreland, Palaeogeogr. Palaeocl., 72, 141–146, https://doi.org/10.1016/0031-0182(89)90138-7, 1989.

Schlüchter, C.: The Swiss glacial record – a schematic summary, Developments in Quaternary Science, 2, 413–418, https://doi.org/10.1016/S1571-0866(04)80092-7, 2004.

Schultheiss, P. and Weaver, P.: Multi-sensor Core Logging For Science And Industry, in: OCEANS 92 Proceedings@m_Mastering the Oceans Through Technology, vol. 2, 608–613, 1992.

Schwenk, M. A., Schlunegger, F., Gribenski, N., Schläfli, P., Bandou, D., Douillet, G. A., and Krbanjevic, J.: Stratigraphic and Multi Scanner Core Logging (MSCL) data plus supplementary luminescence dating material obtained from the scientific drilling QDR-RE-IfG and its drill site in the Aare Valley, Bern CH, GFZ Data Services [data set], https://doi.org/10.5880/fidgeo.2021.021, 2021.

Stockmarr, J.: Tabletes with spores used in absolute pollen analysis, Pollen spores, 13, 615–621, 1971.

Sutherland, J. L., Carrivick, J. L., Shulmeister, J., Quincey, D. J., and James, W. H.: Ice-contact proglacial lakes associated with the last glacial maximum across the Southern Alps, New Zealand, Quaternary Sci. Rev., 213, 67–92, https://doi.org/10.1016/j.quascirev.2019.03.035, 2019.

Valla, P. G., Shuster, D. L., and Van Der Beek, P. A.: Significant increase in relief of the European Alps during mid-Pleistocene glaciations, Nat. Geosci., 4, 688–692, https://doi.org/10.1038/ngeo1242, 2011.

van der Wateren, D. M.: Processes of glaciotectonism, in: Modern and Past Glacial Environments, Elsevier, 417–443, https://doi.org/10.1016/B978-075064226-2/50017-9, 2002.

Welten, M.: Pollenanalytische Untersuchungen im Jüngeren Quartär des nördlichen Alpenvorlandes der Schweiz, Beiträge zur Ge-

ologischen Karte der Schweiz – Neue Folge, Schweizerischen Geologischen Kommission, Bern, 156, 210 pp., 1982.

Welten, M.: Neue pollenanalytische Ergebnisse über das Jüngere Quartär des nördlichen Alpenvorlandes der Schweiz (Mittel- und Jungpleistozän), Beiträge zur Geologischen Karte der Schweiz – Neue Folge, Schweizerischen Geologischen Kommission, Bern, 162, 52 pp., 1988.

Winsemann, J., Lang, J., Polom, U., Loewer, M., Igel, J., Pollok, L., and Brandes, C.: Ice-marginal forced regressive deltas in glacial lake basins: geomorphology, facies variability and large-scale depositional architecture, Boreas, 47, 973–1002, https://doi.org/10.1111/bor.12317, 2018.

Wintle, A. G. and Murray, A. S.: A review of quartz optically stimulated luminescence characteristics and their relevance in single-aliquot regeneration dating protocols, Radiat. Meas., 41, 369–391, https://doi.org/10.1016/j.radmeas.2005.11.001, 2006.

Wüthrich, L., Morabito, E. G., Zech, J., Trauerstein, M., Veit, H., Gnägi, C., Merchel, S., Scharf, A., Rugel, G., Christl, M., and Zech, R.: ^{10}Be surface exposure dating of the last deglaciation in the Aare Valley, Switzerland, Swiss J. Geosci., 111, 295–303, https://doi.org/10.1007/s00015-018-0298-3, 2018.

Sci. Dril., 30, 43–57, 2022
https://doi.org/10.5194/sd-30-43-2022

Scientific Drilling
Open Access

COSC-2 – drilling the basal décollement and underlying margin of palaeocontinent Baltica in the Paleozoic Caledonide Orogen of Scandinavia

Henning Lorenz[1], Jan-Erik Rosberg[2], Christopher Juhlin[1], Iwona Klonowska[3], Rodolphe Lescoutre[1], George Westmeijer[4], Bjarne S. G. Almqvist[1], Mark Anderson[5], Stefan Bertilsson[6], Mark Dopson[4], Jens Kallmeyer[7], Jochem Kück[8], Oliver Lehnert[9], Luca Menegon[10], Christophe Pascal[11], Simon Rejkjær[2], and Nick N. W. Roberts[12]

[1]Department of Earth Sciences, Uppsala University, Villavägen 16, 752 36 Uppsala, Sweden
[2]Engineering Geology, Lund University, John Ericssons väg 1, 221 00 Lund, Sweden
[3]Faculty of Geology, Geophysics and Environment Protection, AGH University of Science and Technology, al. Mickiewicza 30, 30-059 Kraków, Poland
[4]Centre for Ecology and Evolution in Microbial Model Systems (EEMiS) Linnæus University, Stuvaregatan 4, 39231 Kalmar, Sweden
[5]School of Geography, Earth and Environmental Sciences, University of Plymouth, B527 Portland Square, Plymouth PL4 8AA, United Kingdom
[6]Department of Aquatic Sciences and Assessment, Swedish University of Agricultural Sciences, Lennart Hjelms väg 9, 75 651 Uppsala, Sweden
[7]Section 3.7 Geomicrobiology, GFZ German Research Centre for Geosciences, Telegrafenberg, 14473 Potsdam, Germany
[8]Section 4.2: Geomechanics and Scientific Drilling, GFZ German Research Centre for Geosciences, Telegrafenberg, 14473 Potsdam, Germany
[9]Geozentrum Nordbayern, Friedrich-Alexander University Erlangen–Nuremberg, Schloßgarten 5, 91054 Erlangen, Germany
[10]Njord Centre, Department of Geosciences, University of Oslo, Sem Sælands vei 24, 0371 Oslo, Norway
[11]Institute of Geology, Mineralogy and Geophysics, Ruhr University Bochum, Universitätsstraße 150, 44780 Bochum, Germany
[12]NERC Isotope Geosciences Laboratory, British Geological Survey, Nottingham NG12 5GG, United Kingdom

Correspondence: Henning Lorenz (henning.lorenz@geo.uu.se)

Received: 31 August 2021 – Revised: 17 January 2022 – Accepted: 23 January 2022 – Published: 25 February 2022

Abstract. The Collisional Orogeny in the Scandinavian Caledonides (COSC) scientific drilling project aims to characterise the structure and orogenic processes involved in a major collisional mountain belt by multidisciplinary geoscientific research. Located in western central Sweden, the project has drilled two fully cored deep boreholes into the bedrock of the deeply eroded Early Paleozoic Caledonide Orogen. COSC-1 (2014) drilled a subduction-related allochthon and the associated thrust zone. COSC-2 (2020, this paper) extends this section deeper through the underlying nappes (Lower Allochthon), the main Caledonian décollement, and the upper kilometre of basement rocks. COSC-2 targets include the characterisation of orogen-scale detachments, the impact of orogenesis on the basement below the detachment, and the Early Paleozoic palaeoenvironment on the outer margin of palaeocontinent Baltica. This is complemented by research on heat flow, groundwater flow, and the characterisation of the microbial community in the present hard rock environment of the relict mountain belt. COSC-2 successfully, and within budget, recovered a continuous drill core to 2276 m depth. The retrieved geological section is partially different from the expected geological section with respect to the depth to the main décollement and the expected rock types. Although the intensity of synsedimentary deformation in the rocks in

the upper part of the drill core might impede the analysis of the Early Paleozoic palaeoenvironment, the superb quality of the drill core and the borehole will facilitate research on the remaining targets and beyond. Protocols for sampling in the hard rock environment and subsequent sample preservation were established for geomicrobiological research and rock mechanical testing. For the former, a sparse sample series along the entire drill core was taken, while the target of the latter was the décollement. COSC-2 was surveyed by a comprehensive post-drilling downhole logging campaign and a combined borehole/land seismic survey in autumn 2021. This paper provides an overview of the COSC-2 (International Continental Scientific Drilling Project – ICDP 5054_2_A and 5054_2_B boreholes) operations and preliminary results. It will be complemented by a detailed operational report and data publication.

1 Insights into the lowermost level of a major collisional orogen

The Caledonides are a mid-Paleozoic collisional orogen of Alpine–Himalayan dimension. During closure of the Iapetus Ocean, the palaeocontinent Baltica underthrusted the palaeocontinent Laurentia in the Silurian and Early Devonian. Today, after the opening of the Atlantic Ocean in the Paleogene, remains of the deeply eroded mountain belt are preserved in the continental margins of Greenland and Scandinavia and expose the interior of this major collisional orogen for geoscientific investigations. In Scandinavia, the continental margin is composed of Baltican basement overlain by a stack of increasingly distal allochthons that were emplaced during Caledonian (Scandian) orogeny, having been transported up to several hundreds of kilometres (e.g. Gee et al., 2008). The primary target of the Collisional Orogeny in the Scandinavian Caledonides (COSC) scientific drilling project (Fig. 1) is to study orogenic processes at various scales along a continuous section through the interior of this deeply eroded mountain belt, from the high-grade metamorphic, subduction-related allochthons derived from the distal margin of Baltica, known as the Middle Allochthon, through the low-grade metamorphic continental margin sediments of the Lower Allochthon, the main Caledonian décollement and into the underlying sedimentary basement cover, and, at the deepest level, the crystalline basement of palaeocontinent Baltica (i.e. the Baltoscandian basement of the Fennoscandian Shield). The COSC project comprises two sites, namely COSC-1 drilled in 2014 and COSC-2 drilled in 2020. COSC-1 is located close to the timberline on the eastern slopes of the Åreskutan mountain, with subduction-related ultra high pressure metamorphic rocks of the Middle Seve Nappe exposed on its summit and upper slopes (Klonowska et al., 2017). This drill core samples the underlying gneisses of the Lower Seve Nappe and thrust zone (see Lorenz et al., 2015a for science report and more extensive project background). COSC-2 (this paper) is located ca. 20 km southeast of COSC-1 at the southern shore of the Liten Lake. It starts at a tectonostratigraphic level, below that of the bottom of COSC-1, and samples the low-grade metamorphic siliciclastics of the Lower Allochthon, the main Caledonian décollement, and the Baltoscandian basement, as detailed further below. Thus, the COSC project now has access to a composite geological section spanning the lower part of the Caledonide orogen, from the hot allochthon of the Seve Nappe and into the basement of the lower plate. Ongoing research is testing different hypotheses of nappe emplacement through an investigation of the kinematics and thermochronological development of the different allochthons and their interaction with the basement of the underthrusting plate in this major collisional orogen.

2 COSC-2 objectives

The COSC-2 objectives are derived from the COSC project targets (e.g. Gee et al., 2010) by careful evaluation of the geological premises (site investigations) and practical and financial feasibility. They are formulated here as the scientific targets and geological section that was expected to be drilled with the available resources. The selection of the drill site was based on the geological interpretation of the reflection seismic and magnetotelluric site investigations (Juhlin et al., 2016), of which detail on the drill site is shown in Fig. 2.

2.1 Scientific targets

1. The lower part of the COSC composite geological section, i.e. the COSC-2 drill core, will provide an opportunity for increased understanding of the main Caledonian décollement and associated fault systems, including geometry, stress distribution, and rheology. These investigations will also shed light on how deformation propagated below this orogen-scale detachment horizon into the basement of the Fennoscandian Shield and whether a deeper deformation system played a role in the tectonic cycle from Iapetus formation to the present-day Atlantic.

2. The origin and nature of the prominent, deep basement reflectors imaged in the seismic profiles and their role during passive margin formation and orogeny is a key question in the context of point (1). Eventually, these new insights will utilise analogue studies with modern orogens like the Alpine–Himalayan mountain belt.

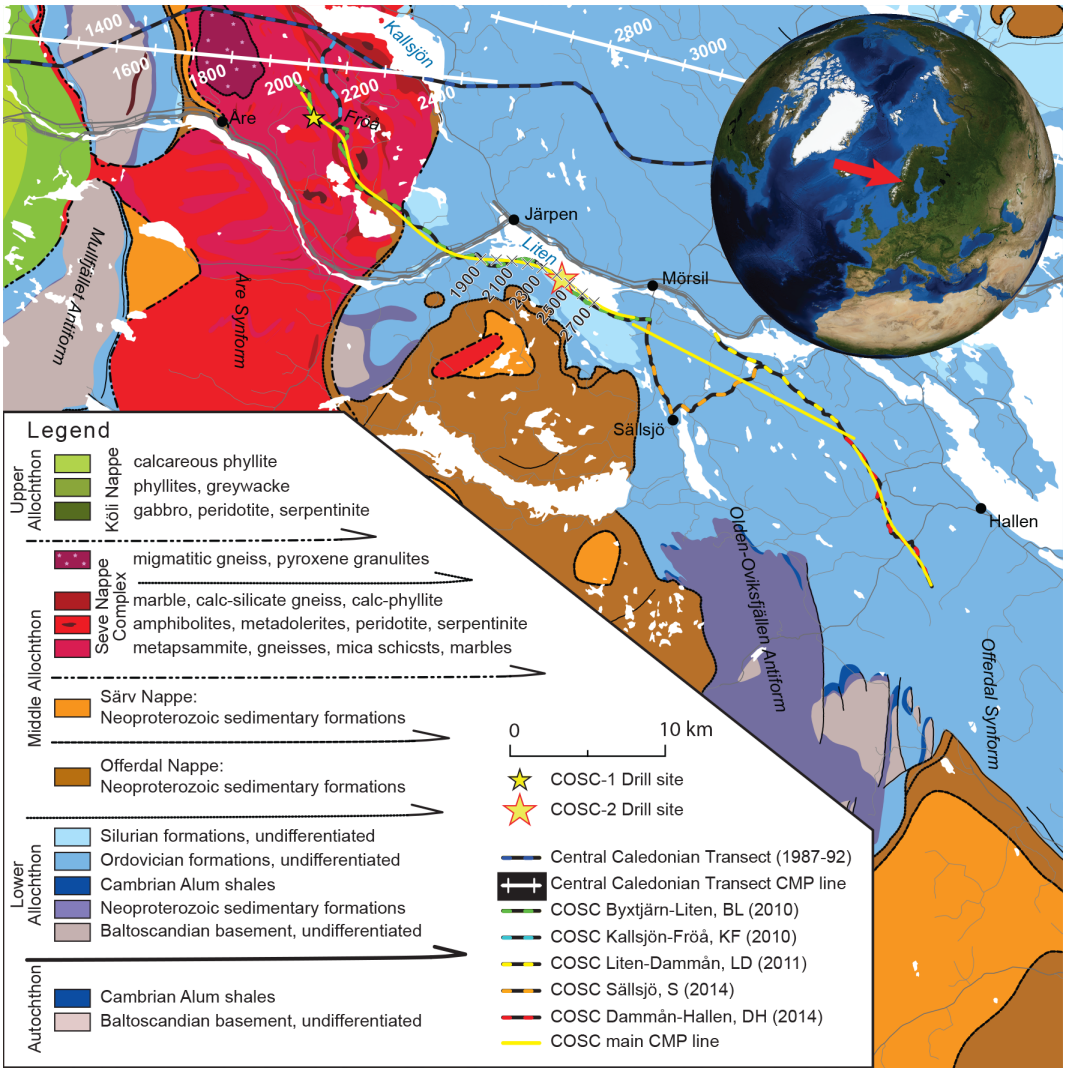

Figure 1. Tectonostratigraphic map of the Åre–Järpen area (based on the 1 : 200 000 scale geological map by the Geological Survey of Sweden, I2014/00601; Strömberg et al., 1984). The map shows the COSC drill sites, the location of the regional seismic profiles of the Central Caledonian Transect (Palm and Lund, 1980; Juhojuntti et al., 2001), and the seismic lines of the COSC site investigations. Note that the common depth point (CDP) on the latter were shifted during reprocessing and, thus, are different from Hedin et al. (2012) and Juhlin et al. (2016). The magnetotelluric survey (Yan et al., 2016) followed the track of the COSC seismics. Figure modified from Juhlin et al. (2016).

3. The Early Paleozoic sediments drilled by COSC-2 were deposited on the continental margin before Scandian orogeny and, subsequently, during orogeny, into a foreland basin. As the most distal location in a multiple-site study of this Paleozoic basin, COSC-2 will add unique information on palaeoenvironmental conditions and facilitate the reconstruction of the palaeoclimate, global biologic crises, faunal turnover, and major glacial events.

4. More recent climate evolution is addressed with the study of the ground surface temperature history, based on high-quality, high-resolution borehole temperature profiles. The two COSC drill sites are situated just east of the ice divide of the Weichselian ice sheet in Fennoscandia but in locations with different (palaeo)environmental and altitude conditions, with COSC-1 on the lower slope of a mountain and COSC-2 in a glacial valley. Thus, COSC will contribute to knowledge about the Weichselian glaciation and climate evolution in northern Europe during the Holocene, including industrial age trends.

5. The hydrogeological and thermal characteristics of mountain belts are defined by their geological history and structure, including for those that are already deeply eroded. Paleozoic orogens exist on all continents and are part of the lithosphere from Central Asia to Europe and

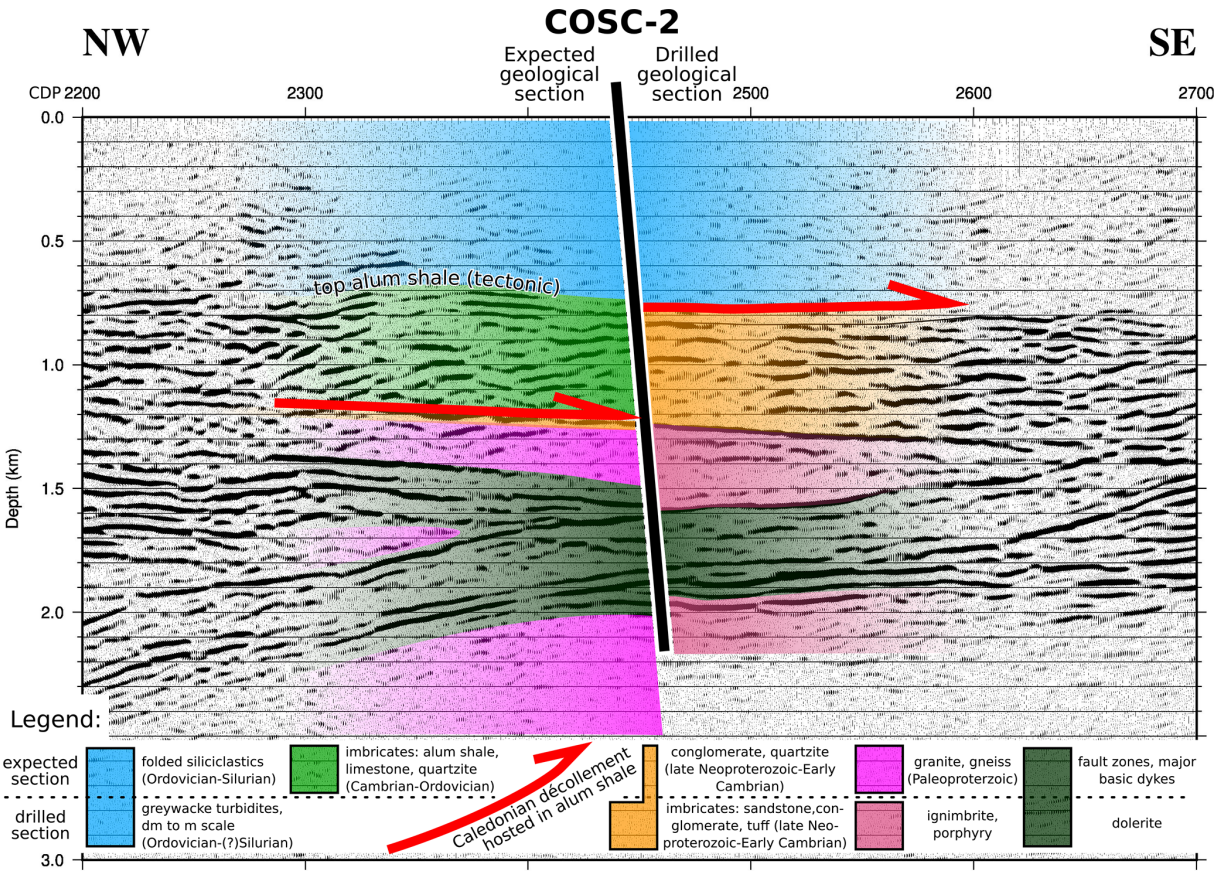

Figure 2. The COSC-2 expected geology (left) and the drilled geology (right) superimposed on the depth-converted seismic section that represents the rock in the vicinity of the COSC-2 drill site. See Fig. 1 for the location and note that, due to reprocessing, CDP points are shifted when compared with the original publications (Hedin et al., 2012; Juhlin et al., 2016).

western North America. COSC-2 investigates how the deep structure of the Scandinavian Caledonides, including large-scale detachments and basement deformation, affect hydraulic conductivity, pressure heads, and heat transfer in the interplay with groundwater flow and concomitant advective heat transport. Eventually, this will increase the understanding about the origin and genesis of fluids and gases and their impact on seismicity and rheology over time.

6. Microbiological research focuses on changes in microbiological community composition as a function of depth and lithology and to investigate long-term evolutionary change. A secondary target is to benchmark and validate the dedicated triple-tube coring and onsite drill core sampling for contamination-free microbial sampling. Strict contamination control ensures the integrity of the sample collection and provides a test bed for protocols to be used for future scientific boreholes dedicated to microbial research. In addition, fracture mineralisation will undergo detailed geochemical and isotopic characterisation, as this can reveal information on the timing and nature of microbial activity through deep time.

2.2 Expected geological section

The expected geological section is based on the interpretation of the geophysical site investigations, which are detailed in Juhlin et al. (2016). At ca. 1200–1250 m depth, a laterally extensive and nearly continuous reflection is present in the seismic section (Fig. 2). It was interpreted as being the detachment between the Lower Allochthon and the autochthonous basement, i.e. the main Caledonian décollement. This inferred detachment was interpreted as being hosted and facilitated by the highly organic-rich and electrically conductive Early to Middle Cambrian Alum Shale Formation (Andersson et al., 1985), and thus, this depth was also interpreted as being the depth to the formation's stratigraphic occurrence. However, the magnetotelluric survey (Yan et al., 2016) predicted the first occurrence of a good conductor, i.e. Alum Shale, already at ca. 750 m depth. Based on this interpretation and the occurrence of Late Ordovician to Early Silurian formations (Kogsta Shale, Ede Quartzite, and Berge

Limestone) in the hills south of the drill site, the borehole was expected to start in or below these formations and extend downwards through turbiditic greywackes, shales, and siltstones (Föllinge and Andersön formations; light blue in Fig. 2) and penetrate the shallowest occurrence of Alum Shale at ca. 750 m. Based on the seismic pattern, the rocks below this depth and down to the décollement (light green in Fig. 2) were interpreted as being an imbricate system consisting of Alum Shale, varying Ordovician limestones, and possibly overlying greywackes (see Karis and Strömberg, 1998, for a detailed description of the stratigraphy). After sampling the Paleozoic section (scientific target 3), including the décollement in the Alum Shale Formation (scientific target 1), the drilling target shifts to the basement. This section was expected to start with a thin layer of Neoproterozoic Vemdalen Quartzite (orange in Fig. 2), which in many (but not all) areas covers the Paleoproterozoic basement (pink in Fig. 2) of ca. 1.7 Ga Rätan granite (see Gorbatschev, 1997; Högdahl et al., 2004). The latter is a major intrusive body that makes up an area of about 5000 km^2 east of the present Caledonian front. Based on magnetic data, it is inferred to extend northwestwards, far below the Caledonian nappes and including the COSC area (Dyrelius, 1980). In addition, the Dala Porphyries (also ca. 1.7 Ga; Welin et al., 1993) extend beneath the Caledonian nappes from their type area 200 km to the south, and similar rocks (basement porphyries) have been reported in basement windows (Mullfjället; Beckholmen, 1978) and tectonic slices (Östberget on Frösön; Karis and Strömberg, 1998). Thus, to encounter such rocks in the borehole was regarded as being possible, although not very likely. In the basement, bedrock would be sampled that corresponds to a prominent series of reflections between about 1.5 and 2.0 km (scientific target 2; olive green in Fig. 2) and which were interpreted to either be (1) major fault zones of yet unknown, but possibly Caledonian age, (2) dolerite intrusions related to the Central Scandinavian Dolerite Group (ca. 1.25 Ga; Gorbatschev et al., 1979), or (3) a combination of both. Drilling would stop, and the borehole would be completed once the nature of the basement rocks beneath these reflections was established.

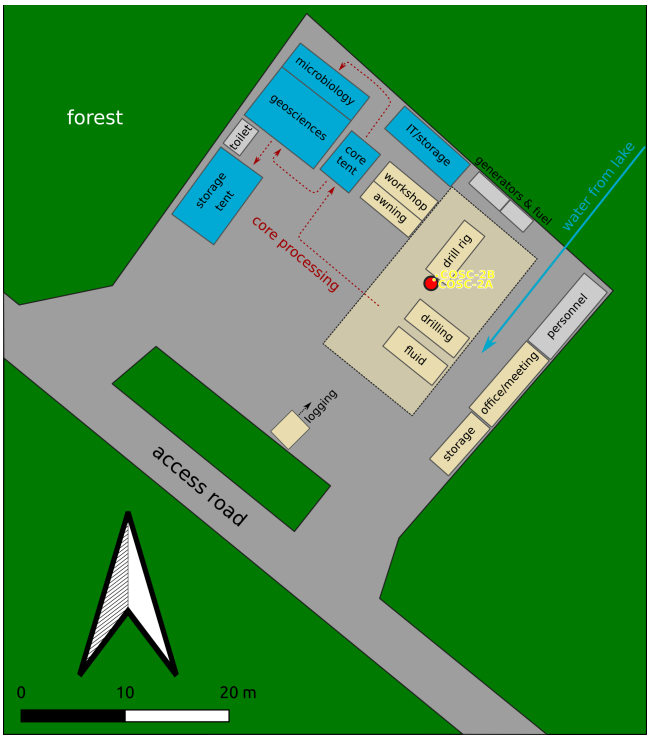

Figure 3. Sketch of the COSC-2 drill site. The area is approximately 1600 m^2 large, with the northwestern half used for the science operations (blue), parking, and storage and the southeastern half used for the technical operations (yellow) and common facilities. The route of the core from drilling deck to storage is marked in red.

3 Technical operations

The drilling operations aimed at full-core coverage from the surface to total depth. For this purpose, two boreholes were drilled, namely COSC-2A and COSC-2B (Table 1). Total core recovery was slightly higher than the total cored length. This indicates that the actual core recovery is very close to 100 %, while the positive error most likely is due to the minimal but repeatedly added distance across fractures in the pieced-together drill core.

The COSC-2 drill site (Fig. 3) has a size of 1600 m^2 and is constructed from compacted soil covered by a geotextile and graded crushed stone. A 1.2 m deep circular cellar was built using concrete rings with an inner diameter of 1.2 m, with the bottom sealed with cement. Electricity at the drill site was supplied by generators, and Liten Lake was used as the water supply. Preparations for the deep-core drilling of borehole COSC-2A started with the installation of a 9 m long surface casing, with an outer diameter (OD) of 193.7 mm and an inner diameter (ID) of 183.7 mm. Thereafter a 165 mm borehole was drilled down to 100 m, using air percussion drilling, and a surface casing (OD 139.7 mm; ID 129.7 mm) was installed and cemented from bottom to surface. Before drilling, a second casing string (HWT casing; OD 114.3 mm; ID 101.6 mm) was cemented from the casing shoe at 100 m to the surface. The smaller diameter reduces the risk for damage to the drill string and guarantees proper transport of cuttings. In addition, a second short casing was installed to 6 m depth, just outside the well cellar. It was first used as support for the drill rig and later as the conductor casing for borehole COSC-2B, with the purpose to core the upper 100 m that were hammer-drilled in COSC-2A.

The COSC-2A drilling operation started on 14 April 2020 and was completed on 7 August 2020 at a total depth of 2276 m. It was only interrupted for 18 h per week while drilling crews changed. For drilling, the Swedish national re-

Table 1. The COSC-2 boreholes. Locations are from real-time kinematic positioning (RTK) global navigation satellite system (GNSS), the geodetic datum is WGS84 (EPSG:4326), and elevation is RH2000 (EPSG:5613). The recovered core is slightly longer than the totally cored length. Note: IGSN – International Geo Sample Number.

Name	Designation	IGSN	Driller's depth (m)	Cored length (m)	Core recovered (m)	Latitude	Longitude	Elevation (m)
COSC-2A	5054-2-A	ICDP5054EH40001	2276.05	2175.7	2177.1	63.31244584° N	013.52647969° E	320.25[a]
COSC-2B	5054-2-B	ICDP5054EH50001	116.25	110.2	110.5	63.31244644° N	013.52648032° E	320.31[b]

[a] Elevation reference for borehole in the cellar is ground elevation. [b] Elevation reference for borehole outside the cellar is the top of the casing.

search infrastructure for scientific drilling at Lund University, Riksriggen, was staffed with three drillers and/or assistants per 12 h shift. The drilling fluid was recirculated during the drilling, and the cuttings were removed by gravitational settling in two compartmentalised 10 m^3 tanks. The tank contents were disposed of in compliance with environmental regulations. A specially designed well head, including a main valve, an annular blow-out preventer (BOP), and a kill line, was used as a safety precaution during the drilling (see Lorenz et al., 2015a, b). In addition, a gas detector was placed on the drill floor, primarily for the potential hazard of H_2S from the Alum Shale Formation. The drilling was conducted as continuous wire line core drilling, and all core assemblies were extended with the core orientation tool REFLEX ACT III™ RD (rapid descent).

HQ3 (triple tube) core drilling (3 m core barrel length; hole diameter 96.0 mm; core diameter 61.1 mm) used water without additives as a drilling fluid and stopped at 1576 m depth, where the drill string was installed as a temporary casing. The drilling continued with NQ3 (3 m core barrel length; hole diameter 75.7 mm; core diameter 45.0 mm) from 1576 to 1883 m depth. From 1850 m downwards, a biodegradable polymer (AMC FS 2000™) was added to the drilling fluid to reduce friction and facilitate the transport of cuttings. After evaluating the high core recovery and the rock quality, it was decided to change to NQ double-tube drilling (6 m core barrel length; 75.7 mm hole diameter; 47.8 mm core diameter) to save time, leading to an approximately 30 %–40 % time saving due to the longer core barrel and, thus, reduced winching time at this depth. NQ drilling started at 1883 m and continued to total depth (TD) at 2276 m.

COSC-2A was flushed clean and left with the casing to 100 m depth and an open-hole completion below. The procedure was similar to COSC-1A (see Lorenz et al., 2015a, b) and left the borehole in a state that is suitable for the downhole surveys that address the scientific targets (4) and (5). In summary, the drilling proceeded well, with high core recovery, and the operation was completed within budget. However, and similar to COSC-1, the drilling was affected by deforming drill rods, which increased friction in the borehole and the lowered revolutions per minute (rpm), thus affecting the penetration rate and bit life negatively. After the completion of COSC-2A, the drill rig was moved slightly and COSC-2B was core drilled in HQ3 down to 116 m depth within 2 d.

COSC-2A was logged by Riksriggen (Lund University) during drilling breaks for preliminary scientific assessment and to secure data in case of a hole loss. An extensive downhole survey in both boreholes was conducted from 8 to 14 September 2020 by ICDP (International Continental Scientific Drilling Project) OSG (Operational Support Group) and Riksriggen (Lund University).

4 Scientific operations and material

The scientific operations planned for COSC-2 resembled closely those of the successful COSC-1 drilling (as described in Lorenz et al., 2015a, b) but with some minor improvements and the addition of an on-site microbiologist during the entire drilling period (scientific target 6). However, as the COVID-19 pandemic struck, the options were either to delay the entire drilling or to continue with a curtailed on-site programme that could be handled entirely by personnel based in Sweden. The latter option was chosen, as the risk of a prolonged delay due to the then-unknown development of the pandemic was judged higher than the disadvantages caused by the absence of foreign personnel and scientific experts while drilling. Eventually, the following curtailments were implemented: the detailed geological drill core description was postponed to the core repository due to insufficient availability of geologists, and online gas monitoring (Wiersberg et al., 2020) had to be cancelled since the necessary equipment was caught in the lockdown. Depending on the depth and drilling progress, one to two scientists per 12 h shift worked on the curation and documentation of the drill core. The latter included the registration of metadata, initial geological assessment, core scans, multi-sensor core logging (MSCL), core box photography, and packaging for transport. On-site sampling was restricted to microbiology and a sample series that was taken from the interval across the main Caledonian décollement (scientific targets 1 and 6).

For the microbiology, core samples 20–30 cm in length were collected from a depth of 100 to 2250 m at 50 m intervals, resulting in a total of 50 core samples. After sam-

ple registration in the mDIS (Drilling Information System), the surface of the core was washed with sterile Milli-Q ultrapure water and brought to the on-site microbiology laboratory. The bench tops used for core processing were chemically disinfected, followed by flame sterilisation. The surface of the core was flamed to combust contaminating nucleic acids from microbes present in the drilling fluid. To assess the success of surface decontamination, fluorescent microspheres (AFN-09, Radiant Color NV) 0.25–0.45 µm in diameter were added to the drilling fluid at a final concentration range of 10^8 to 10^9 beads per millilitre. The concentration of the microspheres in the drilling fluid was determined every 6 h using a fluorescent microscope (CyScope HP equipped with a 470 nm LED set), as previously described (Friese et al., 2017). Simultaneous with the core recovery, 50 mL of the drilling fluid was sampled in a sterile Falcon tube and immediately frozen at −80 °C for the characterisation of the microbial community in the drilling fluid and, thus, to determine which taxa should be considered as contaminants. An evaluation of the core surface sterilisation was carried out, as previously described (Friese et al., 2017), or via an adapted surface sterilisation protocol described as follows. Briefly, a surface fragment of 2–3 g was collected, using a sterile chisel, and washed for 5 min in sterile Milli-Q water (1 mL water per gram of rock) using a vortex. The liquid was filtered on a polycarbonate membrane filter, and the bead concentration on the core's surface was estimated by counting 30 random fields of view using fluorescent microscopy. Flame sterilisation of the core surface was repeated until at least 99.9 % of the microspheres in the drilling liquid had been quenched (quenching of the microsphere fluorescence occurs upon heating above 100 °C). Once the core was deemed free from contamination, it was sampled for subsequent CARD-FISH analysis (fluorescence in situ hybridisation with catalysed reporter deposition; Escudero et al., 2020). Briefly, the core was transferred to the clean part of the on-site laboratory to sample the inner core, by aseptically removing small fragments, followed by fixing the material in 4 % (vol / vol) formaldehyde in Mackintosh minimal media. The fixed sample was stored at 4 °C until transport back to the home laboratory, where it was kept at −20 °C. Finally, the core was packaged in a foil sleeve, partially sealed, flushed with 0.2 µm filtered nitrogen gas, completely sealed, and stored in a −80 °C freezer present on site. Due to the adhesion of the fluorescent microspheres to the clay particles in the drilling fluid, the beads were no longer added to the drilling fluid after reaching 700 m depth. As an alternative decontamination control procedure, the microbiology core was, immediately after retrieval, submersed in a liquid containing the fluorescent microspheres in a concentration of 10^8 to 10^9 beads per millilitre, followed by the same decontamination procedure as described above. In addition to the 50 m sample interval, natural fractures were sampled by first rinsing the surrounding material with autoclaved Milli-Q water, whereafter the material was collected with either a flame-sterilised chisel or a spatula. The material was subsequently washed in 5 mL autoclaved Milli-Q water using a vortex and stored at −80 °C. The drilling fluid was sampled directly after sampling the fracture in an identical manner to that described above. For natural fracture samples, it was not possible to flame the surface, as this would combust all biomolecules in the sample. Consequently, there is a higher risk of contamination of this material compared to the surface-sterilised cores; the significance and influence of this contamination will be assessed during characterisation of the microbial communities. Finally, all samples stored on site at −80 °C were transferred to the home laboratory on dry ice and kept at −80 °C before processing.

A total of 17 samples for rock mechanical tests, each between 20 and 30 cm long, were taken from the Alum Shale Formation and across the main Caledonian décollement, which corresponds to approximately one sample per core run in the depth range from 780 to 820 m. Each sample was placed in a plastic pipe with a diameter slightly larger than the core diameter, and orientation marks were copied from the core to the pipe's outside. The pipe, whose bottom is closed, was then filled with laminating epoxy until the sample was covered completely. The cured epoxy preserves both the sample's fluid content and its structural integrity during transport to the laboratory.

In summary, the scientific material of the COSC-2 drilling consists of the drill core (sample material) and the following data sets:

- technical data acquired at the drill rig
- drill core metadata, as documented in the mDIS, e.g. core run, depth, core sections, length of sections, core recovery, and the location of sections in core boxes
- a preliminary geological overview
- unrolled core scans
- core box images
- geophysical parameters of the drill core measured with a Geotek Ltd. multi-sensor core logger (MSCL), with natural gamma, density, and magnetic susceptibility
- downhole logging data from Riksriggen (Lund University) and the ICDP OSG.

As the first major scientific drilling project that used the new mDIS software for the acquisition of on-site data, COSC-2 could demonstrate that this software is ready for production workflows after 2 years of development. The functionality of the mDIS is mission critical, as it captures the descriptive data of the drill core, including hierarchy, depth, and identifiers (see Conze et al., 2017).

4.1 Drill core

Turbiditic greywackes of the Föllinge Formation were drilled from the bedrock surface at ca. 5 m depth and down to ca. 780 m (light blue in Fig. 2; Fig. 4a). Here, the borehole encountered a strongly sheared black shale unit, which is in accordance with the magnetotelluric site investigations (Fig. 4b). After ca. 45 m, the black shales give way to a unit characterised by sandstones and conglomerates in a turbiditic background sedimentation, which extends downwards to ca. 1250 m (orange in Fig. 2; Fig. 4c). At this depth, ignimbrites and volcanic porphyries were encountered for the first time in the borehole (Fig. 4d). They show only minor signs of deformation and are present in different varieties (green to reddish; different grain sizes) down to the total depth (red in Fig. 2; Fig. 4e and g), interrupted by major (and some minor) dolerite intrusions between ca. 1600 and ca. 1930 m (green in Fig. 2; Fig. 4f), which show signs of deformation (cataclasite and breccia).

After the downhole logging operations, the drill core was depth corrected, as described in the next section. Thus, sample material, drill core data, and downhole data share a common depth system.

4.2 Downhole logging and establishment of a common borehole reference system

In COSC-2A, the following downhole measurements cover the entire, or at least the open (uncased), part of the borehole: caliper, temperature, magnetic susceptibility, formation resistivity, spectral gamma ray, full waveform sonic, and acoustic televiewer with borehole orientation. The sidewall density probe was deployed in the larger diameter (HQ) upper part of the borehole (to ca. 1570 m depth). The borehole was also surveyed with a north-seeking gyro probe (REFLEX GYRO SPRINT-IQ™) in multi-shot mode (25 and 50 m between measurement points). Caliper, formation resistivity and acoustic televiewer were measured in COSC-2B.

All probes include a natural gamma sensor for correlation between logs. First, a depth master log was established as master depth reference for COSC-2A and all other logs from the borehole depth-correlated to it. Then, the entire drill core was corrected to match the master depth reference. This was done by importing core scan images and televiewer imagery into Corelyzer software (https://github.com/corewall/corelyzer, last acccess: 28 Jaunary 2022), where the depth of the unrolled core scans was adjusted until these images matched the structures observed in the acoustic televiewer imagery. The new core section depths were extracted to the mDIS system, which in turn integrates the new depth system into the drill core metadata and, thus, applies it to all core data (e.g. MSCL).

The depth reference for a borehole does not include information about the depth below surface. It is a local linear reference system along the borehole path. Thus, the borehole path is required for the calculation of the absolute depth below surface and a depth's relative location to the borehole origin. It is also necessary for the establishment of the absolute core orientation based on the core marking from the core orientation tool. COSC-2A was surveyed both with a north-seeking gyro probe (REFLEX GYRO SPRINT-IQ™; rented) and the accelerometer-/magnetometer-based orientation of the acoustic televiewer probes, a Robertson Geologging High-Resolution Acoustic Televiewer (HiRAT; Riksriggen) and an ALT Abi43 (ICDP OSG). The gyro and televiewer orientation match closely (Fig. 5) but with a slightly higher deviation of the Abi43. Thus, the acoustic televiewer imagery can be regarded as an appropriate means for extracting drill core orientation (via the core scans and in addition to the depth correction), either for a confirmation of the results from the core orientation tool or as an independent assessment of a core section's orientation. Such a well-established borehole reference system will allow for the easy integration of all borehole data with established spatial reference systems (e.g. regional or national) and, thus, facilitates data comparison, interpretation, and integration (see Grellet et al., 2020).

5 Preliminary scientific assessment

COSC-2 reached all operational targets, with respect to drilling and downhole investigations, that were planned and required to properly address the scientific targets. The main curtailment of the operations due to the COVID-19 pandemic, i.e. the delay of the detailed geological drill core description from on-site work to core repository, was conducted and finalised recently (autumn 2021) at the core repository.

Comparing the expected geological section with the drilled section (Fig. 2) allows a number of observations. Although the drilling encountered strongly sheared Alum Shale at the predicted depth (Fig. 4b), this shale was not transported upwards from the décollement at about 1250 m in an imbricate system, as interpreted from site investigations. This ca. 45 m thick unit at ∼ 800 m is the Alum Shale Formation in its original stratigraphic position. The section below, down to ca. 1250 m, is not the imbrication of the Lower Paleozoic related to deformation along the main Caledonian décollement in the Alum Shale but an imbrication with a possibly substantial thickening of the sedimentary basement cover. The latter is usually only up to some tens of metres thick and of Neoproterozoic age along the present exposed Caledonian front (Andersson et al., 1985; Juhlin et al., 2016). However, at COSC-2, the sedimentation of coarse siliciclastic sediments (sandstones and conglomerates) happened against a potentially younger turbiditic background sedimentation. The upper, drilled part of the basement consists of different Dala Porphyry varieties. The contact between basement and its clastic cover appears to be primary and not affected by deformation (Fig. 4d). Rocks of Rätan-type granite were not

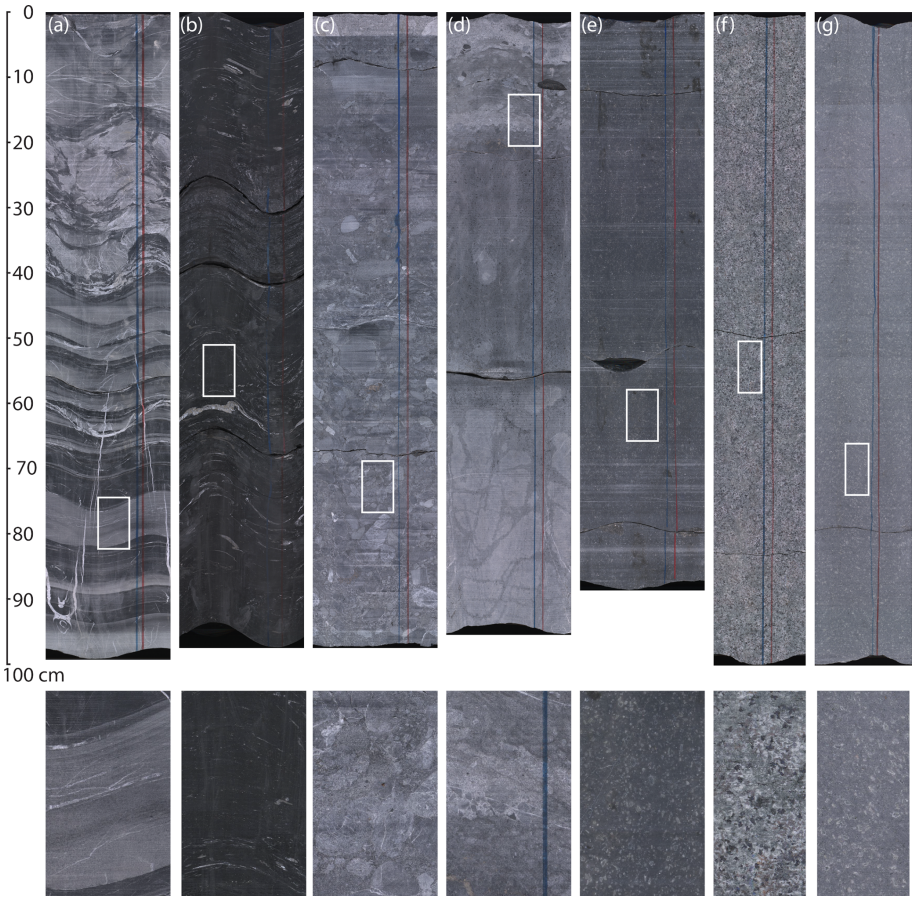

Figure 4. Examples for typical lithologies of the COSC-2 drill core. The upper row shows unrolled core scans of dry core sections (i.e. the entire core surface was scanned and is displayed as a flat image). Visible marks perpendicular to the core are usually caused by the drilling process. The lower row shows enlargements from the unrolled core scans (magnified 4 times when compared to upper row). For the location, see the white box in the corresponding image of the upper row. **(a)** Turbidites with slumping structures (section 91-3; 352 m depth). **(b)** Sheared Alum Shale (section 254-3; 817 m depth). **(c)** Conglomerate (in the clastic section between Alum Shale and top basement; section 354-3; 1096 m depth). **(d)** The preserved contact between basement (porphyry) and overlying clastic sediments (section 395-2; 1215 m depth). **(e)** Volcanic porphyry as it occurs in the upper part of the basement section (section 436-3; 1304 m depth). This interval appears dark due inadvertent variation in the drilling process (polishing of the core surface by the drill bit). **(f)** One appearance of the rock that composes the dolerite intrusions (section 573-3; 1612 m depth). **(g)** Volcanic porphyry close to TD (section 715-7; 2111 m depth).

encountered in the borehole. However, the prominent reflections between ∼ 1.5 and 2 km correspond, as expected, to dolerites, and show at least some deformation along their margins. We conclude the following:

- Deformation in the Alum Shale, and in the sedimentary section of the drill core in general, is less severe than expected.
- Although the Alum shale appears to be less strained than expected, we regard it as being the main detachment horizon that occurs a level of ca. 780–825 m, instead of the expected depth of ca. 1250 m.
- The sedimentary basement cover (between top basement and Alum Shale) in the borehole (825–1250 m) appears to be substantially thicker than observed at the nearest basement window (∼ 30 km to the west) and at the present Caledonian front (∼ 50 km to the east). A thicker Neoproterozoic sedimentary cover exists in northern Jämtland and Västerbotten (ca. 150 km to the north; e.g. Gee and Stephens, 2020). Approximately 200 km farther south, ca. 1.5 Ga Jotnian sandstones (Dala sandstone) discordantly overlie the ca. 1.8–1.7 Ga Dala Porphyries (Lundqvist and Persson, 1999). However, the turbiditic background sedimentation in this depth interval of COSC-2 suggests that the deposition of these coarse siliciclastics happened during the initial stages of the development of the Paleozoic sedimentary basin.

Figure 5. Borehole path of the COSC-2A borehole, based on surveys with a north-seeking gyro (red; REFLEX GYRO SPRINT-IQ™) and the orientation sensors of acoustic televiewers (green; derived from accelerometers and magnetometers). The televiewer data are spliced at 1570 m, with data from the Robertson Geologging High-Resolution Acoustic Televiewer (HiRAT) above this depth and from the ALT Abi43 televiewer below this depth.

- The conspicuous laterally continuous reflection at ca. 1250 m is not related to the main Caledonian décollement but to the top of the Dala Porphyries.
- Most of the prominent reflections in the basement may be caused by dolerite intrusions. The latter may also play a role in how the basement behaved and deformed during Caledonian orogeny (see Lescoutre et al., 2022).
- The basement consists of the weakly magnetic Dala Porphyries down to at least 2.3 km depth. In contrast to former interpretations, the Rätan-type granite that is responsible for the regional magnetic anomaly is now expected to be located at greater depth.
- Synsedimentary deformation (slumping and dewatering structures) frequently disturbs the Palaeozoic section of the drill core and may represent a common feature in the Early Paleozoic environments along this geotectonically active part of the margin of Baltica.

The differences between the expected and drilled geological sections do not affect the project's ability to address the scientific targets (1 and 3), but they will have implications for the scientific results.

An important objective of the COSC-2 drilling was to better understand the nature of the seismic reflectivity (scientific target 2). The P-wave sonic log (Fig. 6) was used as input for generating a preliminary synthetic seismogram that can be compared with the surface seismic data. First, the log was converted from depth to time, using a filtered version of the velocities and the reflection coefficient log calculated assuming constant density. This reflection coefficient log was then convolved with the first derivate of a Gaussian wavelet, with a maximum frequency of 80 Hz, to generate the seismic response as a function of time. Good correlation is observed between the synthetic seismogram and the surface data (Fig. 7). In particular, the Alum Shale at ca. 0.32 s correspond to a strong reflection, as does the top of the Dala Porphyries at ca. 0.48 s. The top of the dolerite sequence at ca. 0.6 s and the base of it at ca. 0.68 s also correlate to reflections, but more detailed studies are necessary to determine which contacts are generating the reflections within the dolerite interval. Data from the borehole seismic survey in autumn 2021 will be used to improve the time/depth conversion.

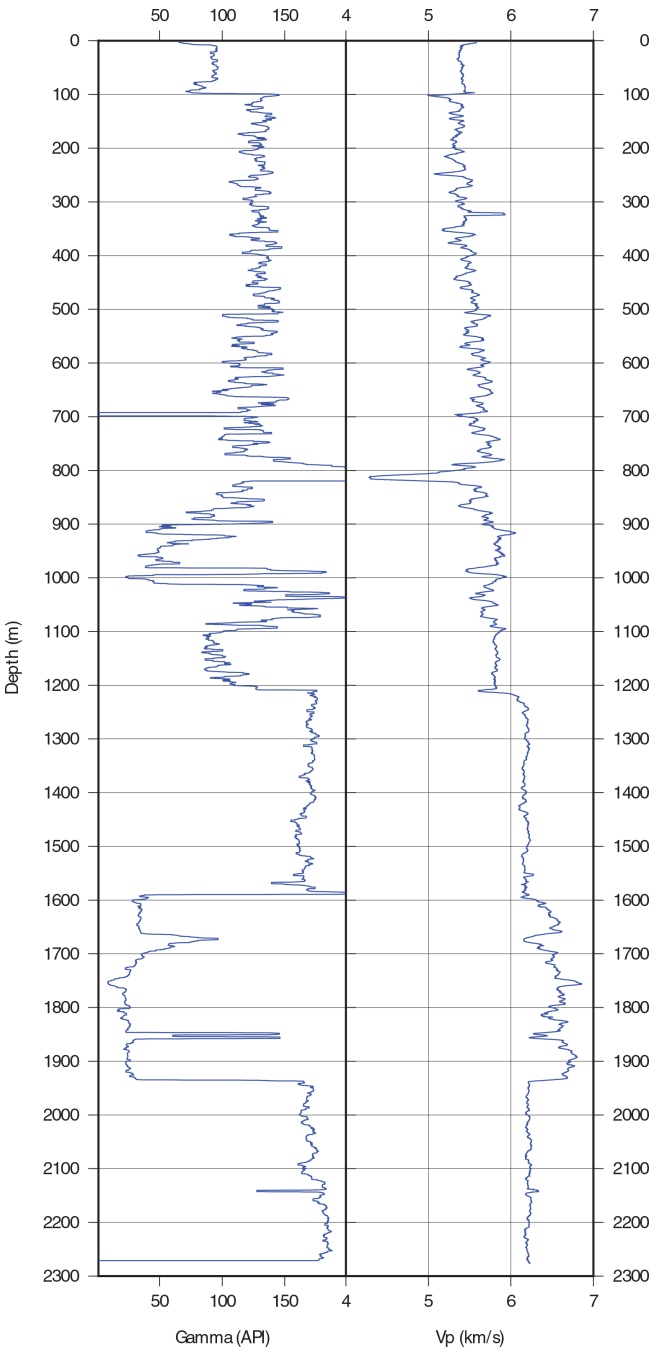

Figure 6. Natural gamma and P-wave sonic logs after smoothing. The sonic log was converted to time to form the basis for the generation of the synthetic seismogram shown in Fig. 7.

6 Outlook

Post-drilling borehole and surface seismic surveys were performed in autumn 2021, with the main aims of (1) investigating the nature of the seismic reflections and allowing depth conversion based on seismic frequencies, (2) increasing 3D seismic coverage in the vicinity of the borehole, and (3) studying potential anisotropy in the upper kilometres of the crust (scientific target 2). Dense sampling of the wavefield in the borehole, a sparse 3D array on the surface, use of an airgun and lake bottom seismometers on and in Liten Lake, respectively, and a vibroseis source along two longer crossing profiles allow these objectives to be met. Field geophysics will be complemented by petrophysical measurements on core samples in the laboratory, including seismic velocities, magnetic properties (anisotropy of magnetic sus-

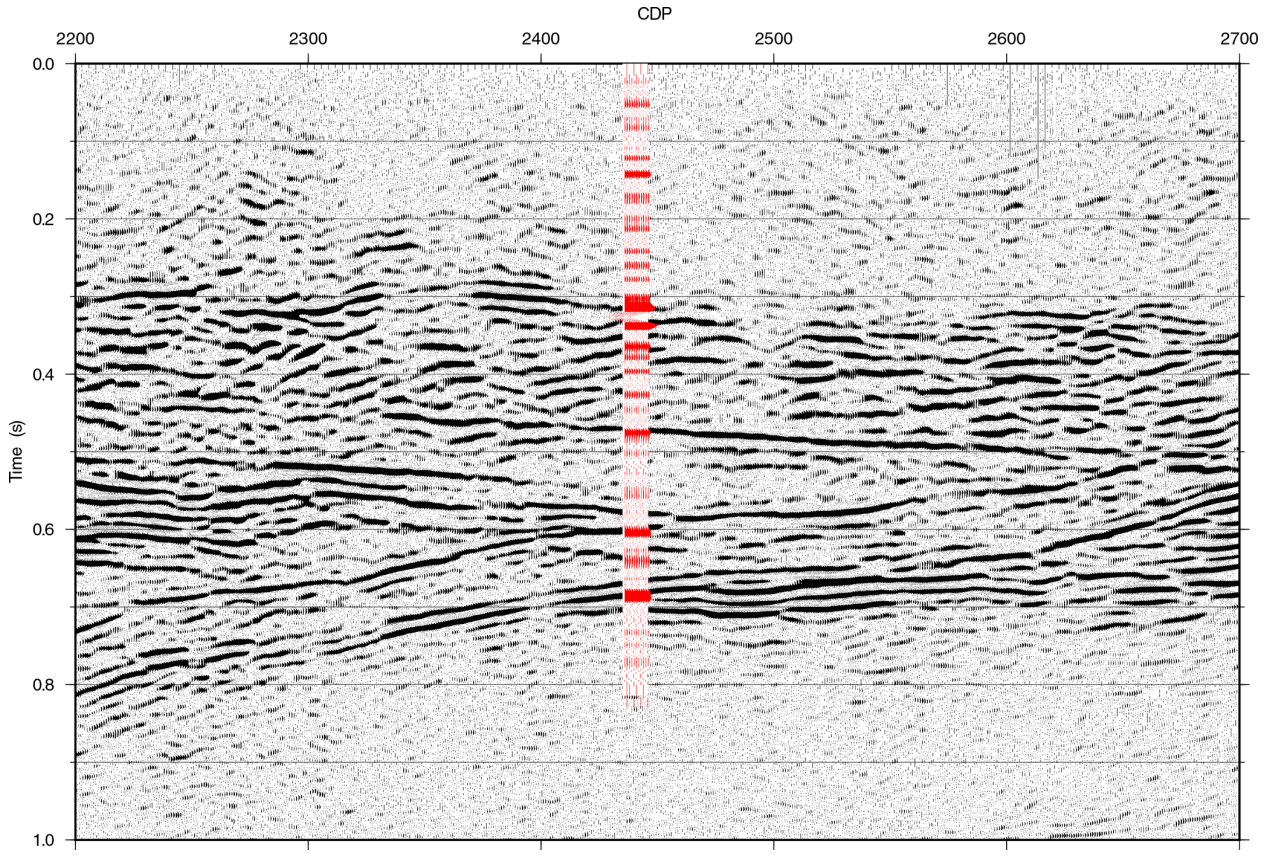

Figure 7. Synthetic seismogram (in red) with the trace repeated 10 times and plotted on top of the time-migrated surface seismic section. The synthetic seismogram was generated using the sonic log shown in Fig. 6 as input.

ceptibility (AMS) and palaeomagnetism), and electric properties of the Alum Shale.

The detailed geological description of the COSC-2 drill core was established recently and will be compiled and published by a dedicated working group from the science team. These data are critical for the scientists' preparations for the sampling party.

Scientific target 1, to understand how deformation propagates along an orogen-scale detachment horizon and into the basement of the Fennoscandian Shield, will be advanced through additional documentation and characterisation of structures and associated alteration above, within, and below the Alum Shale. Establishing criteria for distinguishing between the Caledonian deformation and pre- and post-Caledonian deformation will be critical in this regard, especially in relation to the structures identified in sections below the Alum Shale. Detailed characterisation of the detachment in the Alum Shale will help with this research. Presently, oriented subsamples are drilled from the sample series across this décollement and subjected to rock mechanical testing under controlled environmental conditions. Comprehensive microstructural and geochronological analyses will commence after the sampling party.

Analysis of the geomicrobiological samples is underway (scientific target 6). Intact cells in the prepared drill core material are detected by the CARD-FISH methodology (Escudero et al., 2020), and the diversity and taxa represented in the community are reconstructed by sequencing ribosomal RNA marker genes. If sufficient microbial biomass is retrieved, genomic reconstruction of metabolic potential will also be performed. Combined, these techniques will provide knowledge about microbial biomass, diversity, and functioning in the deep terrestrial subsurface. These will be supplemented by the characterisation of fracture mineralisation that can yield information on microbial activity in deep time (Drake et al., 2020).

Research topics related to downhole investigations have not been fully addressed yet. Hydrogeological investigations (scientific target 5) with flowing fluid electrical conductivity (FFEC) logging and fluid sampling will be conducted during 2022. This campaign is planned to be complemented with fluid sampling for geomicrobiology. The borehole temperature logging for heat flow evaluation and the modelling of palaeotemperature (scientific target 4) requires that the borehole temperature (Fig. 8) equilibrates to a steady state af-

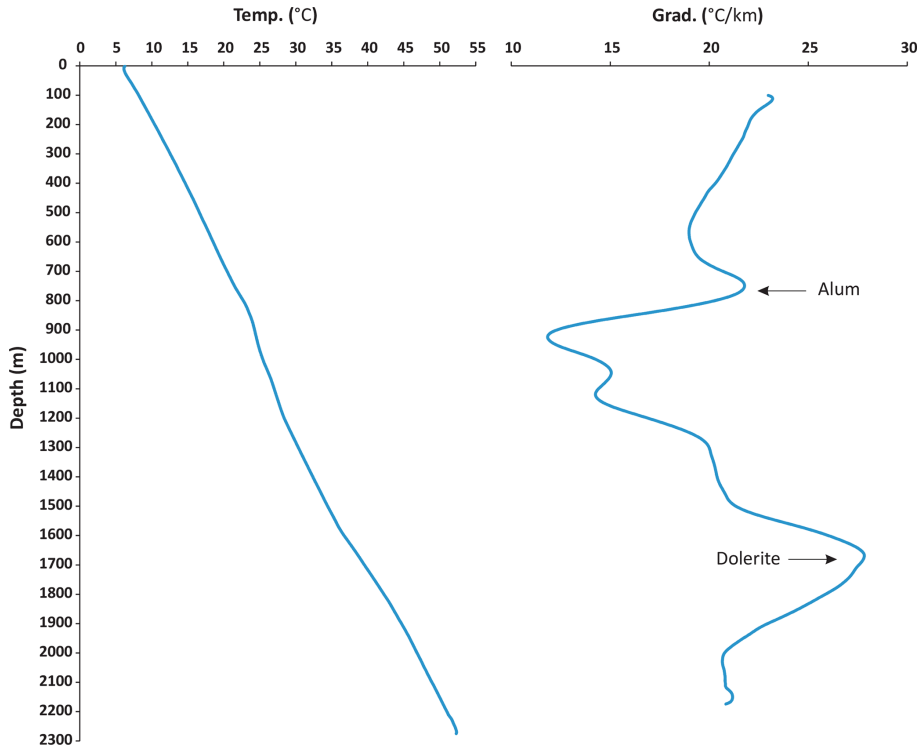

Figure 8. Temperature profile and thermal gradient for the COSC-2 drill hole. The thermal gradient was computed using a moving window of 200 m.

ter the disturbance by the drilling operations, which usually takes several years.

During 2022, the drill site will be dismantled and renatured. A 4 m wide track from the road to the boreholes will provide continued access for future investigations.

7 Summary

The ICDP project COSC-2 drilled successfully, and within budget, to a total depth of 2276 m and recovered a continuous drill core of good quality with negligible core loss. The COVID-19 pandemic required some adaptations to the onsite scientific programme, like the postponement of the detailed geological description of the drill core. Observations at the drill site made clear that the drilled geological section at depth is different from the expected section. This will not affect the ability to address the scientific targets but leads to different and unexpected results. It can be stated already now that the project successfully addressed the target of understanding the seismic reflectivity in the basement by analysing downhole logs and the preliminary geological assessment of the drill core. A large downhole and surface seismic campaign will further improve on this. Expertise on microbiological research in hard rock environments has been built and protocols established that are viable for deep core drilling operations, although laboratory work and research have to show whether the biomass is sufficient, depending on rock type and depth. Geological research has begun with the (postponed) detailed description of the drill core. New insights into orogen-scale deformation are expected, including the main detachment and its influence on underlying units, and the character and age of the deformation in the basement. However, seemingly pervasive deformation in the upper part of the drill core raises the question as to how suitable it will be to help characterise the deep-water environment of the Early Paleozoic margin of Baltica (scientific target 3). Despite some setbacks, the COSC-2 project was an overall success and delivered extensive material for multidisciplinary research at a reasonable cost. The fact that the scientific community now has access to a nearly continuous composite geological section (outcrop and COSC-1 and COSC-2 drill cores) through the lower part of a major collisional orogen can be expected to generate new interest and research far beyond the present COSC project. More details about the COSC-2 operations will become available in the operational report, which will be published after the conclusion of the operational phase. The timing of the latter depends on when the COVID-19 pandemic allows the conduction of its last component, which is the sampling party.

Data availability. The COSC-2 operational data sets are published under Lorenz et al. (2021; https://doi.org/10.5880/ICDP.5054.003).

Sample availability. The drill core of the two COSC-2 boreholes (see IGSN in Table 1 for further information) is archived at the Core Repository for Scientific Drilling at the Federal Institute for Geosciences and Natural Resources (BGR), Wilhelmstr. 25–30, 13593 Berlin (Spandau), Germany.

Author contributions. The scientific project was conceptualised by CJ, MA, MD, OL, LM, CP, and NNWR in their roles as project leader (CJ), topical principal investigators (PIs), and task leaders. Data curation was performed by JoK, for ICDP OSG downhole logging, and HL, for all other data. Funding was acquired by CJ, CP, and IK as the main applicants, with support from the co-authors and the COSC-2 science team. The investigation was led by HL, RL, GW, IK, MD, BSGA, and SB, with support from the COSC-2 on-site team. The methodology of the technical operations was designed by JER and of the operational science by HL. MD, JeK, SB, and GW developed the protocols for geomicrobiology. JER supervised the technical operations, HL supervised the operational science, and JoK and SR supervised the respective downhole logging operations. HL wrote the original draft of the paper, and JER contributed the section about the technical operations. CJ contributed the section about geophysics, and GW, SB, MD, and JeK contributed the section about geomicrobiology. CP contributed the assessment of the temperature profile. All co-authors reviewed and improved the paper.

Competing interests. The contact author has declared that neither they nor their co-authors have any competing interests.

Disclaimer. Publisher's note: Copernicus Publications remains neutral with regard to jurisdictional claims in published maps and institutional affiliations.

Acknowledgements. The authors express their appreciation for the on-site science and the drilling teams' extraordinary efforts in keeping the project running in the middle of the COVID-19 pandemic. A special thanks to drilling supervisor Stellan Larsson (also known as "The Great Wizard of the North"), from Larsson Drilling Consulting AB, for his technical ingenuity that spared the project a lot of trouble. The drilling operations were conducted with the Swedish national research infrastructure for scientific drilling, Riksriggen, which is funded by the Swedish Research Council. The COSC-2 team thanks Nils-Olof Strandberg, for his support in local matters of all kinds. The authors thank two reviewers and the editor, for their comments that helped to improve the paper.

Financial support. A generous grant from the International Continental Scientific Drilling Project (ICDP; grant no. 4-2017) provided the financial basis for the drilling project. Co-funding for the drilling operation and operational science has been provided by the Swedish Research Council (Vetenskapsrådet; grant nos. 2019-03688 and 2017-00642), the German Science Foundation (Deutsche Forschungsgemeinschaft DFG, grant no. SPP 1006), and the National Science Centre of Poland (Narodowym Centrum Nauki, project no. 2018/29/B/ST10/02315).

Review statement. This paper was edited by Tomoaki Morishita and reviewed by Vincent Famin and Makoto Otsubo.

References

Andersson, A., Dahlman, B., Gee, D. G., and Snäll, S.: The Scandinavian Alum Shales, Sveriges geologiska undersökning, Uppsala, 50 pp., ISBN 91-7158-334-3, 1985.

Beckholmen, M.: Geology of the Nordhallen–Duved–Greningen area in Jämtland, central Swedish Caledonides, Geol. Fören. Stockh. Förh., 100, 335–347, https://doi.org/10.1080/11035897809454471, 1978.

Conze, R., Lorenz, H., Ulbricht, D., Elger, K., and Gorgas, T.: Utilizing the International Geo Sample Number Concept in Continental Scientific Drilling During ICDP Expedition COSC-1, Data Sci. J., 16, p. 2, https://doi.org/10.5334/dsj-2017-002, 2017.

Drake, H., Roberts, N. M. W., and Whitehouse, M. J.: Geochronology and Stable Isotope Analysis of Fracture-Fill and Karst Mineralization Reveal Sub-Surface Paleo-Fluid Flow and Microbial Activity of the COSC-1 Borehole, Scandinavian Caledonides, Geosciences, 10, 56, https://doi.org/10.3390/geosciences10020056, 2020.

Dyrelius, D.: Aeromagnetic interpretation in a geotraverse area across the central Scandinavian Caledonides, Geol. Fören. Stockh. Förh., 102, 421–438, https://doi.org/10.1080/11035898009454498, 1980.

Escudero, C., del Campo, A., Ares, J. R., Sánchez, C., Martínez, J. M., Gómez, F., and Amils, R.: Visualizing Microorganism-Mineral Interaction in the Iberian Pyrite Belt Subsurface: The Acidovorax Case, Front. Microbiol., 11, 2833, https://doi.org/10.3389/fmicb.2020.572104, 2020.

Friese, A., Kallmeyer, J., Kitte, J. A., Martínez, I. M., Bijaksana, S., and Wagner, D.: A simple and inexpensive technique for assessing contamination during drilling operations, Limnol. Oceanogr. Methods, 15, 200–211, https://doi.org/10.1002/lom3.10159, 2017.

Gee, D. G. and Stephens, M. B.: Chapter 20 Lower thrust sheets in the Caledonide orogen, Sweden: Cryogenian–Silurian sedimentary successions and underlying, imbricated, crystalline basement, Geol. Soc. Lond. Mem., 50, 495–515, https://doi.org/10.1144/M50-2018-7, 2020.

Gee, D. G., Fossen, H., Henriksen, N., and Higgins, A. K.: From the Early Paleozoic Platforms of Baltica and Laurentia to the Caledonide Orogen of Scandinavia and Greenland, Episodes, 31, 44–51, 2008.

Gee, D. G., Juhlin, C., Pascal, C., and Robinson, P.: Collisional Orogeny in the Scandinavian Caledonides (COSC), GFF, 132, 29–44, https://doi.org/10.1080/11035891003759188, 2010.

Gorbatschev, R.: Beskrivning till berggrundskartan över Jämtlands län. Del 1: Urberget, Sveriges Geologiska Undersökning, Uppsala, 250 pp., ISBN 978-91-7158-569-1, 1997.

Gorbatschev, R., Solyom, Z., and Johansson, I.: The Central Scandinavian Dolerite Group in Jämtland, central

Sweden, Geol. Fören. Stockh. Förh., 101, 177–190, https://doi.org/10.1080/11035897909448572, 1979.

Grellet, S., Boisvert, E., Simons, B., Rainaud, J.-F., Lorenz, H., Haener, R., Beaufils, M., Lieberman, J., Liu, Y., Nayembil, M., Raymond, O., Sharples, J., and Warren, P.: OGC Borehole Interoperability Experiment Engineering Report, OGC Eng. Rep., 19-075r1, Open Geospatial Consortium, 182, available at: http://www.opengis.net/doc/per/borehole-ie (last access: 28 January 2022), 2020.

Hedin, P., Juhlin, C., and Gee, D. G.: Seismic imaging of the Scandinavian Caledonides to define ICDP drilling sites, Tectonophysics, 554–557, 30–41, https://doi.org/10.1016/j.tecto.2012.05.026, 2012.

Högdahl, K., Andersson, U. B., and Eklund, O.: The Transscandinavian Igneous Belt (TIB) in Sweden: a review of its character and evolution, Geological Survey of Finland, Espoo, 123 pp., ISBN 951-690-889-6, 2004.

Juhlin, C., Hedin, P., Gee, D. G., Lorenz, H., Kalscheuer, T., and Yan, P.: Seismic imaging in the eastern Scandinavian Caledonides: siting the 2.5 km deep COSC-2 borehole, central Sweden, Solid Earth, 7, 769–787, https://doi.org/10.5194/se-7-769-2016, 2016.

Juhojuntti, N., Juhlin, C., and Dyrelius, D.: Crustal reflectivity underneath the Central Scandinavian Caledonides, Tectonophysics, 334, 191–210, https://doi.org/10.1016/S0040-1951(00)00292-4, 2001.

Karis, L. and Strömberg, A.: Beskrivning till berggrundskartan över Jämtlands län. Del 2: Fjälldelen, Sveriges geologiska undersökning, Uppsala, 363 pp., ISBN 91-7158-605-9, 1998.

Klonowska, I., Janák, M., Majka, J., Petrík, I., Froitzheim, N., Gee, D. G., and Sasinková, V.: Microdiamond on Åreskutan confirms regional UHP metamorphism in the Seve Nappe Complex of the Scandinavian Caledonides, J. Metamorph. Geol., 35, 541–564, https://doi.org/10.1111/jmg.12244, 2017.

Lescoutre, R., Almqvist, B., Koyi, H., Berthet, T., Hedin, P., Galland, O., Brahimi, S., Lorenz, H., and Juhlin, C.: Large-scale flat-lying mafic intrusions in the Baltican crust and their influence on basement deformation during Caledonian orogeny, GSA Bulletin, https://doi.org/10.1130/B36202.1, online first, 2022.

Lorenz, H., Rosberg, J.-E., Juhlin, C., Bjelm, L., Almqvist, B. S. G., Berthet, T., Conze, R., Gee, D. G., Klonowska, I., Pascal, C., Pedersen, K., Roberts, N. M. W., and Tsang, C.-F.: COSC-1 – drilling of a subduction-related allochthon in the Palaeozoic Caledonide orogen of Scandinavia, Sci. Dril., 19, 1–11, https://doi.org/10.5194/sd-19-1-2015, 2015a.

Lorenz, H., Rosberg, J. E., Juhlin, C., Bjelm, L., Almquist, B., Berthet, T., Conze, R., Gee, D., Klonowska, I., Pascal, C., Pedersen, K., Roberts, N., and Tsang, C. F.: Operational report about phase 1 of the Collisional Orogeny in the Scandinavian Caledonides scientific drilling project (COSC-1), GFZ German Research Centre for Geosciences, 55 pp., https://doi.org/10.2312/ICDP.2015.002, 2015b.

Lorenz, H., Juhlin, C., Rosberg, J.-E., Bazargan, M., Klonowska, I., Kück, J., Lescoutre, R., Rejkjær, S., Westmeijer, G., and Ziemniak, G.: COSC-2 operational report – Operational data sets, GFZ Data Services [data set], https://doi.org/10.5880/ICDP.5054.003, 2021.

Lundqvist, T. and Persson, P.-O.: Geochronology of porphyries and related rocks in northern and western Dalarna, south-central Sweden, GFF, 121, 307–322, https://doi.org/10.1080/11035899901214307, 1999.

Palm, H. and Lund, C.-E.: A seismic refraction study in the Caledonian front of Jämtland, Sweden, Geol. Fören. Stockh. Förh., 102, 561–568, https://doi.org/10.1080/11035898009454508, 1980.

Strömberg, A., Karis, L., Zachrisson, E., Sjöstrand, T., Skoglund, R., Lundegårdh, P. H., Gorbatschev, R., and Kornfält, K.-A.: Berggrundskarta över Jämtlands län utom förutvarande Fjällsjö kommun, Sveriges geologiska undersökning, Stockholm, ISBN 91-7158-605-9, 1984.

Welin, E., Christansson, K., and Kähr, A.-M.: Isotopic investigations of metasedimentary and igneous rocks in the Palaeoproterozoic Bothnian Basin, central Sweden, Geol. Fören. Stockh. Förh., 115, 285–296, https://doi.org/10.1080/11035899309453915, 1993.

Wiersberg, T., Pierdominici, S., Lorenz, H., Almqvist, B., and Klonowska, I.: Identification of gas inflow zones in the COSC-1 borehole (Jämtland, central Sweden) by drilling mud gas monitoring, downhole geophysical logging and drill core analysis, Appl. Geochem., 114, 104513, https://doi.org/10.1016/j.apgeochem.2019.104513, 2020.

Yan, P., Garcia Juanatey, M. A., Kalscheuer, T., Juhlin, C., Hedin, P., Savvaidis, A., Lorenz, H., and Kück, J.: A magnetotelluric investigation of the Scandinavian Caledonides in western Jämtland, Sweden, using the COSC borehole logs as prior information, Geophys. J. Int., 208, 1465–1489, https://doi.org/10.1093/gji/ggw457, 2016.

Sci. Dril., 30, 59–74, 2022
https://doi.org/10.5194/sd-30-59-2022

Scientific Drilling
Open Access

Comparison of sediment composition by smear slides to quantitative shipboard data: a case study on the utility of smear slide percent estimates, IODP Expedition 353, northern Indian Ocean

Stephen C. Phillips[1] **and Kate Littler**[2]

[1]U.S. Geological Survey, Woods Hole, MA 02543, USA
[2]Camborne School of Mines and Environment and Sustainability Institute, University of Exeter, Penryn Campus, Penryn, Cornwall, TR10 9FE, UK

Correspondence: Stephen C. Phillips (scphillips@usgs.gov)

Received: 10 May 2021 – Revised: 3 November 2021 – Accepted: 7 November 2021 – Published: 25 February 2022

Abstract. Smear slide petrography has been a standard technique during scientific ocean drilling expeditions to characterize sediment composition and classify sediment types, but presentation of these percent estimates to track downcore trends in sediment composition has become less frequent over the past 2 decades. We compare semi-quantitative smear slide composition estimates to physical property (natural gamma radiation, NGR) and solid-phase geochemical (calcium carbonate, $CaCO_3$ %) measurements from a range of marine depositional environments in the northern Indian Ocean (Bay of Bengal, Andaman Sea, Ninetyeast Ridge) collected during International Ocean Discovery Program (IODP) Expedition 353. We show that presenting smear slide estimates as percentages, rather than abundance categories, reveals similar downcore variation in composition to the more quantitative core analyses. Overall downcore trends in total calcareous components from smear slides (foraminifers + nannofossils + shell fragments + authigenic carbonate) follow similar downcore trends to samples measured by $CaCO_3$ coulometry. Total lithogenic components (clay + mica + quartz + feldspars + lithic grains + vitric grains + glauconite + heavy minerals + iron oxides) and clay from smear slides track reasonably well with NGR measurements. Comparison of site averages of absolute percentages of total calcium carbonate from coulometry and total calcareous components from smear slide observations reveals an overestimation in carbonate percentages in smear slides (likely due in part to underestimation of the clay fraction), especially in sediments rich in smectite clays. Differences in sediment color between sites and settling of clay particles during slide preparation may contribute to this discrepancy. Although smear slide estimates range in accuracy depending on the training of the operator, we suggest that sedimentologists describing cores obtained during scientific drilling can use the percent estimates of sedimentary components in smear slides to identify trends and cyclicity in marine sediment records.

1 Introduction

Visual estimation has long been used as a standard method for describing sediments and sedimentary rocks (e.g., Folk, 1951; Terry and Chilingar, 1955; Reid, 1985). In particular, smear slide petrography has become a standard procedure for identification of microscopic components and lithology classification for (predominantly unconsolidated) sediments recovered during scientific drilling, including Deep Sea Drilling Project (DSDP), Ocean Drilling Program (ODP), Integrated Ocean Drilling Program/International Ocean Discovery Program (IODP), and International Continental Scientific Drilling (ICDP) expeditions (Musich, 1984; Mazzullo and Graham, 1988; Rothwell, 1989; Myrbo et al., 2011; Marsaglia et al., 2013, 2015). These smear slide descriptions are used in tandem with macro-scale visual core descriptions

for the classification of recovered sediments using a variety of classification and nomenclature schemes (e.g., Folk, 1954; Shepard, 1954; Davies et al., 1977; Dean et al., 1985; Mazzullo et al., 1988; Carozzi, 1988, 1993; Flügel, 2010; Milliken, 2014).

Quantitative and semi-quantitative sediment characterization techniques such as multi-sensor core logging, spectral reflectance, X-ray fluorescence (XRF), X-ray diffraction, coulometry, and carbon–hydrogen–nitrogen–sulfur (CHNS) elemental analysis have become standard techniques for characterizing the composition of marine sediment cores (e.g., Engleman et al., 1985; Schultheiss and McPhail, 1989; Verardo et al., 1990; Weaver and Schultheiss, 1990; Jansen et al., 1991; Mayer, 1991; Fisher and Underwood, 1995; Blum, 1997; Weber et al., 1997; Ortiz et al., 1999; Giosan et al., 2002; Croudace et al., 2006). However, visual microscopic and macroscopic descriptions, as described in the previous paragraph, are still widely used as an effective, fast, and low-cost technique for characterizing sediment core composition. Smear slide petrography allows for characterizing many components in loosely consolidated sediments that cannot be quantified using bulk or scanning analyses, for example, the exact nature of biogenic carbonates (foraminifers or calcareous nannofossils). Estimations of grain percentages are generally accurate to within 5 %–16 %, based on thin sections with known grain percentages (Allen, 1956). More experienced operators can make relatively consistent percentage estimations across samples (Griffiths and Rosenfeld, 1954). Examination of three areas of a smear slide allows for accurate determination of the major mineral and microfossil components (Marsaglia et al., 2013; Drake et al., 2014).

During recent scientific drilling operations, these semi-quantitative smear slide estimates were used primarily to classify the sediment (e.g., to give it an appropriate name such as "nannofossil-rich clay") and present photomicrographs. While this is indeed useful, the percent estimates are often not used to identify trends in sediment composition and tend to be lost within lithostratigraphic unit designations or relegated to archived data. There is little consistency in how abundances of smear slide constituents are presented within IODP reports between different expeditions. Abundance percentages from smear slides are sometimes presented in plots within IODP reports but are often not presented at all or merely as abundance categories (e.g., "very abundant", "rare"). Of the 148 ODP and IODP expeditions between 1985 and 2019 with smear slide observations in the database, 58 (39 %) presented the observed abundances as percentages in plots within expedition reports, while 9 (6 %) presented these abundances as categories (Fig. 1). The majority (54 %) of these expedition reports do not present the smear slide abundances in figures of IODP proceedings. The number of expeditions visually presenting smear slide percentages in the proceedings reports has generally been decreasing: 45 % during ODP, 37 % during the Integrated Ocean Drilling Program, and 22 % during the International Ocean Discovery Program. There is no clear difference in how smear slide data are presented based on the focus of expeditions (e.g., palaeoceanographic, tectonic, biosphere).

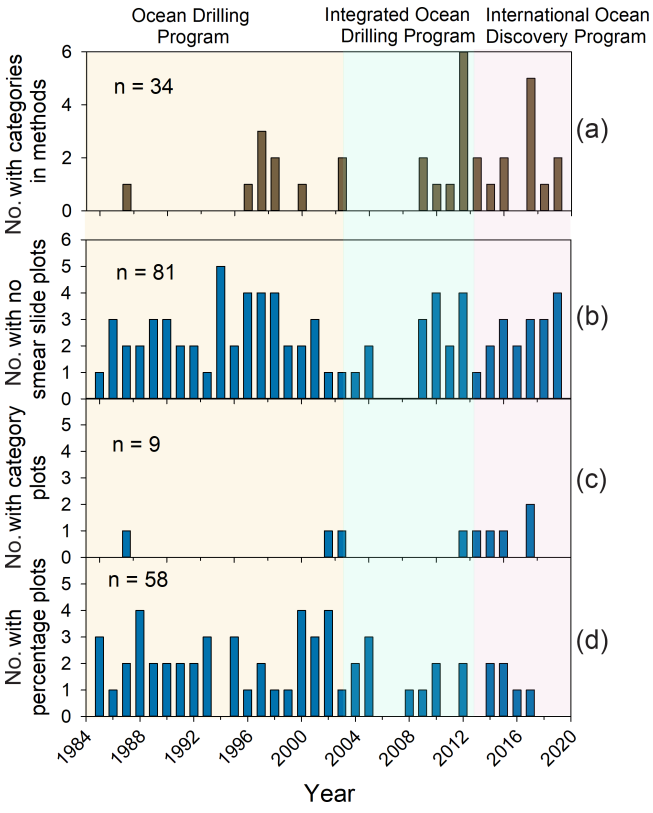

Figure 1. Trends in the presentation of smear slide abundances during the ODP and IODP phases of scientific ocean drilling between 1985 and 2019. Bars represent the number of expedition reports with each mode of presentation by year. **(a)** The number of expedition proceedings that included a description in the methods of smear slides being categorized into abundance categories (rare, common, abundant, etc.). **(b)** The number of expedition reports that did not present smear slide percentages in the report as figures, and these data are only present in the raw data archive. **(c)** The number of expedition reports that present smear slide data as abundance categories in figures. **(d)** The number of expedition reports that present smear slide percentages visually as figures (e.g., downcore line or bar charts).

Many methods sections of IODP proceedings specify abundance categories, especially in recent years (24 expeditions between 2009 and 2019) (Fig. 1), in which abundances were categorized as trace (< 1 %), rare (1 % to 5 %), common (> 5 % to 25 %), abundant (> 25 % to 50 % or 40 % to 75 %), and dominant (> 50 % or > 75 %) or a similar classification scheme. These methods correspond to expeditions that either present abundance categories or do not present figures with smear slide data at all. There appears to be a hesitancy during some IODP expeditions to report observed percentages from smear slides. For example, one IODP methods chapter states that

> Errors can be large, however, especially for fine silt- and clay-size fractions, and reproducibility among different sedimentologists is expected to be poor. Smear slide analysis also tends to underestimate the amount of sand-size grains because they are difficult to incorporate evenly onto the slide. Thus, it would be misleading to report values as absolute percentages (Expedition 330 Scientists, 2012).

Another ODP expedition methods chapter states that "Because estimates of mineral percentages from smear slides are known to be inaccurate (Rothwell, 1989), we abandoned percentage estimates entirely" (Shipboard Scientific Party, 1997).

On the other hand, other expeditions do present smear slide percent estimates in expedition proceedings, allowing for visualization of downcore variation in sediment composition. These are typically presented as individual downcore patterns of each component (e.g., Gallagher et al., 2017; Shipboard Scientific Party, 1994a, b, 1996a) or as stacked 100 % component plots (e.g., Expedition 339 Scientists, 2013a; Shipboard Scientific Party, 1991, 1995a).

Despite having confidence in our smear slide percentages during IODP Expedition 353, we presented our smear slide observations as abundance categories in figures of the IODP proceedings, while the percentages entered into the database were preserved as tables (Clemens et al., 2016b, c, d). As the primary smear slide observers on IODP Expedition 353, we had previously sailed on IODP expeditions in which smear slide abundances were not presented visually (Expedition 324 Scientists, 2010) or were entered into the database as categories (J-CORES on *Chikyu*) (Expedition 337 Scientists, 2013). Looking to previous recent expeditions as examples, we saw numerous methods sections including abundance categories for smear slides (the majority of expeditions in the few years prior to IODP 353, including nearly every expedition in 2012; see Fig. 1) and assumed that this was a standard way to present smear slide data.

In this paper we compare smear slide descriptions (percent estimates) to physical property (natural gamma radiation) and solid-phase geochemical measurements ($CaCO_3$ %) from sediment cores recovered during IODP Expedition 353 in the Bay of Bengal and Andaman Sea (Fig. 2) (Clemens et al., 2016a). We use these comparisons to demonstrate the effectiveness of smear slide petrography and to highlight potential strategies and challenges for using the smear slide technique in fine-grained sediments. We aim to give confidence to those describing smear slides in using the percent abundance estimates for downcore plots and interpretation and for unlocking information on sediment composition and origin that cannot be obtained using other bulk analyses. Although smear slide petrography does not have the accuracy of bulk quantitative analyses and is subject to biases, the percent estimates can still reveal trends in sediment composition that are important to the objectives of scientific drilling expeditions.

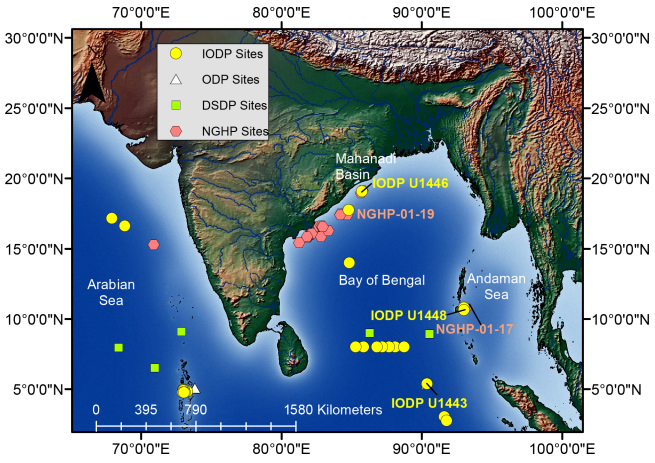

Figure 2. Location map including scientific drilling sites in the northern Indian Ocean. These include expeditions of the International Ocean Discovery Program (IODP), Ocean Drilling Program (ODP), Deep Sea Drilling Project (DSDP), and Indian National Gas Hydrate Program (NGHP). All IODP sites within the scale of this map are from the International Ocean Discovery Program phase of drilling, not the Integrated Ocean Drilling Program phase.

2 Geologic background

During IODP Expedition 353 we recovered sediment cores from the peninsular Indian continental slope in the northern Bay of Bengal (Mahanadi Basin), the Andaman accretionary wedge, Ninetyeast Ridge, and the Bengal Fan (Clemens et al., 2016a) (Fig. 2). In this paper, we focus mainly on three of these sites: (1) U1443 at Ninetyeast Ridge, (2) U1446 in the Mahanadi Basin, and (3) U1448 in the Andaman Sea. Site U1443 (2929 meters below sea level or m b.s.l.) was a re-drill of Ocean Drilling Program (ODP) Site 758 (see Shipboard Scientific Party, 1989). At this site, we recovered a record of calcareous pelagic sediments (Fig. 3a, b) since the Cretaceous (with a very condensed Eocene section) on Ninetyeast Ridge (Barnet et al., 2020; Clemens et al., 2016b). Site U1446 (1430 m b.s.l.) was drilled 75 km offshore of the Indian subcontinent on the continental slope. The 180 m sediment record recovered at this site is entirely Pleistocene in age and consists of hemipelagic clay (Fig. 3c, d) with variable nannofossil and foraminifer content (Clemens et al., 2016c). Site U1448 (1091 m b.s.l.) was drilled in a forearc basin of the Andaman accretionary wedge ∼ 45 km east of Little Andaman Island (Clemens et al., 2016d). The 421 m of sediments recovered at this site are nannofossil-rich clay (Fig. 2e, f) with foraminifers of Pleistocene to Late Miocene age, with an 8 Myr hiatus at 379 m below the seafloor underlain by Early Miocene bio-siliceous ooze with clay and nannofossils.

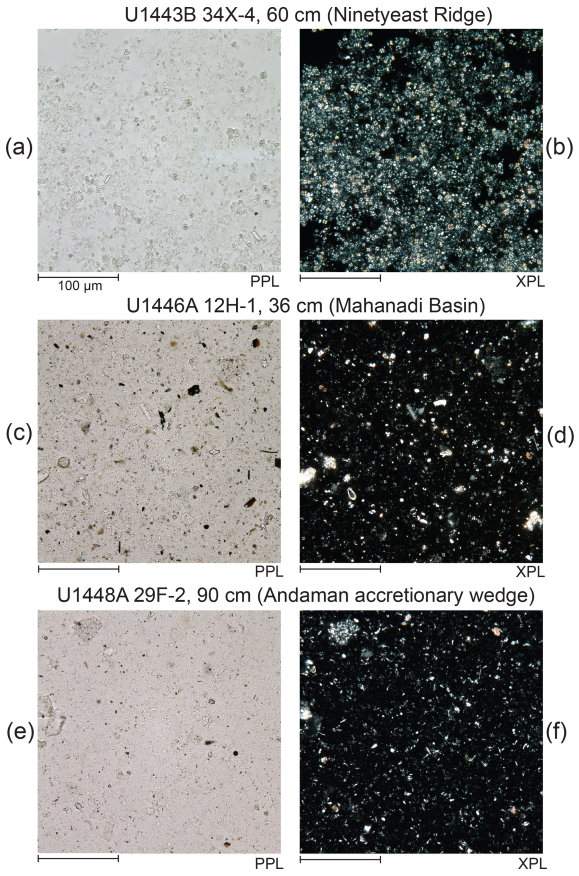

Figure 3. Example photomicrographs of smear slides described during IODP Expedition 353. **(a, b)** Clayey nannofossil chalk with authigenic carbonate from Site U1443 (Ninetyeast Ridge). **(c, d)** Nannofossil-rich clay with foraminifers from Site U1446 (Mahanadi Basin). **(e, f)** Nannofossil-rich clay from Site U1448 (Andaman accretionary wedge). Photomicrographs are shown for both plane-polarized light (PPL; **a, c, e**) and cross-polarized light (XPL; **b, d, f**). The scale bar is 100 µm in each image.

3 Methods

We made smear slides using the methods of Marsaglia et al. (2013). We generated percent estimates for multiple lithogenic, biogenic, and authigenic components in each sample by viewing at least three areas of the slide. Smear slides were made from all sediment types recovered, with a focus on the major lithologies in each core. Most samples were taken from unconsolidated sediments with some more indurated sediments (chalk) from the deeper cores of Site U1443. Smear slide descriptions were performed mainly by only two operators during the expedition (one per shift), except for U1443, the first site drilled during IODP Expedition 353, which had three describers. Since each operator brings their own set of biases in estimation, this allowed for enhanced consistency by limiting the total number of biases affecting the descriptions. We each described the same set of example slides available on the *JOIDES Resolution* during the initial transit to "calibrate" our descriptions. These example slides with varying clay and carbonate composition (Marsaglia et al., 2013) were especially helpful for making consistent clay mineral percent estimates. We made clay size fraction estimates ($< 4\,\mu m$) under $60\times$ magnification and made estimates of clay mineral abundance based on the darkness/lightness of this fraction, calibrated by the training slide set. During coring operations and actual sample descriptions, each of us described one or two overlapping slides at the start of some shifts to maintain consistency. We observed approximately one to three smear slides per core in each hole under plane and cross-polarized light (Fig. 3), capturing primarily the major lithology, with some smear slides targeting minor lithologies (e.g., ash layers, turbidites). In the IODP Expedition 353 Proceedings report, we presented smear slide data in figures only as abundance categories (Clemens et al., 2016b, c, d).

To characterize the utility of our smear slide estimates, we sum the total carbonate components (foraminifers, calcareous nannofossils, shell fragments, and authigenic carbonates) in major lithologies and compare them to the calcium carbonate ($CaCO_3$) content measured by coulometry in Hole A at Sites U1443, U1446, and U1448. Coulometry is a quantitative method for determining carbonate content (Engleman et al., 1985; Pimmel and Claypool, 2001). Total inorganic carbon was measured onboard the *JOIDES Resolution* on freeze-dried and powdered sediment samples using a UIC 5011 CO_2 coulometer to a precision of $\pm 1\,\%$ (Clemens et al., 2016e). One to three samples per core (approximately every 2 m) in Hole A of each site were measured for $CaCO_3$ (see Clemens et al., 2016a, b, c). $CaCO_3$ measurements were not performed on the same subsamples as smear slides, but these measurements capture major downcore trends at a similar resolution. We compare only the major lithology from smear slides and, given the consistent color and gradational change observed in these cores, these comparisons are appropriate for broad downcore trends in composition. Color banding, laminations, or turbidites were rare at these sites, and these minor occurrences are not compared here.

We also compare trends in the clay-mineral fraction and the total lithogenic fraction (clay mineral, mica, quartz, feldspars, lithic grains, vitric grains, glauconite, heavy minerals, and iron oxides) observed from smear slides to the natural gamma radiation (NGR) measured by whole round core logging. Each core section was scanned by a NGR logger consisting of eight sodium iodide detectors behind a lead shield, measured at a resolution of 20 cm and integrated over a core length of 40 cm, with an accuracy of $\pm 1.5\,\%$ (Vasiliev et al., 2011). Toothpick samples collected for smear slides were collected within this integration length. In hemipelagic sediments, NGR is sourced from radioactive decay of potassium (^{40}K), uranium (^{238}U), and thorium (^{232}Th) isotopes within the sediments. K is a major element within clay minerals, glauconite, and feldspars, while Th is present in clay

minerals and monazite. U can be present in marine sediments absorbed to clays and organic matter as well as present in phosphate and some silicate minerals. Works by Dunlea et al. (2013) and De Vleeschouwer et al. (2017) have produced accurate calculations of K, U, and Th content based on NGR energy spectra measured onboard the *JOIDES Resolution*, including IODP Expedition 353 cores (De Vleeschouwer, 2017).

The overall goal of these comparisons is to determine how well smear slide estimates track with the quantitative geochemical and physical property measurements and so to give confidence in the use of smear slide data in determining the detailed composition of the sediment. All data presented vs. depth use the meter CSF-A scale (core depth in meters below the seafloor with no correction for core expansion) (Integrated Ocean Drilling Program Depth Scale Task Force, 2011).

4 Results and discussion

4.1 Trends in smear slide and quantitative compositions

Overall, at each site we observe a similar pattern in the downcore patterns in the total carbonate components estimated by smear slide observation and $CaCO_3$ % measured by coulometer, with varying differences in actual percent (Figs. 4, 5, and 6). We also observe downcore trends in smear slide clay fraction estimates that follow the downcore trends in NGR, which is primarily controlled by the lithogenic content, primarily clay minerals, in the cores. There are subtle shifts in smear slide estimates apparent at each site associated with different observers.

4.1.1 Ninetyeast Ridge

Site U1443 along Ninetyeast Ridge (Fig. 2) was described as nannofossil ooze/chalk with variable clay and foraminifer content and common volcanic ash beds (Clemens et al., 2016b). In smear slides from Hole U1443A, we observe increasing total carbonate and decreasing clay/lithogenic minerals with depth over the upper 150 m CSF-A and then decreasing total carbonate and increasing clay minerals from 250 to 350 m CSF-A (Fig. 4). Clay/lithogenic content follows a pattern inverse to carbonate and generally corresponds to the trend in NGR (Fig. 4). Total lithogenic content ranges from 5 % to 41 %, dominated by the clay fraction. We see a very similar trend in $CaCO_3$ from coulometry and a match to within < 15 % between the two measurements for most of the record. A pronounced decrease in $CaCO_3$ observed in smear slides between 110 and 140 m CSF-A matches the observed Miocene crash in carbonate deposition observed between 13.5 and 8.2 Ma based on XRF records at Site U1443 (Lübbers et al., 2019). We observe a deviation in the smear slide trends and an underestimate of carbonate content (with a corresponding overestimate of clay) below 250 m CSF-A, corresponding to an interval containing high authigenic carbonate and the presence of glauconite. The presence of glauconite and the overall increased lithification of this interval likely prevented full disaggregation of the sediment, and these clumps would impact the accuracy of the clay fraction estimates. The re-precipitation of calcite as authigenic carbonate and coloration from glauconite may have made the determination of clay content more difficult (see Sect. 4.2). These higher carbonate estimates also correspond to our third observer.

4.1.2 Mahanadi Basin

Site U1446 was described as a nannofossil to foraminifer-bearing to foraminifer-rich clay (Clemens et al., 2016c). Based on smear slide observations, variable and cyclic carbonate and clay fraction abundances were observed at Site U1446 with clay ranging from ~ 35 % to 85 % and carbonate minerals ranging from ~ 5 % to 45 % (Fig. 5). Clay is the dominant lithogenic mineral, with less than 13 % other lithogenic minerals. $CaCO_3$ measured by coulometry follows a similar cyclic pattern with a lower range (~ 1 % to 30 % in major lithology). Although the magnitude of the variation in $CaCO_3$ is larger in the smear slide estimates, smear slides capture the same peaks and troughs in $CaCO_3$ abundance. This comparison suggests that smear slide estimates can capture the variation in $CaCO_3$ accumulation due to stratification-driven productivity changes associated with glacial–interglacial cycles in the Bay of Bengal (Phillips et al., 2014a; da Silva et al., 2017; Ota et al., 2019). Similarly, the clay content follows similar trends in NGR, capturing the cyclic variation in relative clay and carbonate content (relative input of terrigenous sediments and biological production) at this site (Fig. 5).

4.1.3 Andaman accretionary wedge

At Site U1448, carbonate content estimates by smear slide and coulometer follow similar trends, although in some intervals there was significant overestimation of absolute carbonate content in the smear slide estimates (e.g., 30 % vs. 50 % $CaCO_3$; Fig. 6). Both the smear slide estimates and coulometer measurements show a declining trend with depth over the upper 180 m CSF-A followed by an increase between ~ 180 and 280 m CSF-A. Both approaches capture the decrease in $CaCO_3$ content that occurs below a hiatus at 379 m CSF-A where the lithology transitions from nannofossil-rich clay to clayey bio-siliceous ooze (Clemens et al., 2016d). Clay mineral content from smear slides follows the trend observed in NGR with minor deviations. The clay content estimates capture the broad maximum in NGR at ~ 200 m CSF-A and the sharp decrease below the hiatus at 379 m CSF-A with the transition to clayey bio-siliceous ooze (Fig. 6).

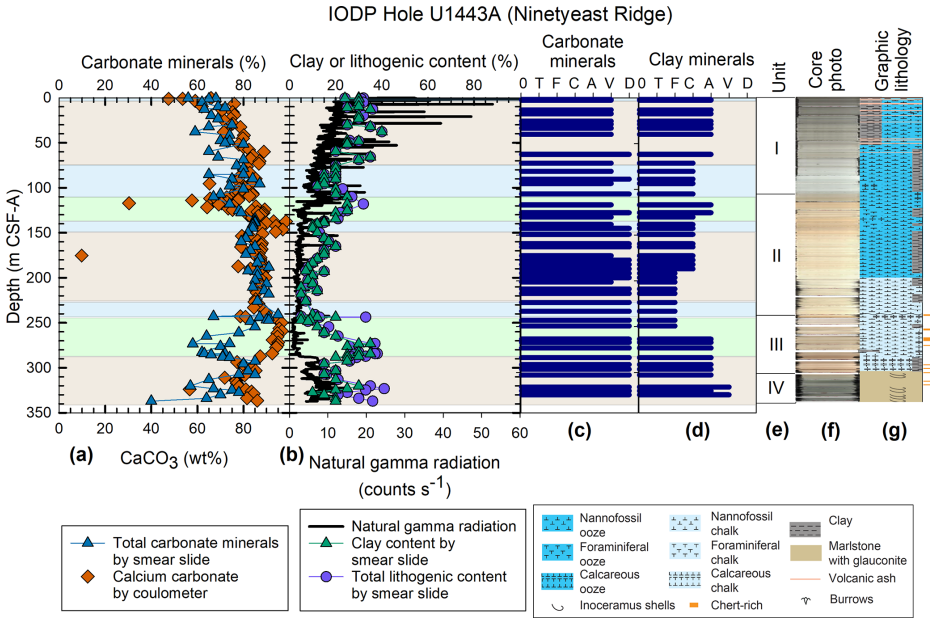

Figure 4. Downcore data from Site U1443. **(a)** Comparison of carbonate mineral percentages estimated from smear slides (blue triangles for major lithology to $CaCO_3$ measured by carbonate coulometer – orange diamonds). **(b)** Comparison of the clay fraction (green triangles) and total lithogenic fraction (purple circles) estimated from smear slides to natural gamma radiation measured by whole round core scanning (black line). The colored zones indicate the smear slide estimates from three observers. Panels **(c)** and **(d)** are the abundance categories of total carbonate minerals and total clay minerals, where 0 is none, T is trace (< 1 %), F is few (1 % to 9 %), C is common (10 % to 24 %), A is abundant (25 % to 40 %), V is very abundant (41 % to 74 %), and D is dominant (> 75 %) as presented in the IODP 353 Proceedings. **(e)** Lithostratigraphic units from visual core description. I: clayey nannofossil ooze with foraminifers, II: nannofossil ooze/chalk with clay and foraminifers, III: clayey calcareous/nannofossil chalk with foraminifers and authigenic carbonate, and IV: marlstone with glauconite (Clemens et al., 2016b). **(f)** Core photo composite. **(g)** Lithologic column.

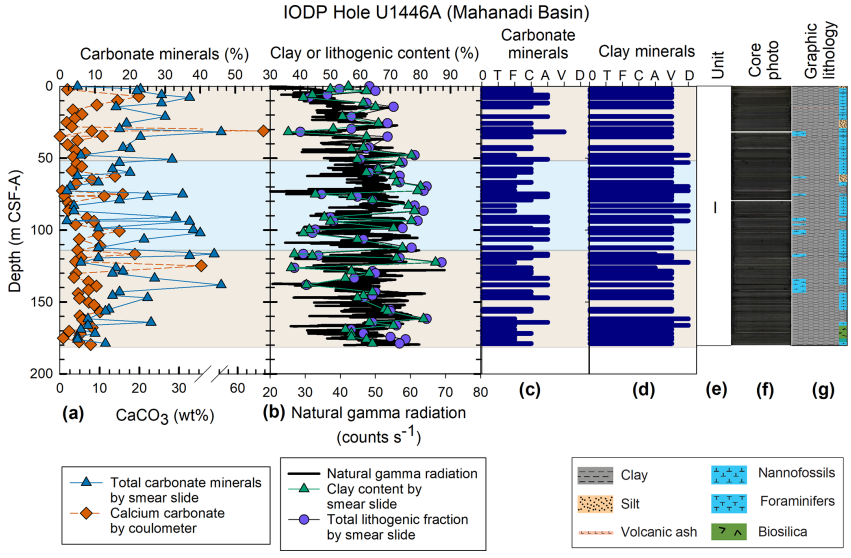

Figure 5. Downcore data from Site U1446. **(a)** Comparison of carbonate mineral percentages estimated from smear slides (blue triangles) taken from within the major lithologies to $CaCO_3$ measured by carbonate coulometer (orange diamonds). **(b)** Comparison of the clay fraction (green triangles) and total lithogenic fraction (purple circles) estimated from smear slides to natural gamma radiation measured by whole round core scanning (black line). The colored zones indicate the smear slide estimates from two observers. The colored zones indicate the smear slide estimates from two observers. Panels **(c)** and **(d)** are the abundance categories of total carbonate minerals and total clay minerals, where 0 is none, T is trace (< 1 %), F is few (1 % to 9 %), C is common (10 % to 24 %), A is abundant (25 % to 40 %), V is very abundant (41 % to 74 %), and D is dominant (> 75 %) as presented in the IODP 353 Proceedings. **(e)** Lithostratigraphic units from visual core description. Unit I is clay with nannofossils, foraminifers, and biosilica. **(f)** Core photo composite. **(g)** Lithologic column.

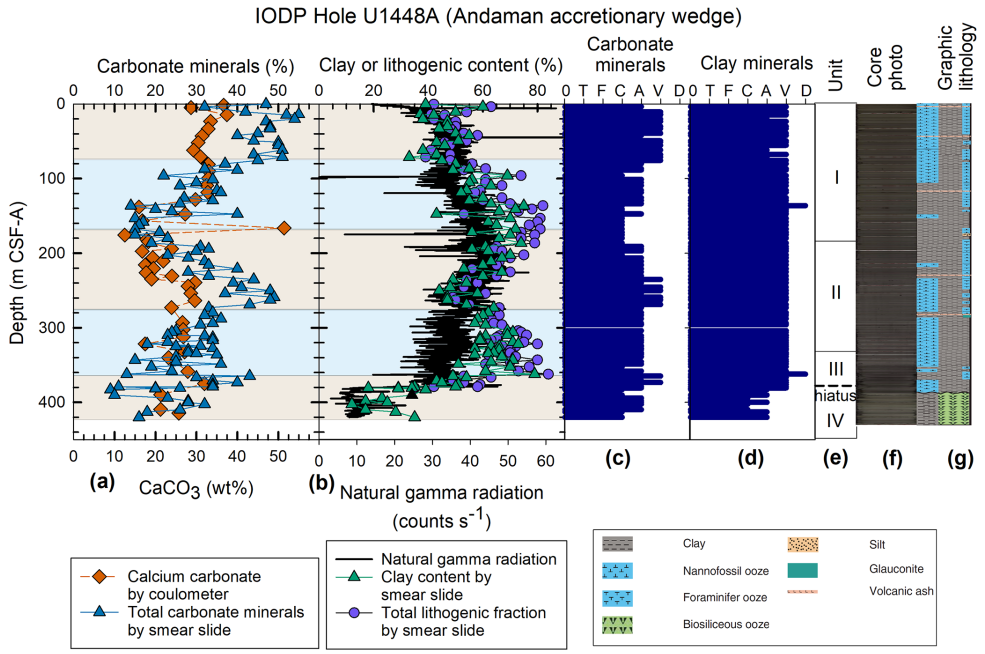

Figure 6. Downcore data from Site U1448. **(a)** Comparison of carbonate mineral percentages estimated from smear slides (blue triangles) for the major lithologies to $CaCO_3$ measured by carbonate coulometer (orange diamonds). **(b)** Comparison of the clay fraction (green triangles) and total lithogenic fraction (purple circles) estimated from smear slides to natural gamma radiation measured by whole round core scanning (black line). The colored zones indicate the smear slide estimates from two observers; panels **(c)** and **(d)** are the abundance categories of total carbonate minerals and total clay minerals, where 0 is none, T is trace (< 1 %), F is few (1 % to 9 %), C is common (10 % to 24 %), A is abundant (25 % to 40 %), V is very abundant (41 % to 74 %), and D is dominant (> 75 %) as presented in the IODP 353 Proceedings. **(e)** Lithostratigraphic units from visual core description. I: nannofossil-rich clay with foraminifers, II: clay with foraminifers, nannofossils, and silt, III: nannofossil-rich clay with foraminifers, and IV: clayey bio-siliceous ooze with nannofossils. There is an ~ 8 Myr hiatus between Units III and IV. **(f)** Core photo composite. **(g)** Lithologic column.

4.2 Correlations with NGR

To better understand the relationship between lithology and NGR, we used cross plots of NGR vs. smear slide clay mineral and total lithogenic mineral abundance with linear regression (Fig. 7a–c). Because the NGR was measured at a relatively high resolution (20 cm) and sediment color is relatively homogenous on the scale of tens of centimeters within the major lithology (see core photos, Munsell soil color, and spectrophotometry results in Clemens et al., 2016b, c, d), it is reasonable to compare to smear slides (discrete toothpick samples) directly. While the similarity in the trends is apparent from the downcore plots (Figs. 4, 5, and 6), the cross plots highlight the large variation in the clay mineral and total lithogenic fraction estimates. For a given NGR value, the clay values can vary by up to ±25 % with an average absolute value of the residual of 8 % (Fig. 7d–f). These relationships show that in sediments with a wide range in clay mineral content (e.g., those with significant microfossil or silt/sand fractions), smear slide estimates can show downcore trends consistent with NGR measurements with a higher goodness of fit, despite the wide range in uncertainty in estimating clay by smear slide.

At these IODP Expedition 353 sites, downcore trends in bulk NGR are largely similar to the trends in the interpreted K, U, and Th (with the exception of U at IODP Site U1448) (Fig. 8). In these hemipelagic sediments, NGR and each of the radiogenic components appear to be representing the relative mixing of lithogenic grains (primarily clay) with biogenic carbonate grains (minimal NGR). Overall, the weak but noticeable correlation of smear slide estimates with NGR gives confidence in the utility of using smear slide estimates for clay and other lithogenic component content to provide general trends in composition in sediments with varying terrigenous and biogenic composition.

4.3 Underestimation of clay content and overestimation of carbonate

Except for Site U1443, we see a consistent overestimation of carbonate content in smear slide estimates across multiple sites in the Bay of Bengal and Andaman Sea, based on the downcore trends and the average $CaCO_3$ % values from coulometer and carbonate content by smear slides at each site (Fig. 9). We observe this consistent overestimation in carbonate at Sites U1446 and U1448 and also expand this com-

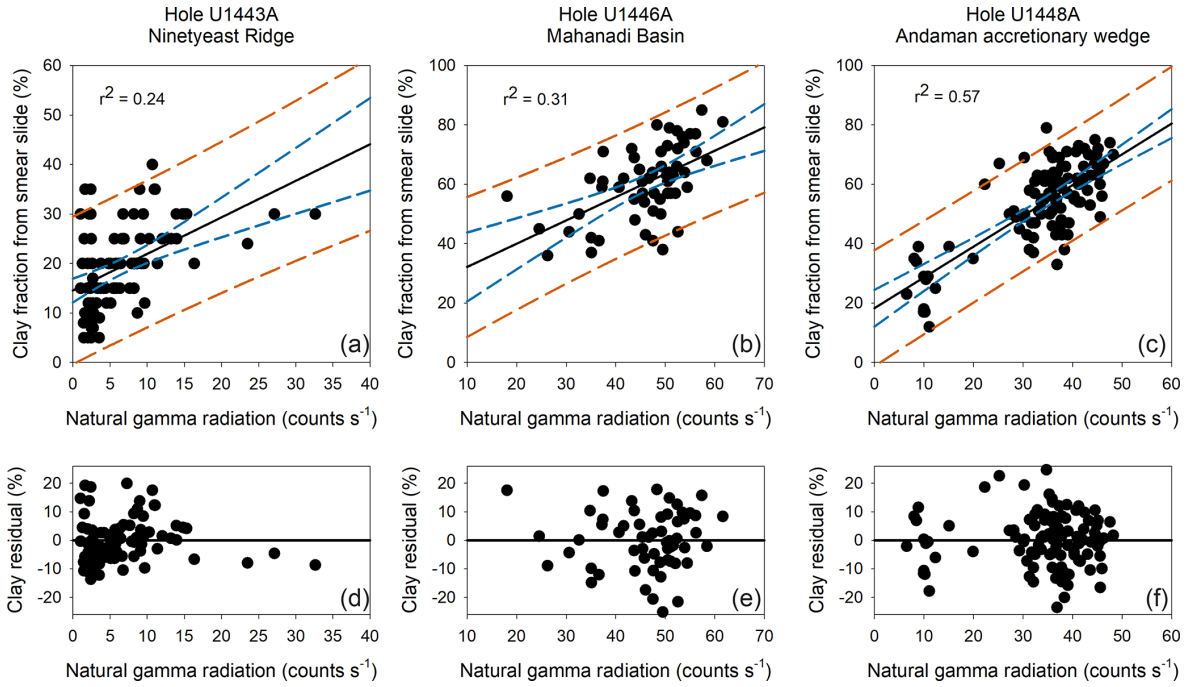

Figure 7. Cross plots of natural gamma radiation vs. estimates of clay minerals from smear slide, where the measurements are within 5 cm of each other in the core. **(a)** IODP Site U1443, **(b)** IODP Site U1446, and **(c)** IODP Site U1448. Grey solid lines are best-fit linear regression, teal dashed lines are 95 % confidence intervals, and red dashed lines are 95 % prediction intervals. Panels **(d)**, **(e)**, and **(f)** show the residuals around the best-fit line for Sites U1443, U1446, and U1448, respectively.

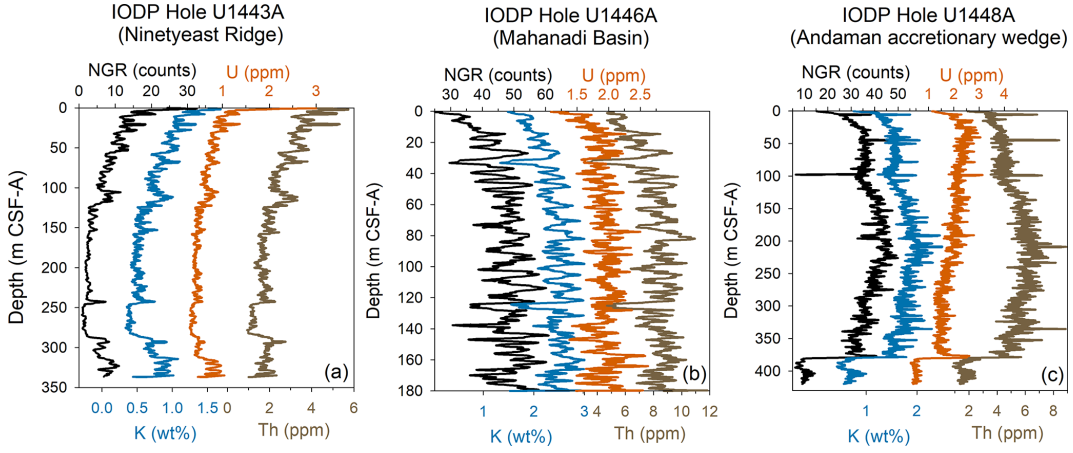

Figure 8. Downcore plots of natural gamma radiation (NGR) and K, U, and Th contents based on NGR spectra (De Vleeschouwer, 2017) from IODP Holes **(a)** U1443A, **(b)** U1446A, and **(c)** U1448A.

parison to other IODP 353 sites as well as sites from Indian National Gas Hydrate Program 01 (NGHP-01) (Collett et al., 2015; Johnson et al., 2014). Although the coulometer and smear slide samples were not collected from the exact same depths, the similar downcore trends suggest that there is no consistent bias due to sampling and that the largely homogeneous lithologies on centimeter/decimeter scales at each core mean exact sample matching is not essential. We also observe a similar overestimation in smear slide carbonate compared to $CaCO_3$ measured by coulometer/elemental analysis at other sites within the Andaman accretionary wedge (IODP Site U1447 and NGHP-01 Site 17) (Clemens et al., 2016f; Collett et al., 2015; Johnson et al., 2014) (Fig. 9). Other Mahanadi Basin sites, IODP Site U1445 and NGHP01 Site 19, similarly show an overestimation in carbonate minerals from smear slides (Clemens et al., 2016g; Collett et al., 2015; Johnson et al., 2014). Although we are comparing percent area estimates to weight percent estimates, the density of

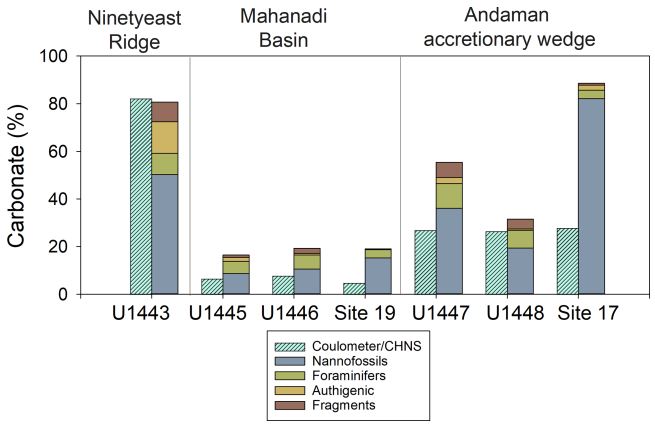

Figure 9. Comparison of total carbonate minerals (nannofossils, foraminifers, authigenic, shell fragments) by smear slide estimation to average $CaCO_3$ measured by carbonate coulometry for **(a)** IODP Expedition 353 (Clemens et al., 2016b, c, d, f, g) and NGHP Expedition 01 (Collett et al., 2015; Johnson et al., 2014).

calcite (2.7102 g cm^{-3}) (DeFoe and Compton, 1925) is close to the grain densities at IODP 353 sites (average grain density at each site ranges from 2.716 to 2.756 g cm^{-3}) (Clemens et al., 2016b, c, d). The uncertainties in the smear slide percent estimates are much greater than the difference in making volume percent (smear slide) to weight percent (coulometer or CHNS) comparisons.

The fine fraction appeared lighter in the Mahanadi Basin and, to an even greater extent, Andaman Sea sites (Fig. 10). Based on our calibration based on training slides and Site U1443 samples, this appeared as an apparent underestimation of the clay fraction. We suggest that the discrepancy between sites is driven by differences in sediment color and/or differences in clay mineral properties between these locations. Although visually estimating the abundance of distinct mineral grains can be relatively accurate and repeatable (Allen, 1956; Griffiths and Rosenfeld, 1954), estimation of clay mineral or size fraction content is generally more difficult due to grain sizes that are too small to be identified individually. Thus, clay mineral percent estimates are made from observation of a diffuse background (grains unable to be individually focused) or from aggregates (e.g., clumps of formation unable to be disaggregated, fecal pellets), which are strongly influenced by the material color. We hypothesize that it is more difficult to estimate the clay content based on the varying fine-grained organic matter, iron oxides, and iron sulfide content within marine sediments that can create a wide range in color of the clay-sized fraction (Marsaglia et al., 2013, 2015). We calibrated our estimations under 60× magnification based on training smear slides of known clay mineral and carbonate content (Marsaglia et al., 2013); however, in our IODP 353 sites we applied these approximations to sediments from different locations in the northern Indian Ocean that may have different pigmentation properties when observed under the microscope.

Each of the three sites we discuss have distinctly different sediment colors on the macro scale based on reflection scanning colorimetry (Figs. 10 and 11). Between Ninetyeast Ridge, the Mahanadi Basin, and the Andaman Sea, sediment lightness (L* from color reflectance scanning) generally increases with $CaCO_3$ content and decreases with total organic carbon content (Fig. 11) (see Clemens et al., 2016b, c, d), which is similar to observations from other ocean drilling expeditions (e.g., Blum, 1997; Expedition 320/321 Scientists, 2010; Shipboard Scientific Party, 1996b; 2001). Similarly, L* increases with total carbonate minerals estimated from smear slides (Fig. 11), which also makes sense given that the relative darkness/lightness of the clay-sized material in the smear slides was a major factor in estimating clay mineral content. In addition to L*, there are differences in red to green (a*) and blue to yellow (b*) ranges between sites that may represent color variations driven by compositional factors other than carbonate content. Between sites and within individual sites, variation in organic matter, iron oxides, etc., can vary downcore, which can lead to shifts in the clay estimations (see Fig. 3f). The presence of larger grains and aggregates may also influence the clay estimates by making it difficult to focus on the fine-grained fraction. In addition, the high birefringence of silt and sand-sized calcite (which is likely underrepresented on the smear slide due to its size) under cross-polarized light makes these grains easy to see and may draw the eye of observers preferentially to these grains relative to the darker and more dispersed clay. However, the nannofossil component is clearly driving the overestimation of carbonate at Expedition 353 sites (Fig. 9), even though these smaller microfossils have lower birefringence than the larger microfossils and calcareous fragments.

This overestimation in carbonate content is highest in the Andaman Sea, especially at Site U1447 and NGHP-01 Site 17 (Fig. 9). IODP Site U1447 and NGHP-01 Site 17 in the Andaman accretionary wedge are rich in smectite-group clays (14 % to 83 % smectite, 19 % to 47 % illite of the < 2 µm fraction) (Lee et al., 2020; Phillips et al., 2014b). In contrast, IODP Sites U1445 and U1446 in the Mahanadi Basin are located near NGHP-01 Sites 18 and 19, which are more illite-rich (9 % to 28 % smectite, 29 % to 54 % illite of the < 2 µm fraction) (Phillips et al., 2014b). Because of the expanding nature of smectite-group clays and smaller grain size, smectite-group clays may disperse in water differently than other common clay minerals (i.e., illite, kaolinite, chlorite) (Gibbs, 1977; Thomas and Murray, 1989) during smear slide preparation and may be more prone to underestimation. Segregation of montmorillonite due to settling and flocculation during slide preparation has been observed to cause underestimation (by up to 250 %) of montmorillonite during X-ray diffraction analyses (Gibbs, 1965; Stokke and Carson, 1973). Due to its smaller size, montmorillonite has a settling velocity $\sim 100\times$ slower than illite or kaolinite (Gibbs, 1965),

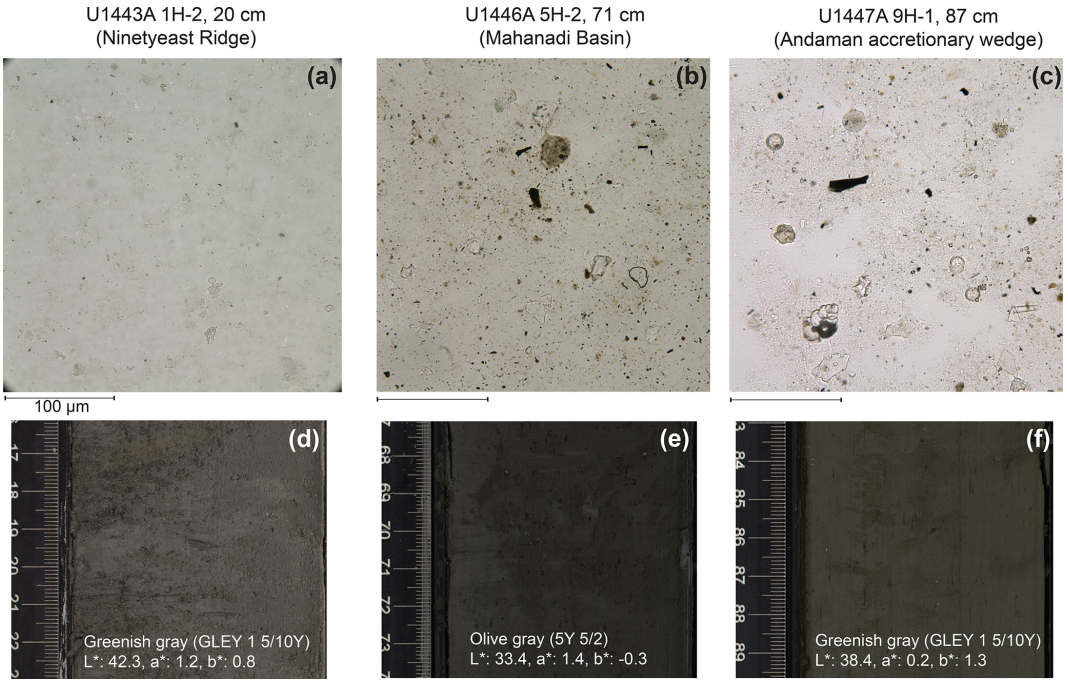

Figure 10. Smear slides from IODP Sites U1443 **(a)**, U1446 **(b)**, and U1447 **(c)** under plane-polarized light. Slides from Andaman Sea sites generally appeared lighter and more dominated by carbonate minerals compared to Mahanadi Basin sites. There are slight differences in sediment color, including Munsell soil color, lightness (L*), and hue-chroma coordinates (a* and b*) **(d, e, f)**. Data from Clemens et al. (2016b, c, d).

which may cause smectite-group clay minerals to accumulate at the top and edges of the slide during preparation (Stokke and Carson, 1973), making it appear less abundant under the microscope.

We suggest that smear slide estimation alone may overestimate the carbonate content and cause a misclassification of calcareous-rich clays as calcareous oozes. Integration of $CaCO_3$ measurements by coulometry or elemental analysis may provide a more robust sediment classification in carbonate-rich clay sediments, especially on expeditions with shipboard geochemical measurement of $CaCO_3$ alongside lithostratigraphic description, such as is standard on IODP expeditions. In particular, Marsaglia et al. (2013, 2015) suggest collecting smear slide and $CaCO_3$ samples from the same depths and using these to calibrate the smear slide estimates during shipboard operations. For example, ODP Legs 154 and 162 calibrated smear slide estimates using coulometer and sediment color data (Shipboard Scientific Party, 1995b, 1996c). This approach allows for a close match between reported smear slide and coulometer percentages, such as those observed during IODP Expedition 361 (Hall et al., 2017).

During IODP Expedition 353, we did not make these corrections to smear slide estimates in real time but did use $CaCO_3$ to refine the sediment names, similarly to what was done on IODP Expedition 339 and ODP Leg 107 (Expedition 339 Scientists, 2013b; Shipboard Scientific Party, 1987). On IODP Expedition 353, core recovery was high (4.2 km of core; 1165 smear slides) and %$CaCO_3$ data often lagged sediment descriptions by 1–2 d. This time constraint did not allow for re-describing or calibrating slides after initial description. Our carbonate mineral estimates from smear slides would be improved with calibration with coulometer $CaCO_3$ measurements at each basin to avoid the overestimation described above. We recommend that expedition scientists plan core flow at the start of the expedition to coordinate core description and coulometer measurements, depending on expedition-specific objectives and core recovery.

5 Summary and conclusions

Overall, we show that the trends in percentage estimates from smear slide descriptions broadly match those from geochemical ($CaCO_3$ %) and physical properties (NGR) at IODP 353 sites. Underestimation of the clay fraction and overestimation of the carbonate abundance appear to be the biggest sources of error in these trends and sometimes misclassification of the sediment. We suggest that where possible lithostratigraphic description incorporate quantitative measurements of $CaCO_3$ abundance when classifying sediment types and to calibrate percentages of calcareous components under smear slides as described by Marsaglia et al. (2013, 2015). This comparison may require creative planning for the

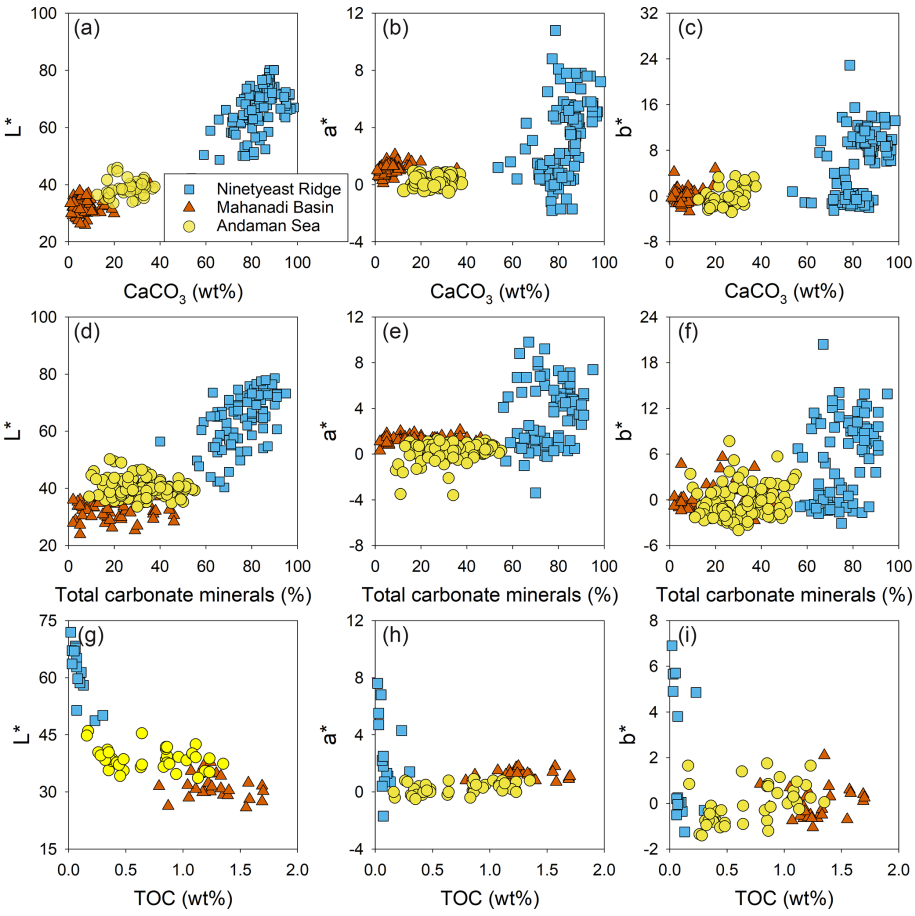

Figure 11. Average sediment lightness (L*) and chromaticity variables (a* and b*) vs. average $CaCO_3$ % **(a–c)**, smear slide total carbonate minerals **(d–f)** and total organic carbon (TOC) % **(g–i)** from IODP Expedition 353 sites: Ninetyeast Ridge, I. (blue squares) IODP Site U1443, Andaman Sea (IODP Site U1448), and Mahanadi Basin (purple circles) IODP Site U1446. Data from Clemens et al. (2016b, c, d).

flow and timing of smear slide sampling and description, especially on high-recovery palaeoceanographic expeditions.

The similarity between downhole trends in smear slide estimates and measured $CaCO_3$ and NGR values gives confidence that microscopic descriptions can be used to track major variation or cyclicity in marine sediments. Our smear slide estimates are consistent with major paleoenvironmental/palaeoceanographic changes characterized by quantitative approaches. We suggest that scientists on future scientific drilling expeditions can gain early insight into sediment variations related to expedition missions by plotting smear slide percent estimates rather than just lithologic units or abundance categories. We are not advocating that smear slides can replace the more quantitative analyses but that these smear slide abundances can provide critical and complementary information on specific sedimentary grain types. While we focused on comparisons between smear slide observations and quantitative measurements, these comparisons give confidence in the smear slide technique to characterize trends in a variety of mineral and microfossil abundances, many of which are not easily quantified through other analyses.

IODP expeditions have archived tables of smear slide percent estimates available in the proceedings, many of which have not been interpreted in terms of downcore trends. These data sets examined in detail may be useful for providing new interpretations or pilot data to guide new analyses of archived cores. Visual estimation has long been an effective technique for characterizing sediments, and smear slide analysts can have confidence in the utility of their estimations to track trends in major lithology, even if the absolute values are somewhat inaccurate. The capability of smear slide petrography to capture these trends can be enhanced by cross-calibration at shift cross-overs, using training slide sets and limiting the number of smear slide observers during an expedition, which reduces the effect of observer bias.

Data availability. All primary data in this paper (smear slide estimates, coulometer $CaCO_3$, NGR, and photomicrographs) generated during shipboard operations of IODP Expedition 353 are

available online as part of the IODP LIMS Online Report Portal: https://web.iodp.tamu.edu/LORE/ (International Ocean Discovery Program JOIDES Resolution Science Operator, 2021). K, U, and Th contents quantified from NGR spectra are available in the EarthChem data library (https://doi.org/10.1594/IEDA/100668, De Vleeschouwer, 2017).

Sample availability. All IODP Expedition 353 cores, including sites U1443, U1446, and U1448, are archived at the IODP repository at the Kochi Core Center (http://www.kochi-core.jp/en/iodp-curation/index.html, last access: 6 December 2021).

Author contributions. KL and SCP contributed equally to conceptualization, investigation, formal analysis, and visualization. SCP prepared the original draft, and KL contributed significantly to review and editing.

Competing interests. The contact author has declared that neither they nor their co-author have any competing interests.

Disclaimer. Any use of trade, firm, or product name is for descriptive purposes only and does not imply endorsement by the US government.

Publisher's note: Copernicus Publications remains neutral with regard to jurisdictional claims in published maps and institutional affiliations.

Acknowledgements. We thank the shipboard scientific party from IODP Expedition 353 as well as the captain, crew, and technical staff of the *JOIDES Resolution* for the initial processing and analysis of cores. We thank Sunghan Kim for contributing to smear slide analysis at Site U1443. We thank reviewers Kathleen Marsaglia and Kitty Milliken for the very constructive comments that greatly improved this paper. We also thank Marci Robinson for additional helpful comments that improved this paper.

Review statement. This paper was edited by Tomoaki Morishita and reviewed by Kathleen Marsaglia and Kitty Milliken.

References

Allen, J. A.: Estimation of percentages in thin sections; considerations of visual psychology, J. Sediment. Res., 26, 160–161, https://doi.org/10.1306/74D704F7-2B21-11D7-8648000102C1865D, 1956.

Barnet, J. S. K., Harper, D. T., LeVay, L. J., Edgar, K. M., Henehan, M. J., Babila, T. L., Ullmann, C. V., Leng, M. J., Kroon, D., Zachos, J. C., and Littler, K.: Coupled evolution of temperature and carbonate chemistry during the Paleocene–Eocene; new trace element records from the low latitude Indian Ocean, Earth Planet. Sc. Lett., 545, 116414, https://doi.org/10.1016/j.epsl.2020.116414, 2020.

Blum, P.: Physical properties handbook: a guide to the shipboard measurement of physical properties of deep-sea cores, ODP Tech. Note, 26, https://doi.org/10.2973/odp.tn.26.1997, 1997.

Carozzi, A. V.: Carbonate rock depositional models: A microfacies approach, Prentice Hall, Hoboken, New Jersey, USA, 604 pp., 1988.

Carozzi, A. V.: Sedimentary Petrography, Prentice Hall, Englewood Cliffs, USA, 263 pp., 1993.

Clemens, S. C., Kuhnt, W., LeVay, L. J., Anand, P., Ando, T., Bartol, M., Bolton, C. T., Ding, X., Gariboldi, K., Giosan, L., Hathorne, E. C., Huang, Y., Jaiswal, P., Kim, S., Kirkpatrick, J. B., Littler, K., Marino, G., Martinez, P., Naik, D., Peketi, A., Phillips, S. C., Robinson, M. M., Romero, O. E., Sagar, N., Taladay, K. B., Taylor, S. N., Thirumalai, K., Uramoto, G., Usui, Y., Wang, J., Yamamoto, M., and Zhou, L.: Expedition 353 summary, in: Indian Monsoon Rainfall, edited by: Clemens, S. C., Kuhnt, W., LeVay, L. J., and the Expedition 353 Scientists, Proceedings of the International Ocean Discovery Program, International Ocean Discovery Program, College Station, TX, USA, 353, https://doi.org/10.14379/iodp.proc.353.101.2016, 2016a.

Clemens, S. C., Kuhnt, W., LeVay, L. J., Anand, P., Ando, T., Bartol, M., Bolton, C. T., Ding, X., Gariboldi, K., Giosan, L., Hathorne, E. C., Huang, Y., Jaiswal, P., Kim, S., Kirkpatrick, J. B., Littler, K., Marino, G., Martinez, P., Naik, D., Peketi, A., Phillips, S. C., Robinson, M. M., Romero, O. E., Sagar, N., Taladay, K. B., Taylor, S. N., Thirumalai, K., Uramoto, G., Usui, Y., Wang, J., Yamamoto, M., and Zhou, L.: Site U1443, in: Indian Monsoon Rainfall, edited by: Clemens, S. C., Kuhnt, W., LeVay, L. J., and the Expedition 353 Scientists, Proceedings of the International Ocean Discovery Program, International Ocean Discovery Program, College Station, TX, USA, 353, https://doi.org/10.14379/iodp.proc.353.103.2016, 2016b.

Clemens, S. C., Kuhnt, W., LeVay, L. J., Anand, P., Ando, T., Bartol, M., Bolton, C. T., Ding, X., Gariboldi, K., Giosan, L., Hathorne, E. C., Huang, Y., Jaiswal, P., Kim, S., Kirkpatrick, J. B., Littler, K., Marino, G., Martinez, P., Naik, D., Peketi, A., Phillips, S. C., Robinson, M. M., Romero, O. E., Sagar, N., Taladay, K. B., Taylor, S. N., Thirumalai, K., Uramoto, G., Usui, Y., Wang, J., Yamamoto, M., and Zhou, L.: Site U1446, in: Indian Monsoon Rainfall, edited by: Clemens, S. C., Kuhnt, W., LeVay, L. J., and the Expedition 353 Scientists, Proceedings of the International Ocean Discovery Program, International Ocean Discovery Program, College Station, TX, USA, 353, https://doi.org/10.14379/iodp.proc.353.106.2016, 2016c.

Clemens, S.C., Kuhnt, W., LeVay, L.J., Anand, P., Ando, T., Bartol, M., Bolton, C.T., Ding, X., Gariboldi, K., Giosan, L., Hathorne, E.C., Huang, Y., Jaiswal, P., Kim, S., Kirkpatrick, J.B., Littler, K., Marino, G., Martinez, P., Naik, D., Peketi, A., Phillips, S.C., Robinson, M.M., Romero, O.E., Sagar, N., Taladay, K.B., Taylor, S.N., Thirumalai, K., Uramoto, G., Usui, Y., Wang, J., Yamamoto, M., and Zhou, L.: Site U1448, in: Indian Monsoon Rainfall, edited by: Clemens, S. C., Kuhnt, W., LeVay, L. J., and the Expedition 353 Scientists, Proceedings of the International Ocean Discovery Program, International Ocean Discovery Program, College Station, TX, USA, 353, https://doi.org/10.14379/iodp.proc.353.108.2016, 2016d.

Clemens, S. C., Kuhnt, W., LeVay, L. J., Anand, P., Ando, T., Bartol, M., Bolton, C. T., Ding, X., Gariboldi, K., Giosan, L., Hathorne, E. C., Huang, Y., Jaiswal, P., Kim, S., Kirkpatrick, J. B., Littler, K., Marino, G., Martinez, P., Naik, D., Peketi, A., Phillips, S. C., Robinson, M. M., Romero, O. E., Sagar, N., Taladay, K. B., Taylor, S. N., Thirumalai, K., Uramoto, G., Usui, Y., Wang, J., Yamamoto, M., and Zhou, L.: Expedition 353 methods, in: Indian Monsoon Rainfall, edited by: Clemens, S. C., Kuhnt, W., LeVay, L. J., and the Expedition 353 Scientists, Proceedings of the International Ocean Discovery Program, International Ocean Discovery Program, College Station, TX, USA, 353, https://doi.org/10.14379/iodp.proc.353.102.2016, 2016e.

Clemens, S. C., Kuhnt, W., LeVay, L. J., Anand, P., Ando, T., Bartol, M., Bolton, C. T., Ding, X., Gariboldi, K., Giosan, L., Hathorne, E. C., Huang, Y., Jaiswal, P., Kim, S., Kirkpatrick, J. B., Littler, K., Marino, G., Martinez, P., Naik, D., Peketi, A., Phillips, S. C., Robinson, M. M., Romero, O. E., Sagar, N., Taladay, K. B., Taylor, S. N., Thirumalai, K., Uramoto, G., Usui, Y., Wang, J., Yamamoto, M., and Zhou, L.: Site U1447, in: Indian Monsoon Rainfall, edited by: Clemens, S. C., Kuhnt, W., LeVay, L. J., and the Expedition 353 Scientists, Proceedings of the International Ocean Discovery Program, International Ocean Discovery Program, College Station, TX, USA, 353, https://doi.org/10.14379/iodp.proc.353.107.2016, 2016f.

Clemens, S. C., Kuhnt, W., LeVay, L. J., Anand, P., Ando, T., Bartol, M., Bolton, C. T., Ding, X., Gariboldi, K., Giosan, L., Hathorne, E. C., Huang, Y., Jaiswal, P., Kim, S., Kirkpatrick, J. B., Littler, K., Marino, G., Martinez, P., Naik, D., Peketi, A., Phillips, S. C., Robinson, M. M., Romero, O. E., Sagar, N., Taladay, K. B., Taylor, S. N., Thirumalai, K., Uramoto, G., Usui, Y., Wang, J., Yamamoto, M., and Zhou, L.: Site U1445, in: Indian Monsoon Rainfall, edited by: Clemens, S. C., Kuhnt, W., LeVay, L. J., and the Expedition 353 Scientists, Proceedings of the International Ocean Discovery Program, International Ocean Discovery Program, College Station, TX, USA, 353, https://doi.org/10.14379/iodp.proc.353.105.2016, 2016g.

Collett, T., Riedel, M., Cochran, J., Boswell, R., Presley, J., Kumar, P., Sathe, A., Sethi, A., Lall, M., and the NGHP Expedition Scientists: Indian National Gas Hydrate Program Expedition 01 report: U.S. Geological Survey Scientific Investigations Report 2012–5054, 1442 pp., https://doi.org/10.3133/sir20125054, 2015.

Croudace, I. W., Rindby, A., and Rothwell, R. G.: ITRAX: description and evaluation of a new multi-function X-ray core scanner, in: New Techniques in Sediment Core Analysis, edited by: Rothwell, R. G., Geological Society of London Special Publications, 267, 51–63, https://doi.org/10.1144/GSL.SP.2006.267.01.04, 2006.

Da Silva, R., Mazumdar, A., Mapder, T., Peketi, A., Joshi, R. K., Shaji, A., Mahalakshmi, P., Sawant, B., Naik, B. G., Carvalho, M. A., and Molletti, S. K: Salinity stratification controlled productivity variation over 300 ky in the Bay of Bengal, Sci. Rep., 7, 14439, https://doi.org/10.1038/s41598-017-14781-3, 2017.

Davies, T. A., Musich, L. F., and Woodbury, P. B.: Automated classification of deep-sea sediments, J. Sediment. Petrol., 47, 650–656, https://doi.org/10.1306/212F720C-2B24-11D7-8648000102C1865D, 1977.

Dean, W. E., Leinen, M., and Stow, D. W.: Classification of deep-sea, fine-grained sediments, J. Sediment. Petrol., 55, 250–256, https://doi.org/10.1306/212F868E-2B24-11D7-8648000102C1865D, 1985.

DeFoe, O. K. and Compton, A. H.: The density of rock salt and calcite, Phys. Rev., 25, 618–620, https://doi.org/10.1103/PhysRev.25.618, 1925.

De Vleeschouwer, D.: Natural Gamma Radiation-derived K, U and Th contents of marine sediments obtained during IODP Expeditions with DV JOIDES Resolution, Version 1.0, Interdisciplinary Earth Data Alliance (IEDA) [data set], https://doi.org/10.1594/IEDA/100668, 2017.

De Vleeschouwer, D., Dunlea, A. G., Auer, G., Anderson, C. H., Brumsack, H., de Loach, A., Gurnis, M. C., Huh, Y., Ishiwa, T., Jang, K., Kominz, M. A., März, C., Schnetger, B., Murray, R. W., Pälike, H., and Expedition 356 shipboard scientists: Quantifying K, U, and Th contents of marine sediments using shipboard natural gamma radiation spectra measured on DV JOIDES Resolution, Geochem. Geophy. Geosy., 18, 1053–1064, https://doi.org/10.1002/2016GC006715, 2017.

Drake, M. K., Aiello, I. W., and Ravelo, A. C.: New method for the quantitative analysis of smear slides in pelagic and hemi-pelagic sediments of the Bering Sea, American Geophysical Union, Fall Meeting 2014, 18 December 2014, San Francisco, California, USA, abstract PP43B-1460, 2014.

Dunlea, A. G., Murray, R. W., Harris, R. N., Vasiliev, M. A., Evans, H., Spivack, A. J., and D'Hondt, S.: Assessment and Use of NGR Instrumentation on the *JOIDES Resolution* to Quantify U, Th, and K Concentrations in Marine Sediment, Sci. Dril., 15, 57–63, https://doi.org/10.2204/iodp.sd.15.05.2013, 2013.

Engleman, E. E., Jackson, L. L., and Norton, D. R.: Determination of carbonate carbon in geological materials by coulometric titration, Chem. Geol., 53, 125–128, https://doi.org/10.1016/0009-2541(85)90025-7, 1985.

Expedition 320/321 Scientists: Site U1333, in: Proc. IODP, 320/321: Tokyo, edited by: Pälike, H., Lyle, M., Nishi, H., Raffi, I., Gamage, K., Klaus, A., and the Expedition 320/321 Scientists, Integrated Ocean Drilling Program Management International, Inc., https://doi.org/10.2204/iodp.proc.320321.105.2010, 2010.

Expedition 324 Scientists: Site U1346, in: Proc. IODP, 324: Tokyo, edited by: Sager, W. W., Sano, T., Geldmacher, J., and the Expedition 324 Scientists Scientists, Integrated Ocean Drilling Program Management International, Inc., https://doi.org/10.2204/iodp.proc.324.103.2010, 2010.

Expedition 330 Scientists: Methods, in: Proc. IODP, 330: Tokyo, edited by: Koppers, A. A. P., Yamazaki, T., Geldmacher, J., and the Expedition 330 Scientists, Integrated Ocean Drilling Program Management International, Inc., https://doi.org/10.2204/iodp.proc.330.102.2012, 2012.

Expedition 337 Scientists: Methods, in: Proc. IODP, 337: Tokyo, edited by: Inagaki, F., Hinrichs, K.-U., Kubo, Y., and the Expedition 337 Scientists, Integrated Ocean Drilling Program Management International, Inc., https://doi.org/10.2204/iodp.proc.337.102.2013, 2013.

Expedition 339 Scientists: Site U1385, in: Proc. IODP, 339: Tokyo, edited by: Stow, D. A. V., Hernández-Molina, F. J., Alvarez Zarikian, C. A., and the Expedition 339 Scientists, Integrated Ocean Drilling Program Management International, Inc., https://doi.org/10.2204/iodp.proc.339.103.2013, 2013a.

Expedition 339 Scientists: Methods, in: Proc. IODP, 339: Tokyo, edited by: Stow, D. A. V., Hernández-Molina, F. J., Al-

varez Zarikian, C. A., and the Expedition 339 Scientists, Integrated Ocean Drilling Program Management International, Inc., https://doi.org/10.2204/iodp.proc.339.102.2013, 2013b.

Fisher, A. T. and Underwood, M. B.: Calibration of an X-ray diffraction method to determine relative mineral abundances in bulk powders using matrix singular value decomposition: a test from the Barbados accretionary complex, in: Proc. ODP, edited by: Shipley, T. H., Ogawa, Y., and Blum, P., Init. Repts, 156, 29–37, https://doi.org/10.2973/odp.proc.ir.156.103.1995, 1995.

Flügel, E.: Microfacies Analysis: Methods, in: Microfacies of Carbonate Rocks, Springer, Berlin, Heidelberg, Germany, https://doi.org/10.1007/978-3-642-03796-2_3, 2010.

Folk, R. L.: A comparison chart for visual percentage estimation, J. Sediment. Petrol., 21, 32–33, https://doi.org/10.1306/D4269413-2B26-11D7-8648000102C1865D, 1951.

Folk, R. L.: The distinction between grain size and mineral composition in sedimentary-rock nomenclature, J. Geol., 62, 344–359, 1954.

Gallagher, S. J., Fulthorpe, C. S., Bogus, K., Auer, G., Baranwal, S., Castañeda, I. S., Christensen, B. A., De Vleeschouwer, D., Franco, D. R., Groeneveld, J., Gurnis, M., Haller, C., He, Y., Henderiks, J., Himmler, T., Ishiwa, T., Iwatani, H., Jatiningrum, R. S., Kominz, M. A., Korpanty, C. A., Lee, E. Y., Levin, E., Mamo, B. L., McGregor, H. V., McHugh, C. M., Petrick, B. F., Potts, D. C., Rastegar Lari, A., Renema, W., Reuning, L., Takayanagi, H., and Zhang, W.: Site U1459, in: Indonesian Throughflow, edited by: Gallagher, S. J., Fulthorpe, C. S., Bogus, K., and the Expedition 356 Scientists, Proceedings of the International Ocean Discovery Program, International Ocean Discovery Program, College Station, TX, USA, 356, https://doi.org/10.14379/iodp.proc.356.104.2017, 2017.

Gibbs, R. J.: Error due to segregation in quantitative clay mineral X-ray diffraction mounting techniques, Am. Mineral., 50, 741–751, 1965.

Gibbs, R. J.: Clay mineral segregation in the marine environment, J. Sediment. Petrol., 47, 237–243, https://doi.org/10.1306/212F713A-2B24-11D7-8648000102C1865D, 1977.

Giosan, L., Flood, R. D., and Aller, R. C.: Paleoceanographic significance of sediment color on western North Atlantic drifts: I. Origin of color, Mar. Geol., 189, 25–41, https://doi.org/10.1016/S0025-3227(02)00321-3, 2002.

Griffiths, J. C. and Rosenfeld, M. A.: Operator variation in experimental research, J. Geol., 62, 74–91, https://doi.org/10.1306/74D704F7-2B21-11D7-8648000102C1865D, 1954.

Hall, I. R., Hemming, S. R., LeVay, L. J., Barker, S., Berke, M. A., Brentegani, L., Caley, T., Cartagena-Sierra, A., Charles, C. D., Coenen, J. J., Crespin, J. G., Franzese, A. M., Gruetzner, J., Han, X., Hines, S. K. V., Jimenez Espejo, F. J., Just, J., Koutsodendris, A., Kubota, K., Lathika, N., Norris, R. D., Periera dos Santos, T., Robinson, R., Rolinson, J. M., Simon, M. H., Tangunan, D., van der Lubbe, J. J. L., Yamane, M., and Zhang, H.: Site U1474, in: South African Climates (Agulhas LGM Density Profile), edited by: Hall, I. R., Hemming, S. R., LeVay, L. J., and the Expedition 361 Scientists, Proceedings of the International Ocean Discovery Program, International Ocean Discovery Program, College Station, TX, USA, 361, https://doi.org/10.14379/iodp.proc.361.103.2017, 2017.

Integrated Ocean Drilling Program Depth Scale Task Force: IODP Depth Scales Terminology, available at: https://www.iodp.org/policies-and-guidelines/142-iodp-depth-scales-terminology-april-2011/file (last access: 6 December 2021), 2011.

International Ocean Discovery Program JOIDES Resolution Science Operator: LIMS Reports, Texas A&M University, College Station, TX, USA, available at: https://web.iodp.tamu.edu/LORE/, last access: 6 December 2021.

Jansen, E., Mayer, L., and Shipboard Scientific Party: GRAPE density records and density cyclicity, in: Proc. ODP, Init. Repts., edited by: Kroenke, L. W., Berger, W. H., Janecek, T. R., and Shipboard Scientific Party, Ocean Drilling Program, College Station, TX, USA, 130, 553–556, https://doi.org/10.2973/odp.proc.ir.130.113.1991, 1991.

Johnson, J. E., Phillips, S. C., Torres, M. E., Piñero, E., Rose, K. K., and Giosan, L.: Influence of total organic carbon deposition on the inventory of gas hydrate in the Indian continental margins, Mar. Petrol. Geol., 58, 406–424, https://doi.org/10.1016/j.marpetgeo.2014.08.021, 2014.

Lee, J., Kim, S., Lee, J. I., Cho, H. G., Phillips, S. C., and Khim, B.-K.: Monsoon-influenced variation of clay mineral compositions and detrital Nd-Sr isotopes in the western Andaman Sea (IODP Site U1447) since the late Miocene, Palaeogeogr. Palaeocl., 538, 109339, https://doi.org/10.1016/j.palaeo.2019.109339, 2020.

Lübbers, J., Kuhnt, Holburn, A. E., Bolton, C. T., Gray, E., Usui, U., Kochhann, K. G. D., Beil, S., and Andersen, N.: The middle to late Miocene "Carbonate Crash" in the equatorial Indian Ocean, Paleoceanography and Paleoclimatology, 34, 813–832, https://doi.org/10.1029/2018PA003482, 2019.

Marsaglia, K., Milliken, K., and Doran, L.: IODP Smear Slide Digital Reference for Sediment Analysis of Marine Mud: Part 1: Methodology and Atlas of Siliciclastic and Volcanogenic Components, Integrated Ocean Drilling Program Technical Note 1, https://doi.org/10.2204/iodp.tn.1.2013, 2013.

Marsaglia, K., Milliken, K., Leckie, R. M., Tentori, D., and Doran, L.: IODP Smear Slide Digital Reference for Sediment Analysis of Marine Mud: Part 2: Methodology and Atlas of Biogenic Components, International Ocean Discovery Program Technical Note 2, https://doi.org/10.2204/iodp.tn.2.2015, 2015.

Mayer, L. A.: Extraction of high resolution carbonate data for paleoclimate reconstruction, Nature, 352, 148–150, 1991.

Mazzullo, J. and Graham, A. G.: Handbook for shipboard sedimentologists, ODP Tech. Note 8, https://doi.org/10.2973/odp.tn.8.1988, 1988.

Mazzullo, J. M., Meyer, A., and Kidd, R. B.: New sediment classification scheme for the Ocean Drilling Program, in: Handbook for shipboard sedimentologists, edited by: Mazzullo, J. M. and Graham, A. G., ODP Tech. Note, 8, 45–67, https://doi.org/10.2973/odp.tn.8.1988, 1988.

Milliken, K.: A compositional classification for grain assemblages in fine-grained sediments and sedimentary rocks, J. Sediment. Res., 84, 1185–1199, https://doi.org/10.2110/jsr.2014.92, 2014.

Musich, L.: Sediment smear slides: Preparation and handling, in: Sedimentology, Physical Properties, and Geochemistry in the Initial Reports of the Deep Sea Drilling Project, Volumes 1–44: An Overview, edited by: Heath, G. R., National Geophysical Data Center, Boulder, Colorado, USA, 63–70, 1984.

Myrbo, A., Morrison, A., and McEwan, R: Tool for Microscopic Identification (TMI), available at: http://tmi.laccore.umn.edu (last access: 6 December 2021), 2011.

Ortiz, J., Mix, A., Harris, S., and O'Connell, S.: Diffuse spectral reflectance as a proxy for percent carbonate content in North Atlantic sediments, Paleoceanography, 14, 171–186, https://doi.org/10.1029/1998PA900021, 1999.

Ota, Y., Kuroda, J., Yamaguchi, A., Suzuki, A., Araoka, D., Ishimura, T., Team, N. E. J. S., and Kawahata, H.: Monsoon-influenced variations in plankton community structure and upperwater column stratification in the western Bay of Bengal during the past 80 ky, Palaeogeogr. Palaeocl., 521, 138–150, https://doi.org/10.1016/j.palaeo.2019.02.020, 2019.

Phillips, S. C., Johnson, J. E., Giosan, L., and Rose, K.: Monsoon-influenced variation in productivity and lithogenic sediment flux since 110 ka in the offshore Mahanadi Basin, northern Bay of Bengal, Mar. Petrol. Geol., 58, 502–525, https://doi.org/10.1016/j.marpetgeo.2014.05.007, 2014a.

Phillips, S. C., Johnson, J. E., Underwood, M. B., Guo, J., Giosan, L., and Rose, K.: Long-timescale variation in bulk and clay mineral composition of Indian continental margin sediments in the Bay of Bengal, Arabian Sea, and Andaman Sea, Mar. Petrol. Geol., 58A, 118–138, https://doi.org/10.1016/j.marpetgeo.2014.06.018, 2014b.

Pimmel, A. and Claypool, G.: Introduction to Shipboard Organic Geochemistry on the JOIDES Resolution, ODP Technical Note 30, https://doi.org/10.2973/odp.tn.30.2001, 2001.

Reid, J. C.: Comparison chart for estimating volume percentages of constituents in rocks and concentrates in the range of 1.0 to 0.1 volume percent, Am. Mineral., 70, 1318–1319, 1985.

Rothwell, R. G.: Minerals and Mineraloids in Marine Sediments: An Optical Identification Guide, Springer Netherlands, 279 pp., https://doi.org/10.1007/978-94-009-1133-8, 1989.

Schultheiss, P. J. and McPhail, S. D.: An automated P-wave logger for recording fine-scale compressional wave velocity structures in sediments, in: Proc. ODP, Sci. Results, edited by: Ruddiman, W., Sarnthein, M., and Shipboard Scientific Party, 108, 407–413, Ocean Drilling Program, College Station, TX, USA, https://doi.org/10.2973/odp.proc.sr.108.157.1989, 1989.

Shepard, F. P.: Nomenclature based on sand-silt-clay ratios, J. Sediment. Petrol., 24, 151–158, https://doi.org/10.1306/D4269774-2B26-11D7-8648000102C1865D, 1954.

Shipboard Scientific Party: Explanatory notes, in: Proc. ODP, Init. Repts., edited by: Kastens, K. A., Mascle, J., Auroux, C., and Shipboard Scientific Party, Ocean Drilling Program, College Station, TX, USA, 107, 65–88, https://doi.org/10.2973/odp.proc.ir.107.104.1987, 1987.

Shipboard Scientific Party: Site 758, in: Proc. ODP, Init. Repts, edited by: Peirce, J., Weissel, J., and Shipboard Scientific Party, 121, 359–453, https://doi.org/10.2973/odp.proc.ir.121.112.1989, 1989.

Shipboard Scientific Party: Site 803, in: Proc. ODP, Init. Repts., edited by: Kroenke, L. W., Berger, W. H., Janecek, T. R., and Shipboard Scientific Party, Ocean Drilling Program, College Station, TX, USA, 130, 101–176, https://doi.org/10.2973/odp.proc.ir.130.105.1991, 1991.

Shipboard Scientific Party: Site 892, in: Proc. ODP, Init. Repts., edited by: Westbrook, G. K., Carson, B., Musgrave, R. J., and Shipboard Scientific Party, Ocean Drilling Program, College Station, TX, USA, 146 (Pt. 1), 301–378, https://doi.org/10.2973/odp.proc.ir.146-1.010.1994, 1994a.

Shipboard Scientific Party: Site 902, in: Proc. ODP, Init. Repts., edited by: Mountain, G. S., Miller, K. G., Blum, P., and Shipboard Scientific Party, Ocean Drilling Program, College Station, TX, USA, 150, 63–127, https://doi.org/10.2973/odp.proc.ir.150.106.1994, 1994b.

Shipboard Scientific Party: Site 907, in: Proc. ODP, Init. Repts., edited by: Myhre, A. M., Thiede, J., Firth, J. V., and Shipboard Scientific Party, Ocean Drilling Program, College Station, TX, USA, 151, 57–111, https://doi.org/10.2973/odp.proc.ir.151.105.1995, 1995a.

Shipboard Scientific Party:. Explanatory notes, in: Proc. ODP, Init. Repts., edited by: Curry, W. B., Shackleton, N. J., Richter, C., and Shipboard Scientific Party, Ocean Drilling Program, College Station, TX, USA, 154, 11–38, https://doi.org/10.2973/odp.proc.ir.154.102.1995, 1995b.

Shipboard Scientific Party: Site 959, in: Proc. ODP, Init. Repts., edited by: Mascle, J., Lohmann, G. P., Clift, P. D., and Shipboard Scientific Party, Ocean Drilling Program, College Station, TX, USA, 159, 65–150, https://doi.org/10.2973/odp.proc.ir.159.105.1996, 1996a.

Shipboard Scientific Party: Site 974, in: Proc. ODP, Init. Repts., edited by: Comas, M. C., Zahn, R., Klaus, A., and Shipboard Scientific Party, Ocean Drilling Program, College Station, TX, USA, 161, 55–111, https://doi.org/10.2973/odp.proc.ir.161.104.1996, 1996b.

Shipboard Scientific Party: Explanatory notes, in: Proc. ODP, Init. Repts., edited by: Jansen, E., Raymo, M. E., Blum, P., and Shipboard Scientific Party, Ocean Drilling Program, College Station, TX, USA, 162, 21–45, https://doi.org/10.2973/odp.proc.ir.162.102.1996, 1996c.

Shipboard Scientific Party: Explanatory notes, in: Proc. ODP, Init. Repts., eduted by: Kimura, G., Silver, E., Blum, P., and Shipboard Scientific Party, Ocean Drilling Program, College Station, TX, USA, 170, 19–42, https://doi.org/10.2973/odp.proc.ir.170.102.1997, 1997.

Shipboard Scientific Party: Site 1168, in: Proc. ODP, Init. Repts., edited by: Exon, N. F., Kennett, J. P., Malone, M. J., and Shipboard Scientific Party, 189, 1–170, https://doi.org/10.2973/odp.proc.ir.189.103.2001, 2001.

Stokke, P. R. and Carson, B.: Variation in clay mineral X-Ray diffraction results with the quantity of sample mounted, J. Sediment. Res., 43, 957–964, https://doi.org/10.1306/74D728C4-2B21-11D7-8648000102C1865D, 1973.

Terry, R. D. and Chilingar, G. V.: Summary of "Concerning some additional aids in studying sedimentary formations" by M. S. Shvetsov, J. Sediment. Petrol., 25, 229–234, https://doi.org/10.1306/74D70466-2B21-11D7-8648000102C1865D, 1955.

Thomas, A. R. and Murray, H. H.: Clay mineral segregation by flocculation in the Porters Creek Formation, Clay. Clay Miner., 37, 179–184, https://doi.org/10.1346/CCMN.1989.0370210, 1989.

Vasiliev, M. A., Blum, P., Chubarian, G., Olsen, R., Bennight, C., Cobine, T., Fackler, D., Hastedt, M., Houpt, D., Mateo, Z., and Vasilieva, Y. B.: A new natural gamma radiation measurement system for marine sediment and rock analysis, J. Appl. Geophys., 75, 455–463, https://doi.org/10.1016/j.jappgeo.2011.08.008, 2011.

Verardo, D. J., Froelich, P. N., and McIntyre, A.: Determination of organic carbon and nitrogen in marine sediments using the Carlo Erba NA-1500 Analyzer, Deep-Sea Res., 37, 157–165, https://doi.org/10.1016/0198-0149(90)90034-S, 1990.

Weaver, P. P. E. and Schultheiss, P. J.: Current methods for obtaining, logging and splitting marine sediment cores, Mar. Geophys. Res., 12, 85–100, https://doi.org/10.1007/BF00310565, 1990.

Weber, M. E., Niessen, F., Kuhn, G., and Wiedicke, M.: Calibration and application of marine sedimentary physical properties using a multi-sensor core logger, Mar. Geol., 136, 151–172, https://doi.org/10.1016/S0025-3227(96)00071-0, 1997.

Sci. Dril., 30, 75–99, 2022
https://doi.org/10.5194/sd-30-75-2022

Scientific Drilling
Open Access

Ship-board determination of whole-rock (ultra-)trace element concentrations by laser ablation-inductively coupled plasma mass spectrometry analysis of pressed powder pellets aboard the D/V *Chikyu*

Mathieu Rospabé[1,2], Fatma Kourim[3], Akihiro Tamura[4], Eiichi Takazawa[5], Manolis Giampouras[6], Sayantani Chatterjee[5], Keisuke Ishii[5], Matthew J. Cooper[7], Marguerite Godard[8], Elliot Carter[9], Natsue Abe[10], Kyaw Moe[11], Damon A. H. Teagle[7], and Oman Drilling Project "ChikyuOman2018 Leg 3" Science Team✚

[1]Research Institute for Marine Geodynamics (IMG), Japan Agency for Marine-Earth Science and Technology (JAMSTEC), 2-15 Natsushima, Yokosuka, Kanagawa 237-0061, Japan
[2]Géosciences Environnement Toulouse (GET), Observatoire Midi-Pyrénées, Université de Toulouse, CNRS, IRD, 14 avenue E. Belin, 31400 Toulouse, France
[3]Institute of Earth Sciences, Academia Sinica, Academia Road, Nangang, Taipei 11529, Taiwan
[4]Department of Sciences, College of Science and Engineering, Kanazawa University, Kanazawa, Ishikawa 920-1192, Japan
[5]Department of Geology, Faculty of Science, Niigata University, Niigata, Niigata 950-2181, Japan
[6]Instituto Andaluz de Ciencias de la Tierra (IACT), Consejo Superior de Investigaciones Científicas-Universidad de Granada, Avd. Palmeras 4, 18100 Armilla, Granada, Spain
[7]School of Ocean and Earth Science, National Oceanography Centre Southampton, University of Southampton, European Way, Southampton SO14-3ZH, UK
[8]Géosciences Montpellier, CNRS, Université Montpellier, Place E. Bataillon, 34095 Montpellier, France
[9]Department of Geology, Trinity College Dublin, Dublin 2, Ireland
[10]Mantle Drilling Promotion Office, Institute for Marine-Earth Exploration and Engineering (MarE3), Japan Agency for Marine-Earth Science and Technology (JAMSTEC), 3173-25 Showa-machi, Kanazawa-ku, Yokohama, Kanagawa 236-0001, Japan
[11]Institute for Marine-Earth Exploration and Engineering (MarE3), Japan Agency for Marine-Earth Science and Technology (JAMSTEC), 2-15 Natsushima, Yokosuka, Kanagawa 237-0061, Japan
✚A full list of authors appears at the end of the paper.

Correspondence: Mathieu Rospabé (mrospabe@jamstec.go.jp)

Received: 28 March 2021 – Revised: 14 July 2021 – Accepted: 22 August 2021 – Published: 25 February 2022

Abstract. The Oman Drilling Project (OmanDP), performed under the International Continental Scientific Drilling Program (ICDP), is an international scientific research project that undertook drilling at a range of sites in the Semail ophiolite (Oman) to collect core samples spanning the stratigraphy of the ophiolite, from the upper oceanic crust down to the basal thrust. The cores were logged to International Ocean Discovery Program (IODP) standards aboard the D/V *Chikyu*. During ChikyuOman2018 Leg 3 (July–August 2018), participants described cores from the crust–mantle transition (CM) sites. The main rock types recovered at these sites were gabbros, dunites and harzburgites, rocks typically forming the base of the oceanic crust and the shallow mantle beneath present-day spreading centres. In addition to the core description, selected samples were analysed by X-ray fluorescence spectrometry (XRF) for their chemical compositions, including major, minor and some trace elements. To complement these standard procedures, we developed new approaches to measure ultra-trace element concentrations using a procedure adapted from previous works to prepare fine-grained pressed powder

Published by Copernicus Publications on behalf of the IODP and the ICDP.

pellets coupled with laser ablation-inductively coupled plasma mass spectrometry (LA-ICP-MS) analysis using instrumentation aboard the D/V *Chikyu*. First, three (ultra)mafic reference materials were investigated to test and validate our procedure (BHVO-2, BIR-1a and JP-1), and then the procedure was applied to a selection of gabbro and dunite samples from the CM cores to explore the limitations of the method in its current stage of development. The obtained results are in good agreement with preferred values for the reference materials and with subsequent solution replicate analyses of the same samples performed in shore-based laboratories following Leg 3 for the CM samples. We describe this procedure for the determination of 37 minor and (ultra-)trace elements (transition elements and Ga, Li and Large-Ion Lithophile Elements (LILE), Rare Earth Elements (REE), High-Field-Strength Elements (HFSE), U, Th, and Pb) in mafic and ultramafic rocks. The presented method has the major advantage that it allows the determination *at sea* of the (ultra-)trace element concentrations in a "dry", safe way, without using acid reagents. Our new approach could be extended for other elements of interest and/or be improved to be adapted to other rock materials during future ocean drilling operations aboard the D/V *Chikyu* and other platforms.

1 Introduction

1.1 Context of the study: the ICDP Oman Drilling Project

Project Mohole was initiated more than 60 years ago, beginning in 1961 initiating several scientific ocean drilling expeditions with the ultimate goal of drilling through the entire oceanic crust and the crust–mantle transition or Moho, to finally reach the Earth's sub-oceanic upper mantle. Despite major improvement in drilling technology (drill ships and equipment) over the past decades, this target has yet to be achieved, and the drilling of a 5 to 6 km-thick oceanic crust accreted in a fast-spreading environment remains a key challenge for present and future generations of Earth scientists. Until 2018, only 20 holes were drilled deeper than 200 m in the oceanic lithosphere igneous basement, with variable core recoveries, which clearly illustrates the major difficulty in reaching such depths by ocean drilling (Michibayashi et al., 2019, and references therein).

In this context, accessing the rocks forming the deep oceanic crust and sub-oceanic mantle is easier through the study of ophiolites, remnants of a former oceanic lithosphere displaced on-land through tectonic plate rearrangements (Anonymous, 1972; Coleman, 1971, 1977; Dilek, 2003, and references therein). To avoid the difficulties of drilling deep hard rocks in present-day oceans, a project to drill the different units of the Semail ophiolite (Sultanate of Oman and the United Arab Emirates) was designed in the early 2010s (Kelemen et al., 2013), since this ophiolite is one of the largest and best preserved on Earth and since all the layers expected to constitute an ideal portion of a fast-spreading oceanic lithosphere are exposed with their original stratigraphy relatively well preserved (e.g. Boudier and Nicolas, 1985; Glennie et al., 1974; Hopson et al., 1981; Lippard et al., 1986). The Oman Drilling Project (OmanDP), implemented by the International Continental Scientific Drilling Program (ICDP), materialized with the drilling operations conducted during the winters 2016 (December 2016–March 2017) for Phase 1 and 2017 (November 2017–February 2018) for Phase 2 (https://www.omandrilling.ac.uk/drilling-program, last access: 27 August 2021; see the Proceedings of the Oman Drilling Project: http://publications.iodp.org/other/Oman/OmanDP.html, last access: 27 August 2021). Following these operations, the cores were moved to Japan for description on-board the drilling vessel (D/V) *Chikyu* during two intensive 60 d core characterization campaigns under an IODP–ICDP joint collaboration during the summers 2017 and 2018 (ChikyuOman2017 and ChikyuOman2018), with each ship-board campaign subdivided into two legs (2017: Legs 1 and 2; 2018: Legs 3 and 4).

1.2 Target of the study: to safely determine (ultra-)trace element concentrations at sea

The D/V *Chikyu* is operated by the IODP Japanese implementing organization Centre for Deep Earth Exploration (CDEX) of the Japan Agency for Marine-Earth Science and Technology (JAMSTEC). It was specifically designed for deep-sea drilling and is equipped with several laboratory facilities, including a sample preparation room and a geochemistry laboratory. The latter is equipped with an X-ray fluorescence spectrometer (XRF) and an inductively coupled plasma-mass spectrometer (ICP-MS) for on-board chemical analyses. The determination of trace element concentrations *at sea*, using the installed ICP-MS, was made for the first time during the ChikyuOman2017 campaign (Legs 1 and 2). The sample preparation procedure has consisted of a mixed acid/alkali-fusion digestion procedure using perchloric and hydrofluoric acids (Senda et al., 2014; see also Kelemen et al., 2020). However, the members of the geochemistry team were concerned by the hazards related to the use of such acid reagents on-board an oceanographic vessel, especially during open ocean operations. Consequently, to address safety concerns during future ocean drilling operations, it was decided to plan for the development of a "dry" sample preparation

and analytical method for the determination of the (ultra-)trace element contents in whole-rock samples during the ChikyuOman2018 campaign (Legs 3 and 4).

The principle was to analyse pressed powder pellets using the newly installed laser ablation system coupled to the on-board ICP-MS (LA-ICP-MS). During Leg 3, the sample preparation procedure was adapted from Garbe-Schönberg and Müller (2014) that described the ablation of powder pellets prepared without a binder. Generally, pressed powder pellets are prepared with a binder (e.g. Arrowsmith, 1987; Gray, 1985; Van Heuzen, 1991; Imai, 1990; Mukherjee et al., 2014; Peters and Pettke, 2017; Zhu et al., 2013), while other authors also described the ablation of fused glass beads as another acid-free technique (e.g. Akizawa et al., 2020; Eggins, 2003; Kon et al., 2011; Kon and Hirata, 2015; Tamura et al., 2015). A requirement was to prepare pellets smaller than the ones prepared for XRF analyses to be better adapted to the size/volume of the laser ablation sample cell. It was also critical to prepare these pellets from powder with an average powder grain size much smaller than the maximum laser spot size that could be set (e.g. Garbe-Schönberg and Müller, 2014; Peters and Pettke, 2017). This new sample preparation and instrument parametrization method (described in Sect. 2) was first tested by analysing three reference materials and then applied to a selection of gabbro and dunite samples from the OmanDP CM1A cores (CM for crust–mantle transition). As discussed below (Sect. 3), analyses of both standard reference materials and of unknown samples compare well with literature values and replicate analyses of the same samples analysed in shore-based laboratories after Leg 3, respectively. The current limitations and possible future improvements of both the presented method and the surrounding analytical environment on-board the D/V *Chikyu* are discussed in Sect. 4.

2 Methodology

2.1 Overview of the materials and analytical methods

Over two drilling seasons, the Oman Drilling Project drilled a suite of 15 holes (nine diamond-cored and six rotary-drilled boreholes) distributed across 10 sites (Kelemen et al., 2021c; https://www.omandrilling.ac.uk/drilling-program, last access: 27 August 2021; the proceedings are available at: http://publications.iodp.org/other/Oman/OmanDP.html, last access: 27 August 2021). The ChikyuOman2018 Leg 3 science team focused on the characterization of Holes CM1A (400 m) and CM2B (300 m) that cored continuously ($\sim$ 100 % recovery) the Oman ophiolite crust–mantle transition (Kelemen et al., 2021a, b). The sample selection has been conducted in two ways. Firstly, during the on-site operations in Oman, samples were systematically collected every 10 m along the OmanDP CM cores. Then, during Leg 3, additional ship-board samples were collected to complete the general, detailed overview of the cores. Samples collected on-site were milled at the University of Southampton (UK) prior to Leg 3 and the powders sent to the D/V *Chikyu* for on-board analyses; ship-board samples collected during Leg 3 were sawed and milled directly aboard the D/V *Chikyu*.

In terms of chemical analyses performed during Leg 3, both on-site and ship-board samples were analysed by XRF for major, minor and some trace elements. For the development of a dry, safe method for the on-board determination of whole-rock (ultra-)trace element concentrations, we investigated the basalts BHVO-2 and BIR-1a (United States Geological Survey, USGS) and the peridotite JP-1 (Geological Survey of Japan, GSJ) as reference materials to test and validate the measurement precision of our procedure. The method was then applied to a selection of gabbro (crust) and dunite (crust–mantle transition) samples from Hole CM1A. These were all ship-board samples that were fully prepared during Leg 3 and analysed using the laser ablation method described and discussed below. Replicate solution analyses for these CM samples were performed following ChikyuOman2018 in different on-shore laboratories for the trace elements. The gabbro samples were analysed by ICP-MS at the University of Southampton. The dunite samples were analysed (ICP-MS) at the Institute of Earth Science, Academia Sinica at Taipei (Taiwan), and the Géosciences Environnement Toulouse laboratory, Université Toulouse III – Paul Sabatier (France). The different steps of the complete methodology are summarized in Fig. 1.

2.2 On-board chemical analysis by existing methods (XRF)

Ship-board samples, selected during the Leg 3 daily sampling meetings, were cut into thin slices to ease the crushing to a < 1 mm grit. Saw marks and alteration blemishes were removed by precision sawing. Sample pieces were first ultrasonicated in deionized water (18.2 MΩ cm) purified with a Milli-Q system (Millipore, Bedford, MA, USA®) for consecutive rounds until the Milli-Q water was clear and dried for 12 h at 60 °C. The samples were then crushed in four steps using a newly installed Jaw Crusher Retsch BB50. The four crushing steps started with a 14 mm jaw gap that was decreased in stages to 7, 4 and 1 mm. Between two samples, all parts of the crusher, including the steel jaws, have been disassembled and carefully cleaned using isopropanol. After the 14 and 7 mm crushing steps, samples were sieved at 250 µm and smaller particles that passed through were discarded to avoid possible cross-contamination with the previously crushed sample. The resulting < 1 mm crushed sample was then powdered using a Fritsch Pulverisette 5 planetary mill with agate grinding bowls (500 mL) and agate balls (13 small balls of 20 mm and 5 large balls of 30 mm in diameter). Grit samples were run at 200 rounds per minute (rpm) for 10 min and allowed to cool for 5 min four times. The obtained powder grain size was below 250 µm (verified by sieving).

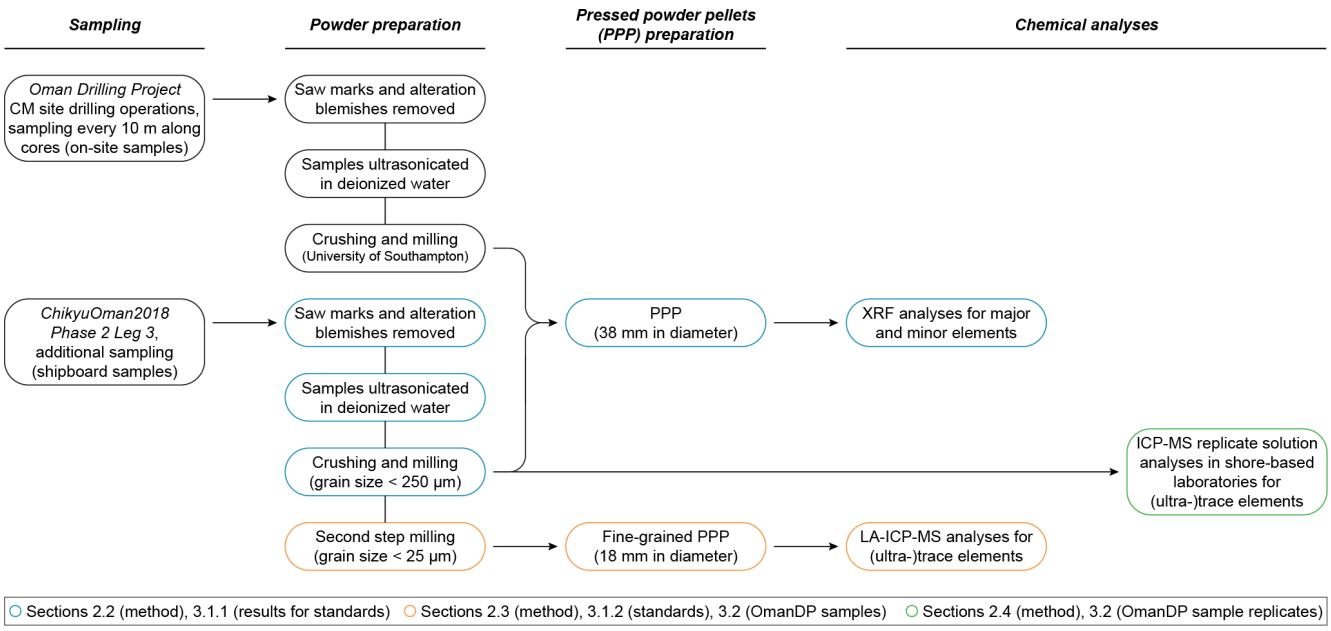

Figure 1. Flow chart summarizing the different steps for sample preparation and chemical analyses.

The agate grinding bowls and agate balls were cleaned with Milli-Q water and isopropanol after each run and decontaminated by milling pure quartz sand when changing between two samples.

The chemical analyses on-board the D/V *Chikyu* are usually performed by XRF on glass beads for the determination of major oxides (SiO_2, TiO_2, Al_2O_3, Fe_2O_3, MnO, MgO, CaO, Na_2O, K_2O, P_2O_5) and on pressed powder pellets for the determination of major and some minor to trace element contents (Sc, V, Cr, Co, Ni, Cu, Zn, Ga, Rb, Sr, Y, Zr, Nb, Ba). Here, we compare only the results obtained for these selected minor to trace elements following the analysis of pressed powder pellets to the concentrations obtained using the newly developed laser ablation-inductively coupled plasma mass spectrometry (LA-ICP-MS) method. To prepare pressed powder pellets for XRF analysis, 4 g of unignited powder was weighed and carefully placed into a 5 mm-high sample holder cut from a 38 mm diameter polypropylene pipe and pressed using a Spex SamplePrep 3630 X-Press. The press was set to ramp up to 15 t and held there for 20 s, followed by a gradational release of the pressure over 66 s.

The major and minor element concentrations were determined using a RIGAKU Supermini wavelength dispersive X-ray fluorescence spectrometer equipped with a 200 W Pd anode tube at 50 kV and 4 mA. The instrument was calibrated using either pre-prepared glass beads for the major elements or pressed pellets for the major and minor to trace elements, made from reference materials from the Geological Survey of Japan. Rock standards JA-1 (andesite), JA-2 (sanukitoid), JB-2 and JB-3 (basalts), JF-1 and JF-2 (feldspars), JG-1a (granodiorite), JG-2 (granite), JGb-1 and JGb-2 (gabbros), JH-1 (hornblendite), JP-1 (peridotite), JR-2 and JR-3 (rhyolites), and JSy-1 (syenite) were commonly used for both calibrations together with JG-1 (granodiorite) for the major elements only (Imai et al., 1995, 1999). An additional 3 : 1 mixture of JGb-2 and JP-1 was also prepared to fill a large (> 2000 ppm) gap in the calibration for Cr and Ni if only the stated standards are used. Cr and Ni are known to occur in high concentrations in mantle peridotites and are expected to be high in the harzburgites and dunites from the CM cores based on previous results for peridotites from the Oman ophiolite mantle section (e.g. Godard et al., 2000; Hanghøj et al., 2010).

2.3 On-board chemical analysis by the newly developed powder pellet method (LA-ICP-MS)

2.3.1 Sample preparation

The approach for the safe determination of whole-rock (ultra-)trace element concentrations on-board the D/V *Chikyu* was to analyse pressed powder pellets using the laser ablation system coupled to the ICP-MS. The maximum laser spot size was 100 µm for the used instrumentation. It was therefore critical to prepare new pellets from powder with an average powder grain size much smaller than this maximum spot size (e.g. Garbe-Schönberg and Müller, 2014; Peters and Pettke, 2017). Following the first stage of milling to prepare powders for pressed pellets for XRF analysis, a second milling step was thus applied to further reduce the powder grain sizes and improve the homogeneity of the samples selected to be analysed by laser ablation. This extra grinding step was ap-

plied to the three reference materials BHVO-2 and BIR-1a (basalts, USGS) and JP-1 (peridotite, GSJ) and to a selection of gabbros and dunites from the OmanDP CM1A cores.

For each selected sample, 3 g of powder (grain size ≤ 250 µm following the first milling step) was further milled using the Fritsch Pulverisette 5 planetary mill in an 80 mL agate grinding bowl with four agate balls 20 mm in diameter. The sample was rotated at 400 rpm for 30 min, for four repeat cycles, alternating with 5 min-long cooling steps between each milling cycle. The content of the jar was then sieved through 100, 60, and 25 µm nylon meshes (Clever, Toyohashi, Japan). Material > 100 µm was returned to the bowl and ground for a further 30 min. The same step was repeated for fractions > 60 and > 25 µm. Once a sample was powdered to < 25 µm, all the powder fractions were recombined and returned to the grinding bowl and milled for 5 min for homogenization. Similarly to the first stage of milling, the agate grinding bowl and agate balls were carefully cleaned with Milli-Q water and isopropanol and decontaminated by milling pure quartz sand after each sample.

Approximately 1.5 g of the < 25 µm powder was pressed using the Spex SamplePrep 3630 X-Press into powder pellets for (ultra-)trace element analyses by LA-ICP-MS. The powder was weighed and placed into a 5 mm-high sample holder cut from an 18 mm diameter polypropylene tube. The powder was isolated from the metal rams that apply the load from the press to the sample powder using Prolene film (CHEMPLEX, Florida, USA). The press was set to ramp up to 15 t and held there for 20 s, and then the pressure was gradually released over 66 s. Figure 2 shows examples (the reference material BIR-1a and a gabbro from Hole CM1A) of the contrast in grain size between pellets prepared with powder after a one-step milling for the XRF analyses (to the left) and with re-milled powder for the analyses by laser ablation (to the right). Concerning the OmanDP samples, it is worth noting that the dunite samples were particularly altered (serpentinized) and thus milled much more easily than the fresher, coarser-grained gabbros. On the other hand, the dunites contain minor spinel that could be much harder to grind relative to other silicate minerals.

2.3.2 Instrumentation and data acquisition

The instrumentation on-board the D/V *Chikyu* comprises a NewWave Research UP-213 Nd:YAG deep UV (213 nm) laser ablation system coupled to an Agilent 7500ce quadrupole ICP-MS. First, initial basic tests and parametrization of the operating conditions were performed by the analysis of the well-known reference glasses BHVO-2G and BIR-1G. Analyses were bracketed by repeated analyses of NIST SRM 612 glass (National Institute of Standards and Technology), used as an external reference material following the reference values from Jochum et al. (2011); NIST SRM 610 has been used for the instrument calibration. In addition to ^{29}Si, analysed as an internal standard for the data reduction (e.g. Longerich et al., 1996; SiO_2 reference values used for BHVO-2G and BIR-1G after Jochum et al., 2005), the isotopes analysed for the 37 selected elements were as follows: ^{7}Li, ^{45}Sc, ^{49}Ti, ^{51}V, ^{52}Cr, ^{55}Mn, ^{59}Co, ^{62}Ni, ^{65}Cu, ^{67}Zn, ^{71}Ga, ^{85}Rb, ^{88}Sr, ^{89}Y, ^{90}Zr, ^{93}Nb, ^{133}Cs, ^{137}Ba, ^{139}La, ^{140}Ce, ^{141}Pr, ^{143}Nd, ^{147}Sm, ^{151}Eu, ^{158}Gd, ^{159}Tb, ^{163}Dy, ^{165}Ho, ^{166}Er, ^{169}Tm, ^{172}Yb, ^{175}Lu, ^{178}Hf, ^{181}Ta, ^{208}Pb, ^{232}Th, ^{238}U.

Once the laser ablation system parameters were set, we started the ablation tests on the prepared fine-grained pressed powder pellets. The ICP-MS configuration was adjusted before each analytical sequence to ensure the high sensitivity required to measure the elements present in very low concentrations, especially those expected in the JP-1 peridotite reference material and the dunite samples from Hole CM1A. Operating conditions are summarized in Table 1. Each analysis consisted of 40 s of background, 60 s of acquisition ablation and 120 s of washout. Instrumental background was analysed before each analysis and then subtracted from the signal obtained during sample ablation (typical values are given in Table 2). Only about 50 s of the signal obtained during sample ablation have been included in the calculation of concentrations, and the first few seconds of the ablation signal have been discarded as they can be fractionated and might integrate surface contamination (e.g. Peters and Pettke, 2017). The NIST SRM 612 glass reference material was used as an external standard for the pressed powder pellets prepared for the reference materials BHVO-2, BIR-1a and JP-1. Analytical sequences consisted of one analysis of NIST SRM 612 between each analysis of pellets. First, the sample ablation signal (i.e. already corrected from the instrumental background) was corrected for the instrumental drift with the bracketing NIST SRM 612 (drift assumed to be linear between two NIST SRM 612 analyses). Data reduction and calculation of concentrations have been made using ^{29}Si as an internal standard, following the SiO_2 obtained by XRF for the reference materials BHVO-2 and JP-1 and following the reference values for the reference material BIR-1a (USGS certificate of analysis).

The results obtained for the BHVO-2 and BIR-1a pressed powder pellets were first compared to the results obtained for the BHVO-2G and BIR-1G glasses to ensure there was no drift or major matrix effect related to alternatingly analysing glass and pressed powder. In addition, the relatively depleted mantle peridotite JP-1 was analysed to evaluate the lowest concentrations we were able to accurately determine by analysing pressed powder pellets by laser ablation. It has been shown that in peridotites, the large difference in concentration between major elements such as in Mg or Fe and the very low contents of trace elements such as the Rare Earth Elements (REE) lowers the efficiency of precisely detecting the less concentrated elements depending on the dilution factor (Makishima and Nakamura, 1997, 2006; Nakamura and Chang, 2007). A preconcentration of the (ultra-)trace elements is a usual method to avoid such a matrix effect (e.g. Bayon et al., 2009; Bizzarro et al., 2003; Qi et al.,

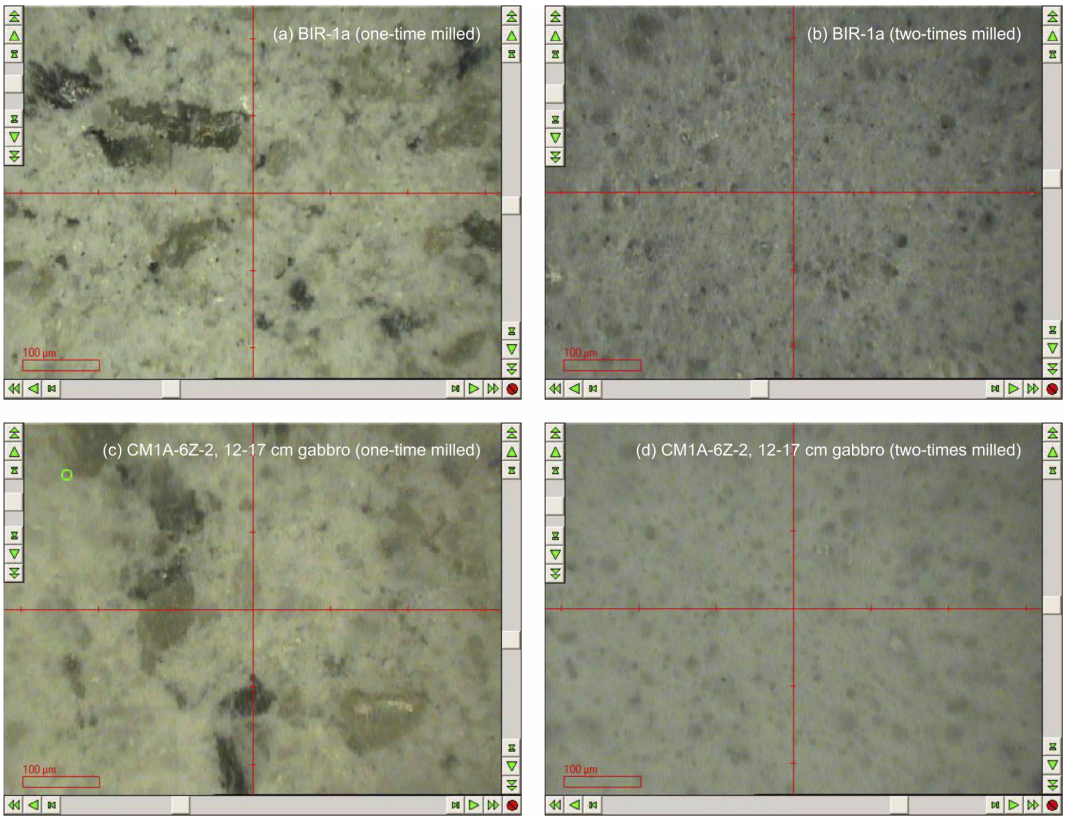

Figure 2. Comparison of the grain sizes in pressed powder pellets before **(a, c)** and after **(b, d)** the second step milling for the reference material BIR-1a **(a, b)** and for the gabbro sample CM1A-6Z-2, 12–17 cm from the OmanDP Hole CM1A **(c, d)** (modified from Fig. F52, Kelemen et al., 2020). The minimum laser spot size that could be parameterized with the laser ablation system used on-board the D/V *Chikyu* was 100 µm in diameter, smaller than the size of some mineral grains when samples have been milled only once.

2005; Rospabé et al., 2018a; Sharma et al., 1995; Sharma and Wasserburg, 1996), but it could not be performed in the context of the presently described "dry", solid (i.e. reagent-free) method development. The results obtained for these three reference materials are compared to preferred or reference values and discussed in the next Sect. 3.1. During subsequent analysis of pressed powder pellets of gabbros and dunites from Hole CM1A, analyses were bracketed by repeated analyses of BHVO-2G (glass), used as an external standard. For these OmanDP samples, data reduction and calculation of concentrations have been made using ^{29}Si as an internal standard, based on the SiO_2 contents obtained by XRF. The results are compared with replicates for the same gabbro and dunite samples analysed after Leg 3 in the next Sect. 3.2.

2.4 Methodologies for post-cruise replicate analyses

Replicate analyses for the CM1A gabbros analysed by laser ablation on-board the D/V *Chikyu* have been performed at the University of Southampton (UK); 100 mg of powder was weighed into Savillex® Teflon PFA vials and digested with HF/HNO_3 overnight, followed by a second overnight digestion step with $HClO_4$. The digested samples were dissolved in 6M HCl to make a mother solution. The mother solution was subsampled to give a final dilution of ∼4000-fold, dried down and redissolved in 3 % HNO_3 containing In, Re and Be as internal standards (internal standard concentrations were 5 ng g^{-1} for In and Re and 20 ng g^{-1} for Be). The samples were analysed on a Thermo Fisher Scientific™ XSERIES 2 ICP-MS using JB-1a, JB-2, JB-3, JGb-1, BIR-1, BHVO-2, AGV-2 and BCR-2 as calibration standards; these were also dissolved in 3 % HNO_3 containing In, Re and Be.

The replicates for the selected dunites have been analysed at the Institute of Earth Science, Academia Sinica (IES-AS, Taiwan), and at the Géosciences Environnement Toulouse laboratory, Université Toulouse III – Paul Sabatier (GET, France). Samples have been dissolved by acid digestion and their trace element concentrations measured by ICP-MS. The measurements conducted at IES-AS were made using an Agilent 7500s ICP-MS and following the procedure described by Ionov et al. (1992) and adapted by Godard et al. (2000) for the analysis of ultra-depleted peridotites. At the GET laboratory, a Thermo Scientific™ Element XR™ HR-ICP-MS was used following the analytical procedure developed in Rospabé et al. (2018a) and adapted from Yokoyama et al. (1999) for the sample digestion method, Bizzarro et

Table 1. Summary of the LA-ICP-MS instrument operating conditions.

ICP-MS instrument	Agilent 7500ce quadrupole
Laser ablation system	NewWave Research UP-213 Nd:YAG deep UV (213 nm)
Plasma power	1500 W
Plasma gas flow	Ar, 13 L min^{-1}
Carrier gas flow	Ar, 1.4 L min^{-1}
Fluence on sample	12.0 J cm^{-2}
Beam diameter	100 µm
Repetition rate	5 Hz (glasses)–10 Hz (pressed powder pellets)
Ablation mode	Single spot
Acquisition mode	Time-resolved analysis with 40 s gas blank, 60 s acquisition, and 120 s washout
Reference materials	NIST SRM 612, BHVO-2G (see text)
Reference values	Jochum et al. (2005, 2011)
Internal standard element	^{29}Si
Monitored isotopes	^{7}Li, ^{45}Sc, ^{49}Ti, ^{51}V, ^{52}Cr, ^{55}Mn, ^{59}Co, ^{62}Ni, ^{65}Cu, ^{67}Zn, ^{71}Ga, ^{85}Rb, ^{88}Sr, ^{89}Y, ^{90}Zr, ^{93}Nb, ^{133}Cs, ^{137}Ba, ^{139}La, ^{140}Ce, ^{141}Pr, ^{143}Nd, ^{147}Sm, ^{151}Eu, ^{158}Gd, ^{159}Tb, ^{163}Dy, ^{165}Ho, ^{166}Er, ^{169}Tm, ^{172}Yb, ^{175}Lu, ^{178}Hf, ^{181}Ta, ^{208}Pb, ^{232}Th, ^{238}U
Control reference materials	BHVO-2/2G, BIR-1a/1G, JP-1 (see text)

al. (2003) and Qi et al. (2005) for the (ultra-)trace element separation, and Barrat et al. (1996) for the Tm addition and calculation of the concentrations using the Tm positive anomaly in the REE pattern. To compare the accuracy and the precision between these two laboratories, trace element measurements were performed on a selection of replicate samples, and the same reference materials have been analysed as unknowns (the GSJ peridotite JP-1 and the USGS dunite DTS-2b).

3 Results and discussion

3.1 Validity of the developed method and measurement precision

Figure 3 shows plots of the results obtained for the reference materials BHVO-2/BHVO-2G, BIR-1a/BIR-1G and JP-1 following their analysis by LA-ICP-MS (glasses and two-time milled pressed powder pellets) and by XRF (one-time milled pressed powder pellets) during Leg 3. Measured concentrations are normalized to preferred values. Error bars represent the standard deviation, reflecting the intermediate precision (or repeatability over the different analytical sessions) of the averaged composition of n measurements (see Fig. 3 caption). The chondrite-normalized REE and multi-element patterns of the analysed pressed powder pellets are shown in Fig. 4, and the evolution of the relative standard deviation (RSD) relative to the measured element concentrations is shown in Fig. 5.

3.1.1 Minor to trace element concentrations determined by XRF

The results obtained by XRF for the minor to trace elements (Sc, V, Cr, Co, Ni, Cu, Zn, Ga, Rb, Sr, Y, Zr, Nb, Ba) for the two reference materials BHVO-2 and JP-1 are described here. For the reference material BHVO-2, the determined concentrations for Cr, Ni, Cu, Zn and Sr are very close to the preferred values (difference $\delta PV < 10\,\%$, with δPV as the relative deviation of measured concentration values from the preferred values (PV) in %) with a repeatability better than 5 % as well as for Ga and Rb but with a poorer repeatability ($< 30\,\%$; Figs. 3a and 4a). The concentrations for Sc, Zr and Nb fall within $\delta PV < 25\,\%$ with a repeatability better than 1.5 % for Sc and Zr and 10 % for Nb. The concentrations are overestimated for Co ($\delta PV \sim +30\,\%$) and especially for Ba and V ($\delta PV > +60\,\%$) and underestimated for Y ($\delta PV \sim -40\,\%$; Fig. 3a). For the reference material JP-1, the concentrations obtained for Cr, Ni and Zn are in good agreement with the preferred values ($\delta PV < 10\,\%$), with a repeatability better than 5 %, as well as for Cu but with a poor repeatability (59 %; Fig. 3c). The Co content is slightly underestimated ($\delta PV \sim -25\,\%$). However, the low concentrations for Sc, V, Ga, Rb, Sr, Y, Zr, Nb and Ba were not ac-

Table 2. Trace element concentrations ($\mu g\,g^{-1}$) for BHVO-2, BIR-1a and JP-1 determined by LA-ICP-MS analyses of pressed powder pellets on-board the D/V *Chikyu*.

	DL[a]	BHVO-2				BIR-1a				JP-1			
		PV[b]	Mean ($n=7$)	SD	% RSD	PV[b]	Mean ($n=5$)	SD	% RSD	PV[b]	Mean ($n=10$)	SD	% RSD
Li	0.0123	4.7	4.42	0.578	13.1 %	3.203	2.95	0.360	12.2 %	1.68	1.58	0.0872	5.5 %
Sc	0.2500	32.3	30.5	0.873	2.9 %	43	40.3	1.81	4.5 %	7.08	10.0	0.753	7.5 %
Ti	0.2754	16364	15650	2785	17.8 %	5400	5151	309	6.0 %	47.8	20.5	3.49	17.0 %
V	0.1020	317	318	19.3	6.1 %	326	348	40.8	11.7 %	40	23.4	2.00	8.5 %
Cr	0.6835	280	280	53.3	19.0 %	392	415	28.2	6.8 %	2959	2385	271.46	11.4 %
Mn	0.5615	1290	1358	55.8	4.1 %	1345	1827	219	12.0 %	919	1056	17.72	1.7 %
Co	0.0112	45	47.1	1.70	3.6 %	52	64.4	11.6	18.0 %	113	136	5.73	4.2 %
Ni	0.0487	121	135	4.03	3.0 %	178	222	43.5	19.6 %	2443	3142	134.26	4.3 %
Cu	0.7973	123	144	7.01	4.9 %	119	158	27.6	17.5 %	3.84	4.15	0.695	16.7 %
Zn	0.0786	101	93.5	11.9	12.7 %	78	107	37.5	35.0 %	45.1	54.2	6.75	12.5 %
Ga	0.0331	20.6	22.5	2.50	11.1 %	15	16.3	2.85	17.5 %	0.518	0.632	0.0589	9.3 %
Rb	0.0060	9.08	8.36	0.638	7.6 %	0.197	0.280	0.0379	13.5 %	0.348	0.356	0.0339	9.5 %
Sr	0.0038	396	385	16.0	4.2 %	109	111	6.49	5.9 %	0.675	0.491	0.0687	14.0 %
Y	0.0020	27.6	22.7	1.22	5.4 %	14.3	15.2	0.649	4.3 %	0.1	0.0938	0.0147	15.7 %
Zr	0.0042	164.9	157	9.07	5.8 %	14	14.6	3.83	26.3 %	8.83	5.58	1.07	19.2 %
Nb	0.0006	16.82	18.4	0.970	5.3 %	0.52	0.626	0.285	45.5 %	0.0298	0.0285	0.0063	22.3 %
Cs	0.0012	0.096	0.0983	0.0165	16.8 %	0.007	0.0419[c]	0.0322	76.9 %	0.037	0.0457	0.0067	14.8 %
Ba	0.0085	131	129	6.39	4.9 %	6.5	7.23	0.780	10.8 %	8.98	8.75	0.861	9.8 %
La	0.0007	15.2	14.9	0.871	5.9 %	0.609	0.613	0.0184	3.0 %	0.0264	0.028	0.0049	17.3 %
Ce	0.0011	37.5	37.9	2.35	6.2 %	1.89	2.13	0.229	10.7 %	0.0576	0.0906[c]	0.0164	18.1 %
Pr	0.0005	5.31	5.19	0.257	5.0 %	0.37	0.388	0.0244	6.3 %	0.00719	0.0077	0.0014	17.7 %
Nd	0.0023	24.5	23.5	0.968	4.1 %	2.37	2.36	0.113	4.8 %	0.0296	0.0327	0.0072	21.9 %
Sm	0.0019	6.07	5.79	0.389	6.7 %	1.09	1.07	0.0947	8.9 %	0.00739	0.0085	0.0018	21.5 %
Eu	0.0010	2.07	2.03	0.127	6.2 %	0.517	0.513	0.0169	3.3 %	0.00162	0.0018	0.0004	22.7 %
Gd	0.0024	6.24	5.83	0.375	6.4 %	1.85	1.72	0.0801	4.7 %	0.00827	0.0087	0.0035	39.9 %
Tb	0.0005	0.94	0.867	0.0498	5.7 %	0.35	0.329	0.0148	4.5 %	0.00164	0.0016	0.0004	24.1 %
Dy	0.0026	5.31	4.97	0.264	5.3 %	2.55	2.41	0.0763	3.2 %	0.0132	0.0131	0.0027	20.3 %
Ho	0.0006	1	0.926	0.0733	7.9 %	0.56	0.542	0.0283	5.2 %	0.00329	0.0030	0.0007	23.3 %
Er	0.0019	2.54	2.31	0.0972	4.2 %	1.7	1.61	0.0814	5.1 %	0.0115	0.0105	0.0026	24.7 %
Tm	0.0006	0.35	0.305	0.0137	4.5 %	0.24	0.245	0.0209	8.5 %	0.0024	0.0025	0.0005	20.7 %
Yb	0.0027	2	1.91	0.117	6.2 %	1.64	1.64	0.0944	5.7 %	0.0198	0.0176	0.0039	22.1 %
Lu	0.0006	0.27	0.264	0.0167	6.3 %	0.248	0.221	0.0101	4.6 %	0.00371	0.0036	0.0005	13.5 %
Hf	0.0011	4.474	4.11	0.113	2.7 %	0.57	0.531	0.0284	5.4 %	0.193	0.128	0.0226	17.6 %
Ta	0.0003	1.10	1.12	0.0482	4.3 %	0.036	0.0344	0.0051	14.7 %	0.00345	0.0026	0.0005	18.7 %
Pb	0.0032	1.51	2.11	0.215	10.2 %	3.7	4.79	1.01	21.2 %	0.0987	0.106	0.0084	7.9 %
Th	0.0002	1.21	1.20	0.0871	7.3 %	0.03	0.0291	0.0026	8.9 %	0.0108	0.0094	0.0016	17.1 %
U	0.0002	0.41	0.503	0.0461	9.2 %	0.023	0.0156	0.0033	21.2 %	0.0106	0.0111	0.0015	13.2 %

[a] Detection limit (or blank) with the used instrumentation, corresponding to the average of the signal background. [b] Preferred values (BHVO-2: Barrat et al., 2012; BIR-1a: GeoReM; JP-1: Barrat et al., 2008 (Ti, V, Sr, Zr, Hf), Makishima and Nakamura, 2006 (Tm), Rospabé et al., 2018a (other elements)). [c] The determined values differed signifcantly from the preferred values and were reported here just as indications.

curately determined for JP-1 using the XRF, and the obtained values differ significantly from the preferred values (Figs. 3c and 4c).

3.1.2 Minor and trace to ultra-trace element concentrations determined by LA-ICP-MS

The parameters of the laser ablation system and of operating conditions (Table 1) were adjusted by analysing the two reference glasses BHVO-2G and BIR-1G. Most of the 37 elements selected to be analysed fall within the 10 % difference range from the preferred values (Fig. 3a, b). Exceptions in BIR-1G are the concentration for Th that is slightly overestimated over the $\delta PV = +20\,\%$ as well as that for Cs that was not determined precisely (the lowest concentration in BIR-1G over the 37 measured elements, $8\,ng\,g^{-1}$ proposed by Jochum et al., 2005). The averaged repeatability for all the analysed elements is better than 7.8 % for BHVO-2G and 12.8 % for BIR-1G, which appeared sufficiently precise to apply the optimized parameters for the analysis of the two-time milled pressed powder pellets.

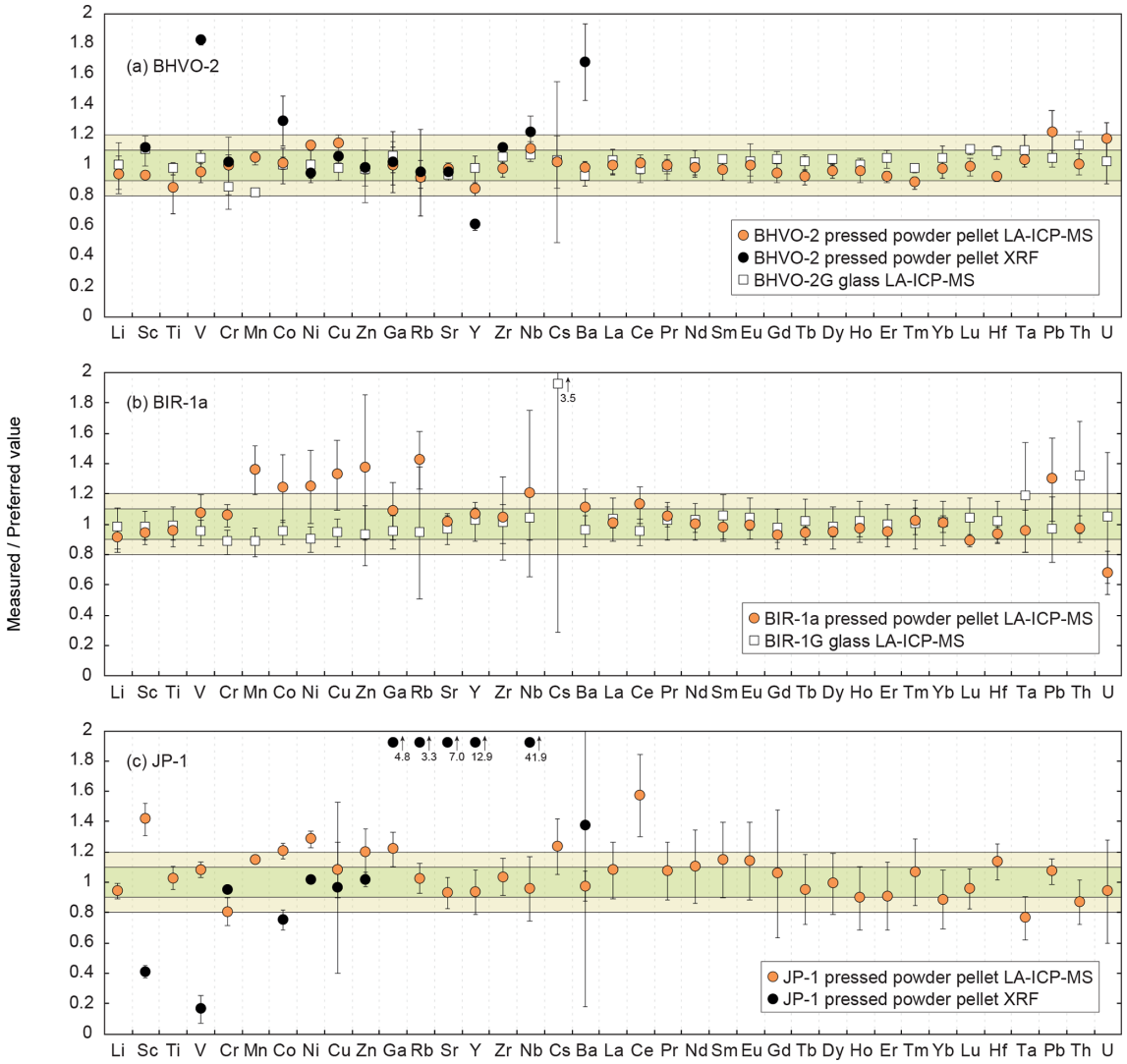

Figure 3. Plots of the results obtained using the LA-ICP-MS dry method developed on-board the D/V *Chikyu* on pressed powder pellets and glass normalized to preferred values for the standard materials **(a)** BHVO-2 ($n = 7$) and BHVO-2G ($n = 4$), **(b)** BIR-1a ($n = 5$) and BIR-1G ($n = 17$), and **(c)** JP-1 ($n = 10$). Data obtained by XRF (D/V *Chikyu*) on pressed powder pellets are shown for BHVO-2 and JP-1. Error bars represent the standard deviation, reflecting the intermediate precision (or repeatability) of the averaged composition of the multiple n measurements. The horizontal green and light green fields indicate the 10 % and 20 % δPV, respectively. Preferred values are from Jochum et al. (2005) for BHVO-2G and BIR-1G, from Barrat et al. (2012) for BHVO-2, from GeoReM (http://georem.mpch-mainz.gwdg.de, 12 July 2018) for BIR-1a, and from Barrat et al. (2008) (Ti, V, Sr, Zr, Hf), Makishima and Nakamura (2006) (Tm), and Rospabé et al. (2018a) (all other elements) for JP-1.

Results obtained by LA-ICP-MS analysis of pressed powder pellets prepared for the three reference materials BHVO-2, BIR-1a, and JP-1 are shown in Fig. 3 with the obtained concentrations normalized to preferred values and in Fig. 4 with their chondrite-normalized REE and multielement patterns plotted. The relative standard deviations relative to the measured element concentrations are shown in Fig. 5. The concentrations determined by LA-ICP-MS for these three reference materials are given in Table 2. The measured concentrations for minor and (ultra-)trace elements are generally close to preferred values, with most elements within $\delta\text{PV} < 10\,\%$ for BHVO-2 and BIR-1a and within $\delta\text{PV} < 20\,\%$ for JP-1 (Fig. 3). The shapes of their normalized REE and multielement patterns are adequate compared to the ones plotted with reference values (Fig. 4). The precision is variable depending on the standard analysed and the element considered and basically decreases with lower concentrations: the averaged repeatability for all the analysed elements is better than 7.1 %, 11.6 %, and 15.1 % for BHVO-2, BIR-1a, and JP-1, respectively. In detail for BHVO-2, the RSD is generally better than 6 % for elements with a concentration higher than 10 µg g^{-1} and comprised between 6 %

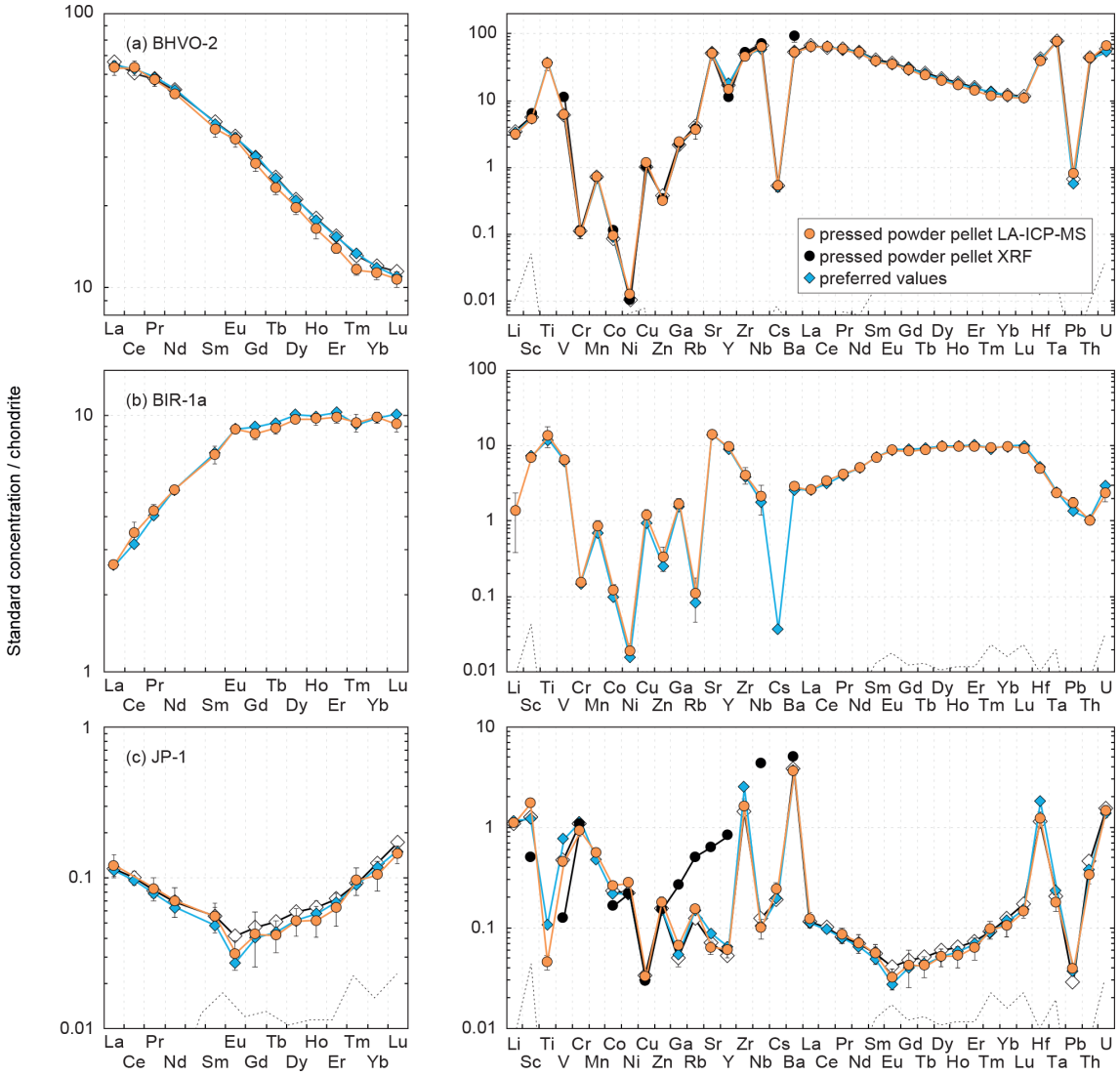

Figure 4. Chondrite-normalized (normalization values from Barrat et al., 2012) REE and multielement patterns obtained for the reference materials **(a)** BHVO-2, **(b)** BIR-1a and **(c)** JP-1 by LA-ICP-MS and XRF analyses of pressed powder pellets performed on-board the D/V *Chikyu*, compared to the preferred values. Preferred values are from the same references given in the Fig. 3 caption. Patterns obtained by Garbe-Schönberg and Müller (2014) for BHVO-2 and Peters and Pettke (2017) for JP-1 by the analysis of pressed powder pellets (prepared without a binder for BHVO-2, with a binder for JP-1) by LA-ICP-MS are also shown for comparison (white diamonds). The black dotted line represents the detection limit with the used instrumentation (values are given in Table 2).

and 10 % for concentrations ranging from 0.1 to 10 µg g^{-1}, with a few exceptions (Fig. 5a). For BIR-1a, with a few exceptions (especially transition elements as discussed below), the RSD is better than 10 % for elements with concentrations higher than 10 µg g^{-1}, better than 15 % for concentrations ranging from 0.1 to 10 µg g^{-1} (including the Rare Earth Elements, among others), and increases up to 20 %–25 % for elements with a concentration lower than 0.1 µg g^{-1} (Ta, Th, U; Fig. 5b). Concerning JP-1, the increase in the RSD with lower concentrations is very clear, better than 15 % for concentrations higher than 0.1 µg g^{-1} (most of the transition elements and large ion lithophile elements) and mostly ranging from 15 % to 25 % for lower concentrations (Rare Earth Elements and other (ultra-)trace elements; Fig. 5c).

In detail:

– Transition elements (Sc, Ti, V, Cr, Mn, Co, Ni, Cu, Zn) and Ga

  Except for Ti, the transition elements and Ga have been determined both by XRF and LA-ICP-MS analytical methods for BHVO-2 and JP-1 (only by laser ablation for BIR-1a). For BHVO-2, with only a few exceptions, the transition elements and Ga ($20.6 \leq PV \leq 16364$ µg g^{-1}) have been determined ac-

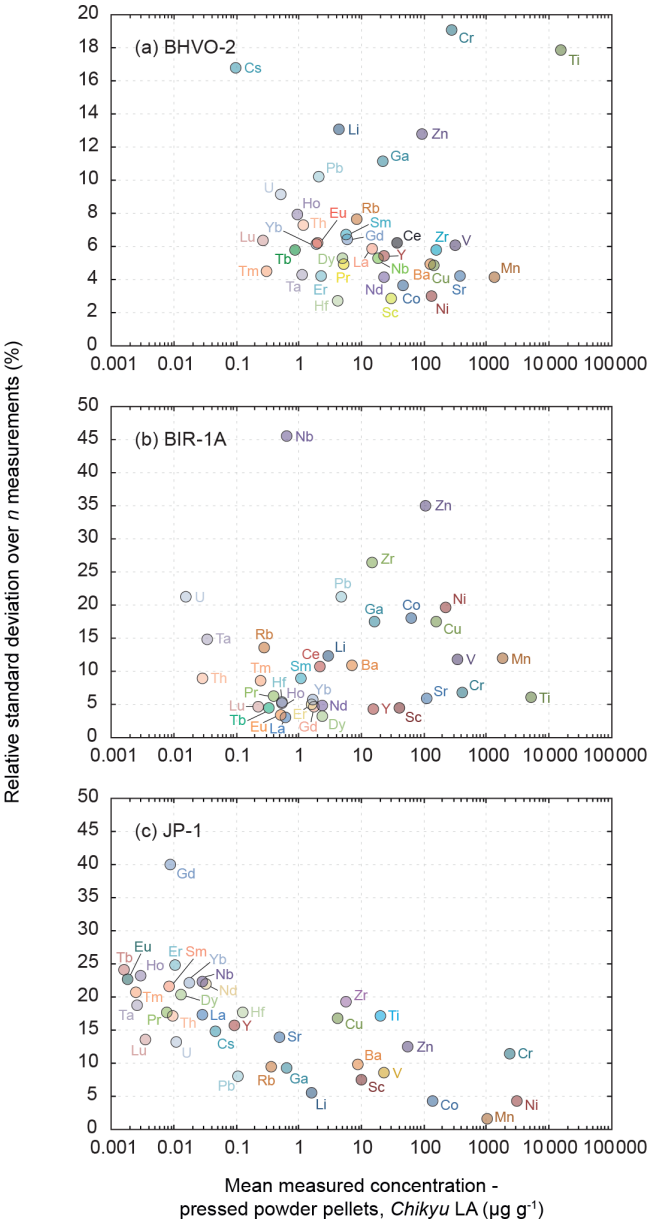

Figure 5. Evolution of the relative standard deviation (RSD, in %) relative to the measured element concentrations in the reference materials **(a)** BHVO-2 ($n = 7$), **(b)** BIR-1a ($n = 5$) and **(c)** JP-1 ($n = 10$). The RSD represents the intermediate precision (or repeatability) of the averaged composition of the multiple n measurements. Note the change in the scale of the y axis from BHVO-2 to BIR-1a and JP-1.

curately by laser ablation, differing by less than 10 % from preferred values (Fig. 3a). The repeatability over the different measurements is better than 5 % for Sc, Mn, Co, Ni and Cu, 10 % for V, 15 % for Zn and Ga, and 20 % for Ti and Cr (Fig. 5a). For BIR-1a, the Sc, Ti, V, Cr and Ga concentrations ($15.0 \leq \mathrm{PV} \leq 1345\,\mu g\,g^{-1}$) have been determined accurately, falling within the $\delta\mathrm{PV} < 10\,\%$ variation range from the preferred values (Fig. 3b). The repeatability is better than 6.8 % for Sc, Ti and Cr, better than 11.7 % for V, and better than 17.5 % for Ga (Fig. 5b). Cobalt ($\mathrm{PV} = 52.0\,\mu g\,g^{-1}$) and Ni ($\mathrm{PV} = 178\,\mu g\,g^{-1}$) are slightly overestimated ($\delta\mathrm{PV} \sim +25\,\%$), but the accuracy is lower for the determination of the Mn, Cu and Zn concentrations that appear overestimated by 30 % to 40 % (Fig. 3b); the precision for these elements is notably worse, with a repeatability better than 12 % for Mn and 20 % for Co, Ni and Cu but reaching 35 % for Zn (Fig. 5b). Concerning the reference material JP-1, the accuracy of the determination of the transition elements is variable according to the element considered: the concentrations determined by LA-ICP-MS are relatively close to preferred values ($\delta\mathrm{PV} < 20\,\%$) for Ti, V, Cr, Mn, Co, Cu and Zn ($3.84 \leq \mathrm{PV} \leq 2959\,\mu g\,g^{-1}$; Fig. 3c), with a repeatability better than 1.7 % for Mn, 4.2 % for Co, 8.6 % for V, 12.5 % for Cr and Zn, and 17 % for Ti and Cu (Fig. 5c). Nickel ($\mathrm{PV} = 1443\,\mu g\,g^{-1}$) and Ga ($\mathrm{PV} = 518\,ng\,g^{-1}$) ($\delta\mathrm{PV} \sim +25\,\%$, with a repeatability better than 4.3 % and 9.4 %, respectively) and especially Sc ($\mathrm{PV} = 7\,\mu g\,g^{-1}$; $\delta\mathrm{PV} \sim +40\,\%$) are slightly to significantly overestimated. For JP-1, the Cr, Ni, Cu and Zn concentrations have thus been determined with a better accuracy using the XRF (Fig. 3c).

– Rare Earth Elements

The Rare Earth Elements (REEs) have been analysed using the LA-ICP-MS method only. The averaged repeatability of their measurement is 5.8 % for BHVO-2 (4.1 %–7.9 %), 5.6 % for BIR-1a (3.0 %–10.7 %), and 20.8 % for JP-1 (13.5 %–24.7 %, excepting 39.9 % for Gd; Fig. 5). Note that the Ce content is not included in the JP-1 REE pattern (Fig. 4c) as the concentration was regularly high for this reference material compared to the preferred value (Fig. 3c; Table 2). For the three reference materials, the REE concentrations are in good agreement with previously proposed values (Fig. 3): with a few exceptions they fall within the 10 % variation range from the preferred values ($\mathrm{PV} = 0.27$–$37.5\,\mu g\,g^{-1}$ for BHVO-2, 0.24–2.55 $\mu g\,g^{-1}$ for BIR-1a, and 1.62–57.6 $ng\,g^{-1}$ for JP-1), and the shape of the chondrite-normalized REE patterns fits with previous analyses (Fig. 4). Interestingly, the measured REEs show a slight fractionation from heavy REEs (slightly underestimated relative to preferred values, $-10\,\% < \delta\mathrm{PV} < 0\,\%$) to light REEs (slightly overestimated, $0\,\% < \delta\mathrm{PV} < 10\,\%$; Fig. 3). Such bias has already been reported and discussed for the analysis of pressed powder pellets by Peters and Pettke (2017, and references therein). They proposed that it could possibly reflect a matrix effect related to the non-matrix-matched calibration (i.e. in the present study, NIST SRM 612 glass used to calibrate pressed powder pellets of standards).

– High-Field-Strength Elements (Zr, Nb, Hf, Ta) and other (ultra-)trace elements (Y, Pb, Th, U)

  For BHVO-2, the measured concentrations are very close to preferred values, $\delta PV < 10\,\%$ for the High-Field-Strength Elements (HFSE) and Th ($1.10 \leq PV \leq 165\,\mu g\,g^{-1}$) and $\delta PV < 20\,\%$ for other trace elements ($0.41 \leq PV \leq 27.6\,\mu g\,g^{-1}$; Fig. 3a). Yttrium, Zr and Nb are more precisely determined using the laser ablation method than by XRF. The repeatability for these elements is better than 5.4 % for Y, 5.8 % for HFSE, 9.8 % for Th and U, and 10.2 % for Pb (Fig. 5a). For BIR-1a, except for Pb and U (repeatability better than 21.2 % for both; Fig. 5b) that are slightly overestimated and underestimated, respectively ($PV_{Pb} = 3.70\,\mu g\,g^{-1}$, $PV_U = 23\,ng\,g^{-1}$), the determined concentrations for HFSE and other (ultra-)trace elements ($30\,ng\,g^{-1} \leq PV \leq 27.6\,\mu g\,g^{-1}$) vary within 10 % from the preferred values ($\delta PV = +20\,\%$ for Nb only; Fig. 3b). The repeatability is better than 5 % for Y, 10 % for Hf and Th, and 15 % for Ta (Fig. 5b). However, the precision is worse concerning the averaged measurements for Zr (26.4 %) and especially Nb (45.5 %) in spite of the apparent good determination of their concentration (Figs. 3b and 4b). It potentially results from microfragments of trace minerals rich in HFSE in this powder standard related to grain size effects (or "nugget effects", Peters and Pettke, 2017; see also Garbe-Schönberg and Müller, 2014) and/or to the analytical difficulty in determining the concentration of these elements (e.g. Ionov et al., 1992; Jochum et al., 1990; Weyer et al., 2002). For JP-1, with the exception of Y, which was also analysed but inaccurately determined by XRF, the measurement of the HFSEs and other (ultra-)trace elements have been determined using the LA-ICP-MS method only (Figs. 3c and 4c), their low concentrations being several orders below the detection limits of the XRF ($3.45\,ng\,g^{-1}$ (Ta) $\leq PV \leq 113\,ng\,g^{-1}$ (Hf), except Zr with $PV = 5.39\,\mu g\,g^{-1}$). The determined Zr and Nb differ by less than 4.5 % from the preferred values, and Hf and Ta are moderately overestimated and underestimated, respectively ($\delta PV = +15\,\%$ and $-24\,\%$, respectively; Fig. 3c). The measured Y, Pb and U fall within the $\delta PV < 7.5\,\%$ variation range and $\delta PV = 13.0\,\%$ for Th ($10.6\,ng\,g^{-1} \leq PV \leq 100\,ng\,g^{-1}$). The repeatability is better than 10 % for Pb and 20 % for other elements (except Nb: 22.3 % and U: 36.1 %; Fig. 5c).

– Lithium and large-ion lithophile elements (Rb, Sr, Cs, Ba)

  The determined concentrations for Li in the three reference materials fall within $\delta PV < 10\,\%$ regarding the preferred values ($PV_{Li} = 4.70\,\mu g\,g^{-1}$ for BHVO-2, $3.20\,\mu g\,g^{-1}$ for BIR-1a, and $1.68\,\mu g\,g^{-1}$ for JP-1; Fig. 3). The repeatability for Li is better than 13.1 %, 12.3 % and 5.5 % for BHVO-2, BIR-1a and JP-1, respectively (Fig. 5). For BHVO-2, the measured contents in Large-Ion Lithophile Elements (LILE) are also very close to reference values ($96\,ng\,g^{-1}$ (Cs) $\leq PV \leq 131\,\mu g\,g^{-1}$ (Ba); Fig. 3a), with a repeatability better than 7.7 % except for Cs (16.8 %) (Fig. 5a). In BIR-1a, Rb and especially Cs have not been determined precisely or accurately, likely related to their low concentration ($PV_{Rb} = 197\,ng\,g^{-1}$, $PV_{Cs} = 7\,ng\,g^{-1}$). The determined Sr and Ba concentrations are close to preferred values ($PV_{Sr} = 109\,\mu g\,g^{-1}$, $PV_{Ba} = 6.50\,\mu g\,g^{-1}$; Fig. 3b), with a repeatability over several measurements better than 6 % and 11 %, respectively (Fig. 4b). For JP-1, the determined concentrations for Rb, Sr and Ba ($0.35\,\mu g\,g^{-1} \leq PV \leq 8.98\,\mu g\,g^{-1}$) are likewise very close to the preferred values (Fig. 2c), with a repeatability better than 10 % for Rb and Ba and better than 14 % for Sr (Fig. 5c). Cs is slightly overestimated ($PV = 37\,ng\,g^{-1}$, $\delta PV = +23\,\%$; Fig. 3c), with a repeatability better than 15 % (Fig. 5c). For BHVO-2 and JP-1, the LILE values have been determined with a similar or better accuracy by using the LA-ICP-MS method than by using the XRF (Figs. 3a, c and 4a, c).

3.2 Application to the OmanDP CM cores

The same procedure for preparation of pressed powder pellets and analysis by LA-ICP-MS has been applied for a selection of gabbro and dunite samples from the OmanDP CM holes during Leg 3. Replicates were analysed for four gabbro and three dunite samples from Hole CM1A in on-shore laboratories after Leg 3. Results are compared and discussed in Figs. 6 and 7 for gabbros and Figs. 9 and 10 for dunites. The chondrite-normalized REE and multielement patterns for both gabbros and dunites are shown in Fig. 8. The element concentrations discussed below for these core samples (both obtained by LA-ICP-MS during Leg 3 and replicate values) are given in the Supplement.

3.2.1 Hole CM1A gabbro samples

The four gabbro samples analysed by laser ablation are CM1A-6Z-2, 12–17 cm (Fig. 6a), CM1A-18Z-1, 26–33 cm (Fig. 6b), CM1A-25Z-4, 50–59 cm (Fig. 6c), and CM1A-41Z-2, 0–6 cm (Fig. 6d). They were also analysed as replicates by solution analysis by ICP-MS at the University of Southampton (see Sect. 2.4). For all elements for which the laser ablation analyses fit with the replicate analyses (i.e. excluding the few elements not accurately determined as detailed below), the averaged δRV (relative deviation of measured concentration values from the replicate values (RV) in %) for the four samples together is +0.6 %. The difference δRV individually varies from −6.7 % (Fig. 6a) to +5.6 % (Fig. 6c), meaning that the difference between the concen-

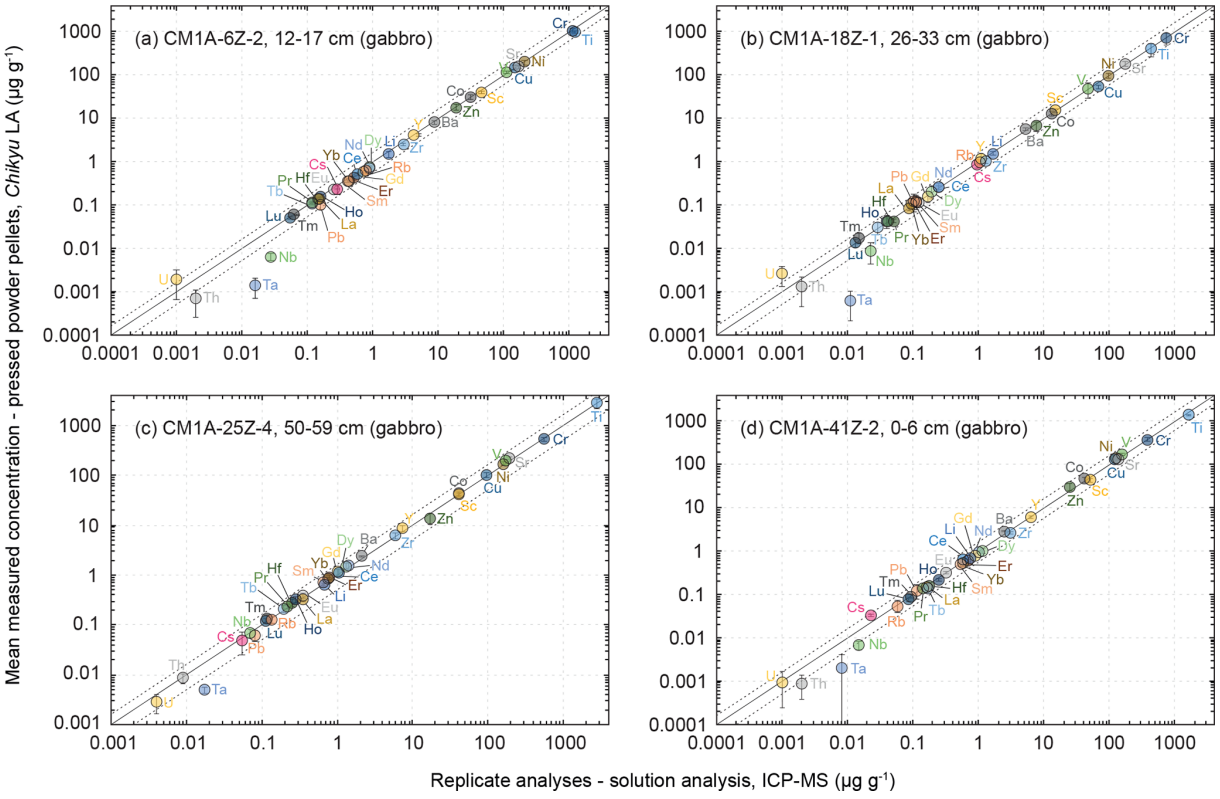

Figure 6. Comparison of the mean measured concentrations obtained by LA-ICP-MS on pressed powder pellets with the analysed replicates for the same samples (solution analysis, University of Southampton, UK) for four gabbro samples from Hole CM1A. The selected samples are **(a)** CM1A-6Z-2, 12–17 cm ($n = 5$), **(b)** CM1A-18Z-1, 26–33 cm ($n = 5$), **(c)** CM1A-25Z-4, 50–59 cm ($n = 6$), and **(d)** CM1A-41Z-2, 0–6 cm ($n = 6$). The black solid line is the 1 : 1 line between the concentrations determined by LA-ICP-MS on-board the D/V *Chikyu* and for the replicates. The black dashed lines represent 50 % deviation from the 1 : 1 line.

trations determined by the laser ablation method developed on-board the D/V *Chikyu* and the replicates analysed after the Leg 3 campaign is on average lower than 7 % for each gabbro sample. Measurements by laser ablation and replicate solution analyses generally correlate well for element concentrations as low as about 50 ng g^{-1} (Fig. 6).

For three of the four analysed gabbros (Fig. 7a, c and d), the relative standard deviation over several measurements is, with a few exceptions, generally better than 10 to 15 % for concentrations higher than 1 to 2 µg g^{-1} and better than 20 % for concentrations ranging from 0.1 to 1 µg g^{-1}. The precision decreases with lower concentrations, especially below 10 ng g^{-1}. The measurements for the gabbro sample CM1A-18Z-1, 26–33 cm (Fig. 7b) have RSDs generally better than 20 % for concentrations higher than 1 µg g^{-1} and 40 % for concentrations ranging from 10 ng g^{-1} to 1 µg g^{-1}. This sample also displays the lowest trace element contents over the four studied gabbros (Fig. 8a), which could explain the poorer precision.

In detail:

– Transition elements (Sc, Ti, V, Cr, Co, Ni, Cu, Zn)

The concentrations determined using the LA-ICP-MS method for the transition elements differ on average by +0.2 % from the replicates' values, and δRV are between −4.0 % and +5.4 % for individual samples. The averaged repeatability of their measurements is better than 11.3 % for samples plotted in Fig. 6a, c, d and better than 19.4 % for the sample in Fig. 6b. With a few exceptions, the precision is better for Sc (RV = 14.5–51.0 µg g^{-1}), Ti (RV = 420–2834 µg g^{-1}), V (RV = 46.2–171 µg g^{-1}) as well as for Mn and Ga (not analysed for replicates), with a repeatability generally better than 9 % than for Cr (RV = 390–1122 µg g^{-1}), Co (RV = 12.9–41.9 µg g^{-1}), Ni (RV = 95.9–208 µg g^{-1}) and Cu (RV = 66.7–151 µg g^{-1}), with a repeatability mostly better than 15 %, and especially Zn (RV = 7.48–24.8 µg g^{-1}), with a repeatability better than 25 % (Fig. 7). The precision here is not directly related to concentrations, and precisions poorer than for other elements have also been observed for Cr, Ni and Zn for reference materials (Fig. 5). It can be related to a grain size effect between plagioclase and clinopyroxene of the gabbros

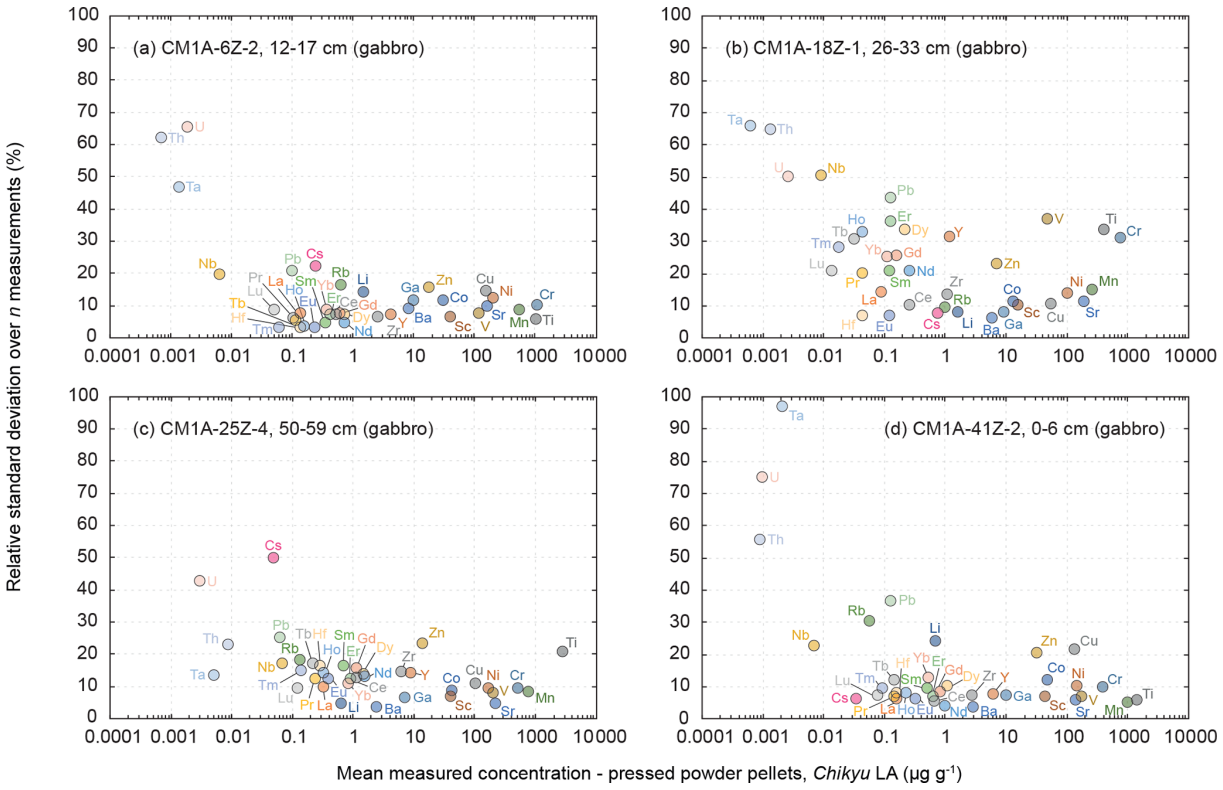

Figure 7. Evolution of the relative standard deviation (RSD, in %) relative to the measured element concentrations for the four gabbro samples from the Hole CM1A **(a)** CM1A-6Z-2, 12–17 cm ($n = 5$), **(b)** CM1A-18Z-1, 26–33 cm ($n = 5$), **(c)** CM1A-25Z-4, 50–59 cm ($n = 6$), and **(d)** CM1A-41Z-2, 0–6 cm ($n = 6$).

that do not incorporate these elements into the same proportions, even if the n measurements (five or six) seem to be numerous enough to get an average concentration for each element fitting relatively well with the replicate values (Figs. 6 and 8). It was also shown that the sample milling (steel jaws of the crusher) or preparation of pellets (the press) could eventually slightly contaminate the powder in metal elements (Garbe-Schönberg and Müller, 2014; Peters and Pettke, 2017). Such contamination during the preparation of the pressed powder pellets is unlikely here, as in the present study, the pellets were pressed using Prolene film to isolate the powder from the load (Sect. 2.3.1), and the ablation signal was integrated in calculations only after a few seconds to discard potential surface contamination (Sect. 2.3.2).

– Rare Earth Elements

As a whole, analyses for the four gabbro samples differ on average by +2.3 % from the replicates' values for the REEs ($-5.0 < \delta RV < +9.8$ %), and the REE patterns obtained by LA-ICP-MS fit relatively well with the ones obtained by replicate solution analyses (Fig. 8a). In detail, the intra-sample repeatability for the REEs analysed by LA-ICP-MS is better than 6.2 % (Fig. 6a; sum of RV REEs = 4.76 µg g^{-1}), 8.3 % (Fig. 6d; sum of RV REEs = 6.64 µg g^{-1}), and 13.4 % (Fig. 6c; sum of RV REEs = 8.61 µg g^{-1}) but reaches 23.4 % for the sample plotted in Fig. 6b (sum of RV REEs = 1.49 µg g^{-1}), with a poorer repeatability for the HREE (Gd-Lu: 29.3 %) than for the LREE (La-Eu: 15.7 %). The poorer precision correlates here with the lower REE contents in this sample (Figs. 7 and 8).

– High-Field-Strength Elements (Zr, Nb, Hf, Ta) and other (ultra-)trace elements (Y, Pb, Th, U)

On average for all the samples, determined Zr (RV = 1.27–5.80 µg g^{-1}) and Hf (RV = 49–250 ng g^{-1}) concentrations are close to the replicates' values, with a mean δRV of −9.4 % ($-16.3 < \delta RV < +5.7$ %) and −3.8 % ($-10.4 < \delta RV < +12.7$ %), respectively. The intra-sample repeatability is better than 15 % for Zr and 10 % for Hf (excepting 16.7 % for the sample in Fig. 6c). For other HFSE, Nb and Ta are among the few elements for which the concentrations are assumed to have not been determined precisely using the LA-ICP-MS for the gabbro samples, as the obtained results do not fit with the replicates' values (RV_{Nb} = 15–70 ng g^{-1}; RV_{Ta} = 8–17 ng g^{-1}). The concentrations obtained for Nb are systematically underestimated by

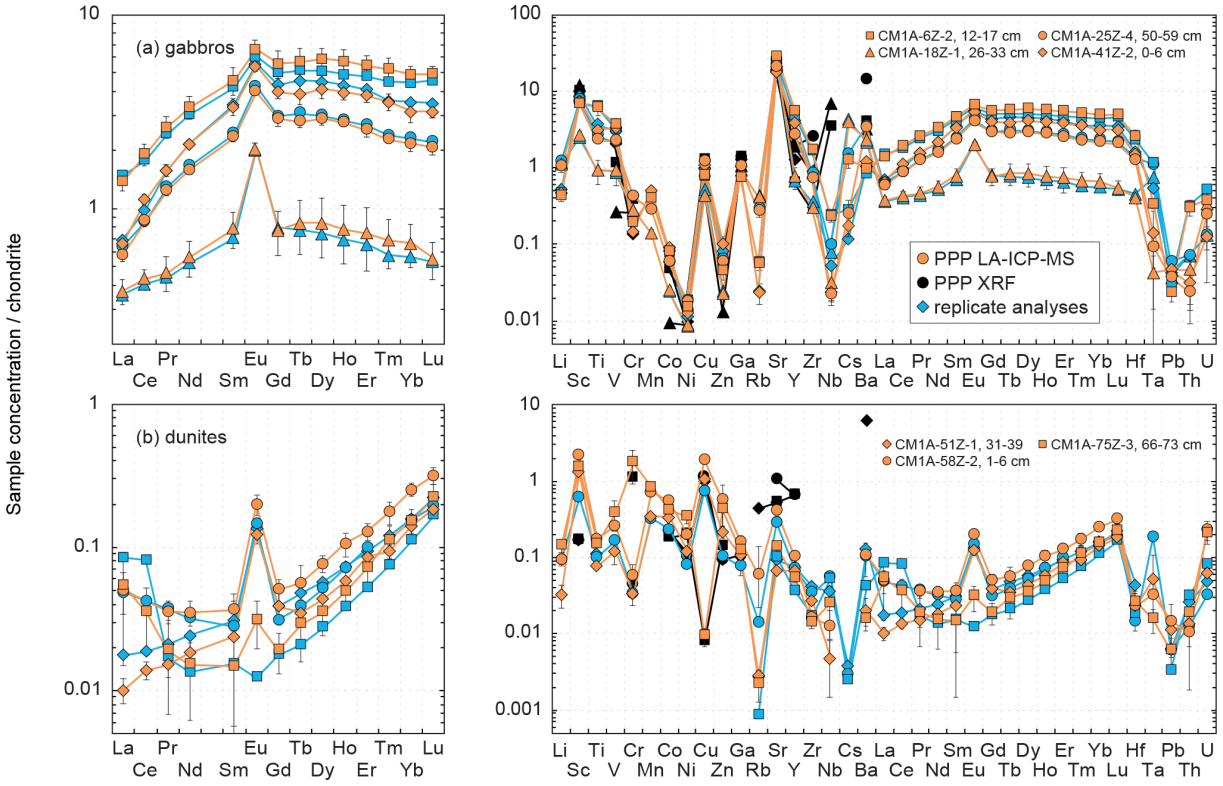

Figure 8. Chondrite-normalized (normalization values from Barrat et al., 2012) REE and multielement patterns obtained for the **(a)** gabbro and **(b)** dunite samples from Hole CM1A by LA-ICP-MS and XRF analyses of pressed powder pellets on-board the D/V *Chikyu*, compared to replicates for the same samples.

more than 50 % excepting the sample in Fig. 6c that shows a $\delta RV = -2.8$ % (with a repeatability better than 17.1 %), while Ta is on average underestimated by more than 80 % (Fig. 6). Concerning other trace to ultra-trace elements, Y (mean $\delta RV = +5.2$ %) and Pb (mean $\delta RV = -6.6$ %) are close to the replicates' values ($RV_{Pb} = 82$–161 ng g^{-1}; $RV_Y = 1.07$–5.46 µg g^{-1}), with an averaged repeatability better than 15.3 % and 31.6 %, respectively. Th, like Nb and Ta, is generally underestimated using the LA-ICP-MS method in comparison with the replicates' values, by about 40 % on average ($RV_{Th} = 2$–9 ng g^{-1}), while U is generally overestimated by about 50 % ($RV_U = 1$–4 ng g^{-1}). Exceptions are the concentrations for Th for the sample shown in Fig. 6c ($\delta RV = -4.0$ %, repeatability better than 23.2 %) and for U for the sample shown in Fig. 6d ($\delta RV = -1.7$ %, with a worse repeatability of 75.1 %). The apparently unreliable determination of Nb, Ta, Th and U in most gabbro samples could likely be attributed to the nugget effect related to grain sizes as evoked above. On the other hand, those elements have concentrations among the lowest in the studied gabbros (Fig. 7), and we thus attribute this unreliable determination to instrumental limitations with the used equipment.

– Lithium and large-ion lithophile elements (Rb, Sr, Cs, Ba)

The concentrations obtained by LA-ICP-MS for Li in the gabbro samples are relatively close to the replicates' values ($RV_{Li} = 0.67$–1.75 µg g^{-1}), with $\delta RV = -8.4$ % on average ($-15.1 < \delta RV < -4.0$ %; Figs. 6 and 8), with a repeatability better than 13.0 % on average (Fig. 7). Measured Cs concentrations are slightly underestimated for samples in Fig. 6a, b and c ($-16.1 < \delta RV < -7.0$ %) but significantly overestimated for the sample in Fig. 6d ($\delta RV = +50.1$ %, with $RV_{Cs} = 22$–813 ng g^{-1}). The repeatability for Cs is also variable, comprised between 6.3 % and 22.4 % for samples in Fig. 6a, b and d, but reaching 50.2 % for the sample in Fig. 6c. In detail, the Cs content for the samples in Fig. 6a and b is 286 and 813 ng g^{-1}, respectively, and 22 and 54 ng g^{-1} for the samples in Fig. 6c and d, respectively. These lower concentrations explain the higher deviation from replicate values and/or the poorer precision for these two latter samples. For other LILE (Rb, Sr, Ba), the obtained results are close to the replicates' values, with an averaged δRV of +2.5 % for these three elements (57 ng g$^{-1} < RV_{Rb} < 1.02$ µg g^{-1}; $RV_{Sr} = 137$–189 µg g^{-1}; $RV_{Ba} = 2.09$–8.54 µg g^{-1}).

The determination of Rb is slightly more accurate ($-8.3 < \delta RV < -2.6\,\%$; mean $-5.1\,\%$) than for Sr ($-8.9 < \delta RV < +16.9\,\%$, mean $+4.3\,\%$) and Ba ($-5.5 < \delta RV < +14.8\,\%$, mean $+8.2\,\%$). The repeatability over the different measurements is on average better than 18.7 % for Rb, 8.0 % for Sr, and 5.8 % for Ba (Fig. 7). The precision here is thus better, with higher concentrations (Sr and Ba), while the accuracy (lower deviation from the replicate values) is better for the less concentrated Rb.

According to the presented results, the lowest concentrations assessed with a high accuracy and good precision (e.g. repeatability better than 10 %) for the gabbro samples fall within the range 50 to 100 ng g^{-1} (Figs. 6 and 7). For a few exceptions we were able to accurately determine concentrations as low as nearly 1 to 10 ng g^{-1} but generally with a poorer repeatability (Fig. 7). For example, we measured concentrations of 13.5 ng g^{-1} for Lu, with a repeatability better than 21.2 % (CM1A-18Z-1, 26–33 cm; Fig. 6b), 8.6 ng g^{-1} for Th with a repeatability better than 23.2 % (CM1A-25Z-4, 50–59 cm; Fig. 6c), and 0.98 ng g^{-1} for U with a repeatability better than 75.1 % (CM1A-41Z-2, 0–6 cm; Fig. 6d).

3.2.2 Hole CM1A dunite samples

The three dunite samples analysed by laser ablation and as replicates are CM1A-51Z-1, 31–39 cm (Fig. 9a), CM1A-58Z-2, 1–6 cm (Fig. 9b), and CM1A-75Z-3, 66–73 cm (Fig. 9c). We will focus here only on the results obtained for the REE, HFSE and other trace to ultra-trace elements in order to evaluate the accuracy on the lowest concentrations (mainly below 100 ng g^{-1}, right part of Fig. 9) reachable using the sample preparation procedure and laser ablation method developed on-board the D/V *Chikyu*.

The measured REE concentrations and the chondrite-normalized REE patterns differ between results obtained by the LA-ICP-MS method and the replicates (Figs. 8b and 9), but only moderately considering that the REE concentrations are mostly below 25 ng g^{-1} in these dunite samples (e.g. $RV_{La} = 4$–20 ng g^{-1}; $RV_{Sm} = 2$–5 ng g^{-1}; $RV_{Yb} = 19$–27 ng g^{-1}). As a whole for the three dunite samples, REE concentrations determined by laser ablation differ on average by $+11.0\,\%$ from the replicates' values. For individual samples, the concentrations appear slightly to moderately underestimated for the sample in Fig. 9a ($\delta RV = -20.2\,\%$) and overestimated for the samples in Fig. 9b and c ($\delta RV = +22.5\,\%$ and $+24.4\,\%$, respectively) in comparison with the replicates' values. In detail, the LREE (La–Eu) are on average generally slightly underestimated ($\delta RV = -8.8\,\%$), especially in La and Ce, while the HREE (Gd–Lu) are slightly overestimated $\delta RV = +14.3\,\%$). It is the reverse trend of the one observed for the slightly overestimated LREE and underestimated HREE in the reference materials (Fig. 3 and Sect. 3.1.2). The repeatability is on average about 20 % for the samples in Fig. 9a and b and reaches 40 % for the sample in Fig. 9c. In detail, the precision decreases with the decreasing concentration in REEs, especially concerning samples in Fig. 10b and c. For sample CM1A-58Z-2, 1–6 cm (Fig. 10b), the RSD increases from about 10 % for REEs with a concentration near 20 ng g^{-1} to 35 % for concentrations near 2 ng g^{-1}. For sample CM1A-75Z-3, 66–73 cm (Fig. 10c), the RSD roughly increases from 20 % (25 ng g^{-1}) to 45 % (1 ng g^{-1}). Concerning sample CM1A-51Z-1, 31–39 cm in Fig. 10a, the precision is better than 20 % for all REEs excepting Gd (RSD = 25.7 %). Similarly to the reference materials and gabbro samples for some elements, the stronger deviation from replicate values together with the poorer precision for the sample in Figs. 9c and 10c correlate with the lower measured REE contents.

Concerning the HFSE, only the concentrations for Hf (averaged $\delta RV = +19.1\,\%$, averaged repeatability better than 42.2 %) and Zr for the sample in Fig. 9c ($\delta RV = -16.2\,\%$, repeatability better than 18.2 %) were determined with a deviation of less than 20 % from the replicates' values ($RV_{Hf} = 2$ ng g^{-1} and $RV_{Zr} = 60$ ng g^{-1} in this sample). The Nb and Ta were significantly underestimated by more than 70 % and 80 %, respectively, using the laser ablation method, similarly to the results obtained for the gabbro samples. It is likely related to the analytical difficulty of precisely determining such elements (e.g. Ionov et al., 1992; Jochum et al., 1990; Weyer et al., 2002) and/or to their low concentrations in such depleted dunites. For example, the determined concentrations for Nb were comprised between 1.4 and 7.3 ng g^{-1} when analysed by laser ablation on-board the D/V *Chikyu* and between 10.3 and 15.9 ng g^{-1} for the replicates' values. Similarly, the determined concentrations for Ta were between 0.2 and 0.8 ng g^{-1} by laser ablation analyses and 2.7 ng g^{-1} for one replicate analysis only. The Th concentration is likewise moderately to significantly underestimated (averaged $\delta RV = -34.3\,\%$ with $RV_{Th} = 0.4$–0.9 ng g^{-1}, except $-16.5\,\%$ for the sample in Fig. 9b but with a poor repeatability of 82.3 %). By contrast, Pb and U are systematically strongly overestimated ($RV_{Pb} = 9$–17 ng g^{-1}, $RV_U = 0.2$–0.6 ng g^{-1}; Fig. 9), once again reminiscent of what was observed for the gabbro sample.

To summarize, the analysis of the dunite samples using the LA-ICP-MS method developed on-board the D/V *Chikyu* allowed us to determine the REE concentrations with a relatively good accuracy with regard to their very low contents in such lithologies and to reach concentrations about an order of magnitude lower in dunites (sum of REEs = 0.10–0.16 µg g^{-1}) than in gabbros (sum of REEs = 1.6–9.5 µg g^{-1}). Regarding these results, the lowest REE contents assessed with relatively high accuracy and good precision (e.g. repeatability better than 20 %) for the dunite samples are as low as 1.5–2 ng g^{-1}. Except for Hf, which seems to have been determined relatively accurately, the accurate determination of concentrations in other HFSE (especially Nb and Ta) and (ultra-)trace elements (Pb, Th,

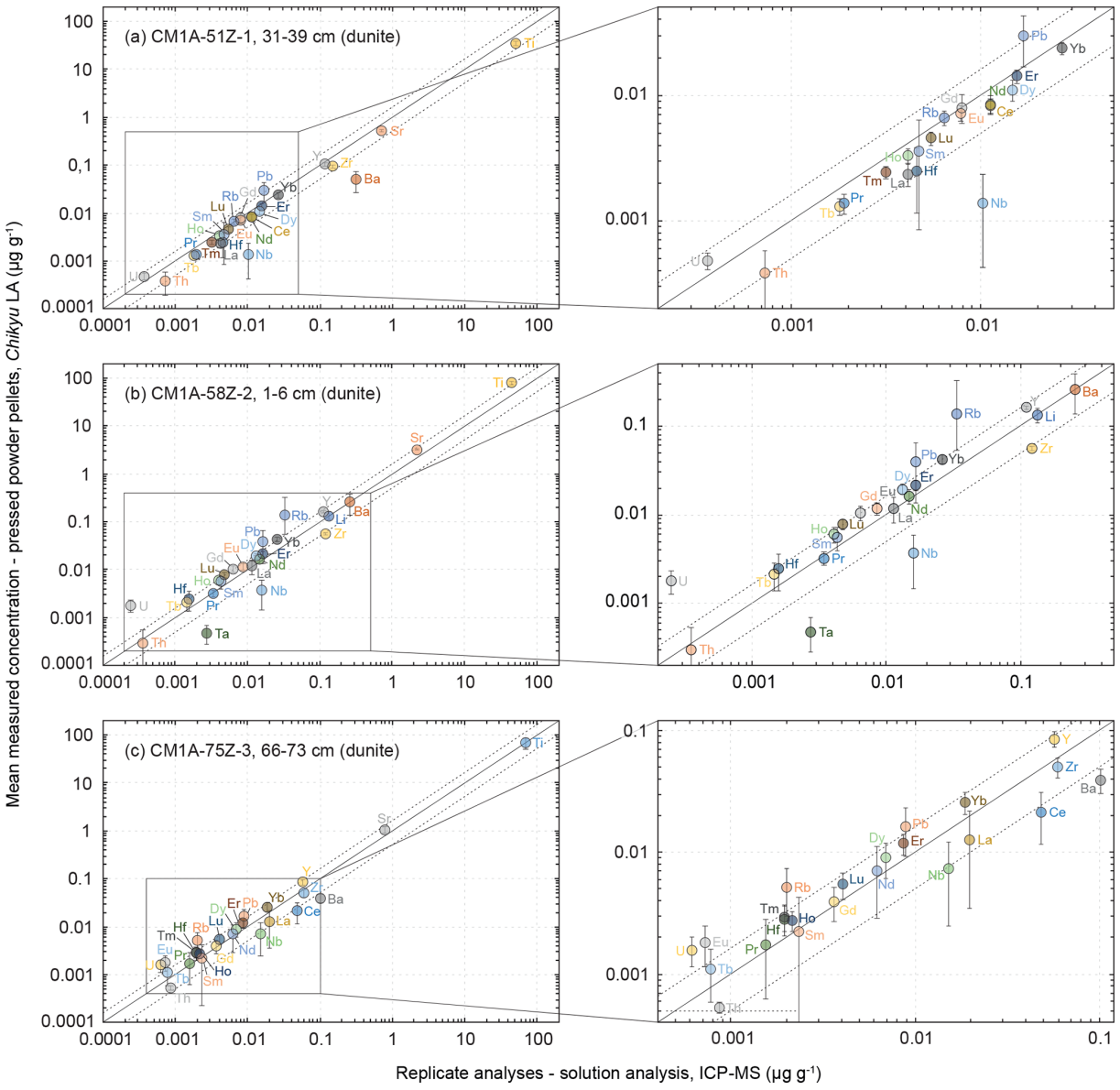

Figure 9. Comparison of the mean measured concentrations obtained by LA-ICP-MS on pressed powder pellets with the analysed replicates for the same samples (solution analysis, IES-AS (Taiwan) for samples in **(a)** and **(c)** and GET (France) for the sample in **(b)**) for three dunite samples from Hole CM1A. The selected samples are **(a)** CM1A-51Z-1, 31–39 cm ($n = 6$), **(b)** CM1A-58Z-2, 1–6 cm ($n = 6$), and **(c)** CM1A-75Z-3, 66–73 cm ($n = 5$). The black solid line is the 1 : 1 line between the concentrations determined by LA-ICP-MS on-board the D/V *Chikyu* and for the replicates. The black dashed lines represent 50 % deviation from the 1 : 1 line.

U) appears to be beyond the analytical limitations of the developed method. However, it is worth noting that the concentrations determined by LA-ICP-MS roughly follow the 1 : 1 line when plotted as a function of the replicates' values (Fig. 9). The analysed elements are as a whole globally slightly underestimated (Fig. 9a) or overestimated (Fig. 9b, c) for a given dunite sample, independently of the laboratory which analysed the replicates, IES-AS (Taiwan) for Fig. 9a and c and GET (France) Fig. 9b, and do not plot randomly. It thus cannot be ruled out that a part of the difference from the replicates may be due to a slight uncertainty related to their analysis in these two external laboratories after Leg 3.

3.3 Effects of the two-step milling

In order to briefly illustrate the necessity of a second-step milling to obtain an average powder grain size fine enough to obtain reliable results for the determination of whole-rock trace elements by LA-ICP-MS, the chondrite-normalized patterns obtained for pressed powder pellets milled one time only (to the left) and two times (in the centre) are shown

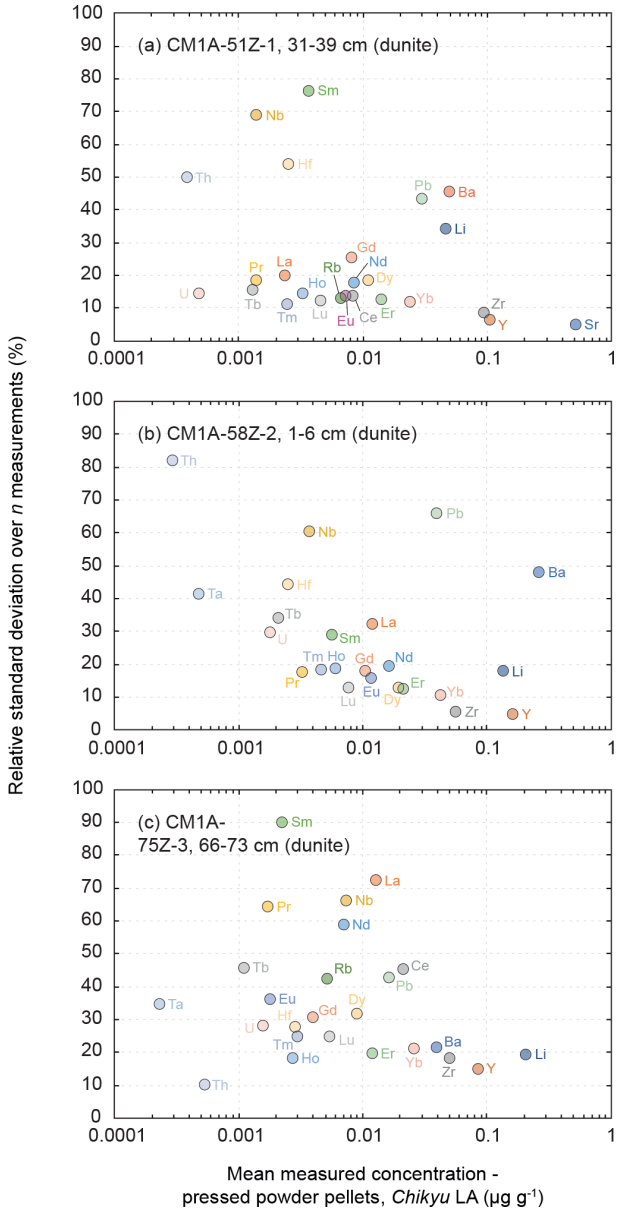

Figure 10. Evolution of the relative standard deviation (RSD, in %) relative to the measured element concentrations for the three dunite samples from the Hole CM1A **(a)** CM1A-51Z-1, 31–39 cm ($n = 6$), **(b)** CM1A-58Z-2, 1–6 cm ($n = 6$), and **(c)** CM1A-75Z-3, 66–73 cm ($n = 5$).

in Fig. 11. The three examples are the reference materials BIR-1a and BHVO-2 and the gabbro sample CM1A-6Z-2, 12–17 cm. For BIR-1a and the gabbro sample, the different grain sizes after one-step and two-step millings are shown in Fig. 2.

The chondrite-normalized REE patterns for individual analyses are much more variable when obtained for one-time milled pressed powder pellets. This is observed for all elements for BIR-1a (Fig. 11a) and BHVO-2 (Fig. 11b) and particularly for HREEs in the gabbro sample (Fig. 11c). The mean measured concentrations for BIR-1a are slightly overestimated in the lighter REEs (> 21 % for La and Ce) and significantly underestimated in HREEs, by 22 % on average from Gd to Lu, relative to preferred values and to the results obtained for the pellet prepared with powder two-time milled (to the right in Fig. 11a). Similar bias in the determination of the REE concentrations has been obtained in analysing a one-time milled pressed powder pellet prepared for the reference material BHVO-2 (+17 % for the $LREE_{La-Eu}$ and −14 % for the $HREE_{Gd-Lu}$), in addition to a slight positive Eu anomaly (Fig.11b). For the gabbro sample CM1A-6Z-2, 12–17 cm, all the REEs are significantly overestimated, by about 40 % on average (Fig. 11c). These examples illustrate well that trace element analysis by LA-ICP-MS of pressed powder pellets with too coarse a grain size produce unreliable results (see also Garbe-Schönberg and Müller, 2014). Such unreliable whole-rock compositions likely result from analyses dominated by individual mineral-phase compositions, as illustrated by the grain sizes presented in Fig. 2. For example, several analyses for the gabbro sample CM1A-6Z-2, 12–17 cm will successively be dominated by clinopyroxene (green grains in Fig. 2c) or plagioclase (whitish grains in Fig. 2c) rather than by a homogenized, fine mix of all the phases.

4 Summary of the developed LA-ICP-MS method: limitations and perspectives

In this article we show that the method developed for sample preparation of fine-grained pressed powder pellets analysed by LA-ICP-MS allows the determination of (ultra-)trace element concentrations on-board the D/V *Chikyu*. It enables the accurate determination *at sea* of concentrations by 4 to 5 orders of magnitude lower than the ones reachable previously using on-board XRF. According to the results obtained for the reference materials and gabbro samples from the Oman Drilling Project Hole CM1A, reliable results with a high accuracy and a precision better than 10 % can be achieved for elements with concentrations in the range 50–100 ng g^{-1} and higher (e.g. transition elements, REE for BHVO-2, BIR-1A and part of the gabbros). Regarding the presented results for the reference material JP-1 (peridotite) and the dunites from CM cores, analysed to test the limitations of the method, reliable results with a precision better than 20 % to 25 % can be achieved for concentrations as low as 1–2 ng g^{-1}, especially for the REEs. For a few exceptions, lower concentrations have been analysed (e.g. Th = 0.3 ng g^{-1} for the sample in Fig. 9b) but with a poorer repeatability related to the limits of detection. The presented method does not yet allow the accurate determination of ultra-trace element concentrations in depleted dunites from the oceanic crust–mantle transition nor mantle peridotites as low as those analysed by ICP-MS after acid digestion, and some elements such as HFSE

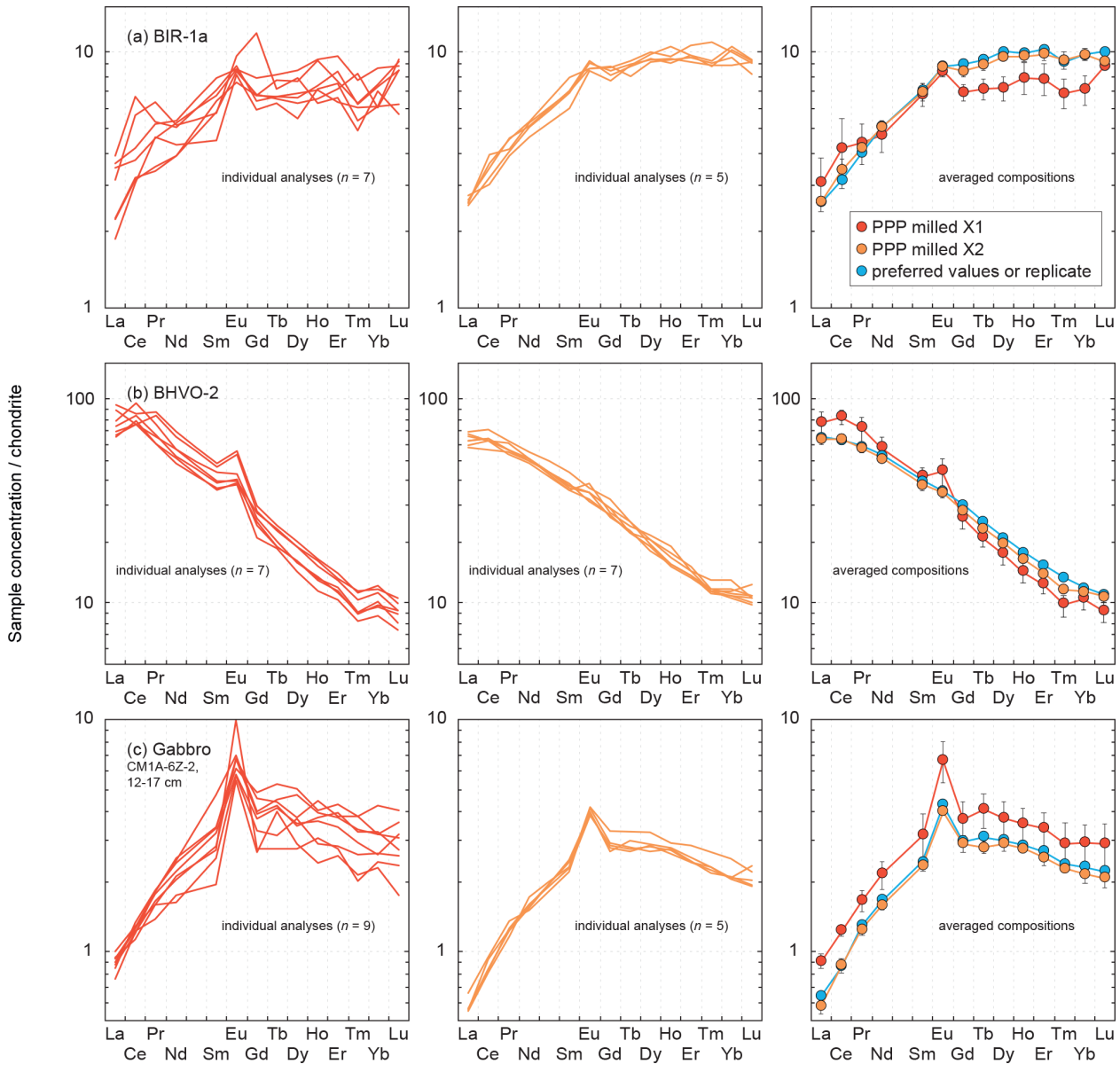

Figure 11. Comparison of the chondrite-normalized (normalization values from Barrat et al., 2012) REE patterns obtained for the reference materials **(a)** BIR-1a and **(b)** BHVO-2 and for **(c)** the gabbro CM1A-6Z-2, 12–17 cm after LA-ICP-MS analyses of one-time milled pressed powder pellets (left) and of two-time milled pressed powder pellets (centre). The determined concentrations show a greater variability after only one milling step, and the averaged compositions (right) differ significantly from the results obtained both after the second-step milling and for the replicates.

are still difficult to determine precisely. Indeed, mantle peridotites and especially dunites are known to be highly depleted in trace elements with concentrations in middle Rare Earth Elements such as Sm or Eu or in other elements such as Ta, Th or U, regularly below 1 ng g^{-1} (for solely the Oman ophiolite, e.g. Gerbert-Gaillard, 2002; Godard et al., 2000, 2008; Hanghøj et al., 2010; Le Mée et al., 2004; Monnier et al., 2006; Rospabé, 2018; Rospabé et al., 2018b, 2019; Takazawa et al., 2003). In addition, the signal during solution ICP-MS measurements generally has a greater stability than laser ablation signals. Here we show both for the reference materials and OmanDP core samples that the accuracy and precision decrease with decreasing element concentrations (Figs. 5, 7 and 10), allowing us to consider the unreliable results, at first order, to be directly related to instrumental limitations. However, the obtained results are promising, and further adjustments of the operating conditions could improve this safe, "dry" (acid-free) method to routinely analyse trace to ultra-trace elements *at sea* during ocean drilling operations. It could be adapted to other research topics such

as (paleo-)volcanism (e.g. Sato et al., 2020) and applied to other materials such as sedimentary cores for chemostratigraphic studies – for the analysis of metal- and/or REY-rich sediments as an example for recent studies in the North Pacific Ocean (Tanaka et al., 2020a, b; Yasukawa et al., 2018, 2020) – and be extended to the analysis of other chemical elements which were not investigated here.

In addition to a possible analytical limitation regarding accurate assessment of very low concentrations, a few other limitations have to be considered in the application of this new technical tool on-board the D/V *Chikyu*. In particular, this procedure needs more time to perform the second milling step for the preparation of fine-grained pressed powder pellets and for the laser ablation analyses in comparison with the one-time milled pellets routinely analysed by XRF for their concentrations in major, minor and some trace elements.

- The diameter of the agate balls used for the second milling step was 20 mm. A smaller diameter could be used. For example, 10 mm-large balls have been acquired and used on-board the D/V *Chikyu* during Leg 4, following Leg 3 during which we developed the method described in the present article (Kelemen et al., 2020), but agate balls even smaller than 10 mm exist. The use of such smaller agate balls has two potential advantages. First, it could allow us to mill the samples more quickly, allowing time gains during the sample preparation procedure. Second, it could allow us to mill the powder to a finer grain size that could in turn make the pressed powder pellets more homogeneous and thus the signal more stable during measurements and the results more reliable. In addition, a wet milling using water for the second milling step might further reduce the grain size and improve the pellet homogeneity, as shown by Garbe-Schönberg and Müller (2014) and Peters and Pettke (2017). Accordingly, a possible "nugget effect" as evoked earlier (see also Peters and Pettke, 2017) could be minimized.

- Following the different steps tested during Leg 3, it appears that a minimum of three analyses on each sample is the minimum required to account for the sample powder heterogeneity so that the averaged compositions are adequately close to reference or preferred values. In the examples we presented and especially for the dunite samples that are particularly depleted in (ultra-)trace elements, we decided to perform a minimum of five or six measurements per sample to improve the repeatability and more accurately determine the lowest concentrations. Further improving the two-step milling process could allow for a reduction in the number n of replicate measurements, especially if an analytical sequence is made of alternating analyses on reference glasses and pressed powder pellet samples to ensure the measurements are not affected by the different matrix.

- The current procedure requires changing of sample pellets – and thus opening of the laser ablation sample cell – between each sample. An alternative design for the two-time milled pellets, with a smaller diameter, could allow loading of two or more samples at the same time in the laser ablation sample cell. In addition, modifications to the settings of the laser ablation system could allow us to set a laser spot larger than the maximum size (100 µm large in diameter) used in the present study and thus be complementary to the improvement of the preparation procedure of the pressed powder pellets.

- In the course of the 30 d-long Leg 3, during which we developed the presented method, we did not perform a procedural blank related to (1) the crushing of the samples and to (2) the second milling step and pressed powder pellet preparation.

    a. Indeed, it has been shown that the milling can slightly contaminate the powder (Peters and Pettke, 2017), especially with metals and trace elements when using a crusher with steel jaws. After the 14 and 7 mm crushing steps, samples were sieved at 250 µm, and smaller particles that passed through were discarded to avoid possible cross-contamination with the previously crushed sample and possible tiny steel sequins from the jaws. The contamination of the powder by the steel jaws during the next two crushing steps would result in tiny sequins irregularly distributed within the pressed powder pellets and subsequently would allow highly variable ablation signals for a given element compared to the homogenized signal during the replicate solution analyses of the same samples (same powders). The good correlation between element concentrations measured by laser ablation and replicate analyses for many elements allows us to estimate such potential contamination as unlikely or very limited – we processed five or six measurements per sample, while probably tens of measurements would be required to get a homogeneous integration of the whole sample plus the potential, irregularly distributed contamination to reproduce the replicate values if the powder was contaminated during the sample crushing step. In the present study, such contamination is thus considered unlikely, and the inaccurate measurements associated with poorer precision observed for the elements with the lowest concentrations are at first order attributed to instrumental limitations. In addition, the used Jaw Crusher Retsch BB50 was new, and this model is well adapted to gently crush small samples, but to check the possible blank contribution could be useful through time to ensure the crushing step does not contaminate the samples after many uses of the crusher.

b. Concerning the second milling step and pressed powder pellet preparation, we used Prolene film to isolate the surface powder from the load, as described in Sect. 2. In addition, the ablation signal was integrated in calculations after only a few seconds to discard potential surface contamination. The reliable results obtained for the three analysed reference materials show that the second step milling and pressed powder pellets preparation do not induce any contamination.

– In the present study, ^{29}Si was used as an internal standard and the calculations performed using the SiO_2 content (reference values or certificate for standards, determined by XRF on-board during Leg 3 for the OmanDP samples). We chose this internal standard as SiO_2 was expected to be highly concentrated in all the analysed reference materials and core samples. As an example, ^{42}Ca, which is regularly used as an internal standard for laser ablation analyses, could not be applied to dunites that have a too low CaO content. However, the milling bowl and balls are made of agate, and it cannot be ruled out that the balls could be slowly abraded over time and possibly variably contaminate the powder with silicon. Such contamination can be excluded concerning the second milling step as we were able to precisely determine the chemical compositions for the three analysed standards (Sect. 3.1), but the first milling step using two different sizes of agate balls could eventually be more critical through time. In the present study, we were able for many elements to reproduce by laser ablation analyses, using ^{29}Si as an internal standard, the replicate values obtained by solution analyses using other internal standards (In, Re and Be for gabbros, In or Tm for dunites). In the course of future ship-board operations, other internal standard elements could be adapted for the trace element analyses *at sea*, particularly for lithologies with a low silica content (e.g. carbonates).

– The argon gas supply on-board the D/V *Chikyu* is currently limited to 4230 L (90 bottles each with a capacity of 47 L at a pressure of 14.7 MPa). In case new Ar bottles cannot be delivered during drilling operations (i.e. if the drilling site is too far from the coast), (1) the sample selection and the analytical schedule have to be well organized and the operating conditions optimized to cover the duration of the cruise according to the expected goals and/or (2) to plan an increase in the Ar gas supply capacity of the D/V *Chikyu*. Otherwise, He is frequently used as a carrier gas before being mixed with Ar downstream of the ablation cell. In the present study, we used an Ar gas line only, and a different procedure coupling the use of both He and Ar could be adapted to increase the instrument sensitivity.

An alternative to the analysis of whole-rock trace element concentrations is the in situ analysis in minerals. The Lab Street Deck of the D/V *Chikyu* is equipped with a sample preparation room where thin sections and epoxy mounts for separated minerals can be prepared. In this way during Leg 3, laser ablation analyses have been performed on epoxy mounts containing pyroxenes separated from the CM core mantle harzburgites, and replicate analyses performed at the IES-AS laboratory (Taiwan) were in good agreement with results obtained on-board. Similarly, the method presented here could thus be applied for the trace element analysis of thin sections prepared from heterogenous materials or of epoxy plots prepared for separated minerals.

5 Conclusion

We presented a "dry" safe method to assess whole-rock trace to ultra-trace element concentrations in mafic and ultramafic rocks from the oceanic lithosphere, developed *to be used at sea*. The reliability of the results obtained for the reference materials (BHVO-2, BIR-1a and JP-1) and for gabbro and dunite samples from the Oman ophiolite (OmanDP Hole CM1A) is shown for concentrations as low as 1–2 ng g^{-1}, especially for Rare Earth Elements. This method can be well adapted for a low-resolution study of the chemical evolutions along cores recovered during scientific ocean drillings, especially in light of the major element compositions previously obtained by XRF and/or for the study of more specific intervals along the cores. Sixty years after the initiation of Project Mohole in 1961 that initially aimed to drill under the oceans in order to cross the Moho and reach the Earth's mantle, this striving target for Earth scientists has not yet been achieved. The perspective of the Mohole to Mantle (M2M) drilling project that could be conducted within the next few years in the Pacific Ocean using the D/V *Chikyu* (Michibayashi et al., 2019; Morishita et al., 2019; Teagle and Ildefonse, 2011; Umino et al., 2021) is a stimulating motivation for the development of new on-board techniques and instruments that could contribute to make this ultimate objective of the scientific ocean drilling a success. Alternatively, this method could be improved and/or adapted for other materials recovered in the course of future ocean drillings as well as for other chemical elements of interest in addition to the 37 elements investigated here (transition elements and Ga, Li and LILE, REE, HFSE, Y, Pb, Th, and U).

Data availability. The whole-rock (ultra-)trace element concentrations obtained by LA-ICP-MS for the pressed powder prepared for the three reference materials BHVO-2, BIR-1a and JP-1 are given in Table 2. The measured elements discussed for the Oman Drilling Project CM gabbros and dunites, both obtained by LA-ICP-MS on-board the D/V *Chikyu* and replicate analyses after Leg 3, are given in the Supplement.

Supplement. The supplement related to this article is available online at: https://doi.org/10.5194/sd-30-75-2022-supplement.

Team list. Yuya Akamatsu (Department of Earth and Planetary Systems Science, Hiroshima University, Japan), Anwaar Al-Hajri (Department of Applied Geoscience, German University of Technology in Oman, Oman), Said Almusharrafi (Geological Survey, Public Authority for Mining, Oman), Ibrahim AlSawafi (Geological Research and Heritage Department, Public Authority for Mining, Oman), Elena Amador-French (Division of Geological and Planetary Sciences, California Institute of Technology, USA), Valentin Basch (Scienze della Terra dell'Ambiante e della Vita, University of Genova, Italy), Mike Cheadle (Department of Geology and Geophysics, University of Wyoming, USA), Saebyul Choe (Department of Earth and Planetary Sciences, American Museum of Natural History, USA), Jude Coggon (School of Ocean and Earth Science, University of Southampton, United Kingdom), Nick Dygert (Department of Earth and Environmental Science, University of Tennessee – Knoxville, USA), Bethany Ehlmann (Division of Geological and Planetary Sciences, California Institute of Technology, USA), Aled Evans (School of Ocean and Earth Sciences, University of Southampton, United Kingdom), Gretchen Früh-Green (Department of Earth Sciences, ETH Zurich, Switzerland), Marta Grabowska (Geography, Earth and Environmental Sciences, University of Plymouth, United Kingdom), Nadine Grambling (Department of Earth and Environmental Science, University of Tennessee - Knoxville, USA), Rebecca Greenberger (Department of Geological and Planetary Sciences, California Institute of Technology, USA), Annika Greve (R&D Center for Ocean Drilling Science, JAMSTEC, Japan), Juan Miguel Guotana (Division of Natural System, Kanazawa University, Japan), Kohei Hatakeyama (Department of Earth and Planetary Systems Science, Hiroshima University, Japan), Greg Hirth (Earth, Environmental and Planetary Sciences, Brown University, USA), Max Jansen (School of Earth and Ocean Sciences, Cardiff University, United Kingdom), Kevin Johnson (Department of Geology and Geophysics, University of Hawaii, USA), Mary-Alix Kaczmarek (Géosciences Environnement Toulouse, University Paul Sabatier Toulouse III, France), Peter Kelemen (Department of Earth and Environmental Sciences, Columbia University, USA), Kosuke Kimura (Department of Earth and Planetary Systems Science, Hiroshima University, Japan), Frieder Klein (Department of Marine Chemistry and Geology, Woods Hole Oceanographic Institution, USA), Juergen Koepke (Institut für Mineralogie, Leibniz University Hannover, Germany), Juerg Matter (School of Ocean and Earth Science, University of Southampton, United Kingdom), Katsuyoshi Michibayashi (Institute of Geosciences, Shizuoka University, Japan / Graduate School of Environmental Studies, Nagoya University, Japan), Tomoaki Morishita (Earth Science Course, Kanazawa University, Japan), Atsushi Okamoto (Graduate School of Environmental Studies, Tohoku University, Japan), Keishi Okazaki (Kochi Institute for Core Sample Research, JAMSTEC, Japan), Ryosuke Oyanagi (Department of Solid Earth Geochemistry, JAMSTEC, Japan), Gyuseung Park (School of Earth and Environment System, Seoul National University, Republic of Korea), Betchaida Payot (National Institute of Geological Sciences, University of the Philippines, Philippines), Philippe Pezard (Géosciences Montpellier, CNRS, Université de Montpellier, France), Marie Python (Department of Natural History Science, Hokkaido University, Japan), Nehal Warsi (AZD Engineering, Oman).

Author contributions. MR, FK, AT and ET settled the laser ablation system installed on-board the D/V *Chikyu*. FK, MR, MGi, SC, KI, MGo and EC developed the sample preparation procedure. MR, FK and MJC analysed the replicates. NA and KM provided technical information about the laboratory facilities and equipment installed on-board the *Chikyu* and support for the method development. DAHT and ET were the co-chiefs of the ChikyuOman2018 Leg 3. MR wrote the initial draft of the manuscript and all the authors contributed improvements to the final paper.

Competing interests. The authors declare that they have no conflict of interest.

Disclaimer. Publisher's note: Copernicus Publications remains neutral with regard to jurisdictional claims in published maps and institutional affiliations.

Acknowledgements. We greatly thank Abigail Barker and Daniel Peters for their very constructive reviews that helped to improve the quality of this manuscript, as well as Thomas Wiersberg for editorial handling. We also warmly thank the workers from Marine Works Japan on their great assistance during the ChikyuOman2018 Leg 3 core characterization campaign, in particular for their help in settling the instruments and developing the sample preparation and analytical procedure presented in the present article, as well as Jude Coggon for her great support on-board. We are also grateful to Lena Maeda (CDEX/JAMSTEC) to have checked with us some details concerning the characteristics of equipment installed on-board the D/V *Chikyu*.

Financial support. This research used samples and/or data provided by the Oman Drilling Project. The Oman Drilling Project (OmanDP) has been possible through co-mingled funds from the International Continental Scientific Drilling Project (ICDP; Peter B. Kelemen, Juerg Matter, Damon A. H. Teagle Lead PIs), the Sloan Foundation – Deep Carbon Observatory (grant no. 2014-3-01, Kelemen PI), the National Science Foundation (grant no. NSF-EAR-1516300, Kelemen lead PI), NASA – Astrobiology Institute (grant no. NNA15BB02A, Templeton PI), the German Research Foundation (DFG: grant no. KO 1723/21-1, Koepke PI), the Japanese Society for the Promotion of Science (JSPS (grant no. 16H06347), Michibayashi PI; and KAKENHI (grant no. 16H02742), Takazawa PI), the European Research Council (Adv: grant no. 669972; Jamveit PI), the Swiss National Science Foundation (SNF: grant no. 20FI21_163073, Früh-Green PI), JAMSTEC, the TAMU-JR Science Operator, and contributions from the Sultanate of Oman Ministry of Regional Municipalities and Water Resources, the Oman Public Authority of Mining, Sultan Qaboos University, CNRS-Univ. Montpellier, Columbia University of New York, and the University of Southampton. Mathieu Rospabé's participation in onsite and shipboard operations was made possible through a fi-

nancial support provided by the Centre National de la Recherche Scientifique-Institut National des Sciences de l'Univers (CNRS-INSU), IODP-France (regular fund).

Review statement. This paper was edited by Thomas Wiersberg and reviewed by Daniel Peters and Abigail Barker.

References

Akizawa, N., Ishikawa, A., and Kogiso, T.: A simple determination of whole-rock major- And trace-element composition for peridotite by micro-XRF spectrometer and ICP-MS using fused-glass bead, Geochem. J., 54(2), 81–90, https://doi.org/10.2343/geochemj.2.0587, 2020.

Anonymous: Penrose Field Conference on ophiolites, Geotimes, 17, 24–25, 1972.

Arrowsmith, P.: Laser ablation of solids for elemental analysis by inductively coupled plasma mass spectrometry, Anal. Chem., 59, 1437–1444, https://doi.org/10.1021/ac00137a014, 1987.

Barrat, J.-A., Keller, F., Amossé, J., Taylor, R. N., Nesbitt, R. W., and Hirata, T.: Determination of Rare Earth Elements in Sixteen Silicate Reference Samples by Icp-Ms After Tm Addition and Ion Exchange Separation, Geostand. Newsl., 20, 133–139, https://doi.org/10.1111/j.1751-908X.1996.tb00177.x, 1996.

Barrat, J. A., Yamaguchi, A., Greenwood, R. C., Benoit, M., Cotten, J., Bohn, M., and Franchi, I. A.: Geochemistry of diogenites: Still more diversity in their parental melts, Meteor. Planet. Sci., 43, 1759-1775, https://doi.org/10.1111/j.1945-5100.2008.tb00641.x, 2008.

Barrat, J.-A., Zanda, B., Moynier, F., Bollinger, C., Liorzou, C., and Bayon, G.: Geochemistry of CI chondrites: Major and trace elements, and Cu and Zn Isotopes, Geochim. Cosmochim. Acta, 83, 79–92, https://doi.org/10.1016/j.gca.2011.12.011, 2012.

Bayon, G., Barrat, J.-A., Etoubleau, J., Benoit, M., Bollinger, C., and Révillon, S.: Determination of rare earth elements, Sc, Y, Zr, Ba, Hf and Th in geological samples by ICP-MS after Tm addition and alkaline fusion, Geostand. Geoanal. Res., 33, 51–62, https://doi.org/10.1111/j.1751-908X.2008.00880.x, 2009.

Bizzarro, M., Baker, J. A., and Ulfbeck, D.: A new digestion and chemical separation technique for rapid and highly reproducible determination of Lu/Hf and Hf isotope ratios in geological materials by mc-ICP-MS, Geostand. Newsl., 27, 133–145, https://doi.org/10.1111/j.1751-908X.2003.tb00641.x, 2003.

Boudier, F. and Nicolas, A.: Harzburgite and lherzolite subtypes in ophiolitic and oceanic environments, Earth Planet. Sci. Lett., 76, 84–92, https://doi.org/10.1016/0012-821X(85)90150-5, 1985.

Coleman, R. G.: Plate tectonic emplacement of upper mantle peridotites along continental edges, J. Geophys. Res., 76, 1212–1222, https://doi.org/10.1029/JB076i005p01212, 1971.

Coleman, R. G.: Ophiolites: ancient oceanic lithosphere?, Springer-Verlag, Berlin Heidelberg, Germany, https://doi.org/10.1007/978-3-642-66673-5, 1977.

Dilek, Y.: Ophiolite concept and its evolution, Spec. Pap.-Geol. Soc. Amer., 373, 1–16, https://doi.org/10.1130/0-8137-2373-6.1, 2003.

Eggins, S. M.: Laser ablation ICP-MS analysis of geological materials prepared as lithium borate glasses, Geostand. Newsl., 27, 147–162, https://doi.org/10.1111/j.1751-908X.2003.tb00642.x, 2003.

Garbe-Schönberg, D. and Müller, S.: Nano-particulate pressed powder tablets for LA-ICP-MS, J. Anal. At. Spectrom., 29, 990–1000, https://doi.org/10.1039/c4ja00007b, 2014.

Gerbert-Gaillard, L.: Caractérisation Géochimique des Péridotites de l'ophiolite d'Oman: Processus Magmatiques aux Limites Lithosphère/Asthénosphère, PhD thesis Université Montpellier II, France, 2002 (in French).

Glennie, K. W., Boeuf, M. G. A., Hughes Clarke, M. W., Moody-Stuart, M., Pilaar, W. F. H., and Reinhardt, B. M.: Geology of the Oman Mountains, Verhandling Koninkelijk Nederlands Geologisch Mijnboukundig Genootschap, 31, 423 pp., 1974.

Godard, M., Jousselin, D., and Bodinier, J.-L.: Relationships between geochemistry and structure beneath a palaeo-spreading centre: A study of the mantle section in the Oman ophiolite, Earth Planet. Sci. Lett., 180, 133–148, https://doi.org/10.1016/S0012-821X(00)00149-7, 2000.

Godard, M., Lagabrielle, Y., Alard, O., and Harvey, J.: Geochemistry of the highly depleted peridotites drilled at ODP Sites 1272 and 1274 (Fifteen-Twenty Fracture Zone, Mid-Atlantic Ridge): Implications for mantle dynamics beneath a slow spreading ridge, Earth Planet. Sci. Lett., 267, 410–425, https://doi.org/10.1016/j.epsl.2007.11.058, 2008.

Gray, A. L.: Solid sample introduction by laser ablation for inductively coupled plasma source mass spectrometry, Analyst, 110, 551–556, https://doi.org/10.1039/AN9851000551, 1985.

Hanghøj, K., Kelemen, P. B., Hassler, D., and Godard, M.: Composition and genesis of depleted mantle peridotites from the Wadi Tayin massif, Oman ophiolite; Major and trace element geochemistry, and Os isotope and PGE systematics, J. Petrol., 51, 201–227, https://doi.org/10.1093/petrology/egp077, 2010.

Hopson, C. A., Coleman, R. G., Gregory, R. T., Pallister, J. S., and Bailey, E. H.: Geologic section through the Samail ophiolite and associated rocks along a Muscat-Ibra transect, southeastern Oman Mountains, J. Geophys. Res.-Sol. Ea., 86, 2527–2544, https://doi.org/10.1029/JB086iB04p02527, 1981.

Imai, N.: Quantitative analysis of original and powdered rocks and mineral inclusions by laser ablation inductively coupled plasma mass spectrometry, Anal. Chim. Acta, 235, 381–391, https://doi.org/10.1016/S0003-2670(00)82097-8, 1990.

Imai, N., Terashima, S., Itoh, S., and Ando, A.: 1994 compilation values for GSJ reference samples, "Igneous rock series", Geochem. J., 29, 91–95, https://doi.org/10.2343/geochemj.29.91, 1995.

Imai, N., Terashima, S., Itoh, S., and Ando, A.: 1998 compilation of analytical data for five GSJ geochemical reference samples: The "instrumental analysis series", Geostand. Newsl., 23, 223–250, https://doi.org/10.1111/j.1751-908X.1999.tb00576.x, 1999.

Ionov, D. A., Savoyant, L., and Dupuy, C.: Application of the ICP-MS technique to trace element analysis of peridotites and their minerals, Geostand. Newsl., 16, 311–315, https://doi.org/10.1111/j.1751-908X.1992.tb00494.x, 1992.

Jochum, K. P., Seufert, H. M., and Thirlwall, M. F.: High-sensitivity Nb analysis by spark-source mass spectrometry (SSMS) and calibration of XRF Nb and Zr, Chem. Geol., 81, 1–16, https://doi.org/10.1016/0009-2541(90)90035-6, 1990.

Jochum, K. P., Willbold, M., Raczek, I., Stoll, B., and Herwig, K.: Chemical characterisation of the USGS refer-

ence glasses GSA-1G, GSC-1G, GSD-1G, GSE-1G, BCR-2G, BHVO-2G and BIR-1G using EPMA, ID-TIMS, ID-ICP-MS and LA-ICP-MS, Geostand. Geoanal. Res., 29, 285–302, https://doi.org/10.1111/j.1751-908x.2005.tb00901.x, 2005.

Jochum, K. P., Weis, U., Stoll, B., Kuzmin, D., Yang, Q., Raczek, I., Jacob, D. E., Stracke, A., Birbaum, K., Frick, D. A., Günther, D., and Enzweiler, J.: Determination of reference values for NIST SRM 610-617 glasses following ISO guidelines, Geostand. Geoanal. Res., 35, 397–429, https://doi.org/10.1111/j.1751-908X.2011.00120.x, 2011.

Kelemen, P., Al Rajhi, A., Godard, M., Ildefonse, B., Köpke, J., MacLeod, C., Manning, C., Michibayashi, K., Nasir, S., Shock, E., Takazawa, E., and Teagle, D.: Scientific Drilling and Related Research in the Samail Ophiolite, Sultanate of Oman, Sci. Dril., 15, 64–71, https://doi.org/10.2204/iodp.sd.15.10.2013, 2013.

Kelemen, P. B., Matter, J. M., Teagle, D. A. H., Coggon, J. A., and the Oman Drilling Project Science Team (Eds.): Methods and explanatory notes, in: Proceedings of the Oman Drilling Project: College Station, TX (International Ocean Discovery Program), https://doi.org/10.14379/OmanDP.proc.2020, 2020.

Kelemen, P. B., Matter, J. M., Teagle, D. A. H., Coggon, J. A., and the Oman Drilling Project Science Team (Eds.): Site CM1: layered gabbros, crustal ultramafic rocks, and mantle harzburgite, in: Proceedings of the Oman Drilling Project: College Station, TX (International Ocean Discovery Program), https://doi.org/10.14379/OmanDP.proc.2020, 2021a.

Kelemen, P. B., Matter, J. M., Teagle, D. A. H., Coggon, J. A., and the Oman Drilling Project Science Team (Eds.): Site CM2: crust-mantle transition zone and into upper mantle, in: Proceedings of the Oman Drilling Project: College Station, TX (International Ocean Discovery Program), https://doi.org/10.14379/OmanDP.proc.2020, 2021b.

Kelemen, P. B., Matter, J. M., Teagle, D. A. H., Coggon, J. A., and the Oman Drilling Project Science Team (Eds.): Oman Drilling Project Phase 1 and 2 Summary, in: Proceedings of the Oman Drilling Project: College Station, TX (International Ocean Discovery Program), https://doi.org/10.14379/OmanDP.proc.2020, in press, 2021c.

Kon, Y. and Hirata, T.: Determination of 10 major and 34 trace elements in 34 GSJ geochemical reference samples using femtosecond laser ablation ICP-MS, Geochem. J., 49, 351–375, https://doi.org/10.2343/geochemj.2.0362, 2015.

Kon, Y., Murakami, H., Takagi, T., and Watanabe, Y.: The development of whole rock analysis of major and trace elements in XRF glass beads by fsLA-ICPMS in GSJ geochemical reference samples, Geochem. J., 45, 387–416, https://doi.org/10.2343/geochemj.1.0133, 2011.

Le Mée, L., Girardeau, J., and Monnier, C.: Mantle segmentation along the Oman ophiolite fossil mid-ocean ridge, Nature, 432, 167–172, https://doi.org/10.1038/nature03075, 2004.

Lippard, S. J., Shelton, A. W., and Gass, I. G.: The ophiolite of the Northern Oman, Geol. Soc. London, Mem., 11, 1–16, https://doi.org/10.1144/GSL.MEM.1986.011.01.01, 1986.

Longerich, H. P., Jackson, S. E., and Gunther, D.: Laser ablation inductively coupled plasma mass spectrometric transient signal data acquisition and analyte concentration calculation, J. Anal. At. Spectrom., 11, 899–904, https://doi.org/10.1039/JA9961100899, 1996.

Makishima, A. and Nakamura, E.: Suppression of matrix effects in ICP-MS by high power operation of ICP: Application to precise determination of Rb, Sr, Y, Cs, Ba, REE, Pb, Th and U at ng g-1 levels in milligram silicate samples, Geostand. Newsl., 21, 307–319, https://doi.org/10.1111/j.1751-908X.1997.tb00678.x, 1997.

Makishima, A. and Nakamura, E.: Determination of major/minor and trace elements in silicate samples by ICP-QMS and ICP-SFMS applying isotope dilution-internal standardisation (ID-IS) and multi-stage internal standardisation, Geostand. Geoanal. Res., 30, 245–271, https://doi.org/10.1111/j.1751-908X.2006.tb01066.x, 2006.

Michibayashi, K., Tominaga, M., Ildefonse, B., and Teagle, D.: What Lies Beneath: The Formation and Evolution of Oceanic Lithosphere, Oceanography, 32, 138–149, https://doi.org/10.5670/oceanog.2019.136, 2019.

Monnier, C., Girardeau, J., Le Mée, L., and Polvé, M.: Along-ridge petrological segmentation of the mantle in the Oman ophiolite, Geochem. Geophy. Geosy., 7, Q11008, https://doi.org/10.1029/2006GC001320, 2006.

Morishita, T., Umino, S., Kimura, J.-I., Yamashita, M., Ono, S., Michibayashi, K., Tominaga, M., Klein, F., and Garcia, M. O.: Workshop report on hard-rock drilling into mid-Cretaceous Pacific oceanic crust on the Hawaiian North Arch, Sci. Dril., 26, 47–58, https://doi.org/10.5194/sd-26-47-2019, 2019.

Mukherjee, P. K., Khanna, P. P., and Saini, N. K.: Rapid determination of trace and ultra trace level elements in diverse silicate rocks in pressed powder pellet targets by LA-ICP-MS using a matrix-independent protocol, Geostand. Geoanal. Res., 38, 363–379, https://doi.org/10.1111/j.1751-908X.2013.00260.x, 2014.

Nakamura, K. and Chang, Q.: Precise determination of ultra-low (sub-ng g-1) level rare earth elements in ultramafic rocks by quadrupole ICP-MS, Geostand. Geoanal. Res., 31, 185–197, https://doi.org/10.1111/j.1751-908X.2007.00859.x, 2007.

Peters, D. and Pettke, T.: Evaluation of Major to Ultra Trace Element Bulk Rock Chemical Analysis of Nanoparticulate Pressed Powder Pellets by LA-ICP-MS, Geostand. Geoanal. Res., 41, 5–28, https://doi.org/10.1111/ggr.12125, 2017.

Qi, L., Zhou, M.-F., Malpas, J., and Sun, M.: Determination of Rare Earth Elements and Y in Ultramafic Rocks by ICP-MS After Preconcentration Using Fe(OH)3 and Mg(OH)2 Coprecipitation, Geostand. Geoanal. Res., 29, 131–141, https://doi.org/10.1111/j.1751-908X.2005.tb00660.x, 2005.

Rospabé, M.: Etude pétrologique, géochimique et structurale de la zone de transition dunitique dans l'ophiolite d'Oman: Identification des processus pétrogénétiques à l'interface manteau/croûte, PhD thesis Université Paul Sabatier, Toulouse III, France, 2018 (in French).

Rospabé, M., Benoit, M., and Candaudap, F.: Determination of Trace Element Mass Fractions in Ultramafic Rocks by HR-ICP-MS: A Combined Approach Using a Direct Digestion/Dilution Method and Preconcentration by Coprecipitation, Geostand. Geoanal. Res., 42, 115–129, https://doi.org/10.1111/ggr.12181, 2018a.

Rospabé, M., Benoit, M., Ceuleneer, G., Hodel, F., and Kaczmarek, M.-A.: Extreme geochemical variability through the dunitic transition zone of the Oman ophiolite: Implications for melt/fluid-rock reactions at Moho level beneath oceanic spreading centers, Geochim. Cosmochim. Acta, 234, 1–23, https://doi.org/10.1016/j.gca.2018.05.012, 2018b.

Rospabé, M., Benoit, M., Ceuleneer, G., Kaczmarek, M.-A., and Hodel, F.: Melt hybridization and metasomatism triggered by syn-magmatic faults within the Oman ophiolite: A clue to understand the genesis of the dunitic mantle-crust transition zone, Earth Planet. Sci. Lett., 516, 108–121, https://doi.org/10.1016/j.epsl.2019.04.004, 2019.

Sato, T., Miyazaki, T., Tamura, Y., Gill, J. B., Jutzeler, M., Senda, R., and Kimura, J. I.: The earliest stage of Izu rear-arc volcanism revealed by drilling at Site U1437, International Ocean Discovery Program Expedition 350, Isl. Arc, 29, e12340, https://doi.org/10.1111/iar.12340, 2020.

Senda, R., Kimura, J. I., and Chang, Q.: Evaluation of a rapid, effective sample digestion method for trace element analysis of granitoid samples containing acid-resistant minerals: Alkali fusion after acid digestion, Geochem. J., 48, 99–103, https://doi.org/10.2343/geochemj.2.0280, 2014.

Sharma, M. and Wasserburg, G. J.: The neodymium isotopic compositions and rare earth patterns in highly depleted ultramafic rocks, Geochim. Cosmochim. Acta, 60, 4537–4550, https://doi.org/10.1016/S0016-7037(96)00280-3, 1996.

Sharma, M., Wasserburg, G. J., Papanastassiou, D. A., Quick, J. E., Sharkov, E. V., and Laz'ko, E. E.: High143Nd/144Nd in extremely depleted mantle rocks, Earth Planet. Sci. Lett., 135, 101–114, https://doi.org/10.1016/0012-821X(95)00150-B, 1995.

Takazawa, E., Okayasu, T., and Satoh, K.: Geochemistry and origin of the basal lherzolites from the northern Oman ophiolite (northern Fizh block), Geochem., Geophy. Geosy., 4, 1021, https://doi.org/10.1029/2001GC000232, 2003.

Tamura, A., Akizawa, N., Otsuka, R., Kanayama, K., Python, M., Morishita, T., and Arai, S.: Measurement of whole-rock trace-element composition by flux-free fused glass and LA-ICP-MS: Evaluation of simple and rapid routine work, Geochem. J., 49, 243–258, https://doi.org/10.2343/geochemj.2.0353, 2015.

Tanaka, E., Nakamura, K., Yasukawa, K., Mimura, K., Fujinaga, K., Ohta, J., Iijima, K., Nozaki, T., Machida, S., and Kato, Y.: Chemostratigraphic correlations of deep-sea sediments in the western north pacific ocean: A new constraint on the distribution of mud highly enriched in rare-earth elements, Minerals, 10, 1–19, https://doi.org/10.3390/min10060575, 2020a.

Tanaka, E., Nakamura, K., Yasukawa, K., Mimura, K., Fujinaga, K., Iijima, K., Nozaki, T., and Kato, Y.: Chemostratigraphy of deep-sea sediments in the western North Pacific Ocean: Implications for genesis of mud highly enriched in rare-earth elements and yttrium, Ore Geol. Rev., 119, 103392, https://doi.org/10.1016/j.oregeorev.2020.103392, 2020b.

Teagle, D. and Ildefonse, B.: Journey to the mantle of the Earth, Nature, 471, 437–439, https://doi.org/10.1038/471437a, 2011.

Umino, S., Moore, G. F., Boston, B., Coggon, R., Crispini, L., D'Hondt, S., Garcia, M. O., Hanyu, T., Klein, F., Seama, N., Teagle, D. A. H., Tominaga, M., Yamashita, M., Harris, M., Ildefonse, B., Katayama, I., Kusano, Y., Suzuki, Y., Trembath-Reichert, E., Yamada, Y., Abe, N., Xiao, N., and Inagaki, F.: Workshop report: Exploring deep oceanic crust off Hawai'i, Sci. Dril., 29, 69–82, https://doi.org/10.5194/sd-29-69-2021, 2021.

Van Heuzen, A. A.: Analysis of solids by laser ablation–inductively coupled plasma–mass spectrometry (LA-ICP-MS) – I. matching with a glass matrix, Spectrochim. Acta Part B At. Spectrosc., 46, 1803–1817, https://doi.org/10.1016/0584-8547(91)80207-J, 1991.

Weyer, S., Münker, C., Rehkämper, M., and Mezger, K.: Determination of ultra-low Nb, Ta, Zr and Hf concentrations and the chondritic Zr/Hf and Nb/Ta ratios by isotope dilution analyses with multiple collector ICP-MS, Chem. Geol., 187, 295–313, https://doi.org/10.1016/S0009-2541(02)00129-8, 2002.

Yasukawa, K., Ohta, J., Mimura, K., Tanaka, E., Takaya, Y., Usui, Y., Fujinaga, K., Machida, S., Nozaki, T., Iijima, K., Nakamura, K., and Kato, Y.: A new and prospective resource for scandium: Evidence from the geochemistry of deep-sea sediment in the western North Pacific Ocean, Ore Geol. Rev., 102, 260–267, https://doi.org/10.1016/j.oregeorev.2018.09.001, 2018.

Yasukawa, K., Kino, S., Azami, K., Tanaka, E., Mimura, K., Ohta, J., Fujinaga, K., Nakamura, K., and Kato, Y.: Geochemical features of Fe-Mn micronodules in deep-sea sediments of the western North Pacific Ocean: Potential for co-product metal extraction from REY-rich mud, Ore Geol. Rev., 127, 103805, https://doi.org/10.1016/j.oregeorev.2020.103805, 2020.

Yokoyama, T., Makishima, A., and Nakamura, E.: Evaluation of the coprecipitation of incompatible trace elements with fluoride during silicate rock dissolution by acid digestion, Chem. Geol., 157, 175–187, https://doi.org/10.1016/S0009-2541(98)00206-X, 1999.

Zhu, Y., Hioki, A., and Chiba, K.: Quantitative analysis of the elements in powder samples by LA-ICP-MS with PMMA powder as the binder and Cs as the internal standard, J. Anal. At. Spectrom., 28, 301–306, https://doi.org/10.1039/c2ja30279a, 2013.

Sci. Dril., 30, 101–112, 2022
https://doi.org/10.5194/sd-30-101-2022

Scientific Drilling
Open Access

Sensitivity of the West Antarctic Ice Sheet to +2 °C (SWAIS 2C)

Molly O. Patterson[1], Richard H. Levy[2,3], Denise K. Kulhanek[1,4], Tina van de Flierdt[5], Huw Horgan[3], Gavin B. Dunbar[3], Timothy R. Naish[3], Jeanine Ash[6], Alex Pyne[3], Darcy Mandeno[3], Paul Winberry[7], David M. Harwood[8], Fabio Florindo[9], Francisco J. Jimenez-Espejo[10], Andreas Läufer[11], Kyu-Cheul Yoo[12], Osamu Seki[13,14], Paolo Stocchi[15], Johann P. Klages[16], Jae Il Lee[12], Florence Colleoni[17], Yusuke Suganuma[13], Edward Gasson[18], Christian Ohneiser[19], José-Abel Flores[20], David Try[2], Rachel Kirkman[2], Daleen Koch[2], and the SWAIS 2C Science Team✚

[1]Department of Geological Sciences and Environmental Studies, Binghamton University, Binghamton, NY, USA
[2]GNS Science, Lower Hutt, New Zealand
[3]Antarctic Research Centre, Victoria University of Wellington, Wellington, New Zealand
[4]Institute of Geosciences, Christian-Albrecht University of Kiel, Kiel, Germany
[5]Department of Earth Science and Engineering, Imperial College London, London, UK
[6]Department of Earth, Environmental and Planetary Sciences, Rice University, Houston, TX, USA
[7]Department of Geological Sciences, Central Washington University, Ellensburg, WA, USA
[8]Department of Earth & Atmospheric Sciences, University of Nebraska-Lincoln, Lincoln, NE, USA
[9]Instituto Nazionale di Geofisica e Vulcanologia, Rome, Italy
[10]Instituto Andaluz de Ciencias de la Tierra, Spanish Research Council (CSIC), Armilla, Spain
[11]Federal Institute for Geosciences and Natural Resources (BGR), Hannover, Germany
[12]Division of Glacial Environment Research, Korea Polar Research Institute, Incheon, Republic of Korea
[13]National Institute of Polar Research, 10-3 Midori-cho, Tachikawa, Tokyo, Japan
[14]Institute of Low Temperature Science, Hokkaidō University, Sapporo, Japan
[15]Department of Coastal Systems, NIOZ Royal Netherlands Institute for Sea Research, Den Burg, the Netherlands
[16]Alfred Wegener Institute, Helmholtz Centre for Polar and Marine Research, Bremerhaven, Germany
[17]Istituto Nazionale di Oceanografia e Geofisica Sperimentale, Trieste, Italy
[18]School of Geographical Sciences, University of Bristol, Bristol, UK
[19]Department of Geology, University of Otago, Dunedin, New Zealand
[20]Department of Geology, University of Salamanca, Salamanca, Spain
✚A full list of authors appears at the end of the paper.

Correspondence: Molly O. Patterson (patterso@gmail.com)

Received: 8 September 2021 – Accepted: 28 January 2022 – Published: 25 February 2022

Abstract. The West Antarctic Ice Sheet (WAIS) presently holds enough ice to raise global sea level by 4.3 m if completely melted. The unknown response of the WAIS to future warming remains a significant challenge for numerical models in quantifying predictions of future sea level rise. Sea level rise is one of the clearest planet-wide signals of human-induced climate change. The Sensitivity of the West Antarctic Ice Sheet to a Warming of 2 °C (SWAIS 2C) Project aims to understand past and current drivers and thresholds of WAIS dynamics to improve projections of the rate and size of ice sheet changes under a range of elevated greenhouse gas levels in the atmosphere as well as the associated average global temperature scenarios to and beyond the +2 °C target of the Paris Climate Agreement.

Despite efforts through previous land and ship-based drilling on and along the Antarctic margin, unequivocal evidence of major WAIS retreat or collapse and its causes has remained elusive. To evaluate and plan for the

interdisciplinary scientific opportunities and engineering challenges that an International Continental Drilling Program (ICDP) project along the Siple coast near the grounding zone of the WAIS could offer (Fig. 1), researchers, engineers, and logistics providers representing 10 countries held a virtual workshop in October 2020. This international partnership comprised of geologists, glaciologists, oceanographers, geophysicists, microbiologists, climate and ice sheet modelers, and engineers outlined specific research objectives and logistical challenges associated with the recovery of Neogene and Quaternary geological records from the West Antarctic interior adjacent to the Kamb Ice Stream and at Crary Ice Rise. New geophysical surveys at these locations have identified drilling targets in which new drilling technologies will allow for the recovery of up to 200 m of sediments beneath the ice sheet. Sub-ice-shelf records have so far proven difficult to obtain but are critical to better constrain marine ice sheet sensitivity to past and future increases in global mean surface temperature up to 2 °C above pre-industrial levels. Thus, the scientific and technological advances developed through this program will enable us to test whether WAIS collapsed during past intervals of warmth and determine its sensitivity to a +2 °C global warming threshold (UNFCCC, 2015).

1 Introduction

Human activities are estimated to have caused an increase in average surface temperature of ∼ 1.0 °C above pre-industrial levels (IPCC, 2018, 2021). Global temperature increase is likely to reach +1.5 °C relative to pre-industrial levels between 2030 and 2052 if it continues to rise at the current rate (IPCC, 2018, 2021). Warming of 2 °C could be reached as early as 2039 or as late as the mid-2060s depending on greenhouse gas emissions pathways (Tebaldi et al., 2021). Global mean sea level (GMSL) has already increased by ∼ 22 cm since 1880 (IPCC, 2013). The rate of sea level rise (SLR) has been accelerating over the last several decades due to ocean thermal expansion and increased ice mass loss from Greenland and Antarctica (Velicogna et al., 2014; Nerem et al., 2018; Shepherd et al., 2018; IMBIE team, 2018) and is currently ∼ 3.6 mm yr^{-1} (Oppenheimer and Alley, 2016). The Intergovernmental Panel on Climate Change (IPCC) has forecast a likely range of SLR between 0.29 and 1.1 m by 2100 (Oppenheimer and Alley, 2016). However, uncertainty in these estimates remains, and multiple new lines of scientific evidence indicate a substantially higher GMSL rise is possible due to relatively large contributions from Antarctica's ice sheets (Bamber and Aspinall, 2013; Kopp et al., 2014, 2017; DeConto et al., 2021; Edwards et al., 2021). The range of estimates is partly due to uncertainty regarding glacial processes including marine ice cliff instability (Pollard et al., 2015; DeConto and Pollard, 2016; Edwards et al., 2019; DeConto et al., 2021; Bassis et al., 2021; Golledge and Lowry, 2021; Crawford et al., 2021) and mantle and ice sheet grounding zone dynamics associated with glacial isostatic adjustment (Catania et al., 2012; Gomez et al., 2015; Kingslake et al., 2018; Whitehouse et al., 2019). Efforts to improve our knowledge of glacial processes and dynamics from modern observations and reconstructions of past ice sheet behavior aim to reduce uncertainty in future projections and are a major objective of the Sensitivity of the West Antarctic Ice Sheet to a Warming of 2 °C (SWAIS 2C) Project.

Response of the West Antarctic Ice Sheet (WAIS) to climate warming is the focus of several major national and international science programs including the International Thwaites Glacier Collaboration (https://thwaitesglacier.org/about/itgc, last access: 10 February 2022), the Subglacial Antarctic Lakes Scientific Access (SALSA) Project (Priscu et al., 2021), and SWAIS 2C. This focus on the WAIS is due, in part, to satellite observations that demonstrate the WAIS is losing mass at an accelerating rate (e.g., Bamber et al., 2018; Shepherd et al., 2018; IMBIE team, 2018), with the potential for future melt to contribute 4.3 m to global sea level (Fretwell et al., 2013). WAIS is considered highly sensitive to future warming because much of it is grounded ∼ 2500 m below sea level, and its associated floating ice shelves are exposed to progressively warming ocean waters.

Quantifying the response of the WAIS to future warming remains a significant challenge. Direct physical evidence of WAIS response in the past, when global mean temperatures were 2 °C warmer than pre-industrial times, offers constraints that will help reduce uncertainty. The international SWAIS 2C Project aims to obtain such records from the West Antarctic interior (Fig. 1) to understand past and current drivers of WAIS dynamics and identify thresholds in the system. Outcomes will improve projections of the rate and size of ice sheet changes under a range of elevated greenhouse gas levels in the atmosphere and associated average global temperature scenarios up to and beyond the 2 °C target of the Paris Climate Agreement (UNFCCC, 2015). The SWAIS 2C Project consists of an interdisciplinary group of engineers, geologists, glaciologist, geophysicists, oceanographers, microbiologists, and climate and ice sheet modelers collaborating to enhance our understanding of (1) WAIS dynamics during past intervals of warm climate and (2) ice, atmosphere, solid Earth, and ocean interactions and feedbacks at the WAIS grounding zone and the margins of the Ross Ice Shelf cavity through the instrumental period. This in-

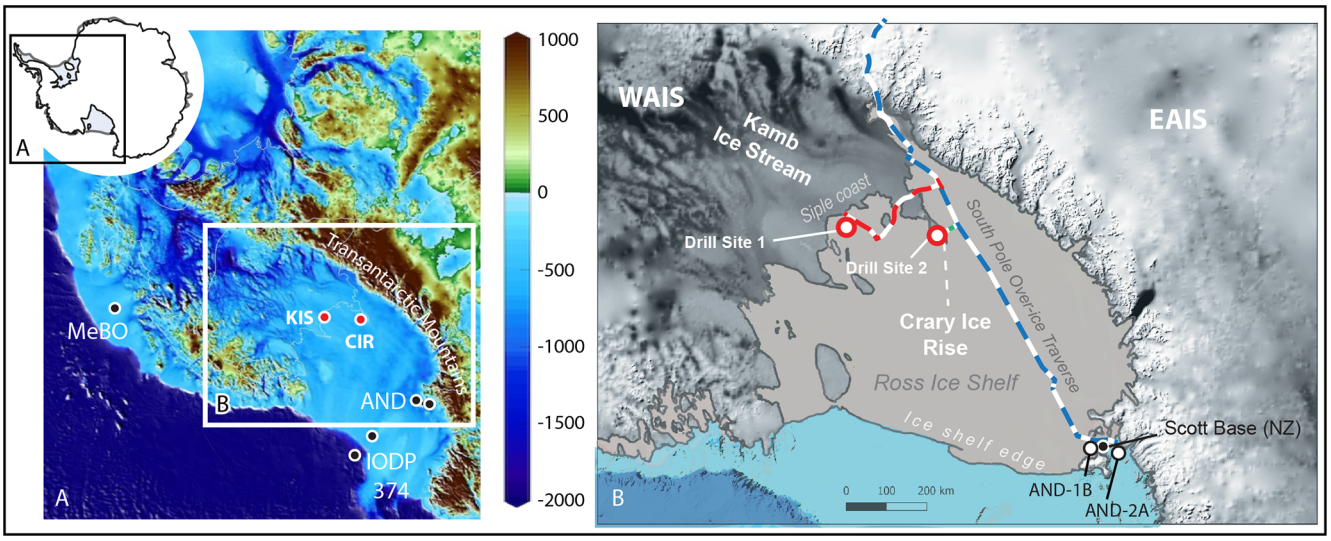

Figure 1. Proposed SWAIS 2C drill sites at Kamb Ice Stream (KIS) and Crary Ice Rise (CIR). **(A)** Topographic/bathymetric map across West Antarctica (color scale in meters). Other key drill sites include MeBO, ANDRILL (AND-1B and -2A), and IODP Exp. 374 sites (Fretwell et al., 2013). **(B)** Detail of the Ross Ice Shelf showing the South Pole Over-Ice Traverse and routes to drill sites 1 (KIS) and 2 (CIR). The new sites would anchor the southern end of a drill site transect deeply within West Antarctica.

formation will help determine the likely future response of the WAIS to projected warming and identify environmental implications for the Ross Sea sector and far-field consequences. The international partnership currently comprises 10 nations (Australia, Germany, Italy, Japan, Netherlands, New Zealand, South Korea, Spain, the United Kingdom, and the United States) but is still developing, with participation contingent on successful outcomes from national and international proposals.

2 SWAIS 2C: testing ice sheet sensitivities to a +2 °C global warming threshold

Integral to the SWAIS 2C Project's overall goal is the recovery of new Neogene and Quaternary sedimentary archives from beneath the Ross Ice Shelf at the grounding zone of the WAIS (Fig. 1). Because the magnitude of climate warming projected for the next century has not been experienced by Earth during the instrumental period, paleoclimate reconstructions of WAIS response during time intervals of analogous warmth to what is projected in the future, such as Pleistocene "super-interglacials" and the warmer-than-present Pliocene and Miocene (e.g., Melles et al., 2012; McKay et al., 2012; Levy et al., 2019), will provide critical insights into its future behavior (Retzlaff et al., 1993; Conway et al., 2002; Joughin and Tulaczyk, 2002; Mitrovica et al., 2009; Joughin et al., 2012; Hay et al., 2014). When integrated with numerical modeling experiments, modern process studies, and biological data, the new drill core data will allow us to examine the influence of climate dynamics and solid Earth processes in driving ice sheet fluctuations. Thus, the SWAIS 2C Project proposes to quantify the Antarctic ice sheet (AIS) contribution to past (with drilling) and future (with modeling) sea level change, through an improved understanding of climate, ocean, cryosphere, biosphere, and solid Earth interactions and feedbacks, so that decision-makers can better anticipate and assess risk associated with SLR and thus make more informed decisions around mitigation pathways. Thus, these unique data archives of late Cenozoic paleoenvironmental history will address the following key question: *what can we learn from past "greenhouse" conditions in Earth's climate to better anticipate future changes in the hydrological and biogeochemical cycle*? This is associated with theme 4, Environmental Change, in the International Continental Scientific Drilling Program (ICDP) 2020–2030 Science Plan.

3 Drill sites

The international SWAIS 2C Project plans to drill at two sites: the first adjacent to the grounding zone at Kamb Ice Stream (November 2022) and the second at Crary Ice Rise (November 2023) (Fig. 1). Both sites are to be accessed by overland traverse using the South Pole Over-ice Traverse (SPOT) route and new routes proved by Antarctica New Zealand. Both sites also offer stable drilling platforms as the Kamb Ice Stream has been stagnant for the past ∼ 150 years (e.g., Retzlaff and Bentley, 1993), and Crary Ice Rise stagnated around ∼ 1 kyr BP (Bindschadler et al., 1990; Catania et al., 2012; Hillebrand et al., 2021).

The Kamb Ice Stream site (KIS-3) is located ∼ 15 km seaward of the contemporary grounding line, where sedi-

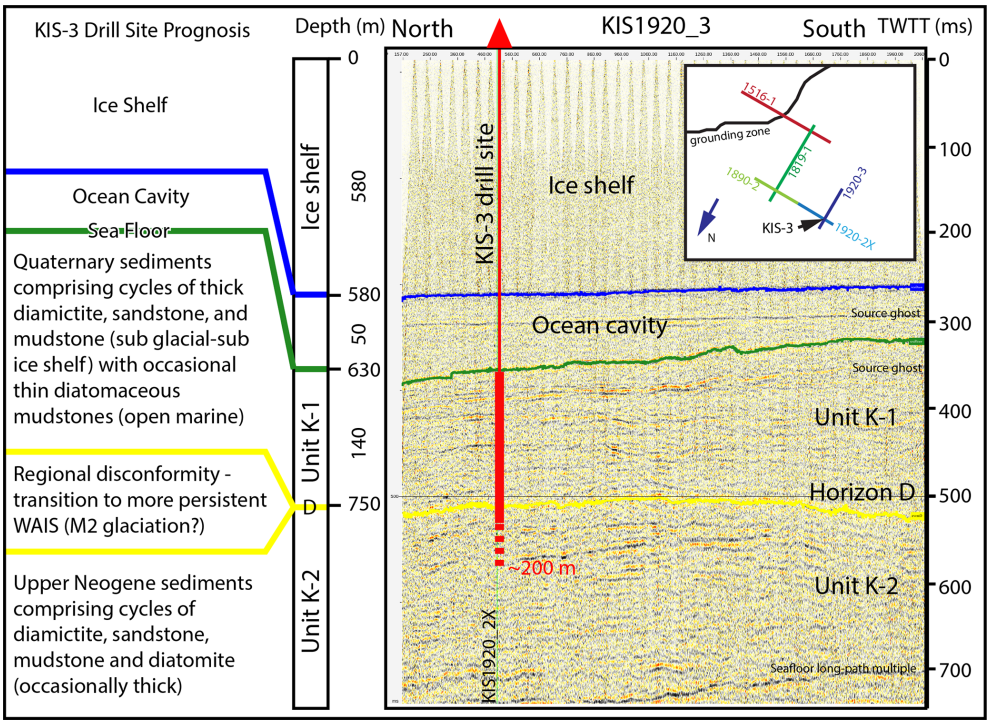

Figure 2. Seismic line KIS 1920_3. The KIS-3 drill site is located on the crossing point with line KIS1920_2X (inset). Drilling prognosis on the left with estimated depths from the surface and a brief description of stratigraphic intervals and horizons. The thick red line shows the 200 m drilling target depth.

ments are overlain by an ocean cavity and the floating Ross Ice Shelf. KIS-3 provides the opportunity to drill a modern ice stream environment from a stable drilling platform as the grounding line is thought to have migrated past the site since stagnation (Horgan et al., 2017). Three seasons of over-snow geophysics and one sub-ice-shelf direct-access program have provided site survey data, including over 70 km of multichannel seismic data. Over-snow seismic data imaged a thin water column (0–60 m) between the ice-shelf base and the seafloor (Fig. 2). Below the seafloor, two units are identified with the upper unit (Unit K-1) characterized by generally homogenous low-amplitude internal reflectivity with occasional high-amplitude horizontal to sub-horizontal internal reflectivity. The unit appears undeformed, and ice sheet modeling experiments suggest negligible glacial erosion at the site. We anticipate that this unit is of Pleistocene age based on the presence of reworked Neogene and Pleistocene diatoms recovered in surface sediments upstream of the drill site. The lower boundary of Unit K-1 is a high-amplitude positive-polarity reflector (Horizon D) at 130–180 m below the seafloor (at 2000 m s^{-1}) and is easily recognized throughout the survey region as well as beneath the adjacent Whillans Ice Stream (Fig. 4) (Horgan et al., 2013; Luthra et al., 2016). Reflectivity within the overlying unit is generally disconformable with Horizon D. The polarity and amplitude of Horizon D suggest the upper sedimentary unit is underlain by more lithified sediment (Unit K-2). Horizon D is likely erosional and may reflect initiation of a more extensive and persistent WAIS, potentially coinciding with the marine isotope stage M2 glaciation event (3.312–3.264 Ma) recorded at AND-1B (McKay et al., 2012).

The Crary Ice Rise site (CIR-1) overlies grounded ice that is frozen at the bed. CIR-1 is downstream of Whillans Ice Stream, adjacent to Kamb Ice Stream, and accounts for over 50 % of the buttressing of the Whillans Ice Stream (Retzlaff et al., 1993). Recent geophysical surveying at CIR collected over 15 km of seismic data that are interpreted to include a Holocene grounding zone wedge (GZW) deposit (Unit C-1) overlying gently dipping strata (Unit C-2) (Fig. 3). The wedge-shaped sequence (Unit C-1) occurs above a regional disconformity (Horizon H) and is characterized by discontinuous (chaotic) reflectors and velocities estimated at 2200 m s^{-1}. Several hundred meters of stratified and lithified sediment characterize Unit C-2, and while the age of this unit is unknown, we suggest that the gently dipping layers represent glacial–interglacial cycles comprising glacial till and open marine strata deposited during the Neogene. This hypothesis is based on sediments recovered from Crary Ice Rise during hot-water drilling efforts in the 1980s, where Neogene marine diatoms (Scherer et al., 1988) were recovered, suggesting grounding line retreat and open-water conditions as recent as the Pliocene (∼ 3 Ma) (Scherer, 1991). Venturelli et

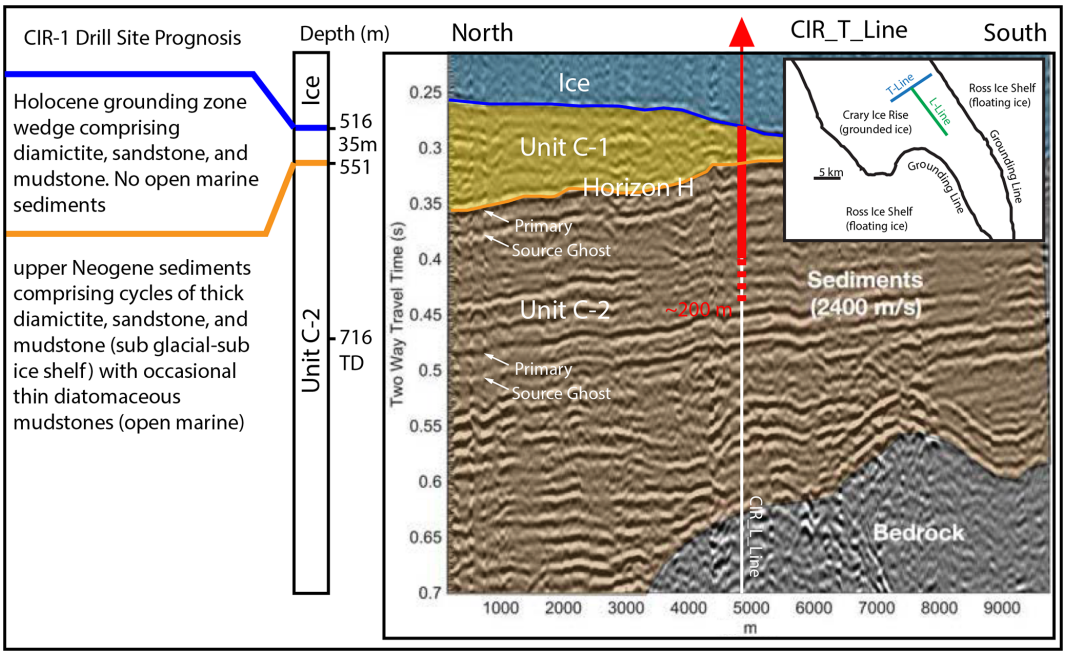

Figure 3. Seismic line CIR_T. The CIR-1 drill site is located on the crossing point with line CIR_L (inset). Drilling prognosis on the left with estimated depths from the surface and a brief description of stratigraphic intervals. The thick red line shows the 200 m drilling target depth.

al. (2020) demonstrated that nearby sediments and upstream deposits reflect periods of sub-ice-shelf deposition as recent as the mid-Holocene.

While there is an extensive network of seismic reflection surveys around the Antarctic margin and across the Ross Sea region, these marine data cannot be directly correlated to our proposed sub-glacial drill sites as over-ice/land-based surveys are logistically challenging, and relevant data do not exist. However, we postulate that sedimentary sequences recovered in the ANDRILL cores (Naish et al., 2009; Levy et al., 2016) and from the central Ross Sea (Hayes et al., 1975a, b; McKay et al., 2019) extend south beneath the Ross Ice Shelf and WAIS (Fig. 4). This hypothesis is based on (1) the character of the seismic sequences we have imaged at the proposed drill sites and, more specifically, the regionally extensive seismic reflector, Horizon D, which likely separates Neogene and Quaternary strata; and (2) reworked late Neogene and Quaternary diatoms recovered in subglacial sediments at CIR, Whillans Ice Stream, and KIS. Recovery of these new interior WAIS stratigraphic records will provide the southern anchor of a drill core transect in the Ross Sea Embayment (McKay et al., 2016), connecting the Ross Sea continental shelf (Naish et al., 2009; Levy et al., 2016; Fielding, 2018; McKay et al., 2019) to the West Antarctic interior, thereby providing a more coherent understanding of the processes regulating WAIS dynamics.

4 New capabilities in drilling subglacial sediment

Engineers from New Zealand's Antarctic Research Centre Science Drilling Office have developed a hot-water/rock drilling system capable of recovering ~ 200 m of sediment in places where the combined depth of the ice shelf (or sea ice) and water column is < 1000 m thick. The Antarctic Intermediate Depth Drilling (AIDD) system is housed in a tent that permits all-weather operation (Fig. 5). The new "light-weight" drilling system is designed for long-distance ice traverse. The sediment/rock drill (Multipower Products Ltd MP1000) is an industry-standard wireline system. Soft sediment coring will use two systems: a hydraulic piston corer (HPC) and a punch corer. Hard rock drilling will require diamond-bit rotary coring technology. Thus, cores will be recovered using three different approaches depending on lithology: (1) a hydraulic piston corer inside an NQ-sized drill rod (bit internal diameter, ID – 57.2 mm, outer tube bit throat ID – 51 mm), the preferred coring tool which will be used until refusal when it will be supplemented with punch coring; (2) rotary coring with NQ2 drill string (bit ID – 50.5 mm); and (3) rotary coring with a BQTK-sized rod (bit ID – 40.7 mm), which may be used in harder lithologies and may be used to cut the NQ drill string if necessary.

The combined rig, drill, and casing package weighs ~ 30 t, making it feasible to deploy within the constraints of existing Antarctic science support programs, with a much smaller logistical footprint than previous Antarctic drilling programs (i.e., ANDRILL; Falconer et al., 2008). This drill system's

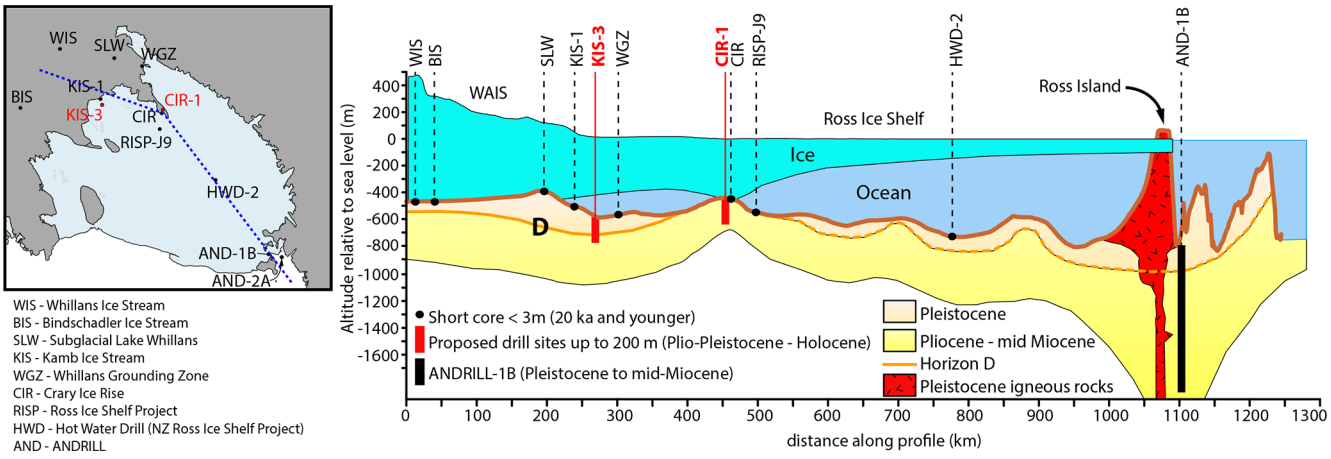

Figure 4. Regional stratigraphic correlation schematic. Dashed blue line is the location of the cross section. D is Horizon D identified at the KIS-3 site.

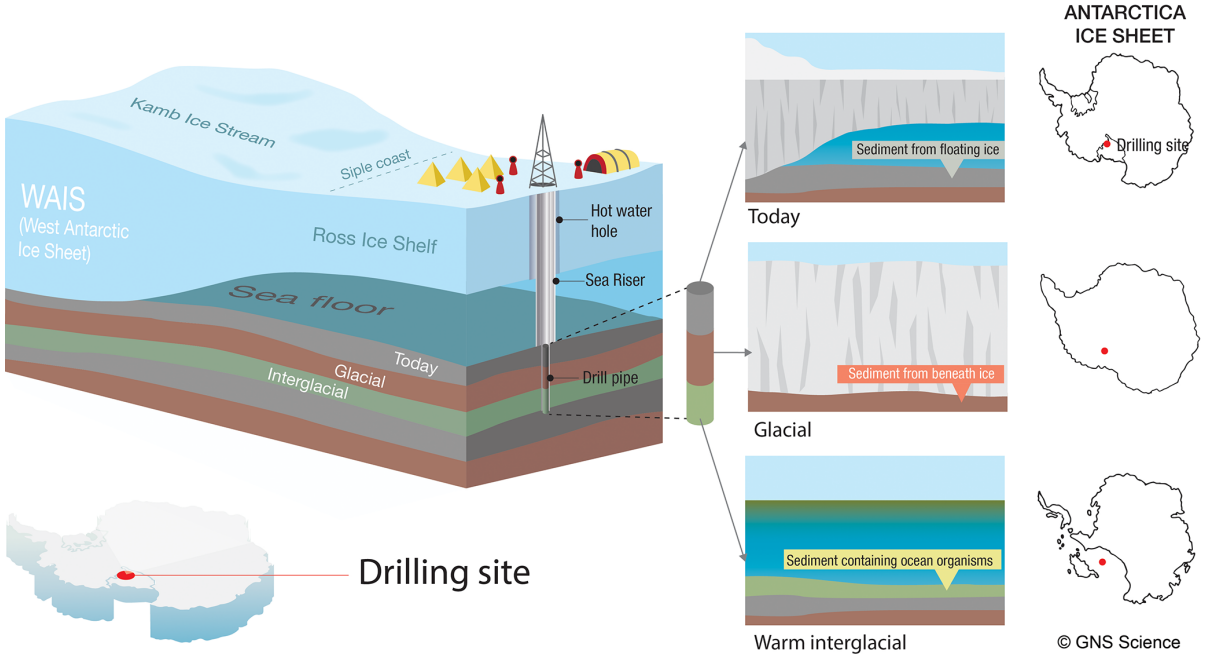

Figure 5. Diagram showing new drilling system sitting on the floating Ross Ice Shelf near the grounding zone at the Kamb Ice Stream site. A drill string up to ~ 1000 m long will be lowered to the seafloor through a hot-water drilled hole in the ice shelf to core ~ 200 m into the seafloor to sample sediments deposited in the past.

small logistical footprint will utilize a 24 h drilling operation to maximize core recovered in the short (~ 14 d) drilling window.

5 The SWAIS 2C Project approach and challenges

Several international workshops have been held to develop the SWAIS 2C Project and to encourage members of the international science community to join. Most recently in October 2020, researchers, engineers, and logistics providers from partner nations attended a 4 h virtual international workshop to further develop the project. Discussions covered project goals, ongoing efforts of site characterization, performance capabilities of the drilling system, logistics, and operational support required to carry out field work, structure and timing of off-ice science workshops, required scientific disciplines for addressing research objectives, potential scheduling and logistical implications due to COVID-19, and numerical modeling experiments. During the workshop, it was acknowledged that areas in which further project development needed to occur centered around downhole logging technologies (e.g., spectral gamma, resistivity, temperature) that are

compatible with the new AIDD system and inclusion of research that aims to address outstanding questions in the field of microbiology. In the months following the virtual workshop, science team members carried out detailed discussions with the staff at the ICDP Operational Support Group (OSG) and the Leibniz Institute for Applied Geophysics (LIAG) regarding downhole logging challenges, and additional science team members have been included to address investigations in microbiology. Here we provide an overview of the SWAIS 2C Project goals and approach that were outlined during the virtual workshop but also provide more detail on areas where shortcomings were identified but have since been addressed.

Currently, nearly 40 % of WAIS discharge is through fast-flowing ice streams along the Siple coast, in the region of the KIS and CIR (Price et al., 2001). Over decadal, centennial, and millennial timescales, the velocity of these ice streams has been highly variable (Bindschadler et al., 1990; Retzlaff et al., 1993; Joughin et al., 2002; Conway et al., 2002; Joughin and Tulaczyk, 2002; Hulbe and Fahnestock, 2007; Joughin et al., 2012). Currently there is a major gap in our understanding surrounding the negative feedbacks associated with dynamically relevant topographic features (i.e., pinning points), such as subglacial ice rises and grounding zone deposits, and thus these are poorly represented in ice-sheet models. Therefore, the temporal range of a Last Glacial Maximum (∼ 21 ka) to Recent record (i.e., the last 21 000 years) would provide a wealth of information concerning long-term grounding line dynamics. Paleoenvironmental records from the Pleistocene interglacials would provide evidence of WAIS response to climatic conditions when temperatures were 1–2 °C warmer than pre-industrial times. Analysis of Pliocene and Miocene sediment records will reveal the duration of marine ice sheet cover during previous intervals of time when CO_2 levels were like those projected for the coming decades if we fail to meet greenhouse gas emission targets that aim to keep global average temperatures below 2 °C warming. Proxy-based reconstructions of WAIS response during these past warm times will be integrated with numerical modeling experiments and modern process studies to provide critical insight into WAIS behavior (e.g., Hay et al., 2014). These new paleoenvironmental reconstructions from the Neogene and Quaternary will directly address the following four guiding hypotheses: (1) Ice–solid-Earth feedbacks influenced ice dynamics along the Siple coast on a multi-millennial timescale trajectory during the Holocene; (2) ocean temperatures and circulation patterns are the key governing factor in driving WAIS dynamics during the warmer-than-present late Quaternary superinterglacials; (3) marine-based ice sheets were highly dynamic and periodically expanded and retreated across the Siple coast during the mid-Pliocene to late Pliocene (3.3–2.6 Ma) but did not advance across the continental shelf during the early Pliocene (a marine-based WAIS could not grow as climate was too warm prior to the M2 glaciation); and (4) a smaller-than-present terrestrial AIS during the Miocene Climate Optimum (MCO) produced by a combination of high atmospheric CO_2 and tectonic land subsidence resulted in an extensive highly productive shallow marine sea, that subsequently drew down CO_2 and culminated in global cooling and Antarctic Ice Sheet expansion during the middle Miocene Climate Transition (MMCT). These new cores will provide the southern end (most proximal to the ice grounding zone) of a transect of recent drill holes in the Ross Embayment (e.g., ANDRILL program and International Ocean Discovery Program (IODP) Expedition 374). Furthermore, the new SWAIS 2C sites will serve as a connection to drill sites in the Amundsen Sea sector of West Antarctica (PS104 Expedition "ASE-MeBo", IODP Expedition 379), and the objectives are complementary to the International Thwaites Glacier Project. Ultimately, this land-to-ocean transect across the WAIS will provide a broader understanding of ice sheet history and more accurate predictions of future change.

The small diameter of our new drilling system presents a technical challenge to traditional downhole logging as there are few "off-the-shelf" logging tools slim enough to be deployed through the drill bit into the open borehole. The short drilling/logging window means duration is also an important factor in our logging strategy. Furthermore, the shallow holes (< 200 m b.s.f.) and the likely unconsolidated nature of the surrounding sediment mean logging in an open hole heightens the risk of losing logging tools in the hole. Our approach to downhole logging is therefore to use the ICDP Operational Support Group (OSG) "slimhole" Memory Logging tools (sondes) (iMLS) (https://www.icdp-online.org/fileadmin/icdp/services/img/Logging/OSG_Slimhole_Sondes_Specs_pics_2019-05.pdf, last access: 10 February 2022). These are self-contained, and no logging winch is required for deployment. While a new version of the iMLS depth measuring device (DMD) needs to be built, the existing spectral gamma (mSGR) and resistivity (mDIL) tools can be used without modification with an NQ-sized rotary bit. Other memory tools (sonic (mBCS) and magnetic susceptibility (mMS)) are too big to pass through the NQ rotary bit, although the mBCS can be used with the slightly wider NQ-hydraulic piston corer bit in place. Logging occurs as the NQ pipe is pulled from the hole upon a bit change or upon completion of drilling, with the MEMBAT module and mSGR (possibly mBCS) and mDIL tools assembled as a string. This approach saves critical time and will allow us to log the hole without casing. If time and hole conditions permit, it may be also possible to deploy four Leibniz Institute for Applied Geophysics (LIAG) wireline tools: resistivity, magnetic susceptibility, acoustic televiewer, and borehole mud temperature and salinity.

Temperature gradients will be measured in the seafloor at both KIS-3 and CIR-1. These measurements will allow for important geothermal flux and thermal transients to be determined. Heat flow is presently only determined by one

shallow (< 3 m) probe measurement at Whillans Ice Stream and one at KIS, yet it is an important variable for calculating sub-ice shelf conditions for sliding (or "freeze-on"). At CIR we will also utilize recent advances in fiber optic distributed temperature sensor technology to instrument the borehole throughout the ice thickness and into the sediment after drilling. This technology has been used successfully in the region and is an inexpensive alternative to thermistor strings (Tyler et al., 2013; Fisher et al., 2015). Vertical temperature profiles through the ice will allow the numerical modeling team to validate and refine previous estimates of geothermal heat flux and CIR stagnation time.

Given the desire for a small on-ice project footprint, on-ice science analysis will be limited to X-ray imaging, smear slide analysis, porewater geochemistry, and microbiology sampling. Fast-track samples from core cutter material will be sent off-ice for paleontological assessment prior to off-ice science workshops. Researchers from partner countries will meet in Dunedin, New Zealand, at the Otago Repository for Core Analysis (ORCA) facility, housed at the University of Otago, for initial core characterization and sampling following each drilling season and operate in a similar fashion to a typical IODP expedition and post-cruise sampling workshop. At the end of initial characterization and sampling, sediment cores will be transported to the Oregon State University Marine and Geology Repository (OSU-MGR) for long-term storage and made available to the scientific community after a 2-year moratorium period. Our research methodology is built around an integrated data–model approach that utilizes paleoclimate data to improve the skill of Antarctic climate and ice sheet models by simulating past Antarctic environmental conditions and the consequences for global sea level (e.g., Naish et al., 2007; Harwood et al., 2008–2009; Pollard and DeConto, 2009; Naish et al., 2009; Golledge et al., 2015; DeConto and Pollard, 2016; Gasson et al., 2016; Levy et al., 2016). This integrated data–model approach will improve understanding of climate, ocean, cryosphere, and solid Earth interactions. This knowledge can reduce uncertainty in sea level projections, thereby allowing coastal communities to anticipate and assess hazards and risks associated with sea level rise under different emissions pathways and to evaluate the efficacy of adaption strategies.

There are very few studies on the deep biosphere from beneath Antarctica's ice shelves and at grounded ice rises (e.g., Carr et al., 2013). Recovery of subglacial material along the Siple coast region provides an unprecedented opportunity to extend our knowledge of the deep biosphere and its biogeochemistry across the Ross Sea and will build upon earlier work from ANDRILL (Carr et al., 2013), WISSARD (Christner et al., 2014; Vick-Majors et al., 2020), and ongoing work from IODP Expedition 374 (Ash et al., 2019) and the United States-based SALSA (Subglacial Antarctic Lakes Scientific Access) projects (Hawkings et al., 2020; Priscu et al., 2021). Specifically, determining the taxonomy and activity of both living and inactive microbial populations in sediments will provide insights to modern element cycling and past environmental conditions. Key questions surrounding the discipline of microbiology that could be addressed from the SWAIS 2C Project and extend beyond the geological studies include the following: (1) which organisms characterize the microbial communities and the structure of microbial food webs in the extreme subglacial and sub-ice-shelf environment? (2) What is the functional potential of the microorganisms in these environments, which metabolic pathways do they encode, and how do they contribute to major and trace element cycling and carbon burial? (3) How do microbial communities respond to varying environmental conditions (e.g., temperature) and inputs in organic matter (i.e., open vs. ice-covered conditions, discharge from subglacial lakes) over time? (4) What do inactive members of subsurface communities like cysts, spores, and other inactive cells, as well as extracellular DNA, tell us about past environmental conditions?

Five of the SWAIS 2C partner nations have secured national funding to participate in the project, and the SWAIS 2C Project Team was recently awarded funds to support drilling through the ICDP. Furthermore, several national-level proposals are currently under review. We plan to begin drilling at the KIS site in December 2022. For more information regarding the SWAIS 2C Project, contact the authors of this article.

Data availability. Seismic data presented in this paper can be accessed through the DMC at IRIS and at http://ds.iris.edu/mda/19-016/ (IRIS consortium, 2022) or by directly contacting coauthors Huw Horgan and Paul Winberry for access to our information regarding seismic data.

Team list. A list of science team members for these projects was assembled following an open call for participation at a PAIS (Past Antarctic Ice Sheet) workshop at the XIII International Symposium on Antarctic Earth Sciences in Incheon, Republic of Korea, in July 2019. We note that this list may not be comprehensive, and additional scientists may join the science team during planning and later stages of each project and as funding from international partners is determined. The current SWAIS 2C science team is as follows (last name alphabetical order): Leanne Armand (Australia National University), Jeanine Ash (Rice University), Jacqueline Austermann (Lamont Doherty Earth Observatory), Catherine Beltran (University of Otago), Mike Bentley (Durham University), Craig Cary (University of Waikato), Jason Coenen (Northern Illinois University), Ester Colizza (University of Trieste), Florence Colleoni (Istituto Nazionale di Oceanografia e di Geofisica Sperimentale), Giuseppe Cortese (GNS Science), Laura Crispini (Università di Genova), Rob DeConto (University of Massachusetts, Amherst), Paola Del Carlo (Istituto Nazional di Geofisica e Vulcanologia), Alessio Di Roberto (Istituto Nazional di Geofisica e Vulcanologia), Justin Dodd (Northern Illinois University), Bella Duncan (Antarctic Research Centre, VUW), Gavin B. Dunbar (Antarctic Research Centre, VUW), Olaf Eisen (Alfred We-

gener Institute, Helmholtz Centre for Polar and Marine Research), José-Abel Flores (Universidad de Salamanca), Fabio Florindo (Istituto Nazional di Geofisica e Vulcanologia), Ed Gasson (University of Exeter), Karsten Gohl (Alfred Wegener Institute, Helmholtz Centre for Polar and Marine Research), Nick Golledge (Antarctic Research Centre, VUW), David M. Harwood (University of Nebraska – Lincoln), Huw Horgan (Antarctic Research Centre, VUW), Angelika Humbert (Alfred Wegener Institute, Helmholtz Centre for Polar and Marine Research), Francisco J. Jimenez-Espejo (Instituto Andaluz de Ciencias de la Tierra), Liz Keller (GNS Science), Jung-Hyun Kim (Korean Polar Research Institute), Sunghan Kim (Korean Polar Research Institute), Jonathan Kingslake (Lamont Doherty Earth Observatory), Johann P. Klages (Alfred Wegener Institute, Helmholtz Centre for Polar and Marine Research), Nikola Koglin (BGR), Jochem Kück (GFZ Potsdam German Research Center for Geosciences), Denise K. Kulhanek (Binghamton University, SUNY; Christian-Albrecht University of Kiel), Andreas Läufer (BGR), Jae Il Lee (Korean Polar Research Institute), Amy Leventer (Colgate University), Richard H. Levy (GNS Science/Victoria University of Wellington), Frank Lisker (Universität Bremen), Gerrit Lohmann (Alfred Wegener Institute, Helmholtz Centre for Polar and Marine Research), Dan Lowry (GNS Science), Rob McKay (Antarctic Research Centre, VUW), Gesine Mollenhauer (Alfred Wegener Institute, Helmholtz Centre for Polar and Marine Research), Juliane Müller (Alfred Wegener Institute, Helmholtz Centre for Polar and Marine Research), Tim Naish (Antarctic Research Centre, VUW), Pierre Offre (Royal Netherlands Institute for Sea Research), Christian Ohneiser (University of Otago), Molly O. Patterson (Binghamton University), Joe Prebble (GNS Science), Sonia Sandroni (Museo Nazionale dell'Antartide, Università di Siena), Francesca Sangiorgi (Utrecht University), Osamu Seki (Hokkaidō University), Louise Sime (British Antarctic Survey), James Smith (British Antarctic Survey), Anja Spang (Royal Netherlands Institute for Sea Research), Paolo Stocchi (Royal Netherlands Institute for Sea Research), Yusuke Suganuma (National Institute of Polar Research), Tina van de Flierdt (Imperial College London), Ryan Venturelli (Tulane University), Paul Winberry (Central Washington University), Thomas Wonik (Leibniz Institute for Applied Geophysics), Kiho Yang (Pusan National University), and Kyu-Cheul Yoo (Korean Polar Research Institute).

Author contributions. MOP, RHL, DKK, DT, and RK organized and facilitated the workshop. MOP, RHL, DKK, TvdF, HH, GBD, TRN, PW, DMH, FF, FJJE, AL, KCY, OS, PS, JPK, JIL, FC, YS, EG CO, JAF, and SWAIS 2C Science Team members contributed to developing the scientific objectives of the SWAIS 2C Project presented in the manuscript. GBD and AL contributed to downhole logging. JA contributed to the microbiology project objectives. AP and DM provided the information presented on the drilling system. PW and HH contributed to site survey information. DT, RK, and DK have managed the project and helped facilitate manuscript development.

Competing interests. The contact author has declared that neither they nor their co-authors have any competing interests.

Disclaimer. Publisher's note: Copernicus Publications remains neutral with regard to jurisdictional claims in published maps and institutional affiliations.

Acknowledgements. Richard H. Levy, Timothy R. Naish, Huw Horgan, Gavin B. Dunbar, Alex Pyne, Darcy Mandeno, Christian Ohneiser, David Try, and Rachel Kirkman acknowledge funding support from the New Zealand Ministry of Business and Innovation and Employment through the Antarctic Science Platform contract (ANTA1801) Antarctic Ice Dynamics Project (ASP-021-01). CIR seismic data collection was supported by US NSF grant 1443552 to Paul Winberry, Howard Conway, and Michelle Koutnik. Molly O. Patterson, Denise K. Kulhanek, Jeanine Ash, Paul Winberry, and David M. Harwood acknowledge funding support by US NSF grants 2035035, 2034999, 2035138, and 2034883.

Financial support. This research has been supported by the New Zealand Ministry of Business and Innovation and Employment through the Antarctic Science Platform contract (ANTA1801) Antarctic Ice Dynamics Project (grant no. ASP-021-01) and the US NSF (grant nos. 1443552, 2035035, 2034999, 2035138, and 2034883).

Review statement. This paper was edited by Ulrich Harms and reviewed by James A. Austin.

References

Ash, J. L., Franca, A., Biddle, J., Giovannelli, D., Singh, S. M., Martinez-Mendez, G., Müller, J., Mollenhauer, G., and Hefter, J.: Microbial Sediment Community Changes from the Last Glacial Maximum to Modern beneath the Ross Sea, in: AGU Fall Meeting Abstracts, 5 October 2020, online, vol. 2019, B53L-2573, 2019.

Bamber, J. L. and Aspinall, W. P.: An expert judgement assessment of future sea level rise from the ice sheets, Nat. Clim. Change, 3, 424–427, https://doi.org/10.1038/nclimate1778, 2013.

Bamber, J. L., Westaway, R. M., Marzeion, B., and Wouters, B.: The land ice contribution to sea level during the satellite era, Environ. Res. Lett., 13, 063008, https://doi.org/10.1088/1748-9326/aac2f0, 2018.

Bassis, J., Berg, B., Crawford, A., and Benn, D.: Transition to marine ice cliff instability controlled by ice thickness gradients and velocity, Science, 372, 1342–1344, 2021.

Bindschadler, R. A., Roberts, E. P., and Iken, A.: Age of Crary Ice Rise, Antarctica, determined from temperature-depth profiles, Ann. Glaciol., 14, 13–16, 1990.

Carr, S. A., Vogel, S. W., Dunbar, R. B., Brandes, J., Spear, J. R., Levy, R., Naish, T. R., Powell, R. D., Wakeham, S. G., and Mandernack, K. W.: Bacterial abundance and composition in marine sediments beneath the Ross Ice Shelf, Antarctica, Geobiology, 11, 377–395, 2013.

Catania, G., Hulbe, C., Conway, H., Scambos, T. A., and Raymond, C. F.: Variability in the mass flux of the Ross ice streams, West

Antarctica, over the last millennium, J. Glaciol., 58, 741–752, 2012.

Christner, B. C., Priscu, J. C., Achberger, A. M., Barbante, C., Carter, S. P., Christianson, K., Michaud, A. B., Mikucki, J. A., Mitchell, A. C., and Skidmore, M. L.: A microbial ecosystem beneath the West Antarctic ice sheet, Nature, 512, 310–313, 2014.

Conway, H., Catania, G., Raymond, C. F., Gades, A. M., Scambos, T. A., and Engelhardt, H.: Switch of flow direction in an Antarctic ice stream, Nature, 419, 465–467, 2002.

Crawford, A. J., Benn, D. I., Todd, J., Åström, J. A., Bassis, J. N., and Zwinger, T.: Marine ice-cliff instability modeling shows mixed-mode ice-cliff failure and yields calving rate parameterization, Nat. Commun., 12, 2701, https://doi.org/10.1038/s41467-021-23070-7, 2021.

DeConto, R. M. and Pollard, D.: Contribution of Antarctica to past and future sea-level rise, Nature, 531, 591–597, https://doi.org/10.1038/nature17145, 2016.

DeConto, R. M., Pollard, D., Alley, R. B., Velicogna, I., Gasson, E., Gomez, N., Sadai, S., Condron, A., Gilford, D. M., Ashe, E. L., Kopp, R. E., Li, D., and Dutton, A.: The Paris Climate Agreement and future sea-level rise from Antarctica, Nature, 593, 83–89, https://doi.org/10.1038/s41586-021-03427-0, 2021.

Edwards, T. L., Brandon, M. A., Durand, G., Edwards, N. R., Golledge, N. R., Holden, P. B., Nias, I. J., Payne, A. J., Ritz, C., and Wernecke, A.: Revisiting Antarctic ice loss due to marine ice-cliff instability, Nature, 566, 58–64, 2019.

Edwards, T. L., Nowicki, S., Marzeion, B., Hock, R., Goelzer, H., Seroussi, H., Jourdain, N. C., Slater, D. A., Turner, F. E., Smith, C. J., McKenna, C. M., Simon, E., Abe-Ouchi, A., Gregory, J. M., Larour, E., Lipscomb, W. H., Payne, A. J., Shepherd, A., Agosta, C., Alexander, P., Albrecht, T., Anderson, B., Asay-Davis, X., Aschwanden, A., Barthel, A., Bliss, A., Calov, R., Chambers, C., Champollion, N., Choi, Y., Cullather, R., Cuzzone, J., Dumas, C., Felikson, D., Fettweis, X., Fujita, K., Galton-Fenzi, B. K., Gladstone, R., Golledge, N. R., Greve, R., Hattermann, T., Hoffman, M. J., Humbert, A., Huss, M., Huybrechts, P., Immerzeel, W., Kleiner, T., Kraaijenbrink, P., Le clec'h, S., Lee, V., Leguy, G. R., Little, C. M., Lowry, D. P., Malles, J.-H., Martin, D. F., Maussion, F., Morlighem, M., O'Neill, J. F., Nias, I., Pattyn, F., Pelle, T., Price, S. F., Quiquet, A., Radić, V., Reese, R., Rounce, D. R., Rückamp, M., Sakai, A., Shafer, C., Schlegel, N.-J., Shannon, S., Smith, R. S., Straneo, F., Sun, S., Tarasov, L., Trusel, L. D., Van Breedam, J., van de Wal, R., van den Broeke, M., Winkelmann, R., Zekollari, H., Zhao, C., Zhang, T., and Zwinger, T.: Projected land ice contributions to twenty-first-century sea level rise, Nature, 593, 74–82, https://doi.org/10.1038/s41586-021-03302-y, 2021.

Falconer, T., Pyne, A., Wilson, D., Levy, R., Nielsen, S., and Petrushak, S.: Operations overview for the ANDRILL Southern McMurdo Sound Project, Antarctica, Terra Antarctica, 15, 41–48, 2008.

Fielding, C. R.: Stratigraphic architecture of the Cenozoic succession in the McMurdo Sound region, Antarctica: An archive of polar palaeoenvironmental change in a failed rift setting, Sedimentology, 65, 1–61, https://doi.org/10.1111/sed.12413, 2018.

Fisher, A. T., Mankoff, K. D., Tulaczyk, S. M., Tyler, S. W., Foley, N., and Team, and the W. S.: High geothermal heat flux measured below the West Antarctic Ice Sheet, Sci. Adv., 1, e1500093, https://doi.org/10.1126/sciadv.1500093, 2015.

Fretwell, P., Pritchard, H. D., Vaughan, D. G., Bamber, J. L., Barrand, N. E., Bell, R., Bianchi, C., Bingham, R. G., Blankenship, D. D., Casassa, G., Catania, G., Callens, D., Conway, H., Cook, A. J., Corr, H. F. J., Damaske, D., Damm, V., Ferraccioli, F., Forsberg, R., Fujita, S., Gim, Y., Gogineni, P., Griggs, J. A., Hindmarsh, R. C. A., Holmlund, P., Holt, J. W., Jacobel, R. W., Jenkins, A., Jokat, W., Jordan, T., King, E. C., Kohler, J., Krabill, W., Riger-Kusk, M., Langley, K. A., Leitchenkov, G., Leuschen, C., Luyendyk, B. P., Matsuoka, K., Mouginot, J., Nitsche, F. O., Nogi, Y., Nost, O. A., Popov, S. V., Rignot, E., Rippin, D. M., Rivera, A., Roberts, J., Ross, N., Siegert, M. J., Smith, A. M., Steinhage, D., Studinger, M., Sun, B., Tinto, B. K., Welch, B. C., Wilson, D., Young, D. A., Xiangbin, C., and Zirizzotti, A.: Bedmap2: improved ice bed, surface and thickness datasets for Antarctica, The Cryosphere, 7, 375–393, https://doi.org/10.5194/tc-7-375-2013, 2013.

Gasson, E., DeConto, R. M., Pollard, D., and Levy, R. H.: Dynamic Antarctic ice sheet during the early to mid-Miocene, P. Natl. Acad. Sci. USA, 113, 3459–3464, 2016.

Golledge, N. R. and Lowry, D. P.: Is the marine ice cliff hypothesis collapsing?, Science, 372, 1266–1267, 2021.

Golledge, N. R., Kowalewski, D. E., Naish, T. R., Levy, R. H., Fogwill, C. J., and Gasson, E. G.: The multi-millennial Antarctic commitment to future sea-level rise, Nature, 526, 421–425, https://doi.org/10.1038/nature15706, 2015.

Gomez, N., Pollard, D., and Holland, D.: Sea-level feedback lowers projections of future Antarctic Ice-Sheet mass loss, Nat. Commun., 6, 1–8, 2015.

Harwood, D., Florindo, F., Talarico, F., and Levy, R. H.: Studies from the ANDRILL, Southern McMurdo Sound Project, Antarctica, Initial Science Report on AND-2A, in: Terra Antartica, vol. 15, 1–235, ISSN 1122-8628, http://192.167.120.37/Editoria/TAP/volume15.html (last access: 17 February 2022), 2008–2009.

Hawkings, J. R., Skidmore, M. L., Wadham, J. L., Priscu, J. C., Morton, P. L., Hatton, J. E., Gardner, C. B., Kohler, T. J., Stibal, M., and Bagshaw, E. A.: Enhanced trace element mobilization by Earth's ice sheets, P. Natl. Acad. Sci. USA, 117, 31648–31659, 2020.

Hay, C., Mitrovica, J. X., Gomez, N., Creveling, J. R., Austermann, J., and Kopp, R. E.: The sea-level fingerprints of ice-sheet collapse during interglacial periods, Quaternary Sci. Rev., 87, 60–69, 2014.

Hayes, D. E., Frakes, L. A., Barrett, P. J., Burns, D. A., Chen, P.-H., Ford, A. B., Kaneps, A. G., Kemp, E. M., McCollum, D. M., Piper, D. J. W., Wall, R. E., and Webb, P. N.: Sites 270, 271, 272, Initial Reports of the Deep Sea Drilling Project 28, Washington, US Government Printing Office, 211–334, https://doi.org/10.2973/dsdp.proc.28.108.1975, 1975a.

Hayes, D. E., Frakes, L. A., Barrett, P. J., Burns, D. A., Chen, P.-H., Ford, A. B., Kaneps, A. G., Kemp, E. M., McCollum, D. M., Piper, D. J. W., Wall, R. E., and Webb, P. N.: Site 273, Initial Reports of the Deep Sea Drilling Project 28, 335–368, https://doi.org/10.2973/dsdp.proc.28.109.1975, 1975b.

Hillebrand, T. R., Conway, H., Koutnik, M., Martín, C., Paden, J., and Winberry, J. P.: Radio-echo sounding and waveform modeling reveal abundant marine ice in former rifts and basal crevasses within Crary Ice Rise, Antarctica, J. Glaciol., 67, 1–12, 2021.

Horgan, H. J., Alley, R. B., Christianson, K., Jacobel, R. W., Anandakrishnan, S., Muto, A., Beem, L. H., and Siegfried, M. R.: Estuaries beneath ice sheets, Geology, 41, 1159–1162, 2013.

Horgan, H. J., Hulbe, C., Alley, R. B., Anandakrishnan, S., Goodsell, B., Taylor-Offord, S., and Vaughan, M. J.: Poststagnation Retreat of Kamb Ice Stream's Grounding Zone, Geophys. Res. Lett., 44, 9815–9822, 2017.

Hulbe, C. and Fahnestock, M.: Century-scale discharge stagnation and reactivation of the Ross ice streams, West Antarctica, J. Geophys. Res.-Earth Surf., 112, F03S27, https://doi.org/10.1029/2006JF000603, 2007.

IMBIE team: Mass balance of the Antarctic Ice Sheet from 1992–2017, Nature, 558, 219–222, 2018.

IPCC: Climate Change 2013: The Physical Science Basis. Contribution of Working Group I to the Fifth Assessment Report of the Intergovernmental Panel on Climate Change, edited by: Stocker, T. F., Qin, D., Plattner, G.-K., Tignor, M., Allen, S. K., Boschung, J., Nauels, A., Xia, Y., Bex, V., and Midgley, P. M., Cambridge University Press, Cambridge, United Kingdom and New York, NY, USA, 1535 pp., ISBN 978-1-107-05799-1, 2013.

IPCC: Summary for Policymakers, in: Global Warming of 1.5 °C. An IPCC Special Report on the impacts of global warming of 1.5 °C above pre-industrial levels and related global greenhouse gas emission pathways, in the context of strengthening the global response to the threat of climate change, sustainable development, and efforts to eradicate poverty, edited by: Masson-Delmotte, V., Zhai, P., Pörtner, H.-O., Roberts, D., Skea, J., Shukla, P. R., Pirani, A., Moufouma-Okia, W., Péan, C., Pidcock, R., Connors, S., Matthews, J. B. R., Chen, Y., Zhou, X., Gomis, M. I., Lonnoy, E., Maycock, T., Tignor, M., and Waterfield, T., World Meteorological Organization, Geneva, Switzerland, 32 pp., https://www.ipcc.ch/site/assets/uploads/sites/2/2019/05/SR15_SPM_version_report_LR.pdf (last access: 17 February 2022), 2018.

IPCC: Summary for Policymakers, in: Climate Change 2021: The Physical Science Basis. Contribution of Working Group I to the Sixth Assessment Report of the Intergovernmental Panel on Climate Change, edited by: Masson-Delmotte, V., Zhai, P., Pirani, A., Connors, S. L., Péan, C., Berger, S., Caud, N., Chen, Y., Goldfarb, L., Gomis, M. I., Huang, M., Leitzell, K., Lonnoy, E., Matthews, J. B. R., Maycock, T. K., Waterfield, T., Yelekçi, O., Yu, R., and Zhou, B., Cambridge University Press, in press, 2021.

IRIS consortium: Collaborative Research: Grounding Line Dynamics: Crary Ice Rise Revisited [data set], 19-016, 9J 2015, http://ds.iris.edu/mda/19-016/, last access: 18 February 2022.

Joughin, I. and Tulaczyk, S.: Positive mass balance of the Ross ice streams, West Antarctica, Science, 295, 476–480, 2002.

Joughin, I., Tulaczyk, S., Bindschadler, R., and Price, S. F.: Changes in west Antarctic ice stream velocities; observation and analysis, J. Geophys. Res.-Solid, 107, 2289, https://doi.org/10.1029/2001JB001029, 2002.

Joughin, I., Alley, R. B., and Holland, D. M.: Ice-sheet response to oceanic forcing, Science, 338, 1172–1176, 2012.

Kingslake, J., Scherer, R. P., Albrecht, T., Coenen, J., Powell, R. D., Reese, R., Stansell, N. D., Tulaczyk, S., Wearing, M. G., and Whitehouse, P. L.: Extensive retreat and re-advance of the West Antarctic Ice Sheet during the Holocene, Nature, 558, 430–434, 2018.

Kopp, R. E., Horton, R. M., Little, C. M., Mitrovica, J. X., Oppenheimer, M., Rasmussen, D. J., Strauss, B. H., and Tebaldi, C.: Probabilistic 21st and 22nd century sea-level projections at a global network of tide-gauge sites, Earths Future, 2, 383–406, 2014.

Kopp, R. E., DeConto, R. M., Bader, D. A., Hay, C. C., Horton, R. M., Kulp, S., Oppenheimer, M., Pollard, D., and Strauss, B. H.: Evolving understanding of Antarctic ice-sheet physics and ambiguity in probabilistic sea-level projections, Earths Future, 5, 1217–1233, 2017.

Levy, R., Harwood, D., Florindo, F., Sangiorgi, F., Tripati, R., von Eynatten, H., Gasson, E., Kuhn, G., Tripati, A., DeConto, R., Fielding, C., Field, B., Golledge, N., McKay, R., Naish, T., Olney, M., Pollard, D., Schouten, S., Talarico, F., Warny, S., Willmott, V., Acton, G., Panter, K., Paulsen, T., and Taviani, M.: Antarctic ice sheet sensitivity to atmospheric CO_2 variations in the early to mid-Miocene, P. Natl. Acad. Sci. USA, 113, 3453, https://doi.org/10.1073/pnas.1516030113, 2016.

Levy, R. H., Meyers, S. R., Naish, T. R., Golledge, N. R., McKay, R. M., Crampton, J. S., DeConto, R. M., De Santis, L., Florindo, F., Gasson, E. G. W., Harwood, D. M., Luyendyk, B. P., Powell, R. D., Clowes, C., and Kulhanek, D. K.: Antarctic ice-sheet sensitivity to obliquity forcing enhanced through ocean connections, Nat. Geosci., 12, 132–137, https://doi.org/10.1038/s41561-018-0284-4, 2019.

Luthra, T., Anandakrishnan, S., Winberry, J. P., Alley, R. B., and Holschuh, N.: Basal characteristics of the main sticky spot on the ice plain of Whillans Ice Stream, Antarctica, Earth Planet. Sci. Lett., 440, 12–19, 2016.

McKay, R., Naish, T., Carter, L., Riesselman, C., Dunbar, R., Sjunneskog, C., Winter, D., Sangiorgi, F., Warren, C., and Pagani, M.: Antarctic and Southern Ocean influences on Late Pliocene global cooling, P. Natl. Acad. Sci. USA, 109, 6423–6428, 2012.

McKay, R. M., Barrett, P. J., Levy, R. S., Naish, T. R., Golledge, N. R., and Pyne, A.: Antarctic Cenozoic climate history from sedimentary records: ANDRILL and beyond, Philos. T. Roy. Soc. A, 374, 1–17, https://doi.org/10.1098/rsta.2014.0301, 2016.

McKay, R. M., De Santis, L., Kulhanek, D. K., and Expedition 374 Scientists (Eds.): Ross Sea West Antarctic Ice Sheet History, International Ocean Discovery Program, https://doi.org/10.14379/iodp.proc.374.2019, 2019.

Melles, M., Brigham-Grette, J., Minyuk, P. S., Nowaczyk, N. R., Wennrich, V., DeConto, R. M., Anderson, P. M., Andreev, A. A., Coletti, A., and Cook, T. L.: 2.8 million years of Arctic climate change from Lake El'gygytgyn, NE Russia, Science, 337, 315–320, 2012.

Mitrovica, J. X., Gomez, N., and Clark, P. U.: The sea-level fingerprint of West Antarctic collapse, Science, 323, 753–753, 2009.

Naish, T., Powell, R., Levy, R., Florindo, F., Harwood, D., Kuhn, G., Niessen, F., Talarico, F., and Wilson, G.: A record of Antarctic climate and ice sheet history recovered, Eos Trans. Am. Geophys. Union, 88, 557–558, 2007.

Naish, T., Powell, R., Levy, R., Wilson, G., Scherer, R., Talarico, F., Krissek, L., Niessen, F., Pompilio, M., Wilson, T., Carter, L., DeConto, R., Huybers, P., McKay, R., Pollard, D., Ross, J., Winter, D., Barrett, P., Browne, G., Cody, R., Cowan, E., Crampton, J., Dunbar, G., Dunbar, N., Florindo, F., Gebhardt, C., Graham, I., Hannah, M., Hansaraj, D., Harwood, D., Helling, D., Henry, S., Hinnov, L., Kuhn, G., Kyle, P., Läufer, A., Mafioli, P., Ma-

gens, D., Mandernack, K., McIntosh, W., Millan, C., Morin, R., Ohneiser, C., Paulsen, T., Persico, D., Raine, I., Reed, J., Riesselman, C., Sagnotti, L., Schmitt, D., Sjunneskog, C., Strong, P., Taviani, M., Vogel, S., Wilch, T., and Williams, T.: Obliquity-paced Pliocene West Antarctic ice sheet oscillations, Nature, 458, 322–328, https://doi.org/10.1038/nature07867, 2009.

Nerem, R. S., Beckley, B. D., Fasullo, J. T., Hamlington, B. D., Masters, D., and Mitchum, G. T.: Climate-change–driven accelerated sea-level rise detected in the altimeter era, P. Natl. Acad. Sci. USA, 115, 2022–2025, https://doi.org/10.1073/pnas.1717312115, 2018.

Oppenheimer, M. and Alley, R. B.: How high will the seas rise?, Science, 354, 1375–1377, 2016.

Pollard, D. and DeConto, R. M.: Modelling West Antarctic ice sheet growth and collapse through the past five million years, Nature, 458, 329–332, https://doi.org/10.1038/nature07809, 2009.

Pollard, D., DeConto, R. M., and Alley, R. B.: Potential Antarctic Ice Sheet retreat driven by hydrofracturing and ice cliff failure, Earth Planet. Sc. Lett., 412, 112–121, https://doi.org/10.1016/j.epsl.2014.12.035, 2015.

Price, S. F., Bindschadler, R. A., Hulbe, C. L., and Joughin, I. R.: Post-stagnation behavior in the upstream regions of Ice Stream C, West Antarctica, J. Glaciol., 47, 283–294, https://doi.org/10.3189/172756501781832232, 2001.

Priscu, J. C., Kalin, J., Winans, J., Campbell, T., Siegfried, M. R., Skidmore, M., Dore, J. E., Leventer, A., Harwood, D. M., Duling, D., Zook, R., Burnett, J., Gibson, D., Krula, E., Mironov, A., McManis, J., Roberts, G., Rosenheim, B., Christner, B. C., Kasic, K., Fricker, H., Lyons, W. B., Barker, J., Bowling, M., Collins, B., Davis, C., Gagnon, A., Gardner, C., Gustafson, C., Kim, O-S., Li, W., Michaud, Al., Patterson, M. O., Tranter, M., Venturelli, R., Vick-Majors, T., Cooper, E., and the SALSA Science Team: Scientific access into Mercer Subglacial Lake: scientific objectives, drilling operations and initial observations, Ann. Glaciol., 62, 1–13, 2021.

Retzlaff, R. and Bentley, C. R.: Timing of stagnation of Ice Stream C, West Antarctica, from short-pulse radar studies of buried surface crevasses, J. Glaciol., 39, 553–561, https://doi.org/10.3189/S0022143000016440, 1993.

Retzlaff, R., Lord, N., and Bentley, C. R.: Airborne-radar studies: Ice streams A, B and C, West Antarctica, J. Glaciol., 39, 495–506, 1993.

Scherer, R. P.: Quaternary and Tertiary microfossils from beneath Ice Stream B: Evidence for a dynamic West Antarctic Ice Sheet history, Glob. Planet. Change, 4, 395–412, https://doi.org/10.1016/0921-8181(91)90005-H, 1991.

Scherer, R. P., Harwood, D. M., Ishman, S. E., and Webb, P. N.: Micropaleontological analysis of sediments from the Crary Ice Rise, Ross ice Shelf, Antarctic JUS, 23, 34–36, 1988.

Shepherd, A., Ivins, E., Rignot, E., Smith, B., van den Broeke, M., Velicogna, I., Whitehouse, P., Briggs, K., Joughin, I., Krinner, G., Nowicki, S., Payne, T., Scambos, T., Schlegel, N., A, G., Agosta, C., Ahlstrøm, A., Babonis, G., Barletta, V., Blazquez, A., Bonin, J., Csatho, B., Cullather, R., Felikson, D., Fettweis, X., Forsberg, R., Gallee, H., Gardner, A., Gilbert, L., Groh, A., Gunter, B., Hanna, E., Harig, C., Helm, V., Horvath, A., Horwath, M., Khan, S., Kjeldsen, K. K., Konrad, H., Langen, P., Lecavalier, B., Loomis, B., Luthcke, S., McMillan, M., Melini, D., Mernild, S., Mohajerani, Y., Moore, P., Mouginot, J., Moyano, G., Muir, A., Nagler, T., Nield, G., Nilsson, J., Noel, B., Otosaka, I., Pattle, M. E., Peltier, W. R., Pie, N., Rietbroek, R., Rott, H., Sandberg-Sørensen, L., Sasgen, I., Save, H., Scheuchl, B., Schrama, E., Schröder, L., Seo, K.-W., Simonsen, S., Slater, T., Spada, G., Sutterley, T., Talpe, M., Tarasov, L., van de Berg, W. J., van der Wal, W., van Wessem, M., Vishwakarma, B. D., Wiese, D., and Wouters, B.: Mass balance of the Antarctic Ice Sheet from 1992 to 2017, Nature, 558, 219–222, https://doi.org/10.1038/s41586-018-0179-y, 2018.

Tebaldi, C., Debeire, K., Eyring, V., Fischer, E., Fyfe, J., Friedlingstein, P., Knutti, R., Lowe, J., O'Neill, B., Sanderson, B., van Vuuren, D., Riahi, K., Meinshausen, M., Nicholls, Z., Tokarska, K. B., Hurtt, G., Kriegler, E., Lamarque, J.-F., Meehl, G., Moss, R., Bauer, S. E., Boucher, O., Brovkin, V., Byun, Y.-H., Dix, M., Gualdi, S., Guo, H., John, J. G., Kharin, S., Kim, Y., Koshiro, T., Ma, L., Olivié, D., Panickal, S., Qiao, F., Rong, X., Rosenbloom, N., Schupfner, M., Séférian, R., Sellar, A., Semmler, T., Shi, X., Song, Z., Steger, C., Stouffer, R., Swart, N., Tachiiri, K., Tang, Q., Tatebe, H., Voldoire, A., Volodin, E., Wyser, K., Xin, X., Yang, S., Yu, Y., and Ziehn, T.: Climate model projections from the Scenario Model Intercomparison Project (ScenarioMIP) of CMIP6, Earth Syst. Dynam., 12, 253–293, https://doi.org/10.5194/esd-12-253-2021, 2021.

Tyler, S. W., Holland, D. M., Zagorodnov, V., Stern, A. A., Sladek, C., Kobs, S., White, S., Suárez, F., and Bryenton, J.: Using distributed temperature sensors to monitor an Antarctic ice shelf and sub-ice-shelf cavity, J. Glaciol., 59, 583–591, https://doi.org/10.3189/2013JoG12J207, 2013.

UNFCCC: Adoption of the Paris Agreement, FCCC/CP/2015/10/Add.1, 1–32, Paris, https://www.un.org/en/development/desa/population/migration/generalassembly/docs/globalcompact/FCCC_CP_2015_10_Add.1.pdf (last access: 10 February 2022), 2015.

Velicogna, I., Sutterley, T. C., and van den Broeke, M. R.: Regional acceleration in ice mass loss from Greenland and Antarctica using GRACE time-variable gravity data, Geophys. Res. Lett., 41, 8130–8137, https://doi.org/10.1002/2014gl061052, 2014.

Venturelli, R. A., Siegfried, M. R., Roush, K. A., Li, W., Burnett, J., Zook, R., Fricker, H. A., Priscu, J. C., Leventer, A., and Rosenheim, B. E.: Mid-Holocene Grounding Line Retreat and Readvance at Whillans Ice Stream, West Antarctica, Geophys. Res. Lett., 47, e2020GL088476, https://doi.org/10.1029/2020GL088476, 2020.

Vick-Majors, T. J., Michaud, A. B., Skidmore, M. L., Turetta, C., Barbante, C., Christner, B. C., Dore, J. E., Christianson, K., Mitchell, A. C., and Achberger, A. M.: Biogeochemical connectivity between freshwater ecosystems beneath the West Antarctic Ice Sheet and the sub-ice marine environment, Glob. Biogeochem. Cy., 34, e2019GB006446, https://doi.org/10.1029/2019GB006446, 2020.

Whitehouse, P. L., Gomez, N., King, M. A., and Wiens, D. A.: Solid Earth change and the evolution of the Antarctic Ice Sheet, Nat. Commun., 10, 1–14, https://doi.org/10.1038/s41467-018-08068-y, 2019.

Schedules

Due to the Corona pandemic situation, several expeditions and drilling projects are postponed until further notice.

IODP – Expedition schedule http://www.iodp.org/expeditions/

USIO operations	Platform	Dates	Port of origin
1 Exp 391: Walvis Ridge Hotspot	JOIDES Resolution	Dec 6, 2021–Feb 5, 2022	Cape Town, South Africa
2 Exp 392: Agulhas Plateau Cretaceous Climate	JOIDES Resolution	Feb 5–Apr 7, 2022	Cape Town, South Africa
3 Exp 390: South Atlantic Transect 1	JOIDES Resolution	Apr 7–Jun 7, 2022	Montevideo, Uruguay
4 Exp 393: South Atlantic Transect 2	JOIDES Resolution	Jun 7–Aug 7, 2022	Montevideo, Uruguay
5 Exp 377: Arctic Ocean Paleoceanography	MSP	Aug–Sep 2022	To be determined

ICDP – Project schedule http://www.icdp-online.org/projects/

ICDP project	Drilling dates	Location
1 A Strainmeter Array Along the Alto Tiberina Fault System (STAR)	Fall 2021–Spring 2022	Central Apennines (Italy)
2 Barberton Archean Surface Environments (BASE)	Fall 2021–Spring 2022	South Africa
3 Bushveld Drilling Project (BVDP)	Spring 2022	South Africa
4 Geological Research through Integrated Neoproterozoic Drilling (GRIND)	Spring–Summer 2022	Namibia, Brazil, China
5 Drilling the Ivrea-Verbano ZonE (DIVE)	Late Spring 2022	North Italy

Locations

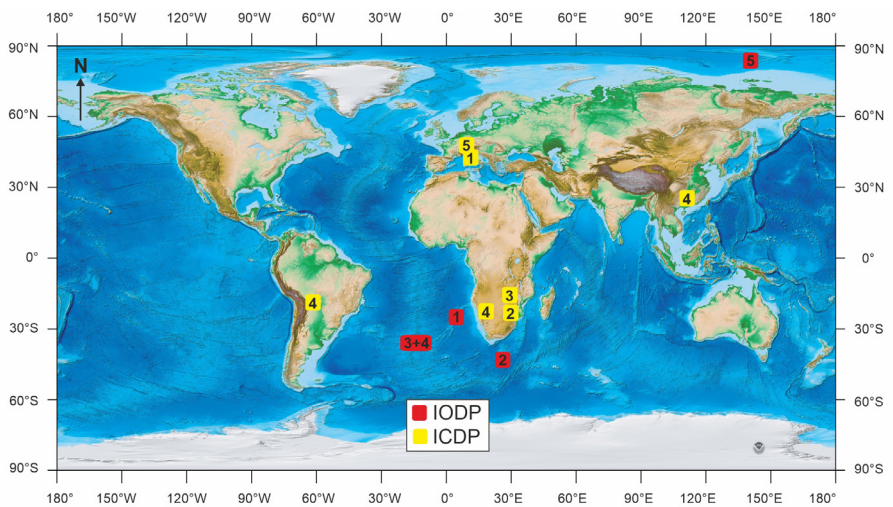

Topographic/bathymetric maps courtesy of NOAA (Amante, C. and B.W. Eakins, 2009. ETOPO1 1 Arc-Minute Global Relief Model: Procedures, Data Sources and Analysis. NOAA Technical Memorandum NESDIS NGDC-24. National Geophysical Data Center, NOAA. doi:10.7289/V5C8276M).